L

Experimental Investigation of a Kaplan Runner Under Steady-State and Transient Operations

Kaveh Amiri

Fluid Mechanics

LULEÅ
UNIVERSITY
OF TECHNOLOGY

Experimental Investigation of a Kaplan Runner Under Steady–State and Transient Operations

Kaveh Amiri

PREFACE

The work presented in this thesis was conducted at the Division of Fluid and Experimental Mechanics, Department of Engineering Sciences and Mathematics, Luleå University of Technology, Sweden between 2011 and 2016. The research presented in this thesis was carried out as a part of the "Swedish Hydropower Centre - SVC". I have learned so much over these years, which would not have been possible without the support of my family, friends, and colleagues. I wish to take this opportunity to thank as many of them as I can.

First, I would like to express my sincere gratitude to my supervisor, Professor Michel Cervantes, for his admirable support and continuous encouragement in each and every step of my research and education. I appreciate his kindness, patience, and self-devotion. I also would like to thank my co-supervisors Dr. Berhanu Mulu and Professor Mehrdad Raisee for all the fruitful discussions and guidance. Special thanks go to Dr. Mulu for his support during the measurements and data analysis.

I would like to thank all my colleagues at the Division of Fluids and Experimental Mechanics for providing a pleasant and enjoyable work environment. Special thanks go to Henrik Lycksam for his help with the laboratory work. I would like to thank my office-mates Joel and Chirag for all the constructive discussions, joy and happiness we shared throughout the years.

My heartfelt thanks go to all my friends in Luleå, especially Saleh, Narges (Khanum Na), Arash, Hamid, Ehsan, Momo, Rasoul, Shahin, and Ali. Your friendship made Luleå a wonderful place full of joy, happiness, and unforgettable memories for me.

I would like to express my deepest gratitude to my immediate family: Meisam, Parisa, Vida, and especially my parents for supporting and encouraging me throughout my life. I could never have made it without their endless love and support.

And last, but far from the least, I would like to express my heartfelt gratitude to my beloved wife, Alaleh, to whom this thesis is dedicated. None of this could have been done without her love, concern, patience and support.

Kaveh Amiri
Luleå, August 2016

ii

ABSTRACT

Hydropower is currently a key component of electricity production. Hydropower electricity production rose to 3579.5 TWh in 2013 and ranked as the second largest source of electricity production in the world after fossil fuels. Hydropower is the principle source of renewable electricity production, producing 16.2% of electricity in 2013, accounting for 78% of renewable electricity production in the world. In Sweden in particular, hydropower is the main source of electricity production, producing 47.5% of all required electricity. Nuclear, biomass, and wind accounted for 38.4%, 6.5%, and 4.3% of all electricity production in 2013, respectively.

In addition to meeting electricity demand through an environmentally friendly method, hydropower has the unique and important role of grid regulation: balancing electricity production and consumption. Gas turbines and hydraulic turbines designated "primary reserves" are the only electricity production systems that can be used for fast regulations because of their short start-up time, which ranges from 1 to 60 s. The obvious environmental problems, air pollution, and costs associated with gas turbines make hydropower a prime alternative whenever applicable. In Sweden, the share of fossil fuels in electricity production is small: 2.8% in 2012 with an average annual growth of -0.7% over the period 2002-2012. Hence, hydropower is practically the only available source used to regulate the grid fluctuations resulting from a deregulated market and the fast growth of intermittent power generation systems, i.e., solar and wind energy.

Hydraulic turbines are subject to frequent off-design and transient operations because of their grid regulation responsibility. Such operating conditions decrease the efficiency of turbines and significantly affect their lifetime. Off-design and transient operation of hydraulic turbines may induce unpredicted pressure fluctuations in the stationary and rotating parts of the turbine. Special attention should be dedicated to the effects of such phenomena on the runner blades because of their importance to the efficiency of the turbine and their vulnerability to pressure fluctuations.

This thesis presents an experimental investigation of the effects of off-design and transient operation of an axial hydraulic turbine on velocity fields and pressure fluctuations exerted on the runner and the draft tube of a turbine. The investigation was performed on a 1:3.1 scaled model of a Kaplan turbine known as Porjus U9. The main objective was to investigate the effect of the operating point on pressure and velocity fluctuations in the runner and the draft tube. Another objective was to study the effect of transient operation on pressure fluctuations exerted on the runner and the draft tube, to investigate the formation and mitigation process of a rotating vortex rope (RVR) within the draft tube. Finally, the effect of the swirl leaving the runner and the draft tube bend on the performance of the turbine was investigated. The study involves pressure measurements on the runner blades and draft tube walls of the turbine, laser Doppler anemometry (LDA) measurements within and after the runner, and particle image velocimetry (PIV) measurements within the draft tube.

The pressure and LDA results acquired during steady-state operation of the turbine revealed different sources of fluctuations on the runner at different operating points, resulting in symmetric and asymmetric fluctuating forces on the runner. The pressure measurements performed during transient operating conditions revealed pressure fluctuations exerted on the runner during load variations and elucidated certain aspects of the formation and mitigation of a RVR within the draft tube. PIV measurements performed after the draft tube bend of the turbine focused on the physical phenomena resulting in flow asymmetry after the draft tube bend of hydraulic turbines, affecting their efficiency.

iv

NOMENCLATURE

A	Area
D	Turbine runner diameter
D_b	Pipe diameter
e	Specific head
f	Frequency
$f_{RVR,\text{st}}$	Frequency of rotating vortex rope in stationary frame (plunging mode)
g	Gravitational acceleration
H	Turbine head
h_{loss}	Head loss
N	Turbine rotational speed (rpm)
n	Turbine rotational frequency (Hz)
n_{11}	Turbine reduced speed
n_{ED}	Speed factor
P	Pressure
P_{out}	Output power
Q	Turbine flow rate
Q_{11}	Turbine reduced flow rate
Q_{ED}	Discharge factor
r	Radial position
R_c	Bend radius
R_h	Hub radius
R_t	Tip radius
Sw	Swirl number

t	Time
t_{gen}	Transition time
U	Axial velocity
u	Fluctuating part of axial velocity
V	Tangential velocity
v	Fluctuating part of tangential velocity
V_θ	Tangential velocity
$\dot{W}$	Power
α_{GV}	Guide vane angle
β_b	Runner blade installation angle
η	Turbine efficiency
θ	Angular position
μ	Dynamic viscosity
ν	Kinematic viscosity
ρ	Density
φ_{rot}	Phase of the pressure fluctuations due to the rotating mode of the RVR
φ_{st}	Phase of the pressure fluctuations due to the plunging mode of the RVR
ω	Rotational speed of runner
σ	Standard deviation

Abbreviations

BEP	Best Efficiency Point
CFD	Computational fluid dynamics
DNS	Direct numerical simulation
FFT	Fast Fourier transform

HL	High load
LDA	Laser Doppler anemometry
PIV	Particle image velocimetry
PL	Part load
PSD	Power spectral density
RVR	Rotating vortex rope

Subscripts, superscripts and operators

'	Random fluctuation of the signal
~	Periodic oscillation of the signal
¯	Time-averaged
*	Normalized parameter; velocities, lengths and frequencies are made dimensionless using reference velocity, runner diameter and runner
<>	Phase-averaged signal

CONTENTS

LIST OF TABLES

LIST OF FIGURES

Chapter 1

INTRODUCTION

"Water is the driving force of all nature."

Leonardo da Vinci

The term "hydraulic turbine" indicates a device in which the operating member (usually runner) receives energy from a liquid that flows through said device [1]. The idea of benefiting from the energy of moving fluids, especially water, to decrease human workload is an ancient one. The Romans were grinding corn with waterwheels as early as 70 B.C. [2]. Using water turbines for electricity production began even before the invention of alternating current generators. The world's first hydroelectric project was used to power a single lamp in the Cragside country house in Northumberland, England, in 1878 [3]. Using water turbines to provide arc lighting to a theater and storefront in Grand Rapids, Michigan in 1880 and providing street lighting at Niagara Falls, New York in 1881 were the first commercial electricity production that used hydropower systems [4]. The Olidan power station, which was constructed in 1910, was the first large-scale attempt to generate electricity from water in Sweden.

Nowadays, hydropower plays a key role in electricity production worldwide, increasing to 3579.5 TWh in 2013, which was ranked as the second largest source of electricity production in the globe after fossil fuels, as presented in Fig 1.1. The six sources of renewable electricity, which are hydropower, wind power, biomass, solar power, geothermal and marine power, comprise 20.8% of the electricity production across the globe. Amongst all the sources, hydropower is the principle source of renewable electricity production, producing 16.2% of all electricity in 2013, and constitutes 78% of all the renewable electricity production in the world.

Figure 1.2 illustrates the mean annual growth rate of different energy sources in the world within a period of ten years. The results show that solar and wind energy experienced the highest annual growth rate among all the resources that are used for electricity production. However, considering the absolute value of the electricity production rise in each source during this period, hydro-electric production ranked second by an increase of 957.5 TWh in electricity production; see Table 1.1. Despite the higher percentage of the annual growth rate in electricity production from the other

renewable resources, the absolute increase in wind and solar electricity production was much smaller than that in hydropower, as presented in Table 1.1. South, East and Southeast Asia experienced the highest hydro-electricity production growth during the investigated period [5].
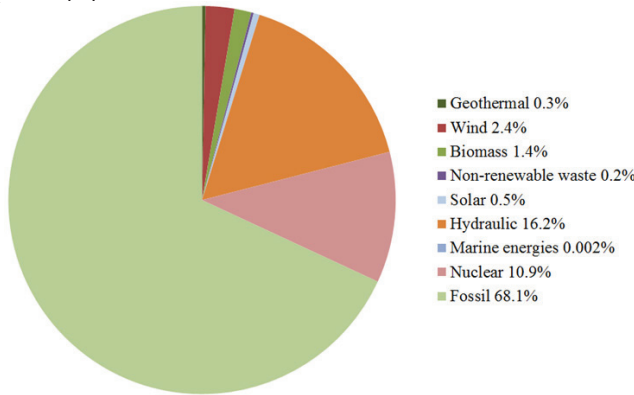
Fig 1.1.   Structure of electricity production in 2013. The graph was reproduced from [5].
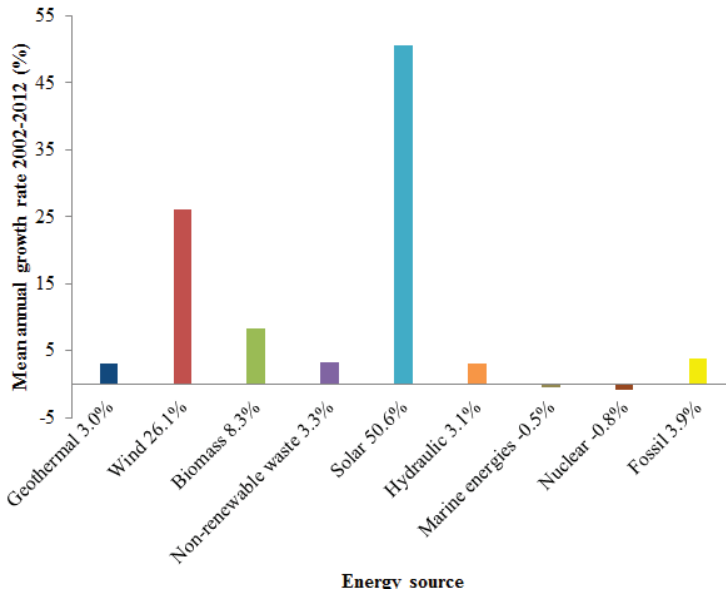
Fig 1.2.   Mean annual growth of the electricity production resources from 2002 to 2012. The graph was reproduced from [5].

Transition to renewable energies in Sweden began in the 1970s following the oil crisis. Sweden decided to limit its dependency on hydrocarbon imports by investing in renewable and nuclear resources. Sweden is one of the few developed countries that produce most of its electricity from renewable energy sources (58.4% in 2012). In 2010, Sweden generated 67 TWh hydro-electricity, making Sweden the largest hydropower producer in the European Union and the tenth largest across the globe [6]. In 2012, hydroelectricity production reached 78.6 TWh, an 18.1% yearly rise, which was a new record, while only 50% of the country's potential was extracted [5].

Table 1.1.   World electricity production by source: 2002 vs. 2012 [5].

Source	2002 (TWh)	2012 (TWh)	10-years growth (TWh)
Geothermal	52.2	70.4	18.2
Wind	52.5	534.3	481.8
Biomass	147.1	326.2	179.1
Non-renewable waste	40.5	56	15.5
Solar	1.7	104.5	102.8
Hydraulic	2 705.9	3 663.4	957.5
Marine energies	0.568	0.54	-0.028
Nuclear	2 660.8	2 463.5	-197.3
Fossil	10 512.4	15 394.3	4881.9

1.1. Development of reaction turbines

Water power has been utilized for thousands of years with different types of water wheels for different purposes, mainly in flour mill industries. However, the first scientific approaches in describing the principles of reaction water turbines occurred with Segner's water wheel and Barker reaction wheel, which were developed in Germany and England around 1770 [7]. A sketch of Segner's reaction water wheel is presented in Fig 1.3. The working liquid, in this case water, is fed to the machine from the pipe inlet on top. The water ejected from the nozzles contrived at the tip of the bent pipes. The produced torque is transferred to a power device. Such turbines have been used for power generation in the 19th century. Segner's water wheel was used to empower the inclined plane lifts along the Morris Canal in New Jersey, for example. However, its current principle application is in irrigation sprinklers.
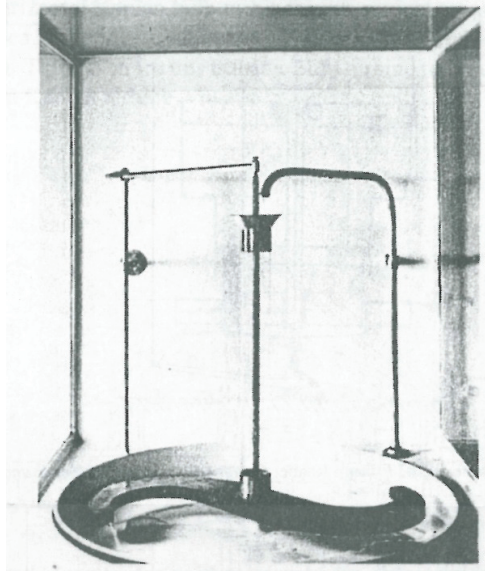
Fig 1.3.   Segner's reaction water wheel from 1770 [7].

In 1836, Hovd patented a centripetal reaction turbine. The famous British engineer, James B. Francis, developed Hovd's idea by introducing movable guide vanes to the turbine, which increased the efficiency and decreased turbine noise. Such turbines are classified as single regulated reaction turbines because their only tool for regulating

the turbine's power is the guide vanes. Figure 1.4 shows a schematic drawing of a Francis turbine. Francis turbines have widely been used for electricity production all over the world. In 1903, the most powerful turbines that were installed in Niagara Falls were Francis turbines, with an output power of 5.2 MW at 79.5 m head. The power capacity of Francis turbines has been increased drastically after a century. For instance, each powerhouse in the Xiangjiaba hydropower plant in China consists of four Francis turbines with 800 MW power. These turbines are claimed to be the most powerful turbines in the world [8]. Each unit can supply the required electricity for approximately 5 million people. The Three Gorges Dam, the world's largest hydropower plant, uses 32 Francis turbines, each with a capacity of 700 MW [9].
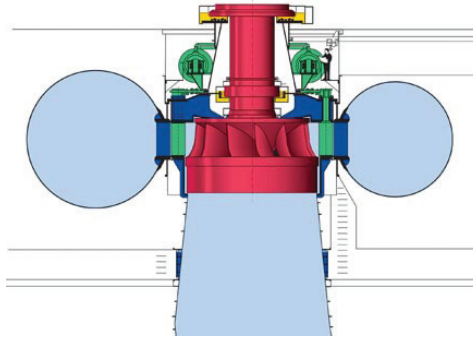
Fig 1.4.   Sectional drawing of the Francis turbine that is used at the Belo Monte power plant, Xingu River, Brazil. Courtesy of Voith-Siemens, Germany.

The other main type of reaction turbines was patented by the Czechoslovakian-Austrian professor Victor Kaplan in 1913. This turbine type is named Kaplan turbines, after the name of the inventor. Kaplan turbines are an axial (i.e. the working fluid enters axially to the runner) propeller-like turbine with adjustable runner blades. Kaplan turbines are classified as double regulated reaction turbines because the flow conditions are controlled by both adjustable guide vanes and runner blades' installation angles. The first Kaplan turbine was commissioned in Velm, Austria.

Water turbines suffered from cavitation-related problems until a Swedish company named Karlstad Mekaniska Verkstad built a cavitation test rig for model testing. In 1926, the world's largest Kaplan turbine with a runner diameter of 5.8 m was designed and manufactured based on the laboratory tests in Karlstad Mekaniska Verkstad [10]. The turbine sketch is illustrated in Fig 1.5. The leverage system that is used to adjust the runner blades still stands as a basic design for large modern Kaplan turbines.

The world's most powerful Kaplan turbine, which was installed at the Manuel Piar Hydropower Plant, Tocoma, Venezuela, has a maximum power output of 232 MW. Kaplan turbines are generally designed for lower heads and higher flow rates compared to Francis turbines. However, one of the main specifications of Kaplan turbines is their flat efficiency curve over a wide operating range compared to Francis turbines, which allows them to operate in a wide range, an ideal case for grid regulations.
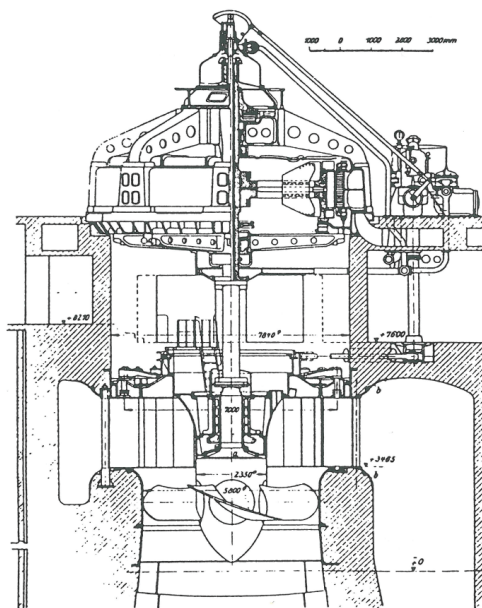
Fig 1.5.   Cross section of the Kaplan turbine at the Lilla Edet power station in Sweden [7].

Horizontal Kaplan bulb turbines and propeller turbines are similar to Kaplan turbines and can be considered in the same family as Kaplan turbines. Horizontal Kaplan bulb turbines have a conical arrangement of guide vanes and propeller turbines are simply Kaplan turbines with a constant runner blade installation angle.

1.2. Principles of Kaplan turbines

Energy from the Sun is the main direct source of energy that drives the hydrological cycle. The Sun warms up water from the oceans and surface water, resulting in water evaporation. As moist air is lifted, it cools down and condenses to form clouds. Clouds are transported around the globe by wind. Moisture returns to the Earth in the form of precipitation, either to the oceans or on land. Rain on the ground and melted snow evaporate again, penetrate the surface to form ground water, or form Earth surface water, which is called runoff. Basically, all water eventually returns back to the oceans. The basic role of a hydropower system is extracting energy from water in this cycle.

Required head and continuous water flow are the main requirements for reaction turbines, including Kaplan turbines, which are the subject of the current study. Building a dam or weir is the main method to provide the required head and store water to be used when needed for electricity production. Current technology cannot store electricity on a large scale[1]. Hence, a balance should exist between electricity production and

---

[1] Although no batteries are included in grids, some technologies are being developed to save electricity. For instance, batteries for electric cars are a device for saving electricity, which can be used afterwards to power other electric devices. However, practical issues such as battery life time, economic issues, the capacity of batteries, etc. are the main limitations in such applications. Pump turbines are also systems

consumption. Managing such a balance requires the availability of natural resources for conversion to electricity and the presence of machines for grid regulations. Such machines should be fast enough to compensate for grid fluctuations. The only electricity production systems with such characteristics are water turbines and machines that use fossil fuels for electricity production, such as gas turbines.

Figure 1.6 illustrates a schematic diagram of a hydropower station with a reaction turbine. A typical hydropower plant with a reaction turbine is composed of a dam, penstock, spiral casing, distributor, runner, draft tube and generator. The dam stores water to be used for electricity production when needed and creates a head difference between the upstream and downstream water level of the power plant, which are marked as "reservoir" and "tailrace" in the figure, respectively. The penstock delivers water from the reservoir to the spiral casing. The spiral casing's function is to distribute water as evenly as possible to the distributor, where stay vanes and guide vanes are located, and ensure symmetrical flow is fed to the runner. A top view of a spiral casing is illustrated in Fig 1.7. Stay vanes are used as structural supports for the spiral casing and distributor and are simply cylindrical rods in some turbines. However, in most cases, these devices are hydraulically shaped to decrease losses and increase turbine efficiency. Guide vanes are moveable vanes that are used to control the flow rate through turbines, which are the main factor in controlling the output power of hydraulic turbines. Then, the swirling water enters the runner, where its energy is extracted and transformed into mechanical energy. This mechanical energy is transferred to the generator through a rotating shaft and converted into electricity. The transformer increases the voltage, and consequently decreases the electrical current (power is the product of the voltage and the current) and loss in transmission lines. Finally, the water is ejected to the tailrace water through the draft tube.
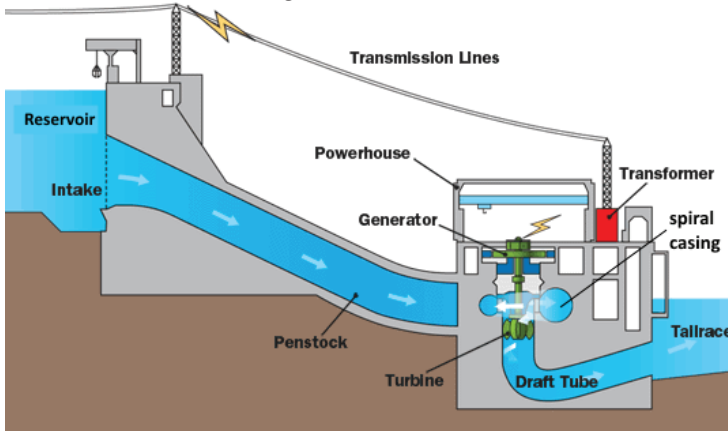
Fig 1.6.   Schematic diagram of a hydropower station [11].

---

that can save electricity. Although they do not actually save electricity; they transform electricity to the potential energy of water when demand is low and convert it to electricity again when demand is high.
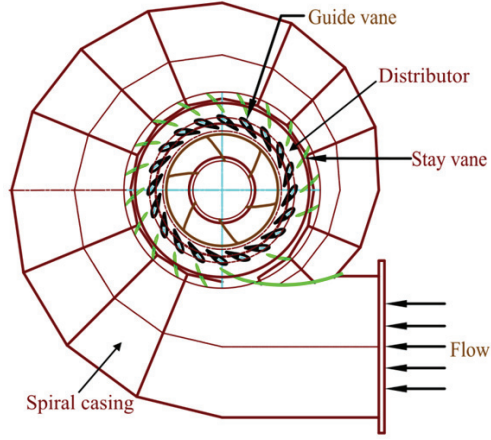
Fig 1.7.   Top view of a spiral casing.

1.2.1. Governing equations

Figure 1.8 shows a schematic of a power plant where a turbine is installed between a headwater and a tailwater. The headwater and tailwater elevations are z_{hw} and z_{tw}, respectively. The difference between z_{hw} and z_{tw} is called the static head:

$$H_{st} = z_{hw} - z_{tw} \tag{1-1}$$

The head of a turbine is defined as the difference between the specific energies between the turbine inlet and outlet, e_1 and e_{out}, respectively:

$$H = e_1 - e_{out} \tag{1-2}$$

which is one of the main parameters affecting turbine power. The turbine power is equal to

$$\dot{W} = \rho g H Q \eta \tag{1-3}$$

where $\dot{W}$ is the turbine's output power, ρ is the fluid density, g is the gravitational acceleration, Q is the volume flow rate and η is the turbine efficiency. The specific energy at turbine inlet is

$$e_1 = \frac{P_1}{\rho g} + z_1 + \frac{\alpha_1 v_1^2}{2g} \tag{1-4}$$

where α is kinetic energy correction factor, which is defined as $\frac{1}{A\bar{v}^3} \iint v^3 dA$. The fluid specific energy at section 0 equals the sum of the fluid specific energy at 1 and the head loss between point 0 and 1:

$$\frac{P_1}{\rho g} + z_1 + \frac{\alpha_1 v_1^2}{2g} + h_{loss} = \frac{P_0}{\rho g} + z_0 + \frac{\alpha_0 v_0^2}{2g} \tag{1-5}$$

The first term on the right-hand side equals h_0, as shown in Fig 1.8, and $h_0 + z_0 = H_{st}$. Substituting the first two terms on the right hand side of (1-5) with H_{st} produces

$$\frac{P_1}{\rho g} = H_{st} - z_1 + \frac{\alpha_0 v_0^2}{2g} - \frac{\alpha_1 v_1^2}{2g} - h_{loss} \tag{1-6}$$

Considering section A-A as the turbine outlet, the specific energy can be written as

$$e_{out} = \frac{P_{A-A}}{\rho g} + z_{A-A} + \frac{\alpha_{A-A} v_{A-A}^2}{2g} = \frac{\alpha_{A-A} v_{A-A}^2}{2g} \tag{1-7}$$

Inserting (1-4), (1-6) and (1-7) in (1-2) produces

$$H = H_{st} - h_{loss} + \frac{\alpha_0 v_0^2}{2g} - \frac{\alpha_{A-A} v_{A-A}^2}{2g} \tag{1-8}$$

Equation (1-8) shows that the turbine head increases when the outlet velocity decreases. Hence, as shown in Fig 1.8, a draft tube is usually installed at the runner outlet to decrease the outlet velocity to extract as much energy as possible from the water and convert it into electricity. Considering the tail water section in Fig 1.8 as the turbine outlet and by using the same method, we have

$$H = H_{st} - h_{loss} + \frac{\alpha_0 v_0^2}{2g} - \frac{\alpha_{tw} v_{tw}^2}{2g} \tag{1-9}$$

Because the difference between the velocity heads at the inlet and outlet is small, the last two terms can be neglected. The resulting expression for the turbine head is widely used in turbine design processes:

$$H = H_{st} - h_{loss} \tag{1-10}$$

Hence, the turbine output power can be written as

$$\dot{W} = \rho g (H_{st} - h_{loss}) Q \eta \tag{1-11}$$
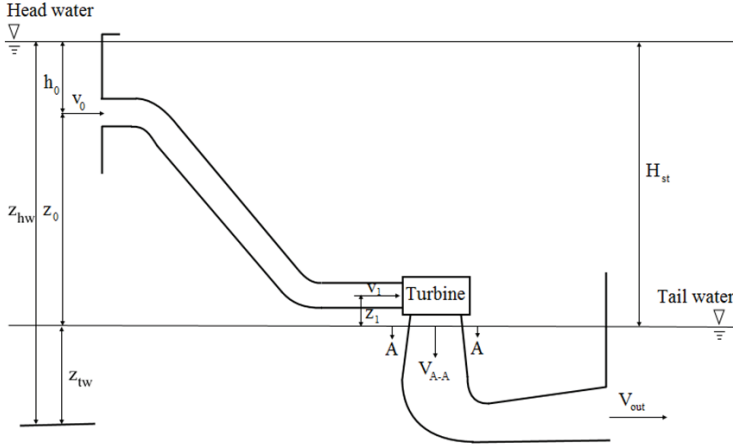
Fig 1.8.   Schematic of a turbine that is installed at a power plant.

The turbine output power can be calculated by considering the conservation of angular momentum, which states that the change in angular momentum in the working fluid equals the sum of the external moments. The equation for a steady state flow at the inlet and outlet of the runner is

$$\tau = \rho Q(r_1 V_{\theta 1} - r_2 V_{\theta 2}) \qquad (1\text{-}12)$$

where $V_{\theta 2}$ and $V_{\theta 1}$ are the flow tangential velocity at the runner outlet and inlet, respectively. The shaft output power equals the product of the torque and the rotational speed of the runner:

$$\dot{W} = \rho Q(\omega r_1 V_{\theta 1} - \omega r_2 V_{\theta 2}) = \rho Q(U_1 V_{\theta 1} - U_2 V_{\theta 2}) \qquad (1\text{-}13)$$

where ω is the runner's rotational speed and U_1 and U_2 are the inlet and outlet runner velocity at a radius where the calculations are performed; usually, this radius is at the blade's mid-span. This equation is called Euler's equation for turbomachines. U_1 equals U_2 in a Kaplan turbine, so the tangential velocity at the runner outlet should be close to zero, and the runner inlet velocity should be maximized to maximize the output power. High swirl at the runner inlet is produced by a combination of the spiral casing's geometry and vanes that are located in the distributor.

1.3. Turbines in grid

Most of the large-scale hydropower plants in Sweden were built in the 1940-70s. Hydropower systems were initially used to produce base load electricity, which is the amount of constantly needed electricity. However, deregulation in the electricity market, changes in electricity production sources by introducing nuclear, wind and solar energies to the grids, and the key role of electricity in everyday life have changed the role of hydropower plants. The electricity demand changes all the time, and electricity generation should follow fluctuations in the demand. Different power plant types have different roles in the grid to meet the requirements at base load, power regulations, and peak load. Nuclear power has a negligible fuel cost, but the more stable production profile of these power plants makes them suitable for base load production [12]. In 2013, nuclear power plants generated 65.8 TWh of electricity in Sweden, which was almost 43% of the electricity demand [13]. In Sweden, nuclear power plants are used for the base load by running day and night most of the year because of the slow and complicated process of regulating the output power of a nuclear reactor. The power output from wind turbines and solar systems varies with the wind speed and the Sun's availability, respectively. Thus, such sources cannot be used as base load as they do not have any storage capabilities. These sources can neither be used as regulating power to cover peak power consumption because they cannot be controlled as a function of demand. Primary reserves (power plants with very short start-up time from 1 to 60 s) are used for fast regulations of grid fluctuations. Power plants that are used for this purpose are gas turbines and hydropower systems [14]. The share of fossil fuels in electricity production in Sweden is very small: 2.8% in 2012 with an average annual growth of -0.7% from 2002 to 2012 [5]. Thus, the only available source for regulating electricity within the grid is hydropower, while these sources were originally designed for base load electricity generation.

These changes substantially increased the number of start-stops, transients and off-design operations of water turbines. Each of these operating conditions can be harmful to water turbines because these devices were not originally designed to be used under such conditions. Thus, researchers have investigated the effect of such operating conditions on the flow conditions within hydraulic turbines and on their lifetime.

1.4. Previous studies

Flow in a reaction turbine is complex because of various flow phenomena that occur simultaneously, such as rotor-stator interactions, swirling flows, vortices, turbulence, unsteadiness, separation and adverse pressure gradients. Understanding the flow conditions within hydraulic turbines and its effects on turbine performance and lifetime and investigating possible remedies for each phenomenon that negatively affects turbines have previously been the subject of different studies. Advanced measurement techniques such as laser Doppler anemometry (LDA or LDV), particle image velocimetry (PIV) and pressure measurements have been implemented to investigate the design and off-design operation of turbines. More recently, special focus has been dedicated to flow investigations during the transient operation of hydraulic turbines, such as load variation, start-stops, runaway, and speed-no-load conditions.

Experimental investigations of flow condition inside the draft tubes of hydraulic turbines have been the subject of numerous studies because of the importance of draft tubes on the performance of turbines, especially low head turbines. Much of this work has been dedicated to Francis turbines, which are the most used hydraulic turbines in the world; Francis turbines produce around 60% of the hydropower-based electricity worldwide. The Laboratory of Hydraulic Machinery in École Polytechnique Fédérale de Lausanne (EPFL) has been the pioneer in investigating Francis turbines. Arpe and Avellan [15] performed intensive pressure measurements on the draft tube wall of a Francis turbine at different operating points. Ciocan et al. [16] performed PIV and LDA measurements at the runner inlet and outlet of a Francis turbine to investigate the rotor-stator interactions and flow conditions at the draft tube inlet of the model. The flow conditions inside the draft tubes of Francis turbines have also been studied at off-design operations with different optical methods [17-23]. The Water Power Laboratory at the Norwegian University of Science and Technology (NTNU) has also contributed in flow investigation inside draft tube of Francis turbines [24-30]. Their scaled model of the Francis turbine that was installed at the Tokke power plant is the test case study of a workshop series (Francis-99 workshop). These workshops aim to study the steady and transient operation of the turbine, rotor-stator interaction, etc. The research group at the Laboratory of Hydraulic Machinery at the University of Laval has also been active in investigating the flow within the draft tubes of hydraulic turbines by experimentally studying a propeller turbine model [31-33]. More recently, the Division of Fluid and Experimental Mechanics at the Luleå University of Technology began to investigate the flow conditions inside a Kaplan turbine model named Porjus U9 under different operating conditions by implementing pressure and LDA measurements within the draft tube [34-39].

Despite draft tubes, measurements have rarely been performed in the runners of hydraulic turbines because of the specific challenges in performing such measurements and the specific instruments that are required. Farhat et al. [40] performed pressure measurements on the runner blades of a Francis turbine model during steady state operations. Investigating the rotor-stator interactions was the main objective of this work. Kobro performed pressure measurements on the runner blades of a Francis model and the corresponding prototype under steady state operation [26]. The effects of the operating point and different transient operations on the loads that are exerted on the runner blades of the Francis model have also been investigated [41-49]. Velocity measurements within the cascade of a propeller [50] and a bulb turbine [51] were performed to investigate secondary flows within the cascades. Stereoscopic PIV and innovative methods of endoscopic PIV were used for these measurements, respectively.

Previous studies have shown that one of the most harmful operating conditions of water turbines is when a single regulated water turbine operates at flow rates that are lower than that at its design point, namely, the part load (PL). Runners of single regulated turbines are designed such that the water leaves the runner nearly parallel to the turbine axis and without swirl at the design point. This criterion is required to optimize the performance of the draft tube and minimize losses in the draft tube. However, these runner blades are not adjusted for the off-design operation of the turbines. When a single regulated turbine operates under PL operating conditions, the flow that leaves the runner has excess swirl. If this swirl exceeds a threshold, the flow is pulled out towards the outer part of the draft tube because of centrifugal forces. Thus, a recirculation bubble region forms at the draft tube center [52] and a rotating vortex rope (RVR) forms between the recirculation region and the outer flow. Figure 1.9 illustrates a schematic of a Francis turbine with an RVR that has formed inside its draft tube.
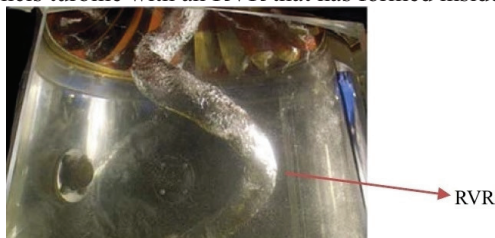
Fig 1.9.   Sketch of a Francis turbine with an RVR that has formed inside the draft tube under part load operation [18].

The formation of RVRs is not specific to water turbines. RVRs may form in swirling flows, which have wide applications in industrial flows. The formation of RVRs is attributed to "vortex breakdown" or "vortex bursting" phenomena. Many studies have been dedicated to understanding vortex breakdown because of its wide application in combustion and fluid dynamics processes, such as in gas turbines, diesel engines, burners, boilers and hydraulic turbines. The review by Lucca-Negro and O'Doherty [53] concluded that "despite the extensive experimental, numerical and theoretical research undertaken over several decades, the phenomenon of vortex breakdown remains controversial and no generally accepted explanation has emerged". Vortex breakdown phenomena have mainly been studied under simplified cases of swirling flows with low Reynolds numbers (generally 10^3 to 10^4) in straight pipes or slightly diverging tubes. Swirling flows may lead to different types of vortex breakdown. The review by Lucca-Negro and O'Doherty [53] proposed seven distinct modes of vortex breakdown, in which "axisymmetric mode or bubble type", "Spiral mode" and "double helix" are the most predominant modes. These authors related the initiation of the recirculation region/vortex breakdown to an adverse pressure gradient and concluded that increasing the swirl reaches a threshold when the adverse pressure gradient along the jet axis cannot be further overcome by the kinetic energy of the fluid particles that are flowing in the axial direction. Consequently, a recirculation flow occurs in the central portion of the jet. This process can also be valid for internal flows. The method by which the swirl is generated, the fluid's Reynolds number, the swirl intensity and the adverse pressure gradient are some of the parameters that affect the type and position of vortex breakdown. Observations have shown that an adverse pressure gradient and a lower Reynolds number can move the breakdown point upstream or even initiate the breakdown phenomenon. Cassidy and Falvey [54] showed that both the pressure parameter ($\Delta P D^3 / \Omega$) and frequency parameter ($f D^3 / Q$), which are representatives of the amplitude and frequency of pressure fluctuations that are

associated with vortex breakdown, respectively, are linearly dependent to the momentum parameter ($\Omega D/\rho Q^2$). However, the winding direction of the spiral has been observed to be both in the sense of the rotation of the outer flow or opposite to that. At the end of their extensive review, Lucca-Negro and O'Doherty [53] concluded that "Many interesting interpretations have been brought up by different investigators. However, while an explanation appears to agree very well with one (or several) characteristic(s) of the phenomenon, it usually cannot satisfy all the observed features."

Delbende et al. [55] proposed the concept of the absolute/convective instability (AI/CI) of azimuthal modes as a criterion for the initiation of vortex breakdown in swirling flows. These authors proposed an AI/CI transition curve that was based on constants of a Rankin vortex (a and q), whose non-dimensional velocity components can be defined as

$$U_a = a + e^{-r^2} \tag{1-14}$$

$$U_r = 0 \tag{1-15}$$

$$U_\theta = q\frac{1 - e^{-r^2}}{r} \tag{1-16}$$

where U_a, U_r, and U_θ are the axial, radial and tangential velocities, respectively; q is the swirl parameter; and a is a measure of the free-stream axial velocity far from the axis. For more details, please refer to Delbende et al. [55]. The AI/CI concept was used to interpret the DNS results of a three-dimensional vortex breakdown by Ruith et al. [56]. Broudhurst [57] investigated the relationship between vortex stability and breakdown and assessed the influence of the pressure gradient on vortex stability and breakdown. This author showed that a Batchelor vortex was unstable to helical modes for a swirl value of $q = 0.8$, and an asymmetric breakdown developed because of the sensitivity to helical disturbances. On the other hand, a Batchelor vortex was stable to helical eigenmodes for a swirl value of q = 1.6, and axisymmetric bubble breakdown predominated. However, this bubble may be succeeded by a spiral in its wake. This author also showed that adverse pressure gradients promote vortex breakdown. Conversely, favorable pressure gradients were found to inhibit breakdown. Zhang et al. [58] estimated the velocity profiles at the draft tube inlet of a Francis turbine with a Rankin vortex and proved the applicability of AI/CI transition curves to complicated flow within the draft tube of the investigated model.

Vortex breakdown and the formation of "spiral mode" vortex instability in the draft tubes of single regulated hydraulic turbines (or RVR formation) is a common phenomenon when turbines are operating at PL operating points. RVRs significantly decrease turbine efficiency. This efficiency decrease was greater than 15 % for a turbine that was operating at PL during measurements by Amiri et al. [59]. In addition to this drop in efficiency, RVRs induce harmful pressure fluctuations to different parts of the turbine, especially the draft tube and the runner. Initial results regarding this phenomenon were reported by Rheingans in 1940 [60]. After more than seventy years of research on this subject, RVRs still remain a subject of research because of associated flow complexity and its negative effects on turbines performance and lifetimes. Several research groups have been attempting to find the source of RVR formation and its effects on turbines [17, 18, 61-64]. Various methods have been proposed to mitigate RVRs: air injection in draft tubes [65], fins that are mounted on the draft tube cone [66], extended cones that are attached to the runner hub [28], J-grooves [67] and water jets from the runner hub [64]. However, no method has been universally

used to address this problem because of the limitations of each method. Air injection is the most commonly used method to suppress RVR-related fluctuations [68]. However, this method cannot be considered as a final solution to this problem because the efficiency loss is not regained and because the pressure amplitudes are sometimes amplified. Such operating conditions should be considered during the design stage of newly designed turbines or during the overhaul of old turbines. Thus, studying the flow conditions during the off-design and transient operation of water turbines is required.

1.5. Scope of the thesis

The off-design operation of hydropower and the number of transient operations and start-stops have recently increased, as discussed earlier. The new role of hydropower in stabilizing grid operation should be considered in the design of new turbines and overhaul of old turbines. Thus, the design and manufacturing of more robust turbines during transient and off-design operations should be considered, which requires more detailed knowledge regarding the fluid dynamics of water turbines. Two main tools for such an investigation include model testing and computational fluid dynamics (CFD).

Model testing is the traditional method of studying flow conditions and controlling the performance of large hydropower systems [34]. More flexible and controlled testing conditions compared to measurements on prototypes, lower costs, a higher level of safety and more accessibility for measurements are the main reasons to perform model investigations rather than prototype measurements. Then, scale-up relationships are used to relate the model results to the corresponding prototype. CFD has largely been used to investigate flow phenomena in different fields of fluid dynamics, including hydraulic turbines. The application of CFD in the design and refurbishment of turbines has become increasingly popular because of the flexibility, cost effectiveness and detailed flow description capability of the method. However, the complexity of the flow within water turbines creates challenging simulations in these cases. Flow separation, unsteadiness, swirling flow, adverse pressure gradients and three-dimensionality are some of the complexities in simulating hydropower systems. More experimental data, especially during transient operating conditions and on the rotating parts, are required to simulate and validate CFD results.

This thesis presents the experimental results of a Kaplan turbine model during on-design, off-design and load variations. A Kaplan turbine was selected as the case study. This turbine, which is known as Porjus U9, was mainly built for R&D purposes and is located along the Lule River in northern Sweden. This turbine was designed and manufactured by Kvärner AB, now Andritz hydro AB, at the end of the 1990s. A 1:3.1 scaled model of Porjus U9 was used for experimental and numerical investigations. The main focus of this study involved the flow conditions within the runner. Pressure and non-intrusive velocity measurement methods were used to measure the pressure and velocity within the runner and in the stationary parts of the turbine during on-design, off-design and load variations. Numerical simulations were also performed to evaluate the capability of CFD simulations in predicting flow conditions in water turbines.

This thesis is divided into two parts: part I presents a summary of the work and part II presents the appended papers. Chapter 2 in part I presents the measurement tools, chapter 3 presents the data analysis methods, and chapter 4 presents the main results, followed by chapters that present conclusions and suggestions for future work.

Chapter 2

MEASUREMENT TOOLS

"You cannot improve what you cannot measure."

Lord Kelvin

Navier-Stokes equations that describe flow motion are one of the most complicated partial differential equations of mathematical physics. Such complexity makes finding a theoretical solution for most industrial or even laboratory flows impossible. The level of flow complexity is even higher in turbomachines. Bradshaw [69] claims that "of all the fluid dynamic devices invented by the human race, axial flow turbomachines are probably the most complicated". High Reynolds numbers, fluid structure interactions, rotor-stator interactions, swirling flows and flow separation are some of the phenomena that contribute to flow complexity in turbomachines, making a direct solution of the Navier-Stokes equations practically impossible. Hence, experimental investigations and numerical simulations are practically the only available tools to study the flow conditions in turbomachines, although such investigations also face specific challenges.

This chapter introduces the test case and the methods that are used to investigate the flow conditions in an axial water turbine. The model, test rig, type of measurements, measurement locations and measurement setups are presented. The measurements that are presented in this thesis correspond to the second measurement campaign on the test case. The focus of the first measurement campaign was mainly on the flow conditions within the draft tube of the turbine; see [34]. The main goal of the second campaign, which is presented in this thesis, was to investigate the flow conditions within the runner. Pressure and velocity measurements were performed at different positions, with a specific focus on the runner, to investigate the flow conditions at different operating points of the turbine as well as during transient operating conditions.

2.1. Porjus U9 turbine

Unit number 9 of the Porjus power plant, which is known as Porjus U9, was selected as the test case for this study. The turbine was designed at the end of the 1990s by Kvärner AB, now Andritz Hydro. This turbine is located along the Lule River in Porjus in northern Sweden. Porjus U9 is a Kaplan turbine that was designed and manufactured for research, development and educational purposes, meaning that the turbine is equipped with extra sensors compared to normal units in power plants. This specification permits correlation studies between the turbine and its scaled model.

The turbine is composed of a penstock, a spiral casing, a distributor that consists of 18 stay vanes and 20 guide vanes, a Kaplan runner with six blades, and an elbow type draft tube that follows the runner. The runner has a diameter of 1.55 m and a rotational speed of 600 rpm. The turbine's nominal head is 55 m. The maximum flow rate through the turbine is approximately 20 m^3/s with an output power of approximately 10 MW.

2.2. U9 model and test rig

Detailed measurements on prototypes are usually not feasible because of safety issues, the large dimensions of the prototypes, limited access to different parts of the turbines, the costs of such measurements, environmental regulations that prohibit the measurements and substances that are used in the river, etc. Model measurements are an available alternative to experimentally investigate turbines under comparably safe and controlled conditions with reasonable costs.

A 1:3.1 scaled model of Porjus U9 was manufactured and used for the experimental and numerical investigations. The model was geometrically similar to the corresponding prototype with a runner diameter of 0.5 m. The model head and rotational speed were selected to be 7.5 m and 696.3 rpm, respectively, to ensure kinematic similarity between the model and the prototype during the measurements. Kinematic similarity requires equal reduced flow rate, Q_{ED}, and reduced speed, n_{ED}, between the model and the prototype:

$$Q_{ED} = \frac{Q}{D^2\sqrt{gH}} \tag{2-1}$$

$$n_{ED} = \frac{nD}{\sqrt{gH}} \tag{2-2}$$

Model measurements were performed at the Hydraulic Machinery Laboratory of Vattenfall AB in Älvkarleby, Sweden. The test rig was a closed loop rig that was designed for testing Kaplan, bulb, and Francis turbines. The test rig's uncertainties in flow rate and hydraulic efficiency are ±0.13% and ±0.18%, respectively. The test rig is illustrated in Fig 2.1. The model was installed between an upstream high-pressure tank and a downstream low-pressure tank. The capability to independently adjust the pressures inside the tanks enabled us to adjust the head and control cavitation within the turbine. All the measurements were performed under cavitation-free conditions.

Investigations of this turbine model consisted of pressure measurements, PIV measurements, and LDA measurements. The measurement locations, operating conditions in which the turbine was investigated, and measurement setup specifications are presented in the following sections.
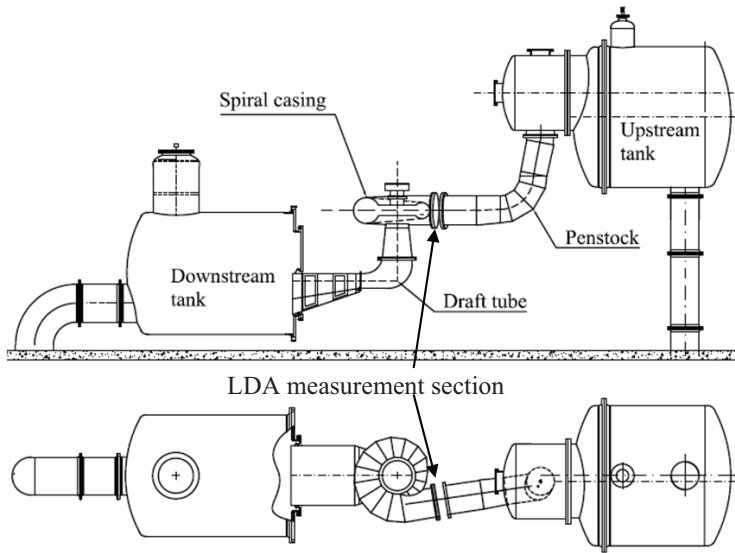
Fig 2.1.   Side and top view of the test rig with the Porjus U9 model installed.

2.3. Pressure measurements

2.3.1. Sensor locations

Pressure measurements were performed at different parts of the turbine. Different types of pressure sensors were used for the measurements as a function of the sensor position, the type of pressure of interest and the magnitude of the pressure. The main focus of these measurements was the pressure fluctuations on the runner at different operating points and during load variations.

Six piezoresistive miniature pressure sensors that were manufactured by Kulite (LL-80 series) were flush mounted on the pressure side of one runner blade. The sensors were located on the vertices of a net of imaginary circles that passed through 1/3 and 2/3 of the blade's span and 1/4, 1/2 and 3/4 of the blade's chord lines. Six pressure sensors were also installed on the suction side of the adjacent blade to investigate the flow conditions in one runner passage. Fig 2.2a and b show the positions of the sensors on the pressure side of Blade 1 and suction side of Blade 2. The operating range of the pressure sensors was 0-7 bar, and their natural frequency was 380 kHz, assuring no interference with the pressure measurements in the range of interest, which was 0-250 Hz. The sensor's wires ran through specific grooves to the turbine's hollow shaft. The wires from each blade were connected to the transmitter of a telemetry system that was manufactured by Summation Research Inc. (SRI-500e) and installed on the rotating shaft. Each transmitter sent analog signals to its corresponding receiver mate.

Ten membrane type pressure transducers (PDCR810 from Druck) were flush mounted on two sides of the draft tube cone, as shown in Fig 2.2c. The sensors were separated by 12.5 cm.

Three differential pressure sensors from Honeywell (FDW series) were used to measure the pressure differences between point 1 and the other three pressure taps on the penstock, as indicated in Fig 2.2d. The first tap was located immediately after the bend in the penstock, and the others were separated by 30 cm.

The signals from the telemetry system and from the sensors that were installed on stationary parts of the model were fed to a data acquisition system (DAQ) with 24-bit resolution that was made by National Instruments (a PXI chassis with four Ni-4472 cards). Signals of the guide vanes' angle, head, flow rate, and a magnetic encoder that was installed on the main shaft were recorded simultaneously by the same DAQ system. The magnetic encoder was used to measure the turbine's angular velocity and phase resolving the pressure measurements with respect to the runner's frequency. The accuracy of the magnetic encoder was 0.03º. The uncertainties in the torque, head and flow rate measurements were 0.082%, 0.102%, and 0.132%, respectively.

a)   b)

c)   d)
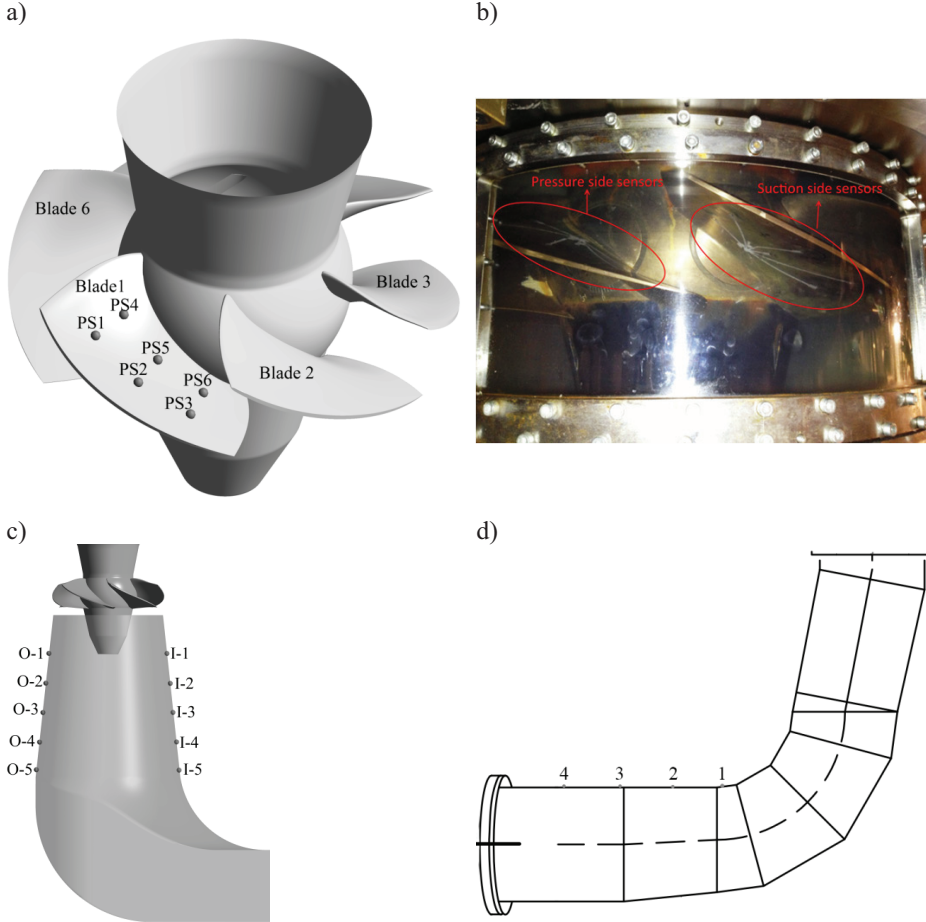
Fig 2.2.   Position of the pressure sensors: a and b) on the runner, c) on the draft tube cone, d) on the penstock.

2.3.2. Sensor Calibration

All the pressure sensors were calibrated by using a DPI 610 pressure calibrator from Druck. A nitrogen tight pressure tank that consisted of steel was designed and manufactured to calibrate the pressure sensors on the blades. The blade and corresponding transmitter were put inside the tank. The Plexiglas cap of the tank permitted the transfer of data from inside the tank without running wires, preventing air leakage during calibration and increasing the calibration accuracy. The maximum uncertainties during the calibration of the draft tube cone sensors ranged from 60 to 130

Pa, from 10 to 20 Pa for the penstock sensors and from 25 to 50 Pa for the runner blade sensors.

2.3.3. Operating conditions

Pressure measurements were performed under a steady state at different operating points and during load variations in the turbine.

2.3.3.1. Steady state pressure measurements

Steady-state pressure measurements were performed at the best efficiency point (BEP) of the turbine. Turbine operation at a guide vane angle of 26.5º was found to correspond to the BEP. The measurements were also performed at two other operating points: at a high load (HL) operating point, with a higher flow rate than that at the BEP, and at a part load (PL) operating point, with a lower flow rate than that at the BEP. The turbine was run during off-cam operation, meaning that the runner blade angle was similar at all operating points. In other words, the turbine was treated like a propeller one. Although such an operational condition is not typical for Kaplan turbines, some power suppliers have investigated regulating power at a constant blade angle to decrease wear despite a decrease in efficiency. Furthermore, the power that is required to adjust the runner blades is also significant and decreases the machine's overall efficiency for temporary off-design operations. Table 2.1 presents the model parameters at the investigated operating points. The operating points were similar to those that were investigated during the first measurement campaign [34-37, 70, 71]. The signals were recorded at a constant sampling frequency of 4 kHz.

Table 2.1.   Operating condition parameters during the steady-state pressure measurements.

Operating point		Part Load	BEP	High Load
Guide vane angle	α_{GV} (deg)	20	26.5	32
Volume flow rate	Q (m^{3}s^{-1})	0.62	0.71	0.76
Discharge factor	Q_{ED} (-)	0.289	0.331	0.354
Speed factor	n_{ED} (-)	0.676	0.676	0.676
Relative efficiency	$\eta\text{-}\eta_{BEP}$ (%)	-5.6	0.0	-1.6

2.3.3.2. Load variation pressure measurements

One of the main goals of the transient measurements was to investigate the formation and mitigation process of RVRs and the effect of RVRs on pressure pulsations that are exerted on the runner. The measurement setup during the load variation measurements was similar to what was used for the steady-state pressure measurements. The turbine was run in off-cam mode during the measurements to trigger the formation and mitigation of RVRs within the draft tube. Pressure measurements were performed during load variations between the three operating points that are presented in Table 2.2.

Table 2.2.   Operating points that were selected for load variation measurements.

Operating point		PL	BEP	HL
Guide vane angle	α_{GV} (deg)	16	26.5	37.5
Volume flow rate	Q (m^{3}s^{-1})	0.51	0.71	0.77
Reduced flow rate	Q_{ED} (-)	0.238	0.322	0.359
Reduced speed	n_{ED} (-)	0.676	0.676	0.676
Relative efficiency	η-η_{BEP} (%)	-15.2	0.0	-3.7
Output power	$(P_{out}-P_{out,BEP})/P_{out,BEP}$ (%)	-26	0	12

2.4. Laser Doppler anemometry measurements

2.4.1. LDA system

A two-component LDA system with an 85-mm optical fiber probe from Dantec was used to measure the velocity distribution at different locations of the turbine. The probe used a backscattering configuration; using forward scattering probes for measurements within the runner and inside the draft tube was impossible because of the runner hub blocking light from traveling in the forward direction and because of the large dimensions of the draft tube, respectively. The system consisted of an Argon-ion laser with a continuous wave of 400 mW, a transmitter which served as an integrated color separator and frequency shifter, and a signal processor. The two pairs of incident beams were green and blue with wavelengths of 514.5 nm and 488 nm, respectively. A beam expander with an expansion factor of 1.98 was mounted on the probe to decrease the measurement volume size. Two lenses with focal lengths of 310 and 600 mm were implemented during the measurements. A three-axis traverse system with the precision of 0.01 mm was used to adjust the measurement locations.

Two burst spectrum analyzers (BSAs) of types BSA 57N21 and BSA 57N35 from Dantec were used to analyze the bursts. BSA flow software from Dantec was used during data acquisition. All the measurements were performed in burst and coincidence mode, meaning that a pair of velocities was recorded for each passing particle through the measurement volume.

The signal from the magnetic encoder on the main shaft of the turbine was used to determine the runner's angular position at each instant. The encoder signal consisted of one step per revolution. The seeding particles that were used in this investigation consisted of Expancel 461 WU 20 with an average diameter of 6 μm.

2.4.2. Spiral casing measurements

Velocity measurements at the inlet of the spiral casing are essential to obtain the inlet boundary conditions for numerical simulations of turbines. Ideally, the flow should be symmetric and similar to a fully developed turbulent flow within a pipe. However, inadequate flow conditions are expected at this location because of the presence of a bend upstream of the spiral casing inlet, followed by a slightly diverging section; see [34, 71].

The spiral casing consisted of a stainless steel pipe with an inner radius of 316 mm at its inlet. A 290-mm-long Plexiglass pipe was installed between the penstock and the spiral casing to provide the required optical access for the LDA measurements; see Fig 2.3.

LDA measurements in circular pipes are challenging because of the wall's curvature. This curvature results in measurement volume distortion and dislocation because of laser beam refraction while transferring from one media to another. This phenomenon results in lower signal quality and inaccuracy in measurements. In the current study, the local index matching box in Fig 2.3 was used to improve the optical performances. The index matching box consisted of a Plexiglass pipe with an axis that was normal to the axis of the penstock and a high-quality glass with a diameter of 100 mm. One end of the Plexiglass pipe was shaped to match the penstock pipe to prevent water leakage. The glass was mounted on the other side of the Plexiglass pipe. The space inside the index matching box was filled with water as the index matching liquid. This mechanism permitted velocity measurements along every desired radius of the pipe.
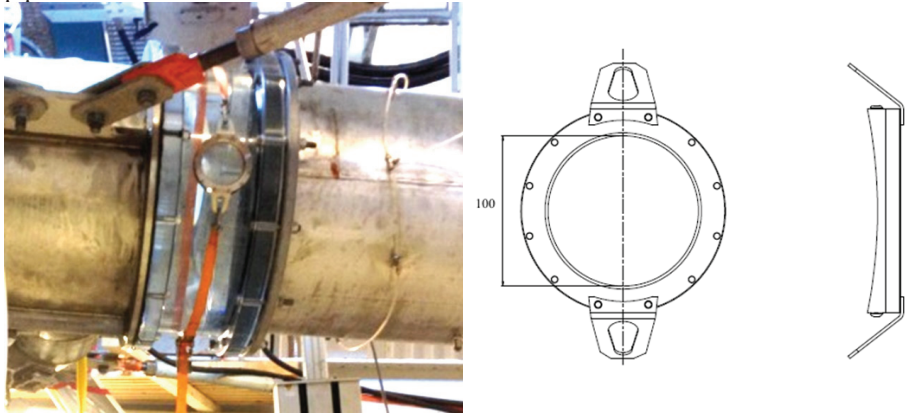
Fig 2.3.   Inlet section of the spiral casing and a sketch of the index matching box.

The measurements at the inlet of the spiral casing were performed along different radii, which were separated by 45°. The measurement locations are presented in Fig 2.4. The insufficient power of the lasers restricted the possible measurement length inside the pipe to around 430 mm. Hence, measurements along C-G were performed from both sides of the pipe to obtain a full velocity profile along the pipe. However, measurements from the top were not possible because of physical limitations.

A front lens with 600-mm focal length was used for the measurements. The measuring volume size based on the e^{-2} Gaussian intensity cut-off point was estimated to be 2.229×0.140 mm and 2.426×0.147 mm for the axial and tangential components, respectively. The measurements were performed at the three operating points in Table 2.1. The measurements were performed in burst and coincidence mode, recording one pair of velocities for each passing particle during the measurements. Velocities were recorded at a minimum of 17 radial positions along each radius. The total sampling time was set to 240 s for each measurement point, which showed a good statistical convergence of the acquired signals. This approach corresponded to 100,000-200,000 bursts at each measurement location as a function of the position and the turbine's operating point. The uncertainties at different measurement locations and different operating points were calculated to lie within ±0.012 of the mean value for the axial component and ±0.011 for the tangential component.
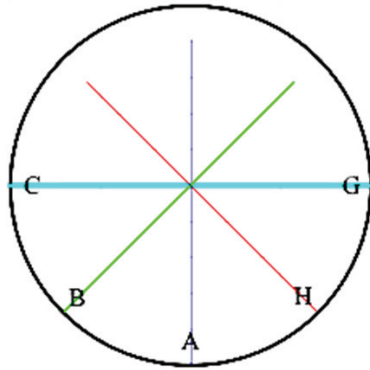
Fig 2.4.   Location of the velocity measurements at the inlet of the spiral casing. The measurement location is shown in Fig 2.1.

2.4.3. Runner measurements

Investigating the flow conditions within the runner was the main focus of this measurement campaign, as mentioned previously. Velocity measurements were performed along a radius within the runner blade and along the runner's outlet. The measurement sections are shown with pink horizontal lines in Fig 2.5. Measurements within the blade channels were performed along RB, which was located 8 mm below the runner hub center, and measurements at the runner outlet were performed along RC, which was located 137 mm below the runner hub center.
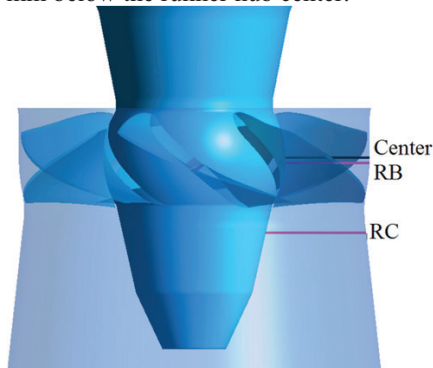
Fig 2.5.   LDA measurement locations. Center: radius along the runner hub center; RB: measurement section between the runner blades; RC: measurement section below the runner blades.

Two optical access windows with high-quality glasses were incorporated to the runner chamber surrounding the runner, as shown in Fig 2.6. The optical access windows contained parallel faces to prevent optical aberrations. Installing this glass on a conical draft tube resulted in a step of approximately 3 mm on top of the window that was used for the measurements at RC, which affected the measurements in the region adjacent to the draft tube wall. However, the window that was installed at RB was almost flush mounted because of the cylindrical shape of the chamber at this location.

a)   b)
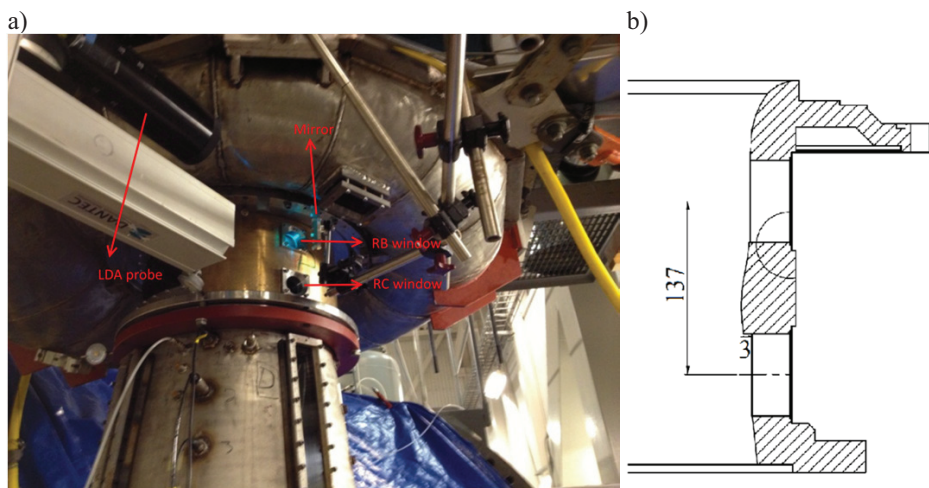
Fig 2.6.   a) LDA measurement sections and b) sketch of the optical access windows; the dashed lines in b represent the centerlines of the windows. The top glass center was aligned with the runner hub center; the dimensions are in mm.

A similar LDA setup to the one that was used for the measurements at the inlet of the spiral casing was used for the measurements within and after the runner. The measurement time was increased to 600 s during the measurements within and after the runner. This sampling time corresponded to 130,000 to 500,000 samples at each measurement point after the runner as a function of the radial location of the measurement. At least 250,000 velocities were recorded at each location, except at the closest locations to the runner hub and the chamber. A total of 100,000 to 300,000 samples were recorded during measurements along RB, except at close to the runner hub and the chamber; the number of recorded samples decreased to around 30,000 at these positions. The large number of samples that were recorded at each measurement location permitted us to phase resolve the recorded velocities.

Two propeller curves of the turbine were selected for the velocity measurements along RB and RC. Three operating points at each propeller curve (the BEP of each curve, together with one PL and one HL) were selected to study the flow conditions during the on-cam and off-cam operation of the turbine. The first propeller curve was similar to what was selected for the steady-state pressure measurements and LDA measurements at the inlet of the spiral casing. This propeller curve was called the 0.8º propeller curve. The second curve corresponded to a runner blade angle of 4º, i.e. the runner blades were opened by 3.2º compared to the previous case. The specifications of the investigated operating points are presented in Table 2.3.

Table 2.3.   Operating condition parameters during LDA measurements within and after the runner.

Operating point	PL$_{0.8}$	BEP$_{0.8}$	HL$_{0.8}$	PL$_4$	BEP$_4$	HL$_4$
β_b (deg)	0.8	0.8	0.8	4	4	4
α_{GV} (deg)	20	26.5	32	26.5	30	33
Q (m^3/s)	0.62	0.71	0.76	0.75	0.8	0.815
$Q_{11} = \dfrac{Q}{D^2\sqrt{H}}\left(\dfrac{\sqrt{m}}{s}\right)$	0.906	1.037	1.11	1.095	1.168	1.19
$n_{11} = \dfrac{ND}{\sqrt{H}}$ (rpm$\sqrt{m}$)	127.3	127.3	127.3	127.3	127.3	127.3
η-$\eta_{BEP0.8}$ (%)	-5.6	0	-1.6	-2.4	-0.2	-0.9

2.4.4. Draft tube measurements

Flow asymmetry after bends in draft tubes in hydraulic turbines has been reported and investigated by different research groups. Gubin et al. [73] studied the effect of the draft tube length and flow "twist" at the entrance of the draft tube on flow asymmetry at the draft tube outlet. These authors concluded that an optimum draft tube length exists that corresponds to a minimum flow asymmetry at the draft tube outlet and maximum efficiency of the turbine. A splitter that controls flow through either half of the draft tube was suggested by the authors as a practical solution. Pressure measurements on the draft tube walls of a Francis turbine showed that higher flow rates may pass through either the right or left half of the turbine's draft tube, depending on the turbine's operating conditions. 3D Particle image velocimetry and LDA measurements at the outlet of the turbine proved the presence of flow asymmetry and secondary flows at the draft tube outlet [20].

The main purpose of performing velocity measurements after the draft tube bend and at the draft tube's outlet was to investigate the flow asymmetry at the measurement locations and parameterize the asymmetry as a function of the flow conditions within the draft tube. This study necessitated an overview of the flow conditions within the draft tube and required 2D or 3D velocity measurements. Such information was acquired by PIV measurements at the two measurement sections that are marked with green boxes in Fig 2.7. Details regarding the PIV measurements are presented in the next section.

LDA measurements were performed along the two red lines within the draft tube, as shown in Fig 2.7. The main purpose of the measurements was to evaluate the PIV measurements as performed in the study by Iliescu et al. [20]. The LDA measurement lines were located in the middle of the optical windows and 136 mm inside the flow. A front lens with a 310-mm focal length was used for these measurements. The LDA system was implemented with a triangular laser beam configuration, enabling measurements close to the wall. The measuring volume size based on the e^{-2} Gaussian intensity cut-off point was estimated to be 0.85 × 0.097 mm and 0.91 × 0.1 mm for the axial and vertical components, respectively. The measurements were performed in burst

and coincidence mode. The sampling time at each measurement point was set to 300 s. A total of 50,000 to 210,000 velocities were recorded at each measurement point.
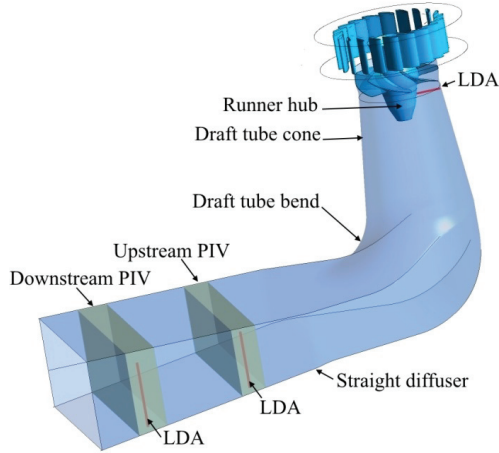
Fig 2.7.   LDA and PIV measurement sections within the draft tube [74].

2.5. Particle image velocimetry measurements

2.5.1. PIV system

A 2-dimensional, 2-component PIV system (2D-2C) from Dantec was used for velocity measurements after the bend in the draft tube and at the draft tube's outlet. The system consisted of two Nd:YAG 400-mJ pulse lasers with a pulse duration of 4 ns. The generated laser beam was diverged to a laser sheet with a thickness of ~3 mm by using a cylindrical concave lens. A CCD FlowSense camera with a resolution of 4 Megapixels was implemented to visualize the illuminated area. The time between images in each set of measurements was set to 200-300 μs as a function of the investigated operating point and the measurement location. Polymer seeding of type Expancel 461 WU 20 powder with an average diameter of 6 μm was fed into the water. One thousand pairs of images with a sampling rate of 10 Hz were recorded at each measurement location.

2.5.2. Measurement locations

The main purpose of the PIV measurements was to investigate the effect of the draft tube's bend and the operating conditions of the turbine on the flow characteristics within the diffuser. Two sections after the draft tube's bend and close to the draft tube's outlet were selected for the measurements. The measurement locations are shown in Fig 2.7. One of the main challenges in performing these PIV measurements was the large cross-sectional area of the measurements: ~1270×375 mm^2 at the upstream window and ~1270×485 mm^2 at the downstream window. Such a large measurement area made performing measurements with a single measurement plane impossible. Moreover, performing stereoscopic PIV (2D3C PIV) with a camera at the draft tube's outlet could be valuable for capturing secondary flows and different modes of the flow after the bend, as performed in the study by Kalpakli and Örlü [75] in a simplified case. However, the existence of the downstream tank at the draft tube's outlet blocked the optical access that was required for performing PIV measurements at planes that were normal to the flow. Hence, rectangular optical access windows were incorporated to the sides and top of the draft tube at the measurement sections. Measurements were

performed along the three horizontal and five vertical planes at each measurement section, as shown in Fig 2.8. Each horizontal plane was divided into eleven PIV windows, and each vertical plane was divided into three windows, i.e., 96 sets of PIV measurements (96000 pairs of images) were stitched together to visualize the velocity field within the draft tube at each operating point. Measurements were performed at the three operating points in Table 2.1.
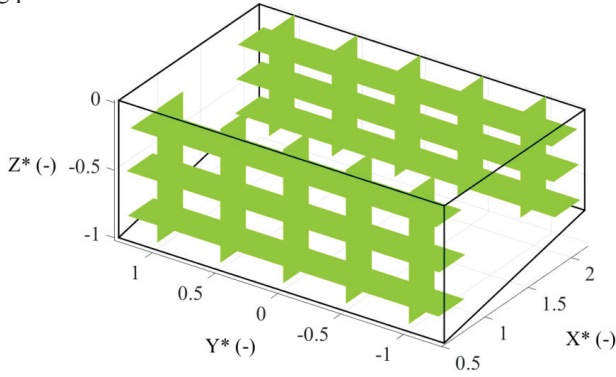
Fig 2.8.   PIV measurement planes.

Chapter 3

DATA ANALYSIS

"See now the power of truth; the same experiment which at first glance seemed to show one thing, when more carefully examined, assures us of the contrary."

Galileo Galilei

The flow in hydraulic turbines is subject to different periodic and random fluctuations in velocity and pressure, depending on the location and the turbine's operating point. Load variations impose non-periodic fluctuations to different parameters and may involve the initiation/dissipation of periodic fluctuations. Care must be taken in the analysis of such flows to distinguish different fluctuations/variations in the acquired signal to draw proper conclusions regarding the flow conditions and different phenomena that occur within the turbine conduit.

3.1. Pressure measurements

Pressure measurements were performed on the stationary and rotating components, as presented in Chapter 2. The measurements included investigations during steady state operation of the turbine at different operating points and during load variation processes. Different methods were implemented to analyze the acquired data.

3.1.1. Steady-state pressure measurements

Our analysis of the pressure signals that were acquired during the steady-state operation of the model included the following:

- Spectrum analysis
- Mode decomposition
- Phase resolving/averaging

3.1.1.1. Spectrum analysis

Amplitude spectrum is a useful technique to estimate the frequencies of periodic fluctuations in a signal and their corresponding amplitude. Fast Fourier transforms (FFT) are a powerful method for that purpose. The pressure signals that were recorded on stationary and rotating parts of the model were uniformly sampled, allowing the implementation of standard FFT methods. Welch's method together with a Hanning window was applied on the signals to more accurately estimate the power spectral density (PSD). Each original set of pressure measurement data was divided into six sub-windows with 50% overlap. The resolution when estimating the frequency was approximately 0.0033 Hz.

3.1.1.2. Mode decomposition

The formation of an RVR in the draft tube cone of a hydraulic turbine may cause pressure oscillations that are associated with rotating and plunging modes (see **Paper A**). Pressure signals that are recorded by pressure sensors on the draft tube cone walls with different angular positions can be used to decompose pressure fluctuations that are associated with the modes. The plunging mode induces synchronous fluctuations with the RVR frequency to the pressure signals of the sensors in the same axial position on the draft tube wall. However, fluctuations that are associated with the rotating mode have similar phase differences as their azimuthal installation position. Hence, signals from any pair of sensors on the inner and outer parts of the draft tube cone (see Fig 2.2) after applying a band-pass filter around the RVR precession frequency can be written as follows:

$$\tilde{P}_I(t) = A\sin\left(2\pi f_{RVR,st}t + \varphi_{st}\right) + B\sin\left(2\pi f_{RVR,st}t + \varphi_{rot}\right) \qquad (1\text{-}3)$$

$$\tilde{P}_O(t) = A\sin\left(2\pi f_{RVR,st}t + \varphi_{st}\right) + B\sin\left(2\pi f_{RVR,st}t + \varphi_{rot} + \pi\right) \qquad (2\text{-}3)$$

where $\tilde{P}_I(t)$ and $\tilde{P}_O(t)$ are the filtered signals from pressure sensors on the inner and outer part of the draft tube, respectively; A and B are the amplitudes of the plunging and rotating modes, respectively; φ_{st} and φ_{rot} are the phases of the plunging and rotating modes, respectively; and $f_{RVR,st}$ is the rotational frequency of the RVR.

The frequency and amplitude of the rotating and plunging modes in the pressure signals that are acquired on the rotating parts are automatically decomposed. The frequency of the plunging mode equals $f_{RVR,st}$, while the rotating mode appears in the signal as the relative frequency of the rotating sensor to the RVR, i.e., $f_{runner} - f_{RVR,st}$, where f_{runner} is the runner's rotational frequency.

3.1.1.3. Phase averaging

Periodic pressure fluctuations are present in rotating machineries. Spectrum analysis is an appropriate tool to find the frequencies of the periodic phenomena that occur inside the flow. However, this method does not provide any detailed information regarding the source of fluctuations, their shape, etc. Phase averaging is a complementary analysis tool to spectrum analysis for more detailed analyses of periodic signals.

Each acquired signal $\Phi(x,t)$ can be decomposed into three components: the time averaged value, $\overline{\Phi}(x)$; the periodic value, $\widetilde{\Phi}(x,t)$; and random fluctuations, $\acute{\Phi}(x,t)$:

$$\Phi(x,t) = \langle\Phi(x,t)\rangle + \acute{\Phi}(x,t) = \overline{\Phi}(x) + \widetilde{\Phi}(x,t) + \acute{\Phi}(x,t) \qquad (3\text{-}3)$$

where $\langle \Phi(x,t) \rangle$ is the phase-averaged signal over the prescribed period.

Spectral analysis of the pressure signals from the sensors on the runner blades showed clear peaks at the runner frequency and its harmonics at all operating points. Hence, the pressure signals were phase resolved with respect to the runner's rotational frequency to distinguish the source of the fluctuations. The recorded signal from the magnetic encoder on the main shaft of the turbine was used to determine the runner's angular position at each instance to angularly resolve the pressure signals. One runner's revolution was then divided into bins of identical size. Then, an average of the recorded pressures at each bean was calculated to draw the phase-averaged curve. A bin size of 0.5°, which resulted in around 1700 recorded pressure values in each bin, provided a smooth phase-averaged curve by removing high-frequency fluctuations in the signal.

A similar procedure was implemented to phase resolve data with respect to different modes of RVR frequencies. The only difference in these cases was the inexistence of an encoder reference signal to record the RVR passage. Hence, a constant frequency was assumed for each RVR mode, and the data were phase resolved with respect to that frequency.

3.1.2. Load variation pressure measurements

3.1.2.1. Spectrograms

The main purposes of the load variation pressure measurements were to investigate the effect of load variations on pressure fluctuations along the runner blades and to investigate the formation/mitigation process of RVR and its effects on the pressure fluctuations in the draft tube and on the runner. The analysis of the acquired data began with smoothing the pressure signals by applying a Savitzky-Golay filter. Figure 3.1 a shows pressure variations in a signal from one of the runner blade pressure sensors during load variation from the BEP to HL. The blue dots show the instantaneous pressure and the black curve shows the filtered signal. Subtracting the smoothed signal from the original signal isolated the fluctuating component of the signal, as presented in Fig 3.1b. Afterwards, the fluctuating signal components were used for further frequency analyses.

Then, the fluctuating signal was used for unsteady spectral analysis of the pressure signals. Guertzel's algorithm was used to perform transient spectral analysis on the signals. Examples of the resulting spectrograms can be found in **Paper D** and **Paper E**.

a)

b)
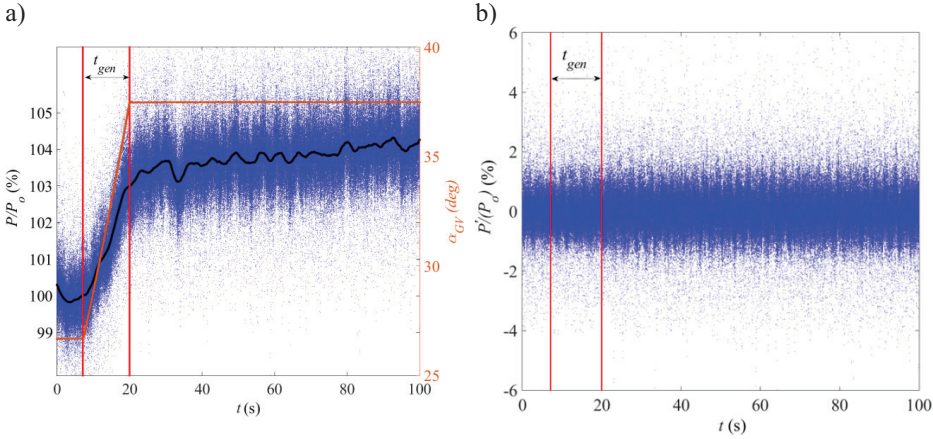
Fig 3.1. a) Example of a raw and corresponding smooth pressure signal during load variation from BEP to HL; blue dots: instantaneous pressure, black line: smoothed pressure, dark orange: GV angle. b) Fluctuating portion of the signal.

3.1.2.2. Mode decomposition

The decomposition of the plunging and rotating modes of RVRs during load variation processes, which involve the formation or mitigation of RVRs, may contribute to understanding the formation/mitigation processes of RVRs. Hence, the method for decomposing the rotating and plunging modes of RVRs in the stationary frame was applied to the transient measurement results. The data were divided into bins of 0.5-s intervals, and the method was applied to the data in each bin. The different modes could be automatically decomposed in the pressure signals from the runner blades by calculating the spectrograms because different modes are represented by different frequencies.

3.2. LDA measurements

Similar data processing procedures to those that were applied to the pressure signals were implemented to the LDA measurement results to calculate the mean, phase average and spectrum of the acquired signals. However, the LDA signals were not uniformly sampled, which introduced specific complexities to the data processing. Moreover, particles with higher velocity were more contingent to pass through the measurement volume, introducing bias to the average values and inaccurate calculations of the other statistical parameters.

3.2.1. Time-averaging

The instantaneous velocities and the transit time of the seeding particles that passed through the measurement volume during the measurements were used to calculate the velocity statistics. The effect of the measurement volume size and the velocity gradient within the volume were neglected. This assumption is considered to be valid because of the low-velocity gradients in the measurement sections, i.e., measurements were generally performed outside the boundary layer. The average velocities, their statistical parameters, and the Reynolds shear stress components were calculated by using a time-weighted averaging method that was based on the residence time of the bursts. The mean axial velocity was calculated as follows:

$$\overline{U} = \frac{\sum_{i=1}^{N} g_i U_i}{\sum_{i=1}^{N} g_i} \tag{3-4}$$

where N is the total number of recorded velocities, U_i is the axial velocity of the ith particle that passes through the measurement volume and g_i is the transit time of the corresponding particle. The variance and the RMS values of the axial velocity are calculated as follows:

$$u'^2 = \frac{\sum_{i=1}^{N} g_i (U_i - \overline{U})^2}{\sum_{i=1}^{N} g_i} \tag{3-5}$$

$$u' = \sqrt{u'^2} \tag{3-6}$$

The average, variance and RMS values of the tangential velocity components were calculated similarly to those of the axial component.

The Reynolds shear stress component is calculated as presented in equation (3-7) by using the velocities that were recorded in coincidence mode:

$$u'v' = \frac{\sum_{i=1}^{N} g_i (U_i - \overline{U})(V_i - \overline{V})}{\sum_{i=1}^{N} g_i} \tag{3-7}$$

3.2.2. Spectrum analysis

The arbitrary passage of seeding particles through LDA measurement volume and performing measurements in burst mode result in unevenly distributed measurement samples in the time domain. This uneven distribution prohibits implementing standard FFT methods for spectrum analysis. Reconstructing the acquired signal with an interpolation method and converting the irregularly sampled signal to an evenly distributed signal for further spectrum analysis with a standard method is a common approach.

The spectral analysis of the LDA signals was performed after resampling the time series by using a linear interpolation with the minimum time interval of the data acquisition. The Welch method with Hanning windows of 50% overlap was implemented on the evenly distributed signals for spectral analysis. The results of this method were expected to be similar to those that were identified by the Lomb-normalized periodogram method, where the evenness of the acquired data is not mandatory [34].

3.2.3. Phase averaging

The spectral analysis of velocity signals that were acquired within and after the runner showed the presence of clear peaks at the runner frequency and its harmonics at all the investigated operating points. Hence, the velocity signals were phase resolved with respect to the runner's rotational frequency. The signal of the magnetic encoder on the main shaft of the turbine was used to phase resolve the data. The phase-resolving procedure was similar to what was implemented when phase resolving the pressure measurement results. However, non-uniformity in the passage of seeding particles through measurement volume with different transit times should be considered when phase averaging the signals. One period, or one rotation of the runner in this case, was divided into different phase intervals. Weighted averaging according to the transition time of particles was applied in each bean to calculate the phase-averaged velocities and

their RMS and Reynolds shear stress, as presented in equations (3-4) to (3-7). Sensitivity analysis on the effect of the bin size on the phase-averaging results showed that a bin size of 1º was an appropriate compromise between statistical uncertainties and the phase resolution. The parabolic gradient compensation method by Glas et al. [76] was adopted for the phase averaging process, as proposed by Mulu [34].

Spectral analysis of the velocity measurement results within and after the runner at specific operating points showed the presence of asynchronous periodic fluctuations that were associated with RVR precession inside the draft tube. The results were phase resolved with respect to the RVR's precession to see the effect of the RVR's rotation on the velocity contours at the measurement locations. However, no reference signal that represented the RVR's rotation was recorded simultaneously with the LDA measurements. The self-resolving technique by Jonsson et al. [36] was implemented to phase resolve the data. The LDA signal from the tangential component was used to phase resolve both velocity components with respect to the RVR's frequency. The tangential velocity signals at each radius were filtered with a band pass filter around the RVR frequency. The filtered signal was used to phase resolve both velocity components.

3.3. PIV measurements

The PIV results were mainly analyzed by using the commercial software Dynamic Studio, which was developed by Dantec Dynamics. The analysis included image processing and PIV data analysis. Inserting appropriate calibration targets inside the draft tube was not straightforward because of limited access to the draft tube. Hence, a Plexiglas tank that simulated optical conditions at the PIV measurement sections was used to conduct the 2D calibration of the PIV images after performing the draft tube measurements. An adaptive correlation scheme with two refinement steps and 50% overlap between the adjacent windows was applied on the acquired data after calibration to calculate velocity and RMS vector maps. The vector maps were then imported to MATLAB for 3D stitching to represent the overall flow conditions inside the draft tube. Similar spectrum analysis to what was applied to the pressure signals was implemented on the evenly distributed velocity signals from the PIV measurements at some specific locations.

3.4. Uncertainty analysis

Measured data can be the best possible estimates of the true values under the requirement that the errors or uncertainties in the measurements are controlled and minimized. The total error in the measurements can be estimated by combining random/precision uncertainty and bias/systematic uncertainty.

Precision errors are associated with the random essence of different phenomena during measurements, which result in a random distribution of the measured values around a mean value when the measurement is repeated. By definition, precision only increases the scattering of the acquired data and does not change the mean value. Precision errors can be estimated by performing repeatability tests. The standard deviation of the measured values is a good indicator of the precision errors in the measurements [77]:

$$s_X = \sqrt{\frac{1}{N-1}\sum_{i=1}^{N}(X_i - \bar{X})^2} \tag{3-8}$$

where $\bar{X}$ is the mean of the sample population, X_i is the ith sample and N is the number of samples.

The errors that remain unchanged throughout repeatability measurements are called bias errors. In other words, bias errors change mean values by a constant value but do not scatter the measurement results. Estimating the bias in a measurement is not as straightforward as estimating precision errors because the exact value of the measured parameter is usually unknown. Bias can be estimated in a variety of ways. The bias in a measurement from a specific source can be estimated through previous experience, manufacturer's specifications, calibration data, results from specially designed side measurements, results of analytical models, etc. The total bias of k uncorrelated bias sources can be estimated as follows:

$$b = \sqrt{\sum_{k=1}^{M} b_k{}^2} \tag{3-9}$$

where b_k is the bias that is associated with the kth source and M is the number of bias sources that are considered for the estimation. The *combined standard uncertainty* can then be calculated as follows:

$$u_c = \sqrt{(s_X{}^2 + b^2)} \tag{3-10}$$

To associate a level of confidence with the uncertainty for the variable, the ISO guide recommends a coverage factor such that

$$U_\% = t_\% u_c \tag{3-11}$$

where $U_\%$ is the overall or "expanded uncertainty" at a given percent level of confidence. $t_\%$, which is known as the *t distribution*, can be found for desired confidence intervals. Assuming a Gaussian distribution for the results and aiming for a 95% confidence interval, $t_\%$ is close to 2 given that a minimum number of repetition measurements was performed for the error analysis.

All the pressure sensors, including those that were mounted on the runner blades, draft tube cone and penstock, were calibrated by using a DPI 610 pressure calibrator from Druck prior to the measurements. Uncertainty analysis was also performed on the test rig sensors. The results of the uncertainty analysis are presented in Table 3.1.

The uncertainties of the pressure measurements from the repeatability tests were ±0.3%, ±0.25% and ±0.15% for the blade sensors, draft tube sensors and penstock sensors, respectively.

LDA measurements in oscillating flows are subject to a specific source of bias. More samples are generated when the velocity is higher, and an ensemble average of the data does not reflect the true time average. This source was the only significant source of biases in the LDA measurements, as reported by Mulu [34]. This bias was eliminated by using a time-weighted average, which weights each velocity estimate by the duration of the underlying burst. Table 3.2 presents the maximum uncertainties for different parameters that were measured with the LDA system far from the clearance regions. The maximum reported uncertainties were at the PL operating point. The uncertainties were lower at other operating points. However, close to the hub and tip, the total

measurement uncertainty at a 95% confidence interval was within 2.1% at different operating points.

Table 3.1.   Calibration uncertainties of the test rig parameters and pressure sensors.

Instrument	Uncertainty	Position
Hydraulic efficiency	$\leq \pm 0.13\%$	Test rig
Volume flow rate (Q)	$\leq \pm 0.18\%$	Test rig
Head (H)	$\leq \pm 0.04\%$	Test rig
Guide vane angle setting (α_{GV})	$\leq \pm 1.3\%$	Test rig
Encoder	$0.03°$	Test rig
Pressure sensors	$\leq \pm 0.18\%$	Runner blades
Pressure sensors	$\leq \pm 0.1\%$	Draft tube cone
Pressure sensors	$\leq \pm 0.1\%$	Penstock

A 2D calibration target was used to calibrate the recorded images by the PIV system to decrease biases that were associated with light aberrations and probable perspective effects that were present in the acquired images. An adaptive correlation scheme with two refinement steps and 50% overlap between the adjacent windows was implemented for the image processing step, which increased the spatial resolution and decreased the biases that were associated with high velocity gradients. The PIV measurement precision at a 95% confidence level was estimated by performing repeatability tests at some sections while the turbine was operating at PL. This operating point exhibited the maximum uncertainty. The uncertainties that were associated with the axial, lateral and vertical velocities were found to be less than 0.05, 0.01 and 0.005 m/s, respectively, which correspond to 4.5%, 15% and 7% of the uncertainties in the axial, lateral and vertical velocities, respectively.

Table 3.2.   Calibration precision of the LDA measurements within and after the runner.

	Within blade channels	At the runner outlet
U	±0.71%	±0.65%
u	±1.1%	±0.96%
V	±0.88%	±0.75%
v	±1.22%	±1.12%

Chapter 4

RESULTS AND DISCUSSIONS

"Refining is inevitable in science when you have made measurements of a phenomenon for a long period of time."

Charles Richter

This chapter presents a summary of the measurement results and the main points of each measurement. The main objectives of this study were to investigate the effect of operating points on the flow conditions within the turbine conduit and to identify the parameters that affect turbine efficiency and lifetime under different operating conditions. Moreover, the results provide a data bank for numerical simulations/validations.

Special attention was dedicated to the runner as one of the most vulnerable parts and the phenomenon of RVR as a complicated and threatening phenomenon in hydraulic turbines, as discussed in Chapter 1. Some of the phenomena that were investigated in this study are as follows:

- Effects of rotor-stator interactions on the level of fluctuations that are exerted on the runner
- Effects of load variations on the level of fluctuations that are exerted on the runner
- Sequential procedure of RVR formation/mitigation
- Velocity distribution within and after the runner cascade blades and the effect of the on-cam and off-cam operation of the turbine on the velocity distributions
- Effect of operating points on flow asymmetry within the draft tube

4.1. Steady state operation results

The flow conditions within the turbine conduit were experimentally investigated at different operating points, as discussed in Chapter 2. The acquired results included pressure measurements at stationary and rotating parts of the turbine; LDA

measurements at the inlet of the spiral casing, within the draft tube, and within and after the runner; and PIV measurements within the draft tube. This section presents a summary of the results.

4.1.1. Pressure measurements

The comparably short lifetime of the pressure sensors that were installed on the runner blades was the main restriction in performing pressure measurements. The results of the sensors PS4, PS5, and SS3, which are shown in Fig 2.2a, could not be recorded because of their deficiency prior to the measurements.

Figure 4.1 presents the phase-averaged pressure results that were acquired on the runner blades while the model operated at the BEP point, as presented in Table 2.1. The results were phase averaged with respect to the runner's rotation. The signal from each sensor was subtracted from its time-averaged value and made dimensionless by using the turbine head during the measurements. The origin of the x-axis indicated where the leading edge of corresponding runner blade passed through the same peripheral position of the tongue of the spiral casing. The results exhibited a sudden increase in the pressure on the pressure side of the runner blade at approximately 45º. The results on the suction side exhibited a deep valley simultaneous to the peak on the pressure side. The peaks and valleys were followed by distinct fluctuations in the interval from 50º to 130º. The fluctuations showed a phase difference of approximately 18º, which equals the guide vanes and stay vanes' angular spacing. The results demonstrate the inability of the spiral casing to symmetrically supply water to the distributor, causing flow separation on the vanes, where flow does not enter the distributor with the appropriate angle. Flow after the separated vanes comprised wake regions with decreased velocity and wake-free regions with high velocity. The intermittent passage of a runner blade through these regions caused fluctuations in the blade pressure and probable structural deformation. Simultaneous fluctuations in the pressure signals between the suction side of the blades and the pressure side with a 180º phase difference may indicate structural deformation. However, the lack of sensors for measuring blade deformations, such as strain gauges, prevents any robust conclusions. The level of pressure fluctuations on the sensors close to the shroud was higher compared to those close to the hub on both the suction and pressure sides. These observations can be explained by the larger distance between the guide vanes and the sensors close to the hub compared to those close to the shroud, which resulted in more dissipated wakes reaching the hub. These observations can also be explained by structural fluctuations in the blades, resulting in the movement of the sensors close to the shroud with larger amplitudes.

a)

b)
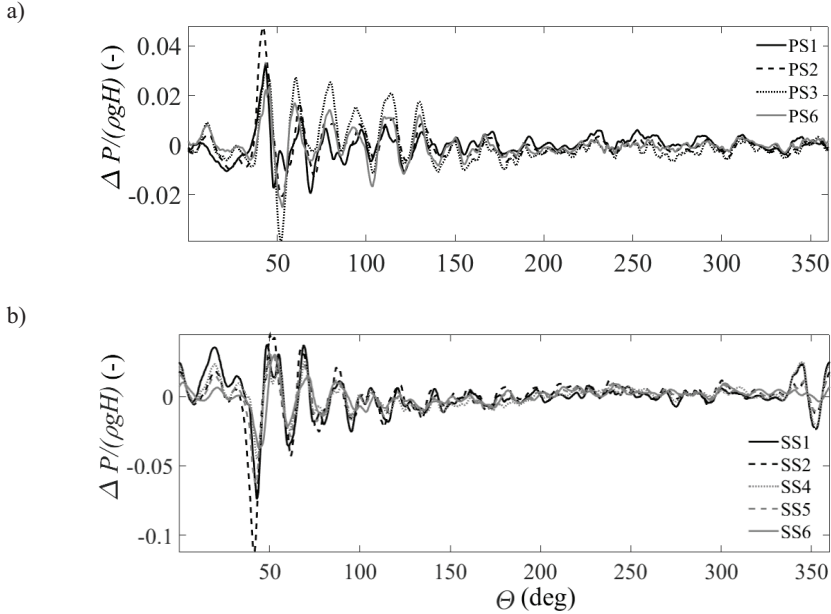
Fig 4.1.   Phase-averaged pressure distribution on the pressure side (a) and suction side (b) of the blades at the BEP. The pressure is made dimensionless with respect to the turbine's operational head.

Figure 4.2a to c illustrate the phase-resolved pressure differences between the sensors on the pressure and suction sides of the blades in the middle of the blade chord and close to the shroud (PS2-SS2) at different operating points. The main features of all the figures in Fig 4.2a to c are similar. A high peak exists in all the pressure difference plots at around 45°, followed by some fluctuations that are separated by 18°, which are attributed to flow asymmetry at the spiral outlet, as discussed earlier. The results exhibited highly scattered data around the highest peak, i.e., at approximately 45°. Similarly scattered data appeared every 60° at 105°, 165°, 225°, 285° and 345°. These highly scattered data points every 60° showed that each time a blade passed through the spiral casing lip-entrance junction region, a flow with an inappropriate angle of attack hit the blade, resulting in a pressure fluctuation on the blades, vibration in the complete runner and shaft wobbling. The results agree with the strain gauge results that were acquired on the main shaft of the prototype; see **paper A**. Figure 4.2d presents the effect of the turbine's operating point on the magnitude of the largest peak in the phase-averaged data. This figure shows that the pressure peak was a monotonically increasing function of the turbine flow rate. The results proved that other parameters, such as the formation of an RVR at PL, did not affect the trend in magnitude of the peak (at least within these operating condition). Hence, the lower the mass flow rate, the lower the detrimental effect of the flow asymmetry on the runner. For a detailed discussion of these results, refer to **Paper A**.

a)

b)

c)

d)
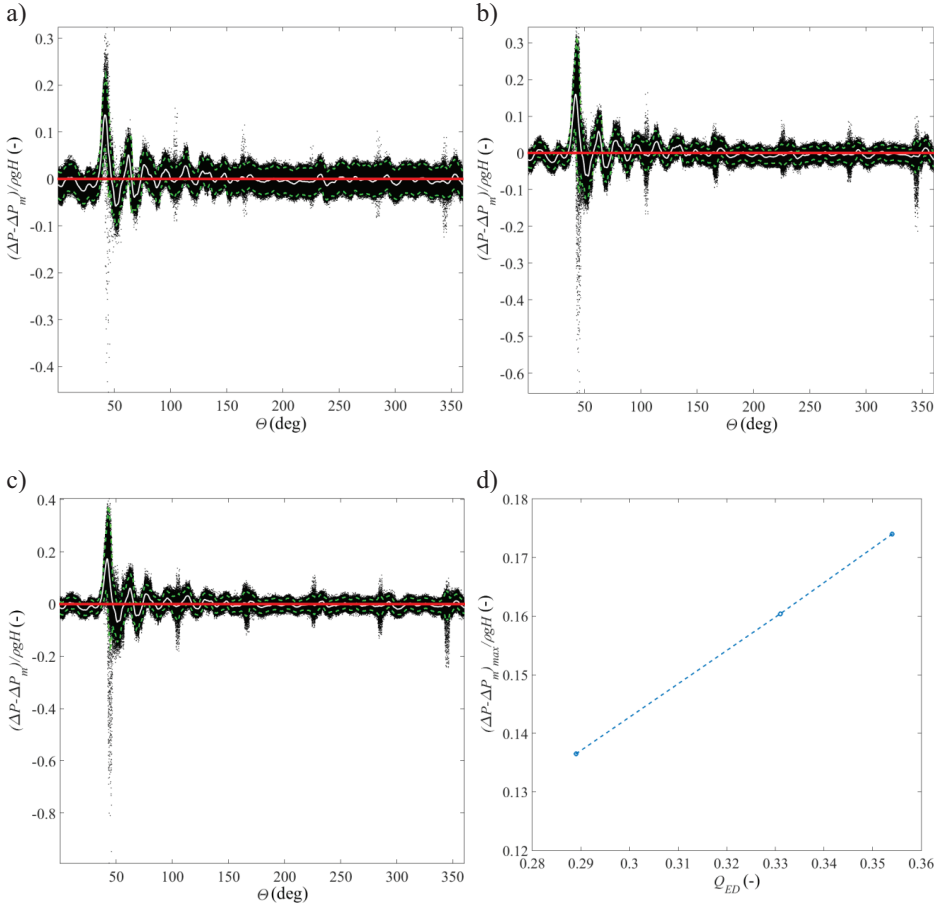
Fig 4.2.   a) Phase-resolved results (black dots), phase-averaged results (white line) and
2σ band (green dashed line) of the signal PS2-SS2 at PL; b) same curve at the BEP; c)
same curve at HL; d) maximum peak in the phase-averaged curves vs. discharge factor.

Figure 4.3 presents the amplitude spectra of the pressure sensors on the runner
blades at the BEP and PL. The dominant dimensionless frequencies at the BEP, which
are presented in Fig 4.3a, are the runner frequencies and its harmonics in all the sensors.
However, two asynchronous dimensionless frequencies, $0.171f^*$ and $0.829f^*$, dominated
the spectrum at PL. The simultaneously recorded pressure measurements at the draft
tube cone and the flow visualizations demonstrated the presence of an RVR in the
diffuser that was co-rotating with the runner with a dimensionless frequency of $0.171f^*$
at this operating point. This result agrees with the LDA and pressure measurements by
Jonsson et al. [36]. According to the co-rotation of the RVR with the runner, a
dimensionless frequency of $(1-0.171)f^*=0.829f^*$ was expected in the rotating domain.
This frequency is referred to as the rotating mode of the RVR. These fluctuations
exerted asymmetric pressure fluctuations on the runner resulting in rotating asymmetric
forces on the runner, rotating bending moment on the shaft, and asymmetric forces on
the bearings of the turbine shaft.

a)

b)
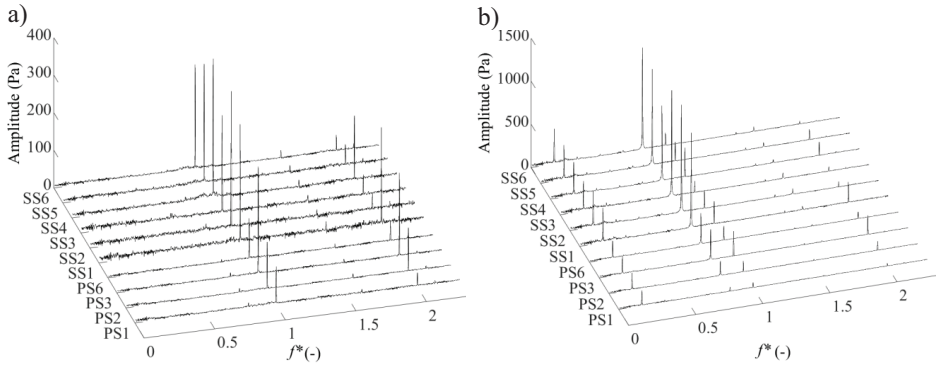
Fig 4.3.   Amplitude spectra of the pressure sensors at a) the BEP and b) PL.

Detailed investigations on the spectra of different sensors on the runner showed that the phase difference between different sensors was independent of the position of the sensors and was close to zero at $0.171f^*$; see **Paper A**. Thus, the RVR induced an axial oscillation through the entire conduit with its frequency. This frequency is referred to as the plunging mode of the RVR. The plunging frequency induced synchronous pressure fluctuations on the runner, thus causing harmonic oscillations in the loads that were exerted on the thrust bearing.

Figure 4.3b shows that the amplitude of the rotating mode in each sensor, especially the sensors that were mounted on the suction side of the runner, dominated the plunging mode. The decomposition method in Chapter 2 was implemented on the pressure results from the draft tube cone. The results in Fig 4.4 show that amplitude of the rotating mode intensified in the upstream direction while it decreased for the plunging mode. These results agree with those from the suction side of the runner, where the amplitude of the rotating mode was more powerful than that of the plunging mode. Generally, the amplitude of the rotating mode decreased in the streamwise direction, while the amplitude of the plunging mode increased. However, both amplitudes decreased at the end of draft tube cone (location 5 in Fig 4.4) because the bend induced some asymmetries in the flow and disturbed the correlation between the signals that were acquired on the sensors.
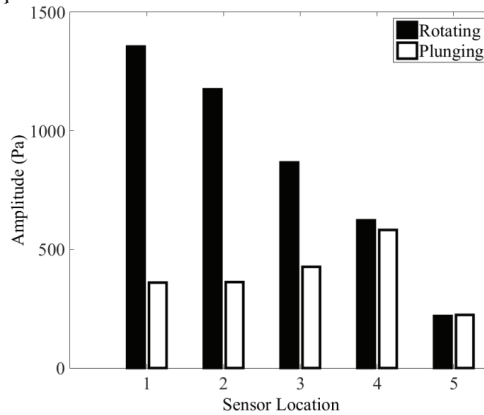
Fig 4.4.   Amplitude of the rotating and plunging modes of the RVR at the draft tube cone.

4.1.2. LDA Measurements

Providing a data bank for numerical simulations of the test case was one of the reasons for investigating the flow conditions at different parts of the turbine. The inlet boundary conditions to the spiral casing of the turbine can be a critical parameter in numerical simulations of a complete turbine. The LDA measurements at the inlet of the spiral casing by Mulu [34] proved the complexity of the flow at this location and showed that the flow conditions deviated from an ideal case of fully developed flow in a straight pipe. The measurements proved the presence of a pair of counter-rotating vortices that were similar to Dean vortices at this location. This phenomenon is attributed to the presence of a nearly 90º bend upstream of the measurement section.

Figure 4.5a and b illustrate the contours of the axial and tangential velocities at the inlet of the spiral casing, respectively. These results were compared to the results of stereoscopic PIV measurements after a pipe bend; see Fig 4.5c and d. Comparing Fig 4.5a with Fig 4.5c, the main features of the axial velocity contours were qualitatively similar. Most of the flow was pushed towards the bottom of the pipe wall (outer part of the bend) because of curvature-induced secondary motion and the flow rate through the inner part of the bend is minimum. The main features of the contours of the tangential velocity were also similar. The maximum tangential velocity regions were located close to the walls and on the upper-right and upper-left because of the formation of Dean vortices in the upper half part of the measurement location. However, some differences existed between the flow conditions at the spiral inlet and those after the pipe bend. The flow after the pipe bend was completely symmetrical as presented in Fig 4.5c and d; however, distinct asymmetries existed in both the axial and tangential velocities at the spiral inlet. This observation can be explained by geometrical asymmetries in the upstream and downstream of the measurement section. As shown in Fig 2.1, the penstock was not aligned with the axis of the upstream tank. Moreover, flow could not be homogeneously fed to the penstock inlet because of the special arrangement that was used to connect the penstock to the upstream tank. These factors are expected to have contributed to the formation of an asymmetric flow after the penstock's bend. The difference in the Reynolds number in the presented cases also contributed to the deviations in the velocity fields.

a)

b)

c)

d)
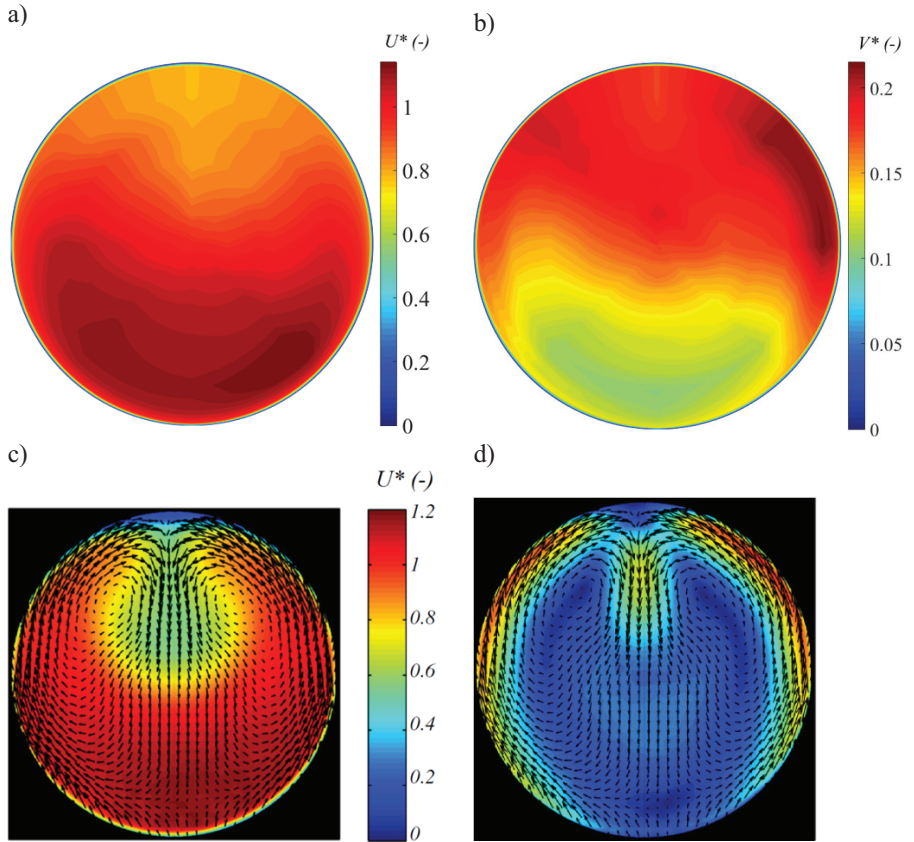
Fig 4.5.   a) Contours of the axial velocity at the inlet of the spiral casing, b) contours of the tangential velocity at the inlet of the spiral casing, c) contours of the axial velocity after a pipe bend [75], d) contours of the tangential velocity after a pipe bend [75].

Figure 4.6 shows the time-averaged velocity profiles within and after the runner at the six operating points in Table 2.3, namely, $BEP_{0.8}$, BEP_4, $HL_{0.8}$, HL_4, $PL_{0.8}$, and PL_4. The velocity profiles showed similar trends at various operating points, except at $PL_{0.8}$. What makes this operating point different from the others is the formation of an RVR downstream of the runner. The turbine operated under RVR-free conditions at the other operating points. An RVR formed because of the high swirling flow that left the runner at this operating point. Its formation inside the draft tube affected the velocity profiles at the LDA measurement sections, resulting in lower axial velocity and higher tangential velocity close to the hub section. For a detailed discussion regarding the velocity profiles, refer to **Paper B**.
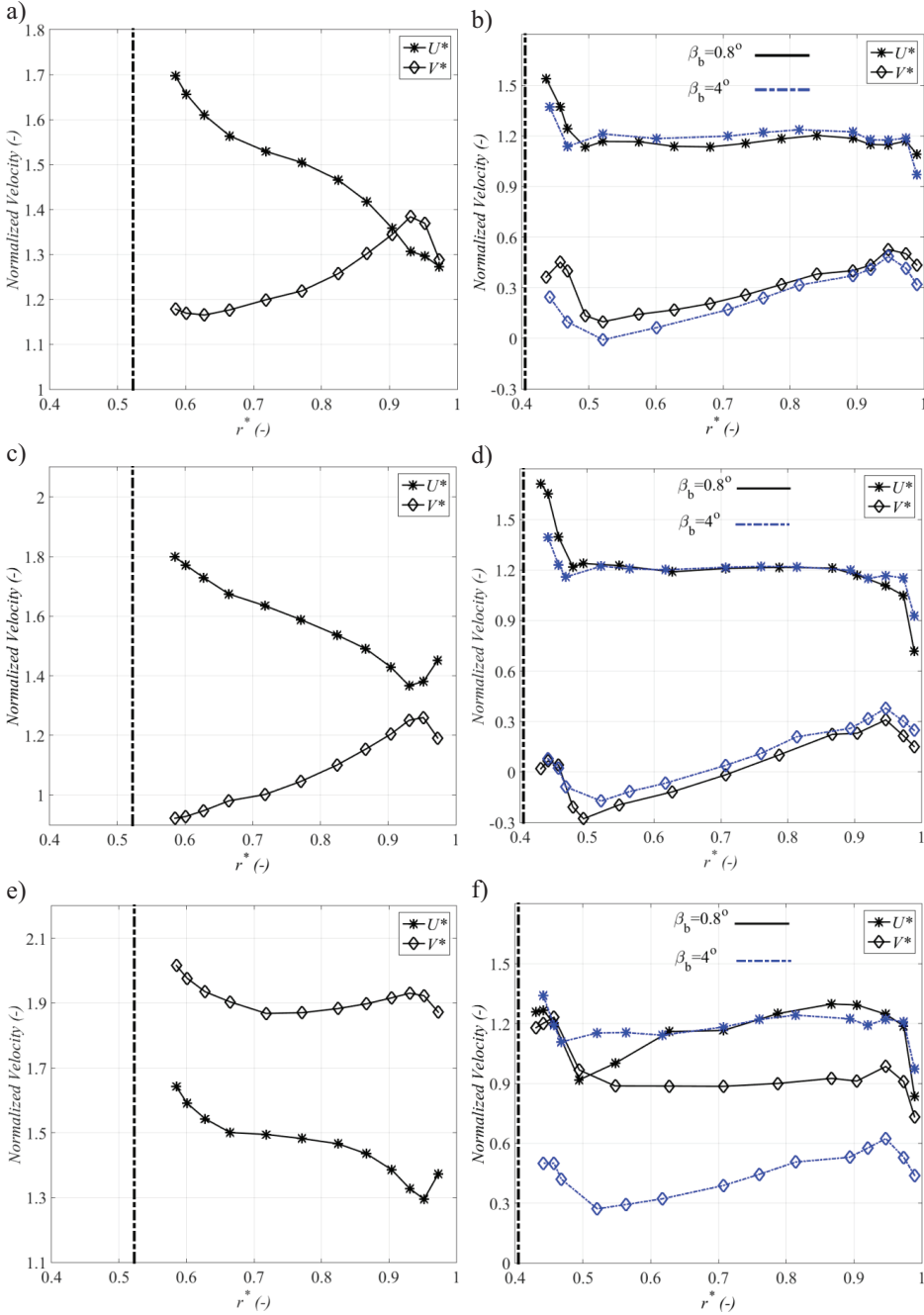
Fig 4.6.   Time-averaged velocity profiles within the runner and at the runner outlet: a) within the runner at $BEP_{0.8}$, b) after the runner at $BEP_{0.8}$ and BEP_4, c) within the runner at $HL_{0.8}$, d) after the runner at $HL_{0.8}$ and HL_4, e) within the runner at $PL_{0.8}$, f) after the runner at $PL_{0.8}$ and PL_4. The bold lines at approximately $r^*= 0.5$ and $r^*=0.4$ represent the runner hub and the runner cone positions, respectively.

The axial and tangential velocity profiles that were acquired at section RC could be used to determine the flow angle either on the global frame of reference or in the rotating frame of reference of the runner. The latter could be used to check the flow angle compared to the runner blade installation angle. Such a graph is presented in Fig 4.7. This figure shows that changing the operating point of the turbine did not affect the flow angle at the runner outlet if the runner blade angle was kept constant. This figure shows that changing the flow conditions at the runner inlet by changing the guide vanes' angle or the formation of an RVR downstream of the runner did not affect the performance of the runner blades, i.e., the flow did not separate on the blades and followed the runner blades at their trailing edges within the studied operating range. The results showed that changing the runner blades' installation angle by 3.2° changed the flow angle by almost an equal amount. This observation can also indicate the operation of the runner blades under separation-free conditions.
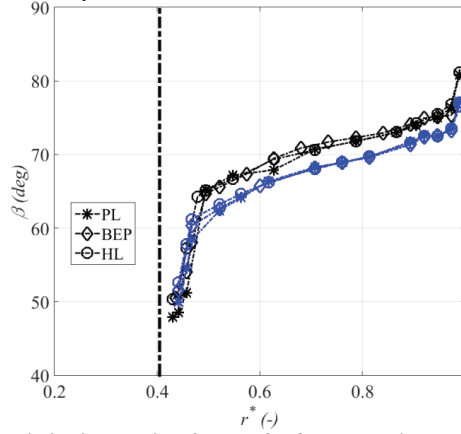
Fig 4.7.   Flow angle in the rotating frame of reference at the runner outlet. Black lines: β_b=0.8°, blue lines: β_b=4°.

Figure 4.8 shows the phase-averaged velocity contours with respect to the runner's rotational speed along section RC at different operating points. The results show that the passage of the blade's trailing edge caused a momentum loss in the axial velocity and an increase in the tangential velocity in the wake region. Six high-axial-velocity regions were located near the runner hub. Each high-axial-velocity spot was coupled with a low-axial-velocity region, demonstrating the formation of vortices at the hub clearances; this region is marked with "hub vortex" in Fig 4.8. Similar vortices formed close to the tip region because of tip clearance effects. Changing the runner blade's angle from 0.8° to 4° decreased the hub clearance and increased the tip clearance, as presented in **Paper B**. This action resulted in stronger tip vortices and weaker hub vortices after the runner blades at a runner blade angle of 4°; compare the marked regions in Fig 4.8a and b. The velocity contours at $HL_{0.8}$, which are presented in Fig 4.8c, show that the flow had similar features as those at $BEP_{0.8}$ at this operating point: the wakes of the runner blades and the hub and tip vortices were observable in the results. The only difference was that increasing the flow rate decreased the tangential velocity and the inner flow counter-rotated with the runner, while the outer flow co-rotated with the runner. As shown in Fig 4.8d, the flow in the region near the hub was distorted while the turbine operated at $PL_{0.8}$. This decrease in the axial velocity and increase in the tangential velocity close to the hub (indicated with a gray dashed circle) compared to the results at the BEP can be attributed to the presence of an RVR and

recirculation bubble in the middle region of the draft tube, which deformed the streamlines upstream.

a)

b)

c)

d)
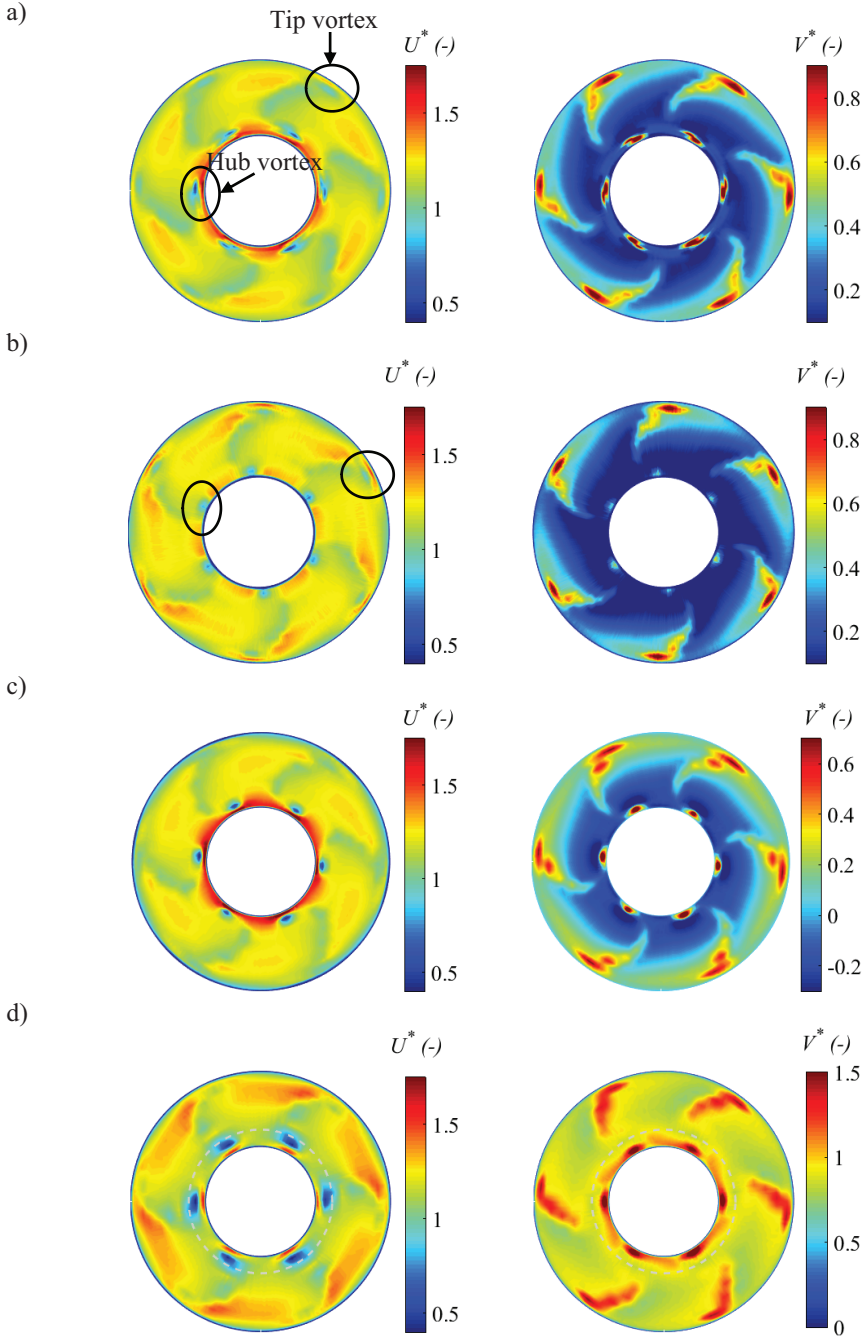
Fig 4.8.   Normalized phase-averaged velocities at the runner outlet: a) $BEP_{0.8}$, b) BEP_4, c) $HL_{0.8}$, d) $PL_{0.8}$.

Frequency analysis of the LDA measurement results that were acquired within and after the runner indicated oscillations in the axial and tangential velocity components with respect to the RVR frequency at both locations while the turbine operated at $PL_{0.8}$. Figure 4.9 presents the phase-averaged velocity contours of the axial and tangential velocities along section RC. Variations in the velocity components in the azimuthal direction showed the temporal evolution of the velocity field over one RVR rotation. The results showed asymmetric velocity fields after the runner rotated with a different frequency from the runner's rotational frequency. This process induced pressure fluctuations on the runner blades and exerted asymmetric forces on the runner, creating a dynamic bending moment on the shaft. These results also confirmed the oscillation of the velocity components with respect to the RVR frequency in the middle of the runner blades; see Fig 4.10. For more details, refer to **Paper B**.
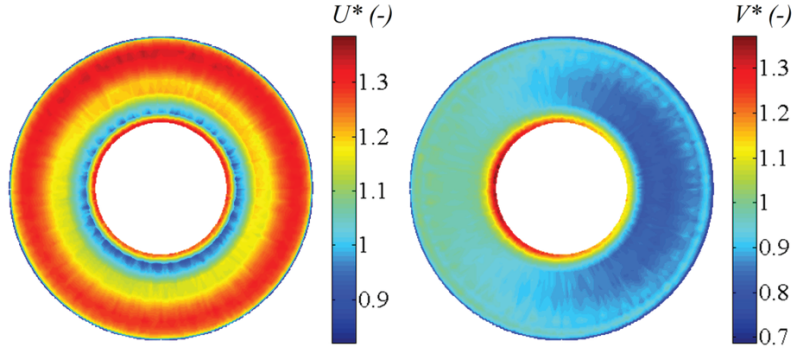
Fig 4.9.   Normalized phase-averaged axial and tangential velocities with respect to the RVR frequency at the runner outlet at $PL_{0.8}$.
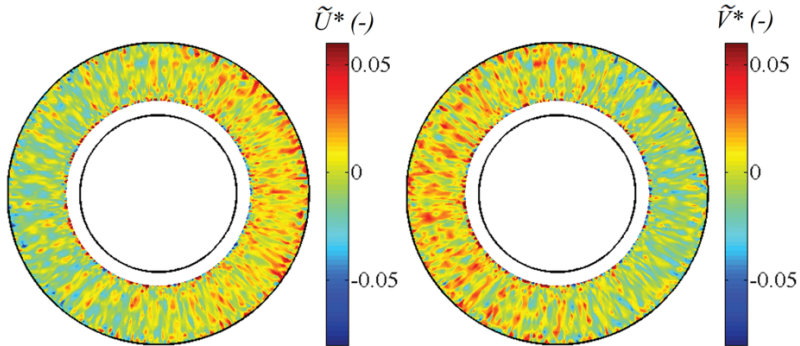
Fig 4.10.   Normalized phase-averaged contours of the oscillating parts of the axial and tangential velocities with respect to the RVR frequency within the runner at $PL_{0.8}$.

The precision in the manufacturing process of runner blades and assembly of turbines may result in different flow conditions through blade channels. This process may result in unequal forces on the runner blades, asymmetric forces on the runner and bending in the turbine shaft. The effect of manufacturing imperfections on the velocity profiles within the runner of Porjus U9 is presented in Fig 4.11. The contours within each blade channel are the result of the subtraction of the velocity contour in the corresponding channel from the average of the six channels. A maximum deviation of approximately 3% of the local velocity was present in both velocity components. The results showed asymmetries within the runner of a real test case, and no intentional asymmetry was applied on the model. Hence, the asymmetry can be representative of a

real case. More detailed investigations that perform sensitivity analysis on the effect of such asymmetries on turbine performance, e.g., asymmetric velocities, bending moments in the shaft, and turbine efficiency, can be considered for future studies.
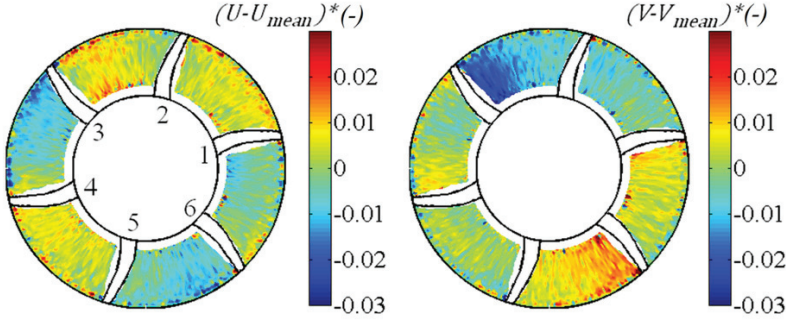
Fig 4.11.   Deviations in the axial and tangential velocity contours in different blade channels from the mean contour: $BEP_{0.8}$.

4.1.3. PIV measurements

The main purpose of the PIV measurements was to investigate the effect of the operating point on the velocity distribution within the draft tube. The acquired results showed that the flow symmetry after the draft tube's bend depended on the turbine operating point and the flow conditions at the draft tube's inlet. The most important parameters that affected the flow conditions were found to be the flow rate and the swirl of the flow at the draft tube's inlet. Another parameter that should logically affect the flow conditions is the geometry of the bend. Two dimensionless parameters that consider these three factors allow us to characterize the flow asymmetry and structure of secondary flows inside the diffuser: the Dean number (De) and the swirl intensity (Sw). These parameters are defined as follows:

$$De = \frac{\rho Q D_b}{A\mu} \sqrt{\frac{D_b}{2R_c}} \tag{4-1}$$

$$Sw = \frac{\int_{R_h}^{R_t} U_a U_\theta r^2 dr}{(R_t - R_h) \int_{R_h}^{R_t} U_a^2 r dr} \tag{4-2}$$

where μ is the dynamic viscosity; D_b is the pipe diameter; R_c is the bend radius; U_a and U_θ are the axial and tangential velocity components, respectively; r is the radius at the measurement location; and R_h and R_t are the runner hub and runner tip radii, respectively. The Dean number is the product of the Reynolds number and the curvature ratio, i.e., the ratio of the product of the inertia and centrifugal forces to the viscous forces. The Dean number represents the intensity of the secondary flows (Dean vortices) that form after a bend. The swirl number is defined as the ratio of the angular momentum flux to the axial momentum flux times the equivalent radius. This number represents the intensity of the swirling motion of the flow that leaves the runner. Table 4.1 presents the swirl and Dean numbers at each operating point of the turbine. The swirl numbers were calculated by using time-averaged velocity profiles that were recorded along section RC, as presented in the previous section. The Dean numbers were calculated based on the average hydraulic diameter at the bend inlet and outlet and the average curvature radii of the inner and outer walls of the bend.

Table 4.1.   Swirl and Dean numbers at different operating points.

Operating point		Part Load	BEP	High Load
Guide vane angle	α_{GV} (deg)	20	26.5	32
Dean number	De (-)	7.92×10^5	9.07×10^5	9.71×10^5
Swirl number	Sw (-)	1.044	0.381	0.092

Figure 4.12 presents the contours of the axial velocities within the diffuser and the structures of the secondary flows that formed after the draft tube's bend at each operating point. The figure shows the results at the HL, BEP, and PL operating points from the top to the bottom. The swirl number increased and the Dean number decreased from the top to the bottom, as presented in Table 4.1. Figure 4.12a and b present the dimensionless contours of the axial velocities after the draft tube's bend and the schematics of the structures of the secondary flows at the upstream windows when the turbine was operating at HL, respectively. The schematic figure was deduced from the lateral and vertical velocity components within the draft tube, as presented in **Paper C**. Both the axial velocity contours and the schematics of the secondary flows resemble the flow conditions after a pipe bend: two counter-rotating vortices formed after the bend, and the maximum axial velocity region was located close to the side walls. However, the Dean structures were distorted, and some asymmetries could be seen in the axial velocity contours and in the schematics of the secondary flows. The flow rate through the right half of the draft tube was slightly higher than that through the left half: 52% versus 48%. Moreover, the right Dean vortex was stronger than the left vortex and moved towards the left half of the draft tube. The two Dean vortices met each other at Y*=0.28. Kaplakli and Örlu [75] showed that the flow symmetry after a pipe bend becomes disturbed when a swirl is imposed to the flow at the entrance of a pipe bend. Their study showed that two symmetrical Dean vortices form after the pipe bend when a swirl-free flow enters the bend. However, imposing a swirl to the flow at the pipe inlet disturbs the flow symmetry. The intensity of the Dean vortex that is co-rotating with the upstream swirl increases, while that of a counter-rotating vortex becomes weaker. The dominating vortex begins to move towards the dominated vortex, and most of the flow rate passes through the half of the pipe where the dominating vortex exists. Figure 4.13a shows the results of Kalpakli and Örlü [75] when a moderate swirl of $Sw = 0.1$ was imposed to the flow. The results were qualitatively similar to those that were acquired within the diffuser at HL with $Sw = 0.092$.

Increasing the swirl number to 0.381 by moving the operating point to the BEP increased the flow asymmetry within the diffuser; see Fig 4.12c and d. Around 56% of the flow rate passed through the right half, the size of the right Dean vortex increased, and the size of the other vortex shrank. Similar results were reported by Kaplakli and Örlu [75] at $Sw = 0.3$, as shown in Fig 4.13b. Running the turbine at the PL resulted in a swirl of 1.044 at the draft tube's inlet. Increasing the swirl intensity induced more asymmetry in the axial velocity after the bend; see Fig 4.12e. Approximately 80% of the flow passed through the right half of the draft tube. The increased asymmetry in the axial velocity agreed with the simplified case of Kalpakli and Örlü [75] with a swirl number of 0.85, as presented in Fig 4.13c. However, a pair of counter-rotating vortices formed inside the diffuser, while the acquired results in the pipe depicted the presence of only one vortex that was co-rotating with the upstream vortex, which moved to the left side of the pipe. This difference can be explained by the geometrical differences between these two cases. Increasing the swirl inside the pipe increased the intensity of the right Dean vortex and decreased the intensity of the left vortex. At $Sw=0.85$, the left vortex completely disappeared from the flow, and the center of the right Dean vortex was located on the left side of the pipe. The same phenomenon also occurred inside the

draft tube. However, the rectangular shape of the draft tube's cross section resulted in the formation of another vortex in the right half of the draft tube. The counter-clockwise rotating flow hit the upper wall of the draft tube at $Y^* = -0.09$, and a secondary clockwise vortex formed on the right half of the draft tube. The results showed that the flow asymmetry was a 2nd-order function of the swirl-to-Dean ratio, as presented in **Paper C**.
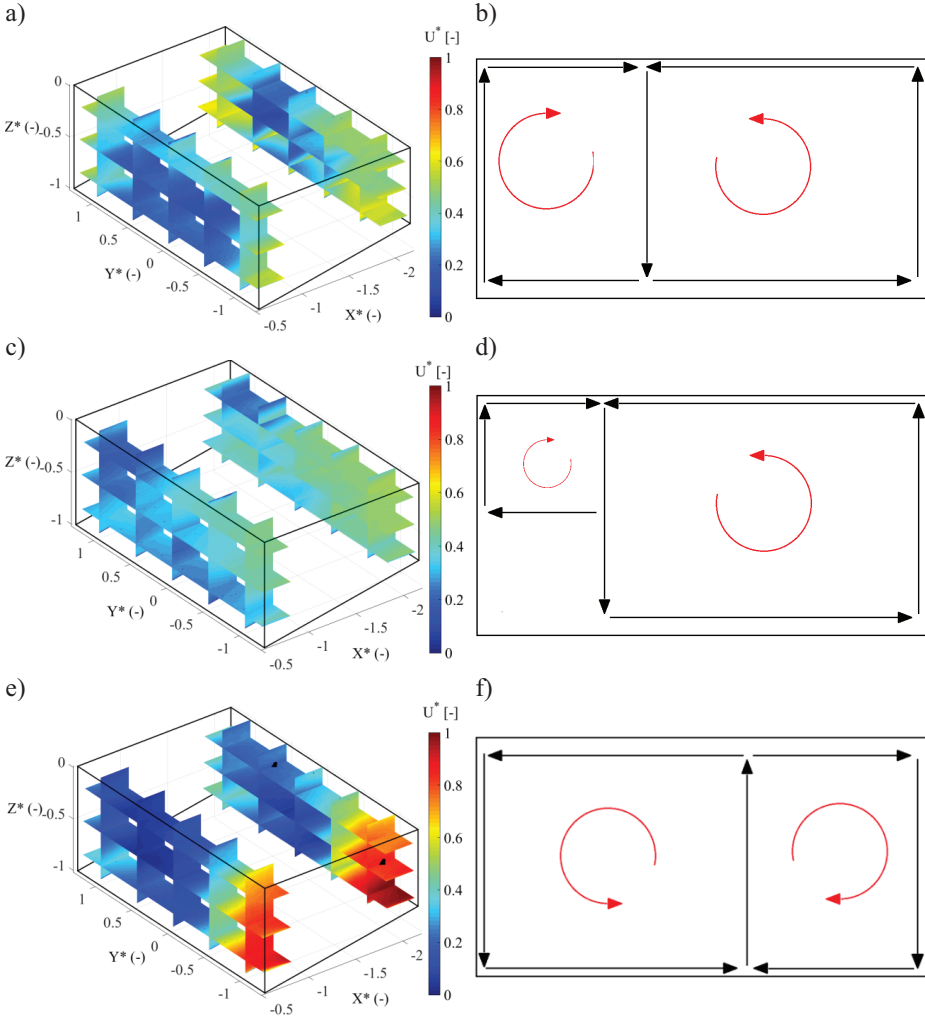
Fig 4.12.   a) Dimensionless axial velocity inside the diffuser at HL, b) schematic of the vortices after the draft tube bend at HL, c) dimensionless axial velocity at the BEP, d) schematic of the vortices at the BEP, e) dimensionless axial velocity at PL, f) schematic of the vortices at PL.

a)   b)   c)
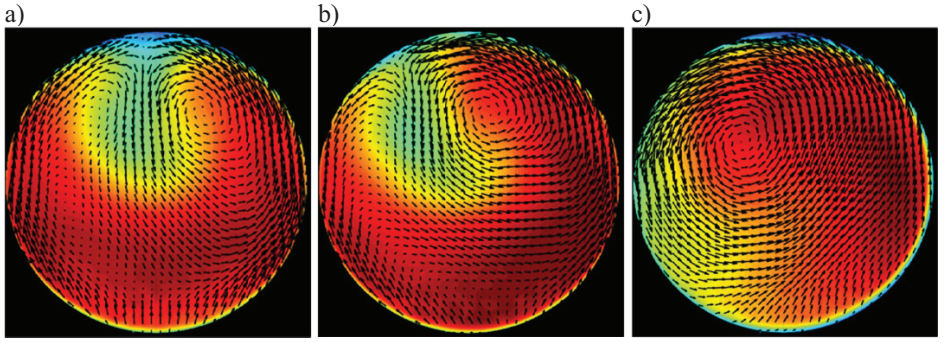
Fig 4.13.   Flow conditions after a pipe bend at a) *Sw*=0.1, b) *Sw*=0.3, and c) *Sw*=0.85. The contours show the magnitude of the axial velocity, and the vector maps show the velocity vector map projected to the measurement plane [75].

Figure 4.14 presents the amplitude spectra of the axial and lateral velocities at two points after the draft tube's bend, i.e., (2, -1, -0.4) and (2, 0.5, -0.15), which are marked with black marks in Fig 4.12e. The results at the point in the high axial velocity region showed that a peak at f^*=0.17 dominated the spectra in both velocity components. This frequency was related to the RVR that formed inside the draft tube cone of the turbine at PL. However, no specific peak was found in the amplitude spectra of the velocity components at the point in the low axial velocity region. Hence, special attention should be dedicated to regions with high flow rates when turbines operate at PL during the structural design of draft tubes to suppress crack propagation associated with RVR fluctuations.

a)   b)
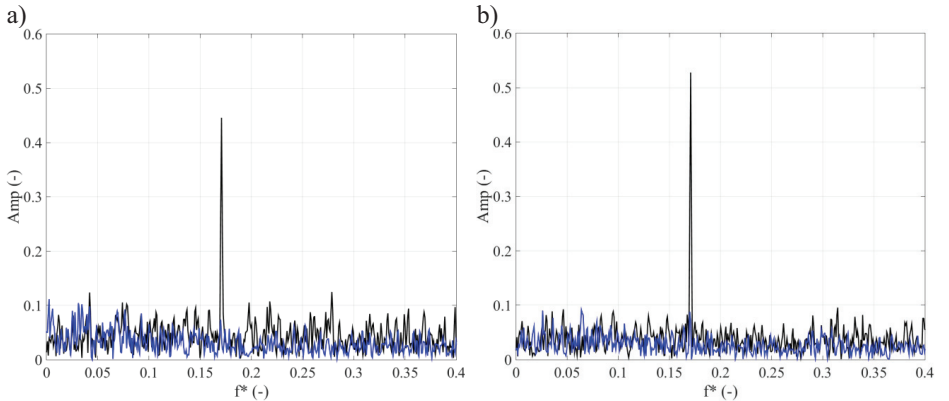
Fig 4.14.   Amplitude spectra of the velocities within the draft tube at PL; a) axial velocity and b) lateral velocity. Black: (2,-1,-0.4); blue: (2, 0.5, -0.15).

4.2. Transient results

Concerns regarding pressure fluctuations that are exerted on different parts of hydraulic turbines during load variations have drawn increased attention, mainly because of the more frequent load variations and starts/stops that hydraulic turbines currently experience [78]. In this context, runner blades are very important because of their effects on the turbine's efficiency, vulnerability, comparably high manufacturing costs, and special technologies that are required for their manufacturing. This section presents the main contribution of the transient pressure measurements in understanding the effect

of transients on fluctuations that are exerted on the runner and the process of RVR formation/mitigation.

Figure 4.15 presents the pressure signals that were recorded at the PS6 and SS6 blade sensors under various load variation schemes. Fig 4.15a and b show the pressure variations during load rejection from HL to the BEP. The pressure signals were normalized by using their initial values. The results showed that the load rejection results in a smooth decrease in pressure on the pressure surfaces of the runner blades and a smooth pressure increase on the suction side, creating a lower pressure difference on the blades, a lower torque, and a lower output power. No specific phenomenon was found during the load variation process. Hence, the load variations between HL and the BEP were considered to be harmless for the runner blades; see **Paper D** and **Paper E** for more details.

Figure 4.15c and d illustrate the corresponding results during load rejection from HL to PL. With the start of the guide vanes closure process, the pressure decreased on the pressure side of the blades and increased on the suction side. As the guide vanes closed further, the plunging mode of the RVR appeared in the signals, and the rotating mode initiated 2 s later. The initiation times of the plunging and rotating modes are indicated by vertical dashed and vertical dot-dashed lines, respectively. As seen in Fig 4.15d, after the initiation of the rotating component of the RVR, the pressure on the sensors on the suction side of the blade and close to the hub tended to decrease momentarily. This phenomenon was not captured on the sensors close to the tip or on the pressure side of the runner blade. This observation resulted in a momentary change in the lift that was exerted on the runner blade and may have temporarily changed the torque that was exerted on the main shaft and the force on the turbine thrust bearing. An increased level of data scattering, especially on the suction side sensors after the formation of the RVR, also occurred when the turbine moved to the PL operating point.

Figure 4.15e and f, which present the PL to HL load variation results, exhibit similar trends as those during load variations from HL to PL but in reverse order. The only difference is that the pressure variation on SS6 was smooth compared to that for the HL to PL case, and no sudden pressure changes occurred in the pressure signal during the RVR's mitigation; compare Fig 4.15d and f.

Figure 4.16 presents spectrograms of two pressure sensors on the suction and pressure sides of the runner blades, namely, SS5 and PS6. Figure 4.16a and b present the corresponding results for load variation from HL to the BEP. The results showed that the transition proceeded in a smooth manner, and no specific frequency appeared in the spectrogram during the transition. For more discussion regarding load variations between the BEP and HL, please refer to **Paper D** and **Paper E**.
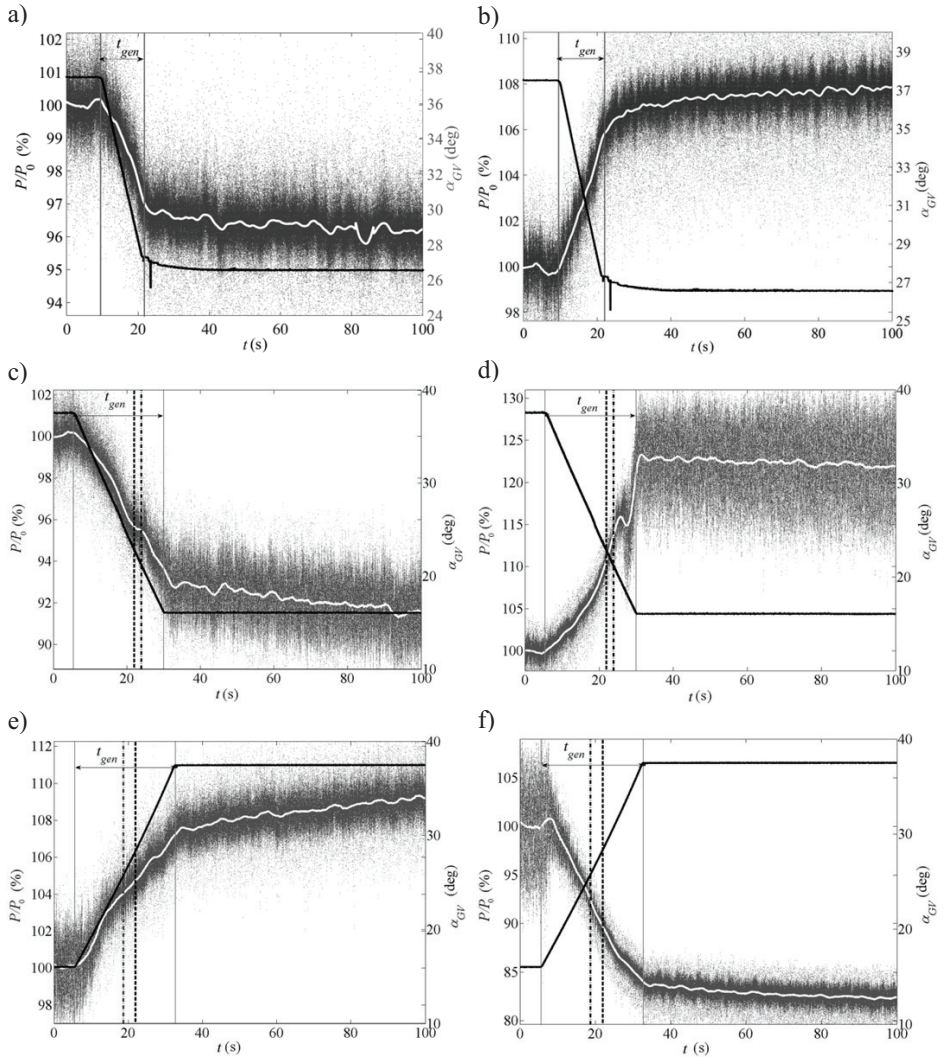
Fig 4.15.   Pressure variations on the runner blade surfaces during various load variation procedures; a) PS6 data from HL to the BEP, b) SS6 data from HL to the BEP, c) PS6 data from HL to PL, d) SS6 data from HL to PL, e) PS6 data from PL to HL, and f) SS6 data from PL to HL. Black dots: instantaneous pressures; white line: smoothed pressure; black line: guide vane angle; dot-dashed and dashed lines: formation/mitigation instant of the rotating and plunging modes, respectively.

Spectrograms of the pressure signals during load variation from HL to PL are presented in Fig 4.16c and d. Unlike the previous case, two sub-asynchronous frequencies appeared in the plots during load rejection and dominated the spectrogram. The frequencies were close to $0.2f^*$ and $0.8f^*$ and were associated with the plunging and rotating modes of the RVR, respectively, as discussed in the steady-state pressure measurements. The spectrograms showed that the frequencies of the plunging and rotating modes of the RVR did not appear simultaneously in the signals from the runner; the rotating mode appeared after a 2-s delay in the signals of all the sensors compared to the plunging mode. The method for decomposing the rotating and plunging

modes of the RVR in the stationary frame was applied to the transient measurement results from the draft tube cone walls to clarify the reason. The results are presented in Fig 4.17. As shown in Fig 4.17a, the plunging mode began to emerge at approximately 21.5 s in all the sensors along the draft tube cone. However, the rotating mode only emerged at the bottom of the draft tube cone (Cone 4) at this instant. Then, the rotating mode emerged sequentially from Cone 3 to Cone 1. The RVR began to form with the formation of a stagnation point at the cone's exit, with a separated flow downstream when the swirl of the flow that was entering draft tube exceeded a certain threshold value. This stagnation point moved upstream as the swirl ratio increased which agrees with the mechanism that was proposed by Dörfler et al. [52]. Moreover, the plunging mode propagated upstream of the RVR's location and could be considered as a sub-critical phenomenon, while the rotating mode affected the flow at the RVR's position and downstream. The rotating mode could then be considered as a super-critical phenomenon. After the formation of the RVR in the draft tube, wide-band noise manifested in the signals from the sensors on the suction side of the runner blade and close to the hub; see Fig 4.16c. This result occurred because of the change in the RVR's radius that occurred as the guide vane's angle varied. Decreasing the guide vane's angle, and consequently the flow rate, increased the diameter of the dead zone region (or recirculation bubble zone) downstream of the runner blades and increased the diameter of the RVR's orbit. As the guide vane's angle reached approximately 19°, the RVR reached the sensors that were located close to the hub, resulting in the manifestation of the wide-band noise in the signal. Thus, the RVR's frequency may not be the only source of the problems that are associated with the PL operation of hydraulic turbines; these problems may also be related to the wide-band noise that is exerted on the turbine's runner.

Figure 4.16e and f present spectrograms of the sensors at SS5 and PS6 during the load acceptance process from PL to HL, respectively. This load variation involved the mitigation of the RVR. The main features of the spectrograms are similar to those in parts c and d of the figure for the case of load rejection, but in reverse order. One distinct difference is the larger time difference between the mitigation time of the rotating mode and the plunging mode in this case, i.e., 3-4 s compared to 2 s during the load rejection process. This phenomenon can be related to hysteresis effects in the flow.
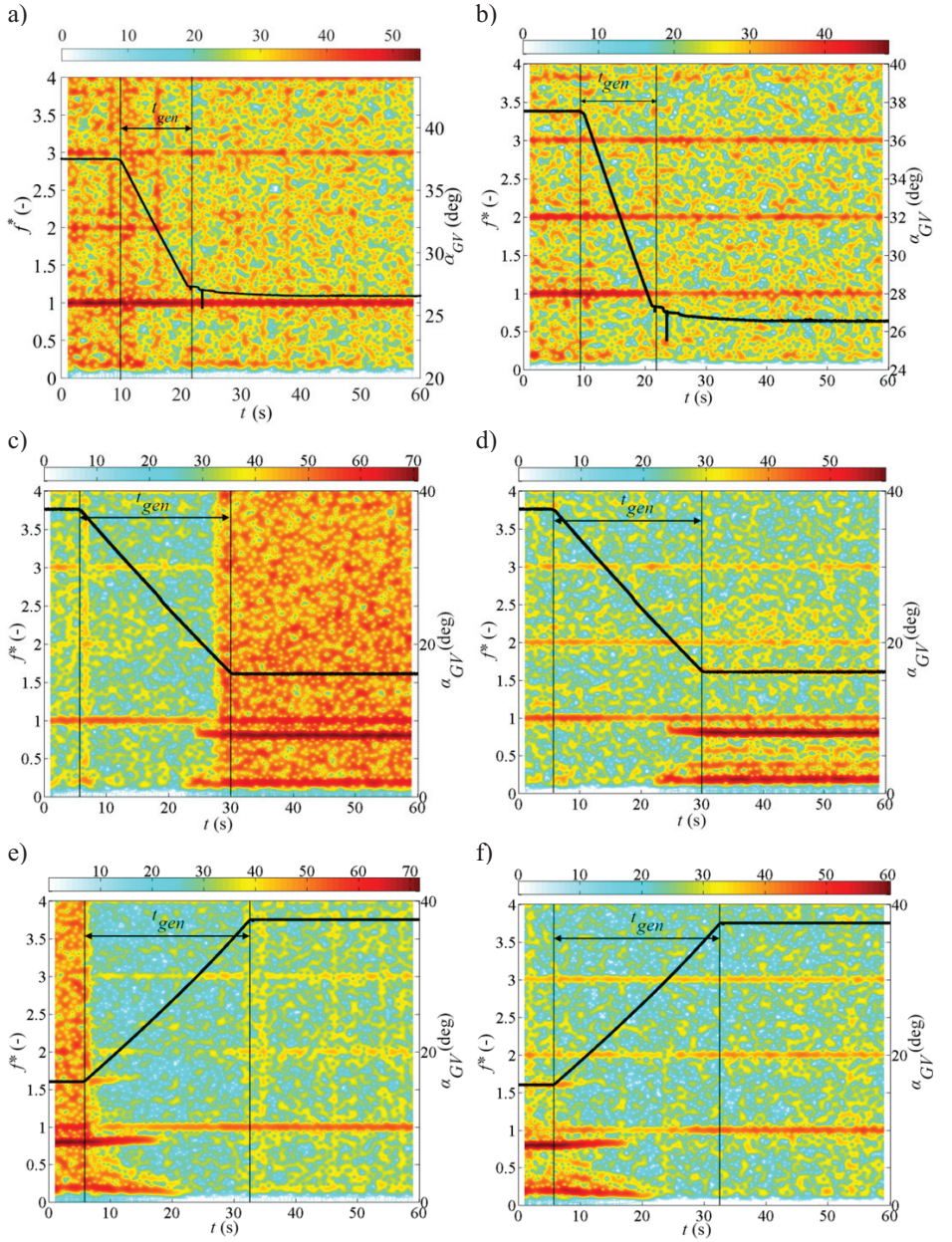
Fig 4.16.   Spectrograms of the pressure sensors on the runner blade. The black curve represents the variation in the guide vane angle. a) SS5 data from HL to the BEP, b) PS6 data from HL to the BEP, c) SS5 data from HL to PL, d) PS6 data from HL to PL, e) SS5 data from PL to HL, and f) PS6 data from PL to HL.
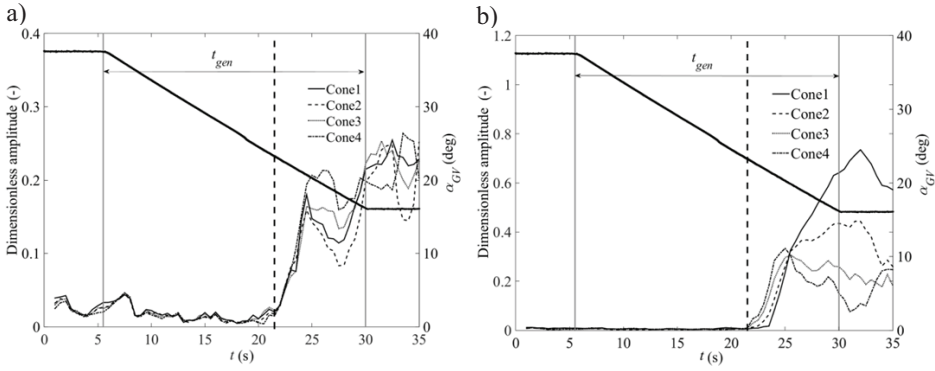
Fig 4.17. Decomposition of the RVR modes from the pressure signals on the conical draft tube during load variation from HL to PL: (a) plunging mode and (b) rotating mode. The dashed line indicates the formation time of the plunging mode.

Chapter 5

CONCLUSIONS

"I have come to the conclusion, after many years of sometimes sad experience, that you cannot come to any conclusion at all."

Vita Sackville-West

In this thesis, the flow through a Kaplan turbine model, the Porjus U9, was investigated. Different measurement techniques were implemented to study the flow condition within the turbine conduit during on-cam, off-cam and transient operation of the Kaplan model. Pressure measurements were performed on the runner blades, penstock, and draft tube of the turbine during on-design and off-design operation of the turbine as well as during various load variation processes. Laser Doppler anemometry (LDA) measurements were performed within and after the runner as well as inside the turbine diffuser. The flow conditions after the draft tube bend of the studied model and at the draft tube outlet were investigated using particle image velocimetry (PIV).

Pressure measurements on the runner at different operating points demonstrated the inability of the spiral casing to supply water to the distributor with an appropriate angle of attack close to the lip-entrance junction region. The poor performance of the spiral casing resulted in flow separation on the vanes located close to this region. This effect induced pressure fluctuations, with the guide vanes passing frequencies to the runner blades. The peak of the pressure fluctuations associated with the flow asymmetry at the lip-entrance region was a monotonically increasing function of the turbine flow rate. A similar asymmetry was observed in torque measurements on the main shaft of the prototype as well as bearing force measurements on the journal bearings of the prototype. The PL operation of the turbine involved a rotating vortex rope (RVR) formation within the draft tube of the model. The RVR induced pressure fluctuations to the runner blades with two different frequencies associated with the plunging and rotating modes of the RVR. The plunging mode of oscillations was found to be a subcritical phenomenon inducing pressure fluctuations both upstream and downstream of the RVR location. On the other hand, the rotating mode was found to be supercritical, inducing pressure fluctuations in the area where the RVR was formed and downstream

of that location. The amplitude of the rotating mode dominated the plunging mode in the pressure signals acquired from the runner blades.

Pressure measurements were also performed during different load variation schemes to investigate the effect of load variations on the pressure fluctuations exerted on the runner and to study the formation/mitigation process of the RVR as a detrimental phenomenon within the draft tube of the turbine. A smooth transition between the BEP and the HL of the Kaplan turbine was observed. However, the transition from BEP and HL to the PL triggered the formation of a RVR inside the draft tube. The formation of the RVR during the load rejection processes began with the appearance of the rotating mode of the RVR close to the end of the draft tube cone. Simultaneous to the rotating mode formation, the plunging mode appeared in all the sensors located on the draft tube wall and on the runner blades. Further closure of the GVs moved the RVR upstream until it reached the runner. Settlement of the RVR close to the runner induced a sudden pressure change on the suction side of the runner blade, followed by wide-band frequency fluctuations in the inner part of the runner. Further closure of the GVs increased the RVR precession radius, RVR precession frequency, and amplitude of the rotating and plunging modes of the RVR induced on the runner pressure sensors. The RVR mitigation process from PL to BEP and HL was similar to the RVR formation process but occurred in the reverse direction. However, the mitigation process was smoother than the formation process, and there was no sudden change in the pressure signals on the runner. Preliminary investigations showed that the RVR formation process was faster than the mitigation process, which can be associated with some hysteresis effects. More detailed measurements aimed at studying this phenomenon are required to draw a clear conclusion.

The LDA measurements performed within and after the runner showed different secondary flows at these locations, e.g., hub and tip vortices at the runner outlet and tip leakage within the runner. The velocity profiles and velocity contours acquired in the measurement sections proved that the flow features are independent of the working conditions as long as the turbine operates under RVR-free condition. Changing the runner blade angle affected the intensity of the hub and tip vortices because of the corresponding variations in the clearances. However, the RVR formation distorted the flow condition within and after the runner. The axial velocity decreased close to the hub region and increased close to the outer part of the runner after RVR formation. The RVR formation resulted in asymmetric velocity fields within and after the runner, rotating with the RVR frequency. This effect resulted in fluctuating and asymmetric forces on the runner, which rotated with respect to the RVR frequency. In turn, oscillating bending forces were exerted on the runner. The inaccuracies in manufacturing processes using the current technology resulted in up to 3% asymmetries in the velocity fields acquired in different channels within the runner.

The PIV measurements performed within the diffuser showed that Dean vortices are the dominant flow structures after the draft tube bend of the turbine while the turbine operates under the HL operating point with a small swirling flow imposed on the draft tube inlet. Increasing the swirl by decreasing the flow rate through the turbine disturbed the flow symmetry within the diffuser. The Dean vortex co-rotating with the upstream swirl dominated the counter-rotating vortex and a larger portion of the flow passed through the half diffuser to which the dominating Dean vortex belongs. Flow asymmetry was shown to be a second-order function of the swirl-to-Dean number ratio.

Chapter 6

SUGGESTIONS AND FUTURE WORKS

"Science, my boy, is made up of mistakes, but they are mistakes which it is useful to make, because they lead little by little to the truth."
Jules Verne, Journey to the Center of the Earth

The flow conditions in different parts of a turbine model were studied in this work using different measurement techniques. New research questions were raised after analyzing the results. Further experimental and numerical investigations may be performed to answer these questions. This section presents recommendations for future work geared toward answering these questions.

Pressure measurements on the runner blades during on-design and off-design operation of the turbine showed induced pressure fluctuations on the runner that were associated with the stationary parts located upstream of the runner, i.e., spiral casing and vanes located in the distributor. The pressure fluctuations can be either purely fluid dynamic in nature or caused by a combination of fluid dynamics and structural fluctuations. Structural measurements on the rotating parts of the turbine may be performed to isolate the effect of fluid dynamic fluctuations from structural vibrations. Strain gauge measurements on the runner blades and the main shaft of the turbine and vibration measurements on the runner blades using accelerometers can be useful for this purpose.

The pressure measurements performed on the runner showed asymmetric flows delivered to the runner, and signs of upstream vanes wake were captured by the pressure sensors located on the runner. The information provided by the pressure measurements is limited to pressure fluctuations and does not provide any detailed information about the source of the fluctuations. The exact position of the asymmetry is not clear; it can begin on the spiral casing tongue or before or after that. The phase-averaged pressure measurements on the runner blades showed that fluctuations with a frequency of 20f*

originated upstream. However, the source of the fluctuations is not clear; they can be associated with either the SVs or the GVs. Moreover, the flow asymmetry at the distributor outlet captured by the runner blade pressure measurements can be related to either the asymmetric radial velocity or tangential velocity or both at the distributor outlet. Clarifying the type of asymmetry is valuable because it can help guide designers in solving the asymmetry problem. Performing PIV measurements at different azimuthal positions of the distributor is recommended to clarify the issues mentioned above. The results are also valuable from a numerical simulation point of view. Currently, no velocity measurement is available between the spiral casing and the middle of the runner, while the flow complexity within the distributor and the vaneless space makes CFD simulations challenging. Velocity measurements in this section are valuable for numerical validation.

The study of the effect of the transient operation of the turbine on the pressure fluctuations exerted on the runner blades began with experimental investigations during load variation procedures. Pressure pulsations exerted on the runner blades and the draft tube walls of the model during different transient scenarios, e.g., start/stop, load rejection, etc., can be studied. Moreover, the transient processes were investigated while the turbine was operating under off-cam operations. Investigating the transient processes while the turbine operates under on-cam operating conditions and optimizing this double-variable process has not yet been performed before to the best of the author's knowledge.

The LDA measurements performed within and after the runner indicated the presence of secondary flows at the measurement locations. However, their evolution in time and space cannot be captured by LDA measurements. It is interesting to observe the shape of the secondary flows and their evolution using time-resolved stereoscopic PIV or through the more complicated method of tomographic PIV. Of particular interest is the interaction between the hub vortices and the runner hub. It is hypothesized that the hub vortices associated with the hub clearances are beneficial for flow stabilization inside the draft tube and for preventing flow separation on the runner hub. Filling the gaps and repeating the PIV measurements previously explained where hub vortex exists in the current setup can be an accurate way to prove/refute this hypothesis.

Time-resolved PIV measurements within the draft tube cone are important, multi-purpose measurements. Such measurements during the steady-state operation of a turbine provide useful information about flow evolution along the draft tube at different operating points. Implementing more advanced flow analysis techniques such as proper orthogonal decomposition (POD) would provide information about the shape and energy content of different modes of the flow. Moreover, the radial component of the velocity field inside the draft tube cone, which is the missing component during the performed LDA measurements, can be measured by the PIV technique. Performing time-resolved PIV measurements during transient processes would provide further insight into the flow condition within the draft tube during load variation processes. Visualization of RVR formation/mitigation processes may be one reason for performing such PIV measurements. Furthermore, applying advanced data analysis techniques such as dynamic mode decomposition (DMD) can provide valuable information about the RVR formation/mitigation mechanism.

The effects of manufacturing deficiencies/inaccuracies on the flow asymmetry within the runner may be studied by intentionally generating geometric deviations on one of the runner blades. This investigation may focus on studying the effects of variations in the blade installation angle, small deviations in the shape of the runner blade, etc., on turbine performance, velocity fields within and after the runner, wobbling of the main shaft and periodical forces exerted on the journal bearings.

The PIV measurements performed within the diffuser of the model provided useful information about the source of flow asymmetry within the diffuser and the secondary flows at the measurement locations. However, flow complexities within the draft tube, the large dimensions of the measurement sections and limited optical access were the main parameters constraining accurate and more detailed investigations. It is suggested that a small-scale model of the draft tube with a swirl control device at its inlet be manufactured. Time-resolved stereoscopic PIV or tomographic PIV may be performed to study the effect of the entering swirl and the draft tube bend on the flow conditions within the draft tube. Implementing such techniques may clarify the modes of the flow and interactions between the Dean vortices and the imposed swirl.

The measurements campaigns on flow conditions in different parts of Porjus U9 model provided valuable information about the characteristics of the turbine. Investigating the flow condition in the corresponding prototype is of interest for studying the scaling effects by comparing the results.

Paper F presents the results of numerical simulations of the whole model at the BEP. The quality of the simulations should be improved and validated against the experimental measurement results. Similar simulations should be performed at HL and PL and under load variations.

Two measurement campaigns aimed at investigating the flow conditions within the model and problem diagnosis provided some information about different sources of harmful pressure fluctuations exerted on the runner and certain flow phenomena negatively affecting turbine performance. Asymmetric flow fed to the runner, RVR formation at PL, flow asymmetry at the draft tube outlet and inappropriate flow conditions at the stationary vanes outlet are among some of the most important phenomena affecting turbine performance observed in this study. Making certain modifications to the turbine to reduce the negative effects and evaluating the effect of the modifications on turbine performance can be profitable research endeavors from an industrial point of view. Special attention can be dedicated to the modification of the spiral casing and distributor and designing swirl controlling devices at the draft tube inlet.

Chapter 7

DIVISION OF WORK

"My opinion, my conviction, gains immensely in strength and sureness the minute a second mind has adopted it."

Novalis

Paper A
Experimental Investigation of the Hydraulic Loads on a Kaplan Turbine Runner Model and the Corresponding Prototype
Amiri K., Cervantes M. J., and Mulu B.

The measurements and analysis were performed by Amiri, while all authors wrote the paper.

Paper B
Experimental Investigation of the Inter-Blade Flow in a Kaplan Runner at several Operating Points using LDA
Amiri K., Mulu B. G., and Cervantes M. J.

The measurements were performed by Mulu and the data analysis was performed by Mulu and Amiri. All authors wrote the paper.

Paper C
Experimental study on flow asymmetry after the draft tube bend of a Kaplan turbine
Amiri K., Mulu B., Raisee M., Cervantes M.J.

The measurements and analysis were performed by Amiri, while all authors wrote the paper.

Paper D
Unsteady Pressure Measurements on the Runner of a Kaplan Turbine during Load Acceptance and Load Rejection
Amiri K., Cervantes M. J., and Mulu B.

The measurements and analysis were performed by Amiri, while all authors wrote the paper.

Paper E
Effects of load variation on a Kaplan turbine runner
Amiri K., Mulu B., Cervantes M.J., Raisee M.

The measurements and analysis were performed by Amiri, while all authors wrote the paper.

Paper F
Numerical investigation of flow asymmetry at spiral casing of a Kaplan turbine
Amiri K., Mulu B., Raisee M., Cervantes M.J.

The numerical simulations and the data analysis were performed by Amiri. All authors wrote the paper.

REFERENCES

[1] Krivchenko, G.I., 1994, "Hydraulic machines: turbines and pumps," CRC Press, 2nd edition, US.

[2] Wikander, Ö, 1985, "Archaeological evidence for early water-mills, an interim report," History of Technology, 10, pp. 151-179.

[3] "A brief history of hydropower," International hydropower association, www.hydropower.org.

[4] "History of hydropower," Office of Energy Efficiency & Renewable Energy, Energy.gov.

[5] Liébard, A., Nahon, C., and Auzet, M., 2013, "Worldwide electricity production from renewable energy sources," Observ'ER.

[6] Rudberg, P.M., 2013, "Sweden's evolving hydropower sector: Renovation, restoration and concession change," Stockholm Environment Institute, Stockholm, Sweden.

[7] Cabrera, E., Espert, V., and Martinez, F., 1996, "Hydraulic machinery and cavitation, Volume I," Kluwer Academic Publishers, Netherlands.

[8] "Xiangjiaba hydropower plant, China," Power technology, www.power-technology.com.

[9] "Three Gorges Dam hydroelectric power plant, China," Power technology, www.power-technology.com.

[10] "Lilla Edet hydro power station and salmon farm," Vattenfall AB, http://powerplants.vattenfall.com/lilla-edet.

[11] "Energy NB Power-Hydro," Energy NB Power, www.nbpower.com.

[12] Nilsson, V., 2014, "Nordic Market Report 2014: Development in the Nordic electricity market," NordReg, Eskilstuna, Sweden.

[13] "Nuclear Power in Sweden," World Nuclear Association, www.world-nuclear.org.

[14] Wizelius, T., 2014, "Windpower ownership in Sweden: Business models and motives," Routledge, New Yourk, US.

[15] Arpe, J., and Avellan, F., 2002, "Pressure wall measurements in the whole draft tube: steady and unsteady analysis," Proceedings of the 21st IAHR Symposium on Hydraulic Machinery and Systems, Lausanne, Switzerland.

[16] Ciocan, G. D., Avellan, F., and Kueny, J. L., 2000, "Optical measurement techniques for experimental analysis of hydraulic turbines rotor-stator interaction," Proceeding of the ASME Fluids Engineering Division Summer Meeting, Boston, Mass., USA.

[17] Iliescu, M. S., Ciocan, G. D., and Avellan, F., 2008, "Analysis of the cavitating draft tube vortex in a Francis turbine using particle image velocimetry measurements in two-phase flow," Journal of Fluids Engineering, 130, pp. 1-10.

[18] Ciocan, G. D., Iliescu, M. S., Vu, T. C., 2007, "Experimental study and numerical simulation of the FLINDT draft tube rotating vortex," Journal of Fluids Engineering, 129, pp. 146-158.

[19] Ciocan, G. D., and Iliescu, M. S., 2007, "Vortex rope investigation by 3D-PIV method," Proceedings of the 2nd IAHR International Meeting of the Workgroup on Cavitation and Dynamic Problems in Hydraulic Machinery and Systems, Timisoara, Romania.

[20] Iliescu, M. S., Ciocan, G. D., and Avellan, F., 2002, "3D PIV and LDV measurements at the outlet of a Francis turbine draft tube," Proceedings of FEDSM'02: The 2002 Joint US ASME-European Fluids Engineering Summer Conference, Montreal, Quebec, Canada.

[21] Muller, A., Favrel, A., Landry, C., 2014, "On the physical mechanisms governing self-excited pressure surge in Francis turbines," IOP Conf. Series: Earth and Environmental Science, 22, pp. 1-9.

[22] Avellan, F., 2000, "Investigation in a Francis draft tube: the FLINDT project," Proceedings of the 20th IAHR Symposium, Charlotte, North Carolina, USA.

[23] Müller, A., Bullani, A., Dreyer, M., 2012, "Interaction of a pulsating vortex rope with the local velocity field in a Francis turbine draft tube," 26th IAHR symposium on hydraulic machinery and systems, Beijing, China.

[24] Kobro, E., Gamboa, A., Bloch, R., 2009, "Onboard pressure measurement in high head Francis prototype runners," 3rd IAHR International Meeting of the Workgroup on Cavitation and Dynamic Problems in Hydraulic Machinery and Systems, Brno, Czech Republic.

[25] Kobro, E., Dahlhaug, O. G., and Nielsen, T. K., 2008, "Onboard pressure measurement in Francis model runner," 24th IAHR Symposium on Hydraulic Machinery and Systems, Foz Do Iguazzu, Brazil.

[26] Kobro, E., 2010, "Measurement of pressure pulsation in Francis turbines," PhD thesis, Norwegian University of Science and Technology (NTNU).

[27] Kobro, E., Nielsen, T. K., and Dahlhaug, O. G., 2010, "Data analysis from onboard Francis model runner," The 13th International Symposium on Transport Phenomena and Dynamics of Rotating Machinery, Honolulu, Hawaii, USA.

[28] Vekve, T., 2004, "An experimental investigation of draft tube flow," PhD thesis, Norwegian University of Science and Technology (NTNU).

[29] Vekve, T., and Skåre, P. E., 2002, "Velocity- and pressure measurements in the draft tube on a model Francis pump turbine," Proceeding of 21st symposium on Hydraulic Machinery and Systems, Lausanne, Switzerland.

[30] Sundstrom, l. R. J., Amiri, K., Bergan, C., 2014, "LDA Measurements in the Francis-99 draft tube cone," Earth and Environmental Science, 22, pp. 1-10.

[31] Gouin, P., Deschenes, C., Iliescu, M., 2009, "Experimental investigation of draft tube flow of an axial turbine by laser Doppler velocimetry," 3rd IAHR International Meeting of the Workgroup on Cavitation and Dynamic Problems in Hydraulic Machinery and Systems, Brno, Czech Republic.

[32] Gagnon, J. M., Aeschlimann, V., Houde, S., 2012, "Experimental investigation of draft tube inlet velocity field of a propeller turbine," Journal of Fluids Engineering, 134(10), pp. 1-12.

[33] Gagnon, J. M., Deschenes, C., Ciocan, G. D., 2008, "Numerical simulation and experimental investigation of the flow in an axial turbine," 24th IAHR Symposium on Hydraulic Machinery and Systems, Foz Do Iguassu, Brazil.

[34] Mulu, B., 2012, "An experimental and numerical investigation of a Kaplan turbine model," PhD thesis, Luleå University of Technology.

[35] Mulu, B. G., Jonsson, P. P., and Cervantes, M. J., 2012, "Experimental investigation of a Kaplan draft tube – Part I: best efficiency point," Applied Energy, 93, pp. 695-706.

[36] Jonsson, P. P., Mulu, B. G., and Cervantes, M. J., 2012, "Experimental investigation of a Kaplan draft tube – Part II: off-design conditions," Applied Energy, 94, pp. 71-83.

[37] Mulu, B., and Cervantes, M., 2011, "Phase resolved velocity measurements in a Kaplan draft tube model," 4th International Meeting on Cavitation and Dynamic Problems in Hydraulic Machinery and Systems, Belgrad, Serbia.

[38] Jonsson, P., 2011, "Flow and pressure measurements in low-head hydraulic turbines," PhD thesis, Luleå University of Technology.

[39] Jonsson, P., and Cervantes, M., 2009, "Time resolved pressure measurements on a Kaplan model," 33rd congress of IAHR, Vancouver, Canada.

[40] Farhat, M., Avellan, F., and Seidel, U., 2002, "Pressure fluctuation measurements in hydro turbine models," 9th International Symposium on Transport Phenomena and Dynamics of Rotating Machinery, Honolulu, Hawaii, USA.

[41] Trivedi, C., Cervantes, M. J., Gandhi, B. K., 2013, "Experimental and numerical studies for a high head Francis turbine at several operating points," Journal of Fluids Engineering, 135 (11), pp. 1-17.

[42] Trivedi, C., Cervantes, M. J., Dahlhaug, O. G., 2015, "Experimental investigation of a high head Francis turbine during spin-no-load operation," Journal of Fluids Engineering, 137(6), pp. 1-10.

[43] Trivedi, C., Gandhi, B. K., Cervantes, M. J., 2015, "Experimental investigations of a model Francis turbine during shutdown at synchronous speed," Renewable Energy, 83, pp. 828-836.

[44] Trivedi, C., Cervantes, M. J., Gandhi, B. K., 2014, "Experimental investigations of transient pressure variations in a high head model Francis turbine during start-up and shutdown," Journal of Hydrodynamics, 26(2), pp. 277-290.

[45] Trivedi, C., Cervantes, M. J., Gandhi, B. K., 2014, "Experimental investigations of transient pressure variations in a high head model Francis turbine during start-up and shutdown," Journal of Hydrodynamics, 26(2), pp. 277-290.

[46] Trivedi, C., Cervantes, M. J., and Gandhi, B. K., 2016, "Investigation of a high head Francis turbine at runaway operating conditions," Energies, 9(3), pp. 1-22.

[47] Trivedi, C., Cervantes, M. J., Gandhi, B. K., 2014, "Transient pressure measurements on a high head model Francis turbine during emergency shutdown, total load rejection, and runaway," Journal of Fluids Engineering, 136(12), pp. 1-18.

[48] Trivedi, C., 2013, "Transients in high head Francis turbines," Licentiate thesis, Luleå University of Technology.

[49] Trivedi, C. H., 2014, "Investigations of transient pressure loading on a high head Francis turbine," PhD thesis, Luleå University of Technology.

[50] Aeschlimann, V., Beaulieu, S., Houde, S., 2013, "Inter-blade flow analysis of a propeller turbine runner using stereoscopic PIV," European Journal of Mechanics - B/Fluids, 42, pp. 121-128.

[51] Lemay, S., Aeschlimann, V., Fraser, R., 2015, "Velocity field investigation inside a bulb turbine runner using endoscopic PIV measurements," Experiments in Fluids, 56, pp. 1-12.

[52] Dörfler, P., Sick, M., and Couto, A., 2013, "Flow-induced pulsation and vibration in hydroelectric machinery," Springer, London, UK.

[53] Lucca-Negro, O., and O'Doherty, T., 2001, "Vortex breakdown: a review," Progress in Energy and Combustion Science, 27(4), pp. 431-481.

[54] Cassidy, J. J., and Falvey, H. T., 1970, "Observations of unsteady flow arising after vortex breakdown," J. Fluid Mechanics, 41(4), pp. 727-736.

[55] Delbende, I., Chomaz, J. M., and Huerre, P., 1998, "Absolute/Convective instabilities in the Batchelor vortex: A numerical study of the linear impulse response," Journal of Fluid Mechanics, 355, pp. 229-254.

[56] Ruith, M. R., Chen, P., Meiburg, E., 2003, "Three-dimensional vortex breakdown in swirling jets and wakes: direct numerical simulation," Journal of Fluid Mechanics, 486, pp. 331-378.

[57] Broadhurst, M. S., 2006, "Vortex stability and breakdown: direct numerical simulation and stability analysis using BiGlobal and Parabolised formulations," PhD thesis, Imperial College.

[58] Zhang, R. K., Cai, Q. D., and Wu, J. Z., 2005, "The Physical Origin of Severe Low-Frequency Pressure Fluctuations in Giant Francis Turbines," Modern Physics Letters B, 19, pp. 1527-1530.

[59] Amiri, K., Mulu, B., Cervantes, M., 2016, "Effects of load variation on a Kaplan turbine runner," International Journal of Fluid Machinery and Systems, 9(2), 182-193.

[60] Rheingans, W. J., 1940, "Power swings in hydroelectric power plants," Transactions of ASME, 62(3), pp. 171-184.

[61] Amiri, K., Cervantes, M. J., and Mulu, B., 2015, "Experimental investigation of the hydraulic loads on a Kaplan turbine runner model and corresponding prototype," J. of Hydraulic Research, 53(4), pp. 452-465.

[62] Amiri, K., Mulu, B. G., Raisee, M., 2016, "Unsteady pressure measurements on the runner of a Kaplan turbine during load acceptance and load rejection," Journal of Hydraulic Research, 54(1), pp. 56-73.

[63] Amiri, K., Mulu, B. G., and Cervantes, M. J., 2015, "Experimental investigation of the inter-blade flow in a Kaplan runner at several operating points using laser Doppler anemometry," Journal of Fluids Engineering, 138, pp. 1-12.

[64] Bosioc, A. L., Susan-Resiga, R., Muntean, S., 2012, "Unsteady pressure analysis of a swirling flow with vortex rope and axial water injection in a discharge cone," Journal of Fluids Engineering, 134, pp. 1-11.

[65] Thicke, R. H., 1981, "Practical solutions for draft tube instability," International Water Power and Dam Construction, 33(2), pp. 31-37.

[66] Miyagawa, K., Sano, T., Kunimatsu, N., 2006, "Flow instability with auxiliary parts in high-head pump–turbines," 23rd IAHR Symposium on Hydraulic Machinery and Systems, Yokohama, Japan.

[67] Kurokawa, J., Kajigaya, A., Matusi, J., 2000, "Suppression of swirl in a conical diffuser by use of J-groove," 20th IAHR Symposium on Hydraulic Machinery and Systems, Charlotte, NC.

[68] Nishi, M., and Liu, S., 2013, "An outlook on the draft-tube-surge study," International Journal of Fluid Machinery and Systems, 6, pp. 33-48.

[69] Bradshaw, P., 1996, "Turbulence modeling with application to turbomachinery," Progress in Aerospace Sciences, 32(6), pp. 575-624.

[70] Mulu, B., and Cervantes, M., 2009, "Experimental investigation of a Kaplan model with LDA," 33rd congress of IAHR, Vancouver, Canada.

[71] Mulu, B., and Cervantes, M., 2010, "LDA measurements in a Kaplan spiral casing model," 13th Symposium on Transport Phenomena and Dynamics of Rotating Machinery, Honolulu, Hawaii, USA.

[72] McLaughlin, D. K., and Tiederman, W. G., 1973, "Biasing correction for individual realization of laser anemometer measurements in turbulent flows," Physics of Fluids, 16(12), pp. 2082-2088.

[73] Gubin, M. F., Volshanik, V. V., and Kazennov, V. V., 1974, "Investigation of curved draft tubes with long exit cones," Gidrotekhnicheskoe Stroitel'Stvo, 10, pp. 32-36.

[74] Amiri, K., Mulu, B., Raisee, M., 2016, "Experimental study on flow asymmetry after the draft tube bend of a Kaplan turbine," Advances and Applications in Fluid Mechanics, 19(2), pp. 441-472.

[75] Kalpakli, A., and Örlü, R., 2013, "Turbulent pipe flow downstream a 90° pipe bend with and without superimposed swirl," International Journal of Heat and Fluid Flow, 41, pp. 103-111.

[76] Glas, W., Forstner, M., Kuhn, K., 2000, "Smoothing and statistical evaluation of laser Doppler velocimetry data of turbulent flows in rotating and reciprocating machinery," Experiments in Fluids, 29, pp. 411-417.

[77] Coleman, H.W., and Steele, W.G., 2009, "Experimentation, validation, and uncertainty analysis for engineers," John Wiley & Sons Inc., New Jersey.

[78] Trivedi, C., Gandhi, B. K., and Cervantes, M. J., 2013, "Effect of transients on Francis turbine runner life: a review," Journal of Hydraulic Research, 51(2), pp. 121-132.

Paper A

Experimental Investigation of the Hydraulic Loads on a Kaplan
Turbine Runner Model and the Corresponding Prototype

Research paper

Experimental investigation of the hydraulic loads on the runner of a Kaplan turbine model and the corresponding prototype

KAVEH AMIRI (IAHR Member), PhD Student*, Department of Engineering Science and Mathematics, Luleå University of Technology, Luleå, Sweden*
Email: *Kaveh.amiri@ltu.se*

MICHEL J. CERVANTES, Professor*, Department of Engineering Science and Mathematics, Luleå University of Technology, Luleå, Sweden;* Professor*, Department of Energy and Process Engineering, Water Power Laboratory, Norwegian University of Science and Technology, Trondheim, Norway*
Email: *Michel.Cervantes@ltu.se* (author for correspondence)

BERHANU MULU, Senior Researcher*, Vattenfall Research and Development, Älvkarleby, Sweden*
Email: *berhanu.mulu@vattenfall.com*

ABSTRACT
This paper reports on unsteady pressure measurements on the runner blades of a Kaplan turbine model as well as torque and radial load bearing measurements on the corresponding prototype at several operating points to investigate the sources of periodic loads exerted on the runner when operating at the best efficiency point and off design. Pressure measurements on the model runner blades indicated that the spiral casing delivers a poorly conditioned flow to the guide vanes close to the lip-entrance junction, resulting in flow separation on the guide vanes. The asymmetric flow delivered to the runner induces large oscillations with respect to the guide vane passing frequency, runner frequency and its harmonics to the runner blades. The torque measurements on the prototype also revealed an asymmetric flow at the distributor outlet. The bearing radial load measurements performed on the prototype support the torque measurement results. The asymmetric hydraulic loads on the runner result in shaft wobbling, and the oscillatory forces exerted on the blades are transferred to the main shaft and bearings. Another source of oscillating forces exerted on the runner blades is the rotating vortex rope (RVR) formation that occurs at part-load operation of the turbine and induces pressure fluctuations at two sub-synchronous frequencies to the runner.

Keywords: Bearing load; blade pressure measurement; flow-induced vibration; Kaplan turbine; prototype measurement; spiral casing performance

1 Introduction

The world population growth rate, the increase in the price of fossil fuels and the associated problems with pollution have increased the demand for renewable energy sources. Renewable energy resources have proven to be a promising alternative to the use of fossil fuels in electrical generation industries. Different resources have been considered for this purpose, including wind power, hydropower, solar, biomass, geothermal, tidal and wave energies (Amin, 2012). Various innovative methods of extracting renewable energy in urban areas as well as at farms and power plants have also been suggested. Carcangiu & Montisci (2012) proposed a centripetal turbine in combination with an aeolian roof for use in urban environments. Many studies have been dedicated to increasing

electricity production by harvesting wave and tidal energies (Bryden & Couch, 2006; Buccino et al., 2012; Vicinanza, Ciardulli, Buccino, Calabrese, & Koefed, 2011). Some research has also focused on economically optimizing renewable energy production (Vieira & Ramos, 2008; Vieira & Ramos, 2009). The study performed by Fecarotta, Aricò, Carravetta, Martino, & Ramos (2015) demonstrated the economic and environmental benefits of using pumps as turbines in water distribution networks instead of pressure-reducing stations for pressure control purposes. However, according to an International Renewable Energy Agency's report (Amin, 2012), hydropower still produces the highest portion of electricity among renewable resources, generating 16–17% of the world's electricity and approximately 80% of the world's renewable electricity.

Among all renewable resources, hydropower represents a good complement to intermittent resources to be used for grid stabilization due to their unrivalled load variation capability. Hence, running hydropower systems at operating points with loads that are higher or lower than the best efficiency point (BEP), generally referred to as off-design operating points, has increased in recent years (Trivedi, Gandi, & Cervantes, 2013). Turbine operations at loads that are higher or lower than the BEP are referred to as high-load and part-load operations, respectively. Off-design operation may result in unfavourable flow conditions that induce oscillating loads on the runner, bearings and other rotating and stationary parts of the turbine. Harmful operating conditions, together with the emergence of water-lubricated bearings to address environmental issues, have increased concerns about the vibrations exerted on the rotating parts of the turbines. The considerably lower viscosity of water (0.66 cSt at 40°C) compared with those of turbine oils (32–68 cSt at 40°C) affects the sustainability of the new generation of turbine bearings, and these turbines can sustain lower specific bearing pressures (Golchin, 2013).

More frequent off-design operation, together with new environmental constraints, necessitates further investigations of the sources of fluid instabilities in hydraulic machines. The complexity of the flow in hydraulic machines (fully turbulent, quasi-periodic phenomena together with rotor-stator interaction) produces various physical phenomena, such as the formation of a rotating vortex rope (RVR) in the draft tube, that remain not clearly understood. Moreover, the accurate simulation of hydraulic machines remains a challenge, particularly at off-design operating points. Hence, additional experimental investigations of the pressures, forces and moments exerted on the rotating parts of turbines are required to better understand the flow conditions in water turbines, find the sources of such instabilities, and to determine the nature of the periodic forces acting on the rotating parts.

Flow conditions in the draft tube of Francis and propeller turbines have been widely investigated to find the sources of instabilities and fluctuating forces during the on-design and off-design operation of such turbines. Transient pressure measurements (Arpe & Avellan, 2002), laser Doppler anemometry (LDA) (Ciocan, Avellan, & Kueny, 2000; Iliescu, Ciocan, & Avellan, 2002) and particle image velocimetry (PIV) (Gagnon, Deschenes, Ciocan, & Iliescu, 2008; Gagnon et al., 2012; Gouin, Deschenes, Iliescu, & Ciocan, 2009; Iliescu, Ciocan, & Avellan, 2008) are the main experimental tools used for this purpose. The main features of the flow in the draft tube of a Kaplan turbine model (unit number 9 of the Porjus power plant, known as Porjus U9) during on-design and off-design operation have been investigated by Jonsson, Mulu, and Cervantes (2012) and Mulu, Jonsson, and Cervantes (2012).

Farhat, Avellan, and Seidel (2002) performed pressure measurements on the blades of a pump turbine model to measure hydraulic pressure fluctuations exerted on the rotating parts of the turbine. In a subsequent study, Kobro (2010) presented blade pressure measurements on a Francis turbine model and its corresponding prototype. Trivedi used the same model as Kobro for steady-state (Trivedi, Cervantes, Gandhi, & Dahlhaug, 2013) and load-variation measurements (Trivedi, 2013) with a focus on the rotor–stator interaction. Similar measurements have also been performed on a propeller turbine model at the LAMH Laboratory (Houde, Fraser, Ciocan, & Deschênes, 2012a, 2012b). In these studies, frequency analysis was performed on the acquired data to clarify the dominant frequencies exerted on different parts of the blades. The results indicated the presence of fluctuating forces at the runner frequency that could be due to the likely introduction of structural asymmetry in the manufacturing process, asymmetrical effects of the draft tube bend located downstream or an asymmetry in the flow entering the runner provided by the water supply system. However, the source of the disturbances was not clarified.

The performance of the spiral casing of the Porjus U9 model was investigated via LDA and pressure measurements to study the effect of the water supply system on the runner force fluctuations. The LDA measurements taken at two different locations of the spiral casing by Mulu and Cervantes (2010) indicated that "the radial velocity has a similar magnitude at both locations, which indicate that an axisymmetric flow entered the distributor". LDA measurements also indicated symmetric flow at the runner outlet at the BEP (Jonsson et al., 2012) and off-design operating conditions (Mulu et al., 2012). However, the pressure measurements taken at four peripheral locations at the distributor indicated the presence of asymmetry at the distributor outlet (Jonsson & Cervantes, 2010). An asymmetrical flow entering the runner may induce undesired forces and de facto vibrations on the runner that can be transferred to the entire system, which may induce fatigue and affect the turbine lifetime. One method of clarifying the source of the asymmetry is to experimentally investigate the flow condition that the runner was subject to, for example by measuring the pressure on the runner blades.

The current study presents unsteady pressure measurement results acquired at the blades of the Porjus U9 model as well as main shaft torque and load measurements on the guide bearings of the corresponding prototype. The main goal of this study is to investigate the main sources of the fluid-dynamics-related fluctuating forces exerted on the rotating parts of the runner. The effect of the water supply system performance (spiral casing, guide vanes and stay vanes) and off-design operation of the turbine on the pressure distribution of the blades and exerted forces on the rotating parts of the turbine was studied. The results can also be used to study the model-prototype relationships and scale-up effects in water turbines. The model measurements were performed at three operating points of the turbine, namely, part load, the BEP and high load, to investigate the sources of oscillating forces exerted on the runner at different operating points. The torque exerted on the main shaft of the prototype was measured by strain gauges installed on the main shaft. The prototype guide bearing pads were also equipped with load cells, and the exerted loads were measured to find the sources of the

loads on the bearings. For comparison purposes, highly similar pressure measurements were performed at the propeller of the Francis turbine models, as noted above. However, in most cases, no comparison was made between the model and the prototype. Another new feature of the current work is the method used to analyse the results. Although some asymmetries of the pressure exerted on the runners of water turbines are reported in certain references, the sources of the asymmetries are not clarified. The phase-averaged results are presented in this paper and used to determine the physical sources of instabilities and the interaction between the runner and the water supply system.

2   Experimental setup

The measurements were performed on the Porjus U9 Kaplan turbine model and the corresponding prototype. The prototype, designed at the end of the 1990 s by Kvarner AB (now Andritz Hydro AB), is situated along the Lule River in northern Sweden. It has an operational head of 55 m, a discharge capacity of 20 m^3 s^{-1}, an output power of 10 MW and a rotational speed of 600 rpm. Its water supply system is composed of a penstock with a bend that delivers water to a spiral casing. The distributor has 20 equally spaced guide vanes and 18 stay vanes. The runner has a diameter of 1.55 m and is composed of six blades. The prototype was investigated at its BEP. The BEP specifications are presented in Table 1.

A 1:3.1-scale model of the prototype, presented in Fig. 1, was used to investigate the flow condition in further detail. The schematic is the same for the model and prototype because they are geometrically similar. The model runner diameter is 0.5 m, and the operational net head during all investigated operating conditions was 7.5 m. The runner rotational speed during the measurements was 696.3 rpm. The selected rotational speed ensured a similar speed factor, n_{ED}, in the model and prototype to ensure kinematic similarity between them.

The measurements at off-design points were performed under off-cam conditions, which means that the blade angle was set to the prescribed angle for the BEP and held constant for the other operating points. Such an operational condition is not typical for Kaplan turbines because they are doubly regulated. However, some power suppliers have investigated regulating power at a constant blade angle to decrease wear despite a decrease in efficiency. Furthermore, the power required to adjust the runner blades is also significant and decreases the machine's overall efficiency for temporary off-design operations. The model operating parameters at the investigated operating points are presented in Table 2.

2.1   Model instruments and measurement techniques

The model measurements were performed at the Vattenfall R&D model test facility in Älvkarleby, Sweden. The test rig is a closed-loop system designed for the testing of Kaplan, bulb and Francis turbines. The uncertainty in the flow rate and

Table 1   Operating condition parameters for the prototype

Operating point		BEP
Guide vane angle	α_{gv} (°)	28
Volume flow rate	Q (m^3 s^{-1})	18.5
Discharge factor	$Q_{ED} = \dfrac{Q}{D^2\sqrt{gH}}$(-)	0.331
Speed factor	$n_{ED} = \dfrac{nD}{\sqrt{gH}}$(-)	0.676

Table 2   Operating condition parameters of the model

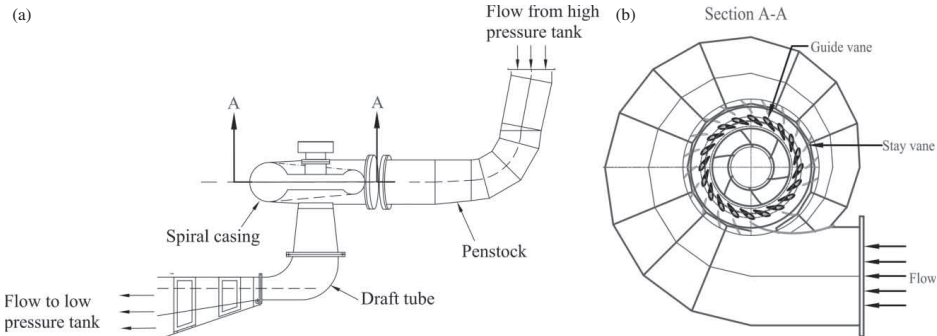| Operating point		Part load	BEP	High load
Guide vane angle	α_{gv} (°)	20	26.5	32
Volume flow rate	Q (m^3 s^{-1})	0.62	0.71	0.76
Discharge factor	Q_{ED}	0.289	0.331	0.354
Speed factor	n_{ED}	0.676	0.676	0.676
Relative efficiency to BEP	$\eta{-}\eta_{BEP}$ (%)	−5.6	0.0	−1.6

Figure 1   Side view of the model (a); top view of the water supply system (b); spiral casing, stay vanes and guide vanes (Section A–A)
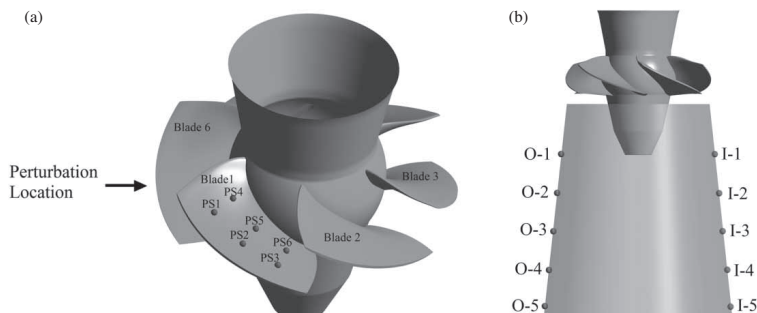
Figure 2   Sketches of the runner with the sensors (dots) on the blade pressure surface (the pressure sensors on the suction side are placed on blade 2, which is not visible in the figure) (a); and the draft tube cone with the pressure sensors (b)

hydraulic efficiency measurements are $\pm 0.13\%$ and $\pm 0.18\%$, respectively; see Mulu et al. (2012) for additional information about the test rig.

Six piezoresistive pressure sensors manufactured by Kulite (LL-080 series) were flush mounted on the pressure side of blade 1, and six sensors were installed on the suction side of blade number 2; see Fig. 2a. The arrow represents a perturbation that will be discussed in the "Data analysis" section. The sensors are located on the vertices of a net formed by the imaginary circles passing through 1/3 and 2/3 of the blade span and 1/4, 1/2 and 3/4 of the blade chord lines. The sensors located on the pressure side of blade 1 were denoted as PS1 through PS6 from the tip leading edge of the blade to the hub trailing edge of the blade. Sensors installed on the suction side of blade 2 (not visible in the figure) were denoted using the same numbering convention from SS1 through SS6. The pressure range of the sensors was selected to be 0–7 bar. The range was higher than the expected range of the pressure exerted on the runner under steady operation to allow for transient and start/stop measurements. The natural frequency of the sensors was 380 kHz, which is well above the expected frequencies during the measurements.

Ten pressure taps were mounted on two sides of the draft tube cone: five taps were equally spaced along the inner part and five taps were located along the outer part of the draft tube bend, as shown in Fig. 2b. Membrane-type pressure transducers from Druck (PDCR810) were flush mounted on the draft tube cone.

Two identical telemetry systems, one for each blade, from Summation Research Inc. (SRI-500e) were used during the calibration process and for the measurements. The system was able to transfer data with a frequency of up to 17 kHz. The transmitters, installed on the rotating shaft, sent signals to the stationary receiver. The analogue signals received by the receiver and pressure sensors on the draft tube cone were directly fed to a data acquisition (DAQ) system with 24-bit resolution (a PXI chassis with four Ni-4472 DAQ cards). The measurements were recorded with a sampling frequency of 4 kHz over a period of 300 s.

The system was calibrated by placing the blades in a specially designed nitrogen-tight steel pressure tank with the radio

transmitters. The Plexiglas cap of the calibration tank permitted radio transmission of the data from inside the tank. A DPI 610 pressure sensor calibrator from Druck was used as the calibration reference pressure. The signal from a magnetic encoder with an accuracy of 0.03° installed on the main shaft was also recorded to determine the runner's angular position at each instant.

2.2 Prototype instruments and measurement techniques

The torque exerted on the main shaft of the prototype was measured with two full-bridge strain gauges (HBM 350 W) installed on the prototype's main shaft. The measurement section is between "Bearing 1" and "Bearing 2", shown in Fig. 3a. An NI cRIO-9014 from National Instruments was installed on the shaft and used to digitalize the strain gauge signals. A wireless local area network (WLAN) was used to transfer the data from the cRIO to a stationary computer. The results were recorded with a sampling frequency of 2.5 kHz for 210 s.

A schematic of the turbine's rotating parts together with the support bearings is presented in Fig. 3a. The cross-section of bearing 1 is shown in Fig. 3b. It is composed of eight similar 44° pads distributed around the shaft. For the measurements, the pivot pins of the pads were replaced with load cells to measure the radial load on each pad during turbine operation. The load cells were installed flush mounted and along the radial lines on each pad in Fig. 3b. The detailed specifications of the pads and bearings are provided in Simmons (2013). Bearing 1 is located on top of the spiral casing shown in Fig. 1b. A comparison of Fig. 3b with the schematic of the spiral casing presented in Fig. 1b indicates that the spiral casing lip entrance peripheral is located where pads 2 and 3 are in contact; the dot in Fig. 3b illustrates this position. The signals from the load cells were recorded with the same data acquisition setup as the one used for the strain gauge measurements.

2.3 Uncertainty analysis

The calibration uncertainties of the test rig parameters and sensors used during the measurements are presented in Table 3. All
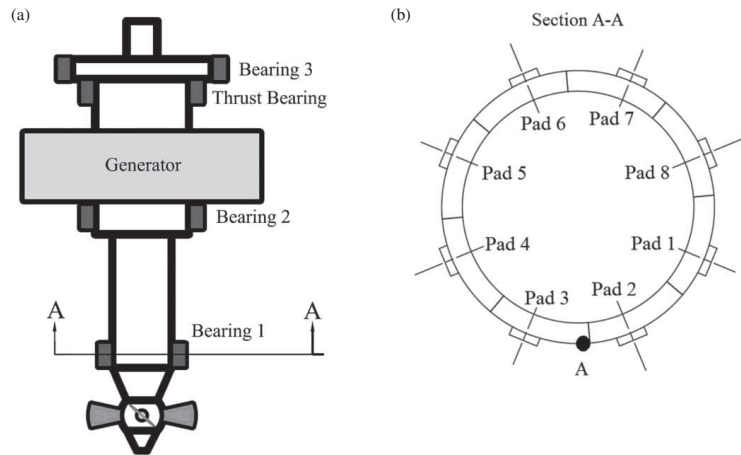
Figure 3   Arrangement of Porjus U9 bearings (a); and a sketch of the pads on bearing 1 (b), (Simmons, 2013)

Table 3   Calibration uncertainties of the test rig parameters and sensors

Instrument	Uncertainty	Position
Hydraulic efficiency	$\leq \pm 0.13\%$	Test rig
Volume flow rate (Q)	$\leq \pm 0.18\%$	Test rig
Head (H)	$\leq \pm 0.04\%$	Test rig
Guide vane angle setting (α_{gv})	$\leq \pm 1.3\%$	Test rig
Encoder	$0.03°$	Test rig
Pressure sensors	$\leq \pm 0.18\%$	Runner blades
Pressure sensors	$\leq \pm 0.1\%$	Draft tube cone
Strain gauge	$\leq \pm 1.5\%$	Prototype shaft
Load sensors	$\leq \pm 0.1\%$	Bearing pads

of the presented uncertainties are estimated from the sensor calibrations performed prior to measurements except for the strain gauges, which are reported by the manufacturer.

The uncertainty in the measurement of the bearing load of the prototype was estimated to be $\pm 0.25\%$, and the uncertainty for the pressure measurements performed on the model runner blades was estimated to be less than $\pm 0.3\%$.

3   Data analysis

The main analysis tools used to investigate the flow features in the rotating parts of the turbine were developed in MATLAB. The analysis was mainly based on frequency analysis and phase-resolving the acquired results. The pressure data obtained using the model were uniformly sampled, which allows the results to be treated with standard fast Fourier transform (FFT) methods. Welch's method was used for the spectral analysis, and a Hanning window was applied on the fluctuating parts of the pressure results, $\hat{P}_i(t)$:

$$\hat{P}_i(t) = P_i(t) - \bar{P}_i \qquad (1)$$

where t is time, $P_i(t)$ is the acquired pressure, and $\bar{P}_i$ is its time-averaged value. This method was used to obtain a more accurate approximation of the amplitudes in the spectral analysis results (Vekve, 2004). The original set of pressure measurement data, composed of data acquired using a 4 kHz sampling rate for 300 s, was divided into six sub-windows with 50% overlap. Hence, the maximum non-aliased frequency in all presented cases was 2 kHz, and the frequency resolution for each sample set was 0.0033 Hz. The results were also used to determine the phase difference between different pressure sensors.

The recorded signal from the encoder was used to determine the runner's angular position to angularly resolve the pressure signals. One runner revolution was then divided into bins of identical size, $\Delta\beta$. The averaged data at each bin centred at β_0 were obtained from the recorded data in the interval $[\beta_0 - \Delta\beta/2, \ \beta_0 + \Delta\beta/2]$. After performing a sensitivity analysis, the bin size was chosen to be 0.5° for all measurements to provide a smoothed curve by filtering out the high-frequency fluctuations in the pressure signals. No gradient compensation was required in the phase averaging based on the use of the small bins. The same methods were used to analyse the results of the prototype. The maximum non-aliased frequency in the strain and load measurements was 1.25 kHz. The frequency resolution for each sample set was 0.0048 Hz.

Due to the applied measuring technique, the same flow may yield different results. A perturbation in the water supply system resulting in an asymmetry of the flow at the distributor outlet is assumed to simplify the interpretation of the experimental results in the next section. The perturbation position is shown in Fig. 2. The pressure on the runner blade pressure surface is assumed to increase whenever the blade passes through the perturbation position. In this case, the pressure value increases whenever the sensor located on the pressure side of blade 1 passes through the disturbed region, resulting in a pressure fluctuation with the runner rotational frequency

in the results. This disturbance will be indicated by a peak at the runner frequency in the frequency analysis results and an increased pressure region in the phase-averaged data. In the torsion measurement case, whenever a blade passes through the disturbance region, the torsion will increase and subsequently decrease again after passing through the disturbance. Hence, a peak at $6f^*$ is expected in the frequency analysis diagrams. From a structural perspective, when a blade (for instance, blade 1) passes through the disturbance, a load asymmetry is formed on the runner, which results in a higher load on blade 1 compared with blade 4, which is located on the opposite side of the runner. This asymmetry results in bending of the main shaft such that the load on the pad located on top of the disturbance position will be decreased and the load on its counterpart pad will be increased. After the blade passes, the runner tends to return to its natural position, and the load on the two pads will be balanced. Then, the next blade (blade 2) comes to the position, and the process repeats. Hence, a peak at $6f^*$ is expected in the pad load results as well. The disturbance peripheral location can be determined by finding the peripheral location on the bearing with the highest peak.

The formation of the RVR in the draft tube cone of a water turbine may result in pressure oscillations with rotating and plunging modes, as discussed in the following sections. The pressure signals acquired at the draft tube cone were used to decompose the plunging and rotating modes of the RVR. Because the sensors are located on the stationary frame, both plunging and rotating modes contribute to pressure oscillations at $f_{RVR,st}$. The plunging mode results in a synchronous oscillation in the pressure signals of the two sensors located at the same height on the inner and outer part of the draft tube cone at $f_{RVR,st}$. The rotating mode results in oscillations of the pressures with $f_{RVR,st}$ but with a phase difference of 180° due to the difference in the angular position of the sensors. The pressure signals acquired at the draft tube cone were filtered with a narrow band-pass filter around $f_{RVR,st}$ to isolate the effect of the RVR and then subtracted from the average signal. The resulting signals can be written as the superposition of the plunging and rotating modes:

$$\tilde{P}_I(t) = A \sin(2\pi f_{RVR,st} t + \phi_{st}) + B \sin(2\pi f_{RVR,st} t + \phi_{rot}) \quad (2)$$

$$\tilde{P}_O(t) = A \sin(2\pi f_{RVR,st} t + \varphi_{st}) + B \sin(2\pi f_{RVR,st} t + \varphi_{rot} + \pi)$$

where $\tilde{P}_I(t)$ is the oscillating part of the pressure signal from a sensor located on the inner part of draft tube cone; $\tilde{P}_O(t)$ is the oscillating part of the pressure signal from a sensor located on the outer part of draft tube cone; A and B are the plunging and rotating mode amplitudes, respectively; and φ_{st} and φ_{rot} are the phase of the plunging and rotating modes of the filtered signals at the inner part of the draft tube, respectively. The amplitude of the rotating and plunging modes can be calculated as:

$$A = \text{amp}\left(\frac{\tilde{P}_I(t) + \tilde{P}_O(t)}{2}\right) \quad B = \text{amp}\left(\frac{\tilde{P}_I(t) - \tilde{P}_O(t)}{2}\right) \quad (3)$$

4 Experimental results

Pressure measurements were performed on the pressure and suction sides of two consecutive runner blades on a Kaplan model at the three operating points listed in Table 2. The prototype was investigated by measuring the torque exerted on the main shaft and loads on the turbine bearing at the BEP presented in Table 1. The corresponding results are presented in the following sections.

4.1 *Best efficiency point*

The BEP of the turbine model was found to be at a guide vane angle of 26.5° for the prescribed runner blade angle. The amplitude spectrum of the pressure sensor at position SS4 is illustrated in Fig. 4 as an example. The spectral analysis results of all other pressure sensors were qualitatively similar to the presented plot. The dominant dimensionless frequencies were $1f^*$ and $20f^*$, corresponding to the runner and guide vane passing frequencies, respectively. All harmonics of f^* are present in the spectrum.

The amplitude spectrums of all pressure sensors at low frequencies are presented in Fig. 5. The dominant dimensionless frequency in all sensors is $1f^*$, corresponding to the runner frequency. The peaks can be due to either asymmetry in the distributor, the effect of the draft tube elbow downstream of the runner, or a mass imbalance in the rotating parts of the turbine. The phase-resolved plots are useful in finding the source of the peaks. Such a graph is presented in Fig. 6 for pressure sensor PS1. The origin on the horizontal axis indicates where the blade leading edge reaches the same peripheral position as the spiral casing's lip-entrance region. The black dots are the phase-resolved data according to the encoder signal, the dashed white line indicates the phase-averaged results, the solid white line shows the 2σ band of the data, and the horizontal dotted line shows the mean value of the signal. Approximately 95% of the data points lie in the 2σ band according to the nearly normal
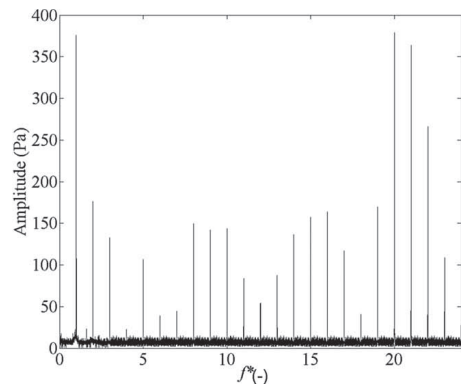

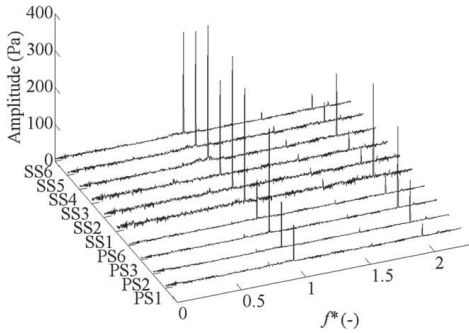Figure 4   Amplitude spectrum of pressure sensor SS4 at the BEP

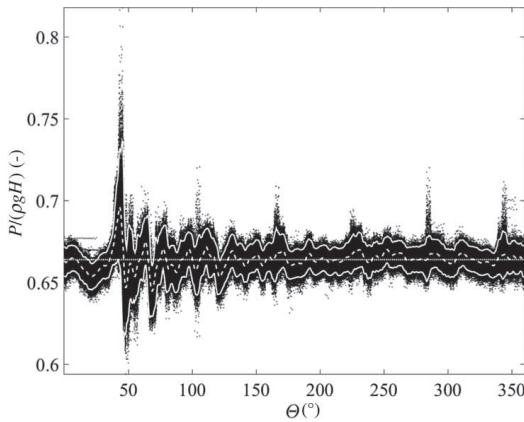Figure 5   Amplitude spectra of pressure sensors at the BEP

Figure 6   Phase-resolved results (black dots), phase-averaged results (white dashed line), mean value (white dotted line) and 2σ-band (white line) of the pressure signal of pressure sensor PS1 at BEP. The pressure is made dimensionless with respect to the operational head
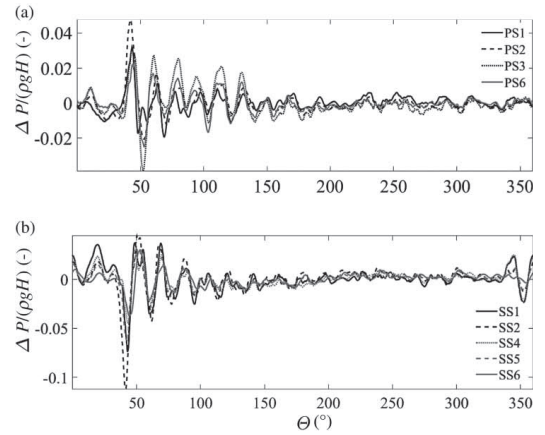

Figure 7   Phase-averaged pressure distribution on the pressure side (a) and suction side (b) of the blades at BEP. The pressure is made dimensionless with respect to the operational head

distribution of the histogram of the pressure data in each bin. The results exhibit a distinct peak with high scattering of the data at approximately 45°. Similar scattering of the data appears every 60° at 105°, 165°, 225°, 285° and 345°. The spiral casing feeds the water to the runner in a quasi-axisymmetric manner in the interval from 130° to 360°. The maximum fluctuation in the phase-averaged results in this region is less than 0.7% of the head. However, the pressure suddenly increases when the blade passes through the lip-entrance junction. Following the jump, there is a fluctuation in the pressure data. In this case, the maximum pressure peak in the 2σ band is close to 7% of the head, and the maximum fluctuation recorded during the measurement at this location is more than 15% of the head. The standard deviation and peak values recorded for this sensor were the lowest of all sensors. The maximum deviation of the 2σ band from the mean value in different sensors varies between 7–17% based on the sensor location.

To investigate the phenomenon in more detail, the phase-averaged results from all sensors are presented in Fig. 7. The

pressure results from the pressure side of the blades are phase shifted by 60°, i.e. the phase difference between two blades. Although the sensors are located at different angular positions on each blade, all of the signals from the sensors located on the pressure side of the blade exhibit synchronous fluctuations. The same phenomenon is observed for the sensors on the suction side. Moreover, in the interval 20–120°, the pressure fluctuations have an opposite sign on the pressure and suction sides. On both surfaces, the pressure sensors located close to the shroud measure the maximum pressure fluctuations as they pass the lip-entrance region. As illustrated in Fig. 7, after the start of the oscillations at 45°, the following fluctuations have a phase difference of approximately 18°.

Figure 8 illustrates the phase-resolved pressure difference between the sensors located on the suction and pressure sides of the blade in the middle of the blade chord and close to the shroud (PS2–SS2) to show the fluctuating forces acting on the blades. The pressure difference is subtracted from its mean value to show the variation around the mean. The main features of the plot are similar to the signal from one pressure sensor; the figure illustrates the high peak and following oscillations as well as the scattered data appearing every 60°. The pressure difference between the suction and pressure sides of the blade can reach up to 63% of the head, and the total range of variation in the pressure difference captured at this point during 300 s of measurement is close to that of the turbine head. The maximum peak in the 2σ curve is 32% of the head, and the highest peak in the phase-averaged curve is approximately 16% of the head.

Torque measurements on the main shaft and load measurements on the bearing pads of the Projus U9 prototype were performed to compare the flow condition in the model with that in the prototype. Figure 9 shows the frequency analysis results of the load measurements performed on the pads of the turbine bearing. The figure shows that in all pads, the amplitude
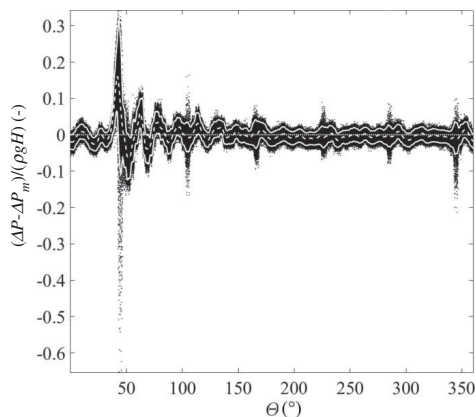
Figure 8   Phase-resolved results (black dots), phase-averaged results (white dashed line) and 2σ-band (white line) of the pressure difference between the pressure and suction sides in the middle of the chord and close to the shroud at BEP (PS2-SS2)

Figure 10   Phase-resolved results (black dots), phase-averaged results (white line) and mean (dotted white line) of the torsion signal. The grey dots represent the phase-resolved shaft torsion band-pass filtered to isolate the runner and blade passing frequencies
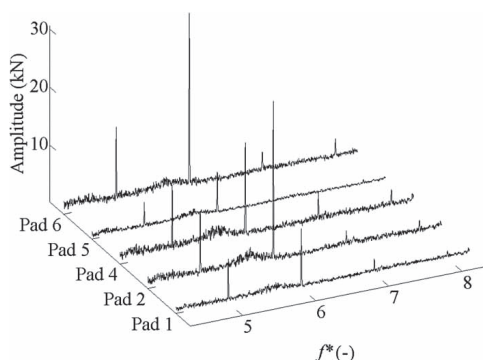

Figure 9   Waterfall of the load on different pads of the prototype bearing

at $6f^*$ is higher than the adjacent harmonics of the runner dimensionless frequency ($5f^*$ and $7f^*$). The frequency is not only a harmonic of the runner frequency but also an indicator of a physical phenomenon in the turbine. The measurements by sensors 1, 2, 5, and 6 show that the counterpart pads exhibit a similar behaviour at the blade passing frequency. The maximum amplitude at the blade passing frequency is found to be at pads 2 and 6; the blade passing frequency has an amplitude of approximately 30 kN on both pads. The amplitude of the exerted load on pads 1 and 5 at the blade passing frequency is approximately 10 kN.

Figure 10 shows the phase-resolved torsion data with respect to the runner frequency, made dimensionless based on its mean value. In the figure, the black dots are the phase-resolved data, the white line is the phase-averaged results, and the white dotted line is the mean value of the shaft torsion. The grey dots in the

figure represent the phase-resolved torsion after applying a narrow band-pass filter around the runner frequency and the blade passing frequency on the original data to isolate the effect of the blade passing frequency on the shaft. The filtered data generally follow the phase-averaged data and oscillate along with the phase-averaged plot. Hence, the oscillations in the phase-averaged data are mainly related to the blade passing frequency. The two dominant frequencies in the pressure measurement results for the model, namely the runner and blade passing frequencies, are representative of the main oscillations in the torque exerted on the prototype shaft.

4.2   High load

The turbine model was also investigated under the high-load operating condition presented in Table 2. The results showed that the main features of the flow on the blade were similar to the BEP case. The main frequencies were the runner rotational frequency and guide vane passing frequency. The magnitude of the pressures on the pressure side was typically 1–2% of the turbine head larger than the pressure magnitude at the BEP and decreased by 1–4% on the suction side, resulting in higher torque and higher turbine output power. The high peak in the phase-averaged results of the pressure difference on the two sides of the blades, presented in Fig. 8 for the BEP, increased by approximately 4% of the turbine head.

4.3   Part load

The blade pressure measurements on the model were also performed at the part-load operating point presented in Table 2. The amplitude spectrum of the SS4 at part-load operation is presented in Fig. 11. The spectrum is qualitatively similar to the two other operating conditions except in the interval of $f^* \sim [0, 1]$.

All harmonics of $f*$ were present in the spectrum with different amplitudes, as in the other cases. However, the peak at $21f*$ dominates the one at the dimensionless guide vane passing frequency, i.e., $20f*$. At low frequencies, two new distinct peaks at $0.171f*$ and $0.829f*$ can be found in the spectrums for all pressure sensors as presented in Fig. 12. The amplitude at $0.171f*$ is as large as the amplitudes at the runner and guide vane passing frequencies, whereas the peak at $0.829f*$ dominates the spectrum. The simultaneous recorded pressure measurements at the draft tube cone, together with the flow visualization, demonstrated the presence of an RVR in the diffuser revolving with a dimensionless frequency of $0.171f*$, which is in agreement with the LDA and pressure measurement results presented by Jonsson et al. (2012). In the following section, these two frequencies are discussed and related to the plunging and rotating modes of the RVR. The frequencies are referred to as $f_{RVR,st}$ $(0.171f)$ and $f_{RVR,rot}$ $(0.829f)$. The results showed that the rotating mode of the RVR dominates the plunging mode.

Figure 13 presents the phase difference at $f_{RVR,st}^*$ between different pressure sensors placed at different locations on the suction side and pressure side of the runner blades. The phase difference between the acquired signals is independent of the position of the sensors at this frequency, and phase differences between different combinations of the pressure signals are close to zero. The small variations from zero are attributed to the superposition of numerous sinusoids with different frequencies and are also a result of comparing the signals acquired on the suction side with the pressure side. This implies a synchronous phenomenon in the turbine.

The pressure signals acquired at the draft tube cone were used to decompose the plunging and rotating modes of the RVR at different locations of the draft tube cone. Figure 14 shows the results. At this operating point, the plunging and rotating mode have the same amplitude at the bottom part of the draft tube cone. However, the amplitude of the rotating mode increases from the bottom to the top. The rotating mode dominates the

Figure 11   Amplitude spectrum of pressure sensor SS4 at part load
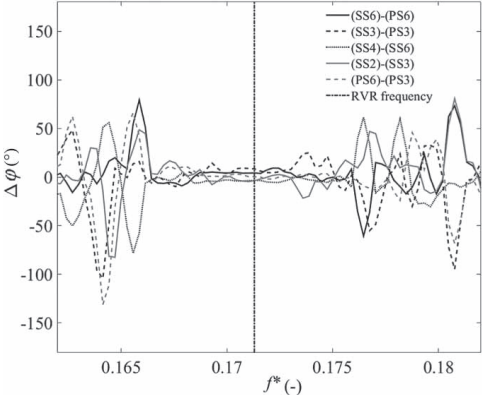
Figure 13   Phase difference between different pressure signals at the RVR frequency

Figure 12   Amplitude spectra of the pressure sensors at part load
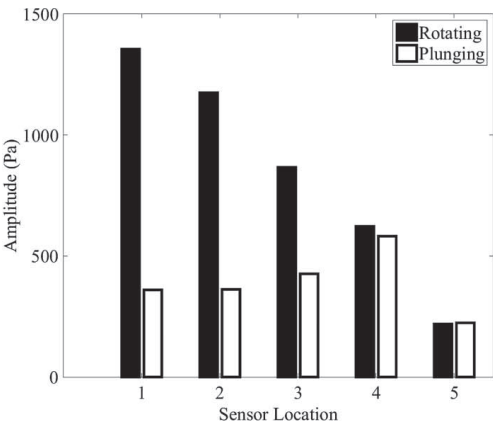

Figure 14   Amplitude of the rotating and plunging modes of the RVR at the draft tube cone
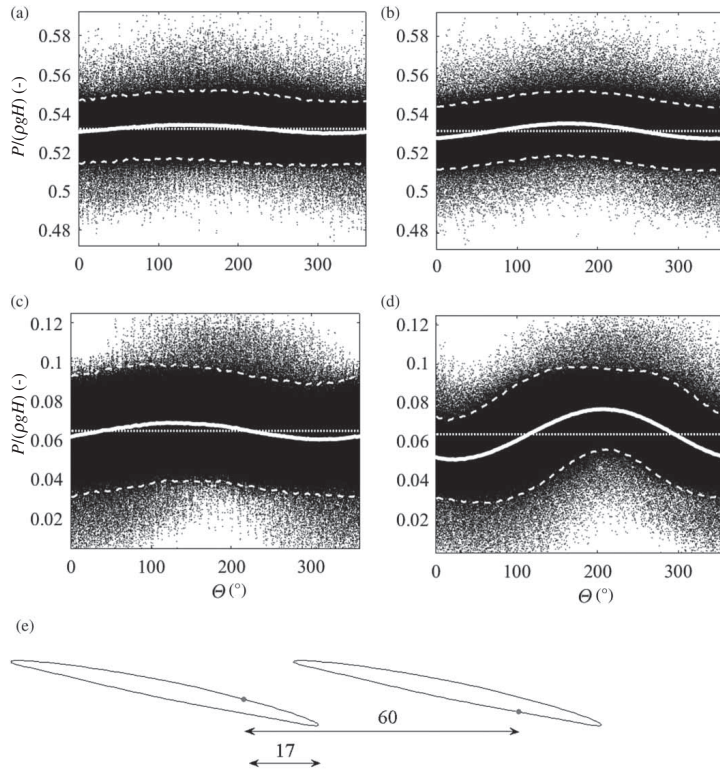
Figure 15   Phase-resolved (black dot) and phase-averaged pressure (white line) on the pressure surface (top) and suction surface (bottom) with respect to $f_{RVR,st}$ (left) and $f_{RVR,rot}$ (right) together with the mean value (dotted white) and 2σ-band (dashed white). The Y-axis limits are different in the top and bottom plots. (a) PS6, resolved at $f* = 0.171$; (b) PS6, resolved at $f* = 0.829$; (c) SS6, resolved at $f* = 0.171$; (d) SS6, resolved at $f* = 0.829$; and (e) location of the sensors

plunging mode at the draft tube inlet, which is in agreement with the measurements acquired on the runner blades.

The phase-resolved data with respect to $f_{RVR,rot}$ and $f_{RVR,st}$ are presented in Fig. 15 for the sensors located at SS6 and PS6. The resolved data with respect to $f_{RVR,st}$ and $f_{RVR,rot}$ are presented on the left- and right-hand side of the figure, respectively. The top figures (Figs 15a and b) show the measurements of the pressure-side sensor, and the measurements from the suction side are presented in the bottom part of the figure (Figs 15c and d). The amplitude of the oscillations on the suction side is larger than that on the pressure side. The resolved data, according to the $f_{RVR,st}$ presented in the left part of the figure, are in phase. However, there is a phase difference between the phase-resolved data according to the $f_{RVR,rot}$; see Figs 15b and d. The RVR hits the two adjacent blades with a phase difference of 60° according to $f_{RVR,rot}$. However, the phase difference in this case is close to 43°.

The phase-averaged results with respect to the runner frequency at part load were qualitatively similar to those acquired

at the BEP and high load. At part load, the mean pressure at different locations on the pressure side of the blade decreased by 1–2% of the turbine head compared with those at the BEP, whereas it increased by 2–10% on the suction side, resulting in a lower pressure difference and thus a lower torque and lower output power. The highest fluctuation in the 2σ plot was located at PS1, with an amplitude of approximately 5% of the head, whereas the amplitude was 7% of the head at the BEP. For the phase-resolved ΔP curve, the maximum deviation of the phase-averaged results was approximately 13%, and the maximum value of the 2σ curve was approximately 22%. The corresponding values at the BEP were 16 and 32%, respectively.

5   Analysis and discussion

The frequency analysis of the pressure measurements performed on the suction and pressure sides of the runner blades showed that the dominant frequencies at the BEP and high load in

the acquired signals were the runner rotation and guide vane passing frequencies. The presence of the runner frequency harmonics illustrated the complexity of the flow passing through the blade channels in Kaplan turbines. In Francis turbines, the pressure measurements on the blades exhibit a neat pattern at the BEP; the occurrence of only one peak at the guide vane passing frequency (Trivedi, 2013), which is due to the small spacing between the rotor and guide vanes. The small spacing amplifies the rotor-stator interaction. However, the measurements showed that in the low-head turbine, the larger spacing between the runner and guide vanes results in a smaller rotor–stator interaction. Hence, the frequency analysis showed that the two frequencies have comparable amplitudes. Moreover, the guide vane trailing edge wakes, propagating downstream from the guide vanes, spread out and are subject to rotation. Thus, the flow entering the blade channel is more complex, and all of the harmonics of the runner frequency can be found in the spectrum. The presence of different harmonics of the runner frequency with frequencies even higher than the guide vane's passing frequency increases the probability of resonance in different parts of the turbine.

The phase-averaged pressure measurement results with respect to the runner frequency indicated a distinct peak on the pressure-side sensors and a valley on the suction-side sensors with high scattering of the data points at all operating points; see Figs 6 to 8. The lip-entrance junction region was found to be the source of the disturbance at the runner frequency. The high scattering of the data points in the phase-resolved data every 60° showed that each time a blade passes through the spiral casing lip-entrance junction region, a flow with an inappropriate angle of attack hits the blade, resulting in a pressure fluctuation on the blades, vibration of the complete runner and shaft wobbling. As shown in Fig. 7, after the oscillations begin at approximately 45°, the following fluctuations from 50° to 130° have a phase difference of approximately 18°. This phase difference is equal to the guide vane angular spacing. The results demonstrate the inability of the spiral casing to supply water to the guide vanes with an appropriate angle of attack in this region. The poor performance of the spiral casing results in flow separation on the guide vanes located close to this region. The flow separation results in a wake region with decreased velocity and a wake-free region with high velocity at the guide vane outlet close to the lip-entrance junction region; see Fig. 16. The difference in the velocities results in a different flow angle of attack to the runner blades within the wakes and in the wake-free regions based on the velocity triangles at the runner inlet. The passage of a runner blade through the wakes and high-velocity regions with different angles of attack results in fluctuations in the blade pressure distribution and probable structural deformation. The guide vane wakes are weaker close to the runner hub, and the flow non-uniformity is lower in this region compared with the runner shroud because the distance between the guide vane trailing edge and the runner blades is larger close to the hub. The larger distance results in more dissipation of the wakes between the guide vanes and the runner close to the hub and lower
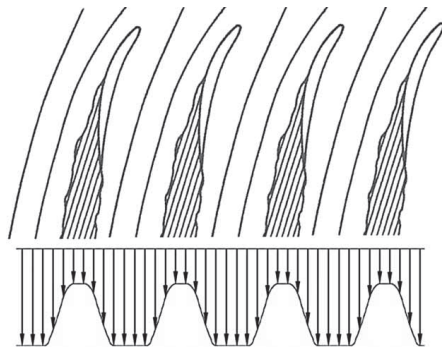
Figure 16   Sketch of the velocity profile at the guide vanes outlet with flow separation

fluctuations in the velocity where the wake reaches the runner blade. Hence, the amplitude of the fluctuations in the pressure signals acquired close to the shroud is larger than the fluctuations in the pressure signals acquired close to the hub; see Fig. 7. The high level of fluctuations in the pressure will be transferred to the supporting parts, i.e. the blade and shaft bearings. The bearings' performance and lifetime may suffer as a result of these pressure fluctuations. From a numerical simulation perspective, the widely used symmetrical boundary condition at the distributor outlet in the simulation of water turbines should be carefully considered based on the simulation purpose.

The asymmetry of the flow at the distributor outlet was not captured in the LDA measurements performed by Mulu & Cervantes (2010) because the locations selected for the LDA measurements were far from the lip-entrance region, where the current pressure measurements indicated the presence of asymmetry. The asymmetry was not captured in the LDA measurements at the runner outlet in the measurements performed by Jonsson et al. (2012) because the wakes propagating downstream from the guide vanes were dissipated while passing through the runner. The main source of such a strong asymmetry at the distributor outlet is not completely clear but should be attributed to either the geometry of the spiral casing, the distributor or the velocity distribution at the spiral casing inlet. There is an elbow upstream of the spiral followed by a smooth diffusing section. The elbow creates an uneven velocity profile at the spiral casing entrance that may affect the spiral casing's performance. LDA measurements performed by Mulu & Cervantes (2010) indicated a larger velocity at the bottom part of the spiral casing entrance.

Prototype measurements confirmed the existence of the asymmetry in the load exerted on the runner due to the asymmetry at the distributor outlet. Load measurements performed on the bearing of the prototype showed a high peak at the blade passing frequency in all pads, and the maximum peaks were found to occur on pad 2, located above the spiral casing lip-entrance junction and its counterpart, pad 6. This finding shows that the performance of the prototype spiral casing is similar

to the model, i.e. when a blade passes through the lip-entrance region, the flow hits the blade, resulting in a sudden change in the lift exerted on the blade passing through the lip-entrance region, and thus an imbalanced force is exerted on the blade and its counterpart. Hence, the main shaft bends toward pad 6, resulting in an increased load on the pad. This process repeats for each blade passing through this region. As a result, there was a distinct peak at $6f^*$ in the frequency spectrum of the load sensors, with the highest amplitudes on pad 2 located above the lip-entrance junction region and its counterpart, pad 6. Even higher peaks were expected to occur on pads 3 and 7 according to the pressure measurements performed on the model runner blades; however, the sensors installed on the pads were found to be defective during the measurements. Torque measurements performed on the main shaft of the prototype showed that each time one blade passes through the region with an inappropriate flow condition, the shaft torsion increases, and the torsion decreases again after passing the blade, similar to the behaviour of the model.

The model's performance at high load was qualitatively similar to that at the BEP. However, two dimensionless frequencies at $0.171f^*$ and $0.829f^*$ were observed at part load, dominating the spectrum. The high swirl leaving the runner at this operating point resulted in the formation of an RVR rotating around a recirculation bubble region formed in the middle of the draft tube cone. According to the co-rotation of the RVR with the runner, a dimensionless frequency of $f_{RVR,rot}^* = 1 - f_{RVR,st}^* = 0.829$ was expected in the rotating domain. This frequency is referred to as the rotating mode of the RVR. The phase-averaged results of the sensors located at PS6 and SS6 with respect to this frequency exhibited a 43° phase difference between the two signals, whereas the difference in their location was 60°; see Figs 15b and d. This difference is due to the fact that one of the sensors is located on the suction side, whereas the other one is on the pressure side. The suction-side sensor senses the RVR as it passes the sensor, but for the other sensor, the blade blocks the wave propagation from the suction side to the pressure side. Thus, the sensor on the pressure side cannot sense the presence of the RVR until it reaches the blade trailing edge. Because the phase difference between the sensor position and blade trailing edge is close to 17°, the phase difference between the two signals is equal to $60 - 17$.

The acquired results indicated that the phase difference between different sensors is independent of the position of the sensors and is close to zero at $0.171f^*$. This implies a synchronous phenomenon in the turbine. An investigation of the wall pressure signals in the test rig indicated the presence of this frequency in the penstock, draft tube and downstream pressure tank. Thus, the RVR induces an axial oscillation through the entire conduit with its frequency. This frequency is referred to as the plunging mode of the RVR. Because the plunging frequency induces synchronous pressure fluctuations on the runner, it produces fluctuations in the loads exerted on the thrust bearing. Furthermore, the rotating mode induces unbalanced forces

on two sides of the runner, resulting in bending moments exerted on the shaft.

In all cases, the amplitude at the RVR frequency on the suction side was higher than that on the pressure side, indicating the propagation of disturbances from the draft tube to the upstream. Meanwhile, the runner blades act as dampers against the wave propagation. After passing through the runner, the amplitude of $f_{RVR,rot}$ decreases significantly, whereas the runner does not have such a damping effect on $f_{RVR,st}$. This result is due to the large mass of water in the test rig that oscillates with $f_{RVR,st}$ in the axial direction.

Although the runner and guide vane passing frequencies dominated the other runner frequency harmonics at the BEP and high load, the non-dimensional frequency of $21f^*$ dominated the guide vane passing frequency at part load. Similar results have been reported by Houde et al. (2012a) at certain operating points. The pressure signal recorded during the measurements is the static pressure on the blade surface. Applying Bernoulli's equation to the rotating frame flow helps to clarify the observed high amplitude at $21f^*$. Bernoulli's equation for relative motion at a constant head can be written as:

$$P(t) - \frac{1}{2}\rho u^2 + \frac{1}{2}\rho w^2 = P_{tot} \qquad (4)$$

where $P(t)$ is the static pressure measured on the runner blades, P_{tot} is the total pressure, u is the runner velocity, and w is the relative flow velocity. The relative velocity is the vector summation of the absolute velocity and the runner angular velocity, which subsequently is a function of the number of guide vanes, the perturbation at the lip entrance and the runner angular frequency. The relative velocity may be written as:

$$w = w_0(1 + a_w^1 \cos(2\pi ft + \phi_w^1) + a_w^{20} \cos(40\pi ft + \phi_w^{20})) \quad (5)$$

where w_0 is the average relative velocity; a_w^1 and a_w^{20} are the dimensionless amplitudes of the relative velocity at the runner and the guide vane passing frequency, respectively; and ϕ_w^1 and ϕ_w^{20} are the corresponding phases. Assuming a constant runner angular velocity, the pressure on the blades is given by:

$$P(t) = P_{tot} + \frac{1}{2}\rho u^2 - \frac{1}{2}\rho w_0^2(1 + a_w^1 \cos(2\pi ft + \phi_w^1) + a_w^{20} \cos(40\pi ft + \phi_w^{20}))^2 \qquad (6)$$

The oscillations of the total pressure are expected to occur at $20f^*$. However, the square of the relative velocity exhibits two peaks at $19f^*$ and $21f^*$. Depending on the amplitude of the relative velocity components at $1f^*$ and $20f^*$, each of the $19f^*$, $20f^*$ and $21f^*$ dimensionless frequencies may dominate.

6   Conclusions

Unsteady pressure measurements on the suction and pressure sides of the runner of a Kaplan turbine model and on the draft tube cone were performed at three operating conditions: part load, the BEP and high load. The frequency spectrum and phase-resolved data indicated flow asymmetry at the outlet of the spiral casing distributor. The main asymmetry of the water supply system was caused by the poor performance of the spiral casing at the lip-entrance junction resulting in flow separation on the guide vanes. Wakes propagating downstream from the guide vanes induced large pressure fluctuations on the runner blades passing through this region. The amplitude of the fluctuations exerted on the runner at the runner and blade passing frequency was comparable to the one at the plunging mode of the RVR, which is known to be detrimental to turbine operation. The separation on the guide vanes may result in pressure oscillations at frequencies other than the guide vane passing frequency. The asymmetric loads on the blades are transferred to the main shaft and bearings, thereby affecting their lifetime and performance. The results also revealed that the co-rotating vortex rope, with respect to the runner at part load, induced pressure fluctuations with two frequencies to the runner blades related to the rotating and plunging modes of the RVR. The plunging mode was a synchronized axial oscillation in the entire turbine conduit. This mode results in synchronous fluctuations in the loads exerted on the runner blades, which affects the lift on the entire runner. However, the rotating mode results in an unbalanced force on two sides of the runner, which leads to a bending moment on the runner. Pressure measurements performed on the runner and the draft tube cone showed that the amplitude of the pressure fluctuations due to the rotating mode dominates the one at the plunging mode.

Load measurements on the prototype bearing, together with the torque measurements on its main shaft, confirmed the existence of the asymmetrical load on the runner due to the flow asymmetry at the spiral casing distributor outlet. The asymmetry resulted in wobbling of the main shaft and oscillation in the output torque. This resulted in oscillatory stresses to the bearings that may affect their performance and lifetime. The measurement results illustrated that consideration of the asymmetrical forces exerted on the runner and the bearings is mandatory when estimating their lifetime and overhaul schedule.

Notation

D	=	runner diameter (m)
f	=	frequency (Hz)
$f_{RVR,st}$	=	frequency of the plunging mode of the rotating vortex rope (Hz)
$f_{RVR,rot}$	=	frequency of the rotating mode of the rotating vortex rope (Hz)
f_s	=	sampling frequency (Hz)
H	=	head (m)
n	=	turbine revolving frequency (Hz)
$n_{ED} = \frac{nD}{\sqrt{gH}}$	=	speed factor (–)
P	=	static pressure (Pa)
P	=	fluctuating part of the static pressure (Pa)
$\bar{P}$	=	time-averaged static pressure (Pa)
$\tilde{P}$	=	oscillating part of the static pressure (Pa)
P_{tot}	=	total pressure (Pa)
Q	=	flow rate (m^{3}s^{-1})
$Q_{ED} = \frac{Q}{D^2\sqrt{gH}}$	=	discharge factor (–)
T	=	torque (Nm)
α_{gv}	=	guide vane angle (°)
β_0	=	bin centre (°)
$\Delta\beta$	=	bin size (°)
η	=	turbine efficiency (–)
Θ	=	angular position (°)
ρ	=	fluid density (kg m^{-3})
σ	=	standard deviation
φ	=	phase (rad)

Subscripts and superscripts

*	=	Dimensionless frequency with respect to the runner rotational frequency
m	=	mean value

References

Amin, A. Z. (2012). *Renewable power generation costs in 2012: An overview*. International Renewable Energy Agency (IRENA).

Arpe, J., & Avellan, F. (2002). Pressure wall measurements in the whole draft tube: Steady and unsteady analysis. *Proceedings of the 21st IAHR Symposium on Hydraulic Machinery and Systems*, Lausanne, Switzerland, 593–602.

Bryden, I. G., & Couch, S. J. (2006). ME1—marine energy extraction: Tidal resource analysis. *Renewable Energy*, *31*, 133–139. doi:http://dx.doi.org/10.1016/j.renene.2005.08.012

Buccino, M., Banfi, D., Vicinanza, D., Calabrese, M., Del Giudice, G., & Carravetta, A. (2012). Non breaking wave

forces at the front face of seawave slotcone generators. *Energies*, *5*, 4779–4803.

Carcangiu, S., & Montisci, A. (2012). A building-integrated eolic system for the exploitation of wind energy in urban areas. *2nd IEEE ENERGYCON Conference and Exhibition*, Florence, Italy, 172–177.

Ciocan, G. D., Avellan, F., & Kueny, J. L. (2000). Optical measurement techniques for experimental analysis of hydraulic turbines rotor-stator interaction. *Proceeding of the ASME Fluids Engineering Division Summer Meeting*, Boston, MA, USA.

Farhat, M., Avellan, F., & Seidel, U. (2002). Pressure fluctuation measurements in hydro turbine models. *Ninth International Symposium on Transport Phenomena and Dynamics of Rotating Machinery*, Honolulu, Hawaii, USA.

Fecarotta, O., Aricò, C., Carravetta, A., Martino, R., & Ramos, H. (2015). Hydropower potential in water distribution networks: Pressure control by PATs. *Water Resources Management*, *29*, 699–714.

Gagnon, J. M., Aeschlimann, V., Houde, S., Flemming, F., Coulson, S., & Deschenes, C. (2012). Experimental investigation of draft tube inlet velocity field of a propeller turbine. *Journal of Fluids Engineering*, *134*(10).

Gagnon, J. M., Deschenes, C., Ciocan, G. D., & Iliescu, M. (2008). Numerical simulation and experimental investigation of the flow in an axial turbine. *24th IAHR Symposium on Hydraulic Machinery and Systems*, Foz Do Iguassu, Brazil.

Golchin, A. (2013). *Tribological behavior of polymers in lubricated contacts (Licentiate thesis)*. Luleå University of Technology, Luleå, Sweden.

Gouin, P., Deschenes, C., Iliescu, M., & Ciocan, G. D. (2009). Experimental investigation of draft tube flow of an axial turbine by laser doppler velocimetry. *Third IAHR International Meeting of the Workgroup on Cavitation and Dynamic Problems in Hydraulic Machinery and Systems*, Brno, Czech Republic.

Houde, S., Fraser, R., Ciocan, G., & Deschênes, C. (2012a). Experimental study of the pressure fluctuations on propeller turbine runner blades: Part 2, transient conditions. *Earth and Environmental Science, 15*.

Houde, S., Fraser, R., Ciocan, G., & Deschênes, C. (2012b). Part 1 – experimental study of the pressure fluctuations on propeller turbine runner blades during steady-state operation. *26th IAHR Symposium on Hydraulic Machinery and Systems*, Beijing, China.

Iliescu, M. S., Ciocan, G. D., & Avellan, F. (2002). 3D PIV and LDV measurements at the outlet of a Francis turbine draft tube. *Proceedings of FEDSM'02: The 2002 Joint US ASME-European Fluids Engineering Summer Conference*, Montreal, Quebec, Canada.

Iliescu, M. S., Ciocan, G. D., & Avellan, F. (2008). Analysis of the cavitating draft tube vortex in a Francis turbine using particle image velocimetry measurements in two-phase flow. *Journal of Fluids Engineering, 130*.

Jonsson, P., & Cervantes, M. (2010). Pressure measurements in the spiral casing of a kaplan turbine model. *13th Symposium on Transport Phenomena and Dynamics of Rotating Machinery*, Honolulu, Hawaii, USA.

Jonsson, P. P., Mulu, B. G., & Cervantes, M. J. (2012). Experimental investigation of a Kaplan draft tube – part II: Off-design conditions. *Applied Energy*, *94*, 71–83. doi:10.1016/j.apenergy.2012.01.032

Kobro, E. (2010). *Measurement of pressure pulsation in Francis turbines (PhD thesis)*. NTNU, Trondheim, Norway.

Mulu, B., & Cervantes, M. (2010). LDA measurements in a Kaplan spiral casing model. *13th Symposium on Transport Phenomena and Dynamics of Rotating Machinery*, Honolulu, Hawaii, USA.

Mulu, B. G., Jonsson, P. P., & Cervantes, M. J. (2012). Experimental investigation of a kaplan draft tube – part I: Best efficiency point. *Applied Energy, 93*, 695–706. doi:10.1016/j.apenergy.2012.01.004

Simmons, G. F. (2013). *Journal bearing design, lubrication and operation for enhanced performance* (PhD thesis). Luleå University of Technology, Luleå, Sweden.

Trivedi, C. (2013). *Transients in high head Francis turbines* (Licentiate thesis). Luleå University of Technology, Luleå, Sweden.

Trivedi, C., Cervantes, M. J., Gandhi, B. K., & Dahlhaug, O. G. (2013). Experimental and numerical studies for a high head Francis turbine at several operating points. *Journal of Fluids Engineering*, *135*(11).

Trivedi, C., Gandi, B. K., & Cervantes, M. J. (2013). Effect of transients on Francis turbine runner life: A review. *Journal of Hydraulic Research*, *51*(2), 121–132.

Vekve, T. (2004). *An experimental investigation of draft tube flow* (PhD Thesis). NTNU, Trondheim, Norway.

Vicinanza, D., Ciardulli, F., Buccino, M., Calabrese, M., & Koefed, J. (2011). Wave loadings acting on an innovative breakwater for energy production. *Journal of Coastal Research*, *64*, 608–612.

Vieira, F., & Ramos, H. M. (2008). Hybrid solution and pump-storage optimization in water supply system efficiency: A case study. *Energy Policy*, *36*, 4142–4148. doi:http://dx.doi.org/10.1016/j.enpol.2008.07.040

Vieira, F., & Ramos, H. M. (2009). Optimization of operational planning for wind/hydro hybrid water supply systems. *Renewable Energy*, *34*, 928–936. doi:http://dx.doi.org/10.1016/j.renene.2008.05.031

Paper B

Experimental Investigation of the Interblade Flow in a Kaplan Runner at Several Operating Points Using Laser Doppler Anemometry

Experimental Investigation of the Interblade Flow in a Kaplan Runner at Several Operating Points Using Laser Doppler Anemometry

Kaveh Amiri
Department of Engineering
Science and Mathematics,
Luleå University of Technology,
Luleå 97187, Sweden
e-mail: kaveh.amiri@ltu.se

Berhanu Mulu
Vattenfall Research and Development,
Älvkarleby 81470, Sweden
e-mail: berhanu.mulu@vattenfall.com

Michel J. Cervantes[1]
Professor
Department of Engineering
Science and Mathematics,
Luleå University of Technology,
Luleå 97187, Sweden;

Department of Energy and Process Engineering,
Water Power Laboratory,
Norwegian University of
Science and Technology,
Trondheim 7491, Norway
e-mail: michel.cervantes@ltu.se

This paper presents laser Doppler anemometry (LDA) measurements within the runner blade channels and at the runner outlet of a Kaplan turbine model. The model was investigated at six operating points located on two propeller curves of the turbine to study the flow condition during on-cam and off-cam operations. Main and secondary flows within and after the runner were analyzed, and the effects of the hub and tip clearances on the velocity fields within and after the runner were evaluated. Operation of the turbine at flow rates that are lower than the designed rate for the corresponding propeller curve resulted in vortex breakdown and the formation of a rotating vortex rope (RVR). The RVR formation produced an asymmetrical velocity distribution within and after the runner. The results demonstrated the occurrence of an oscillating flow with the same frequency as the vortex rope within the blade channels located upstream of the RVR. This results in an asymmetric flow through the runner and oscillating forces on the runner blades. The measured velocities indicated that the geometrical asymmetries in the runner manufacturing process resulted in various flow asymmetries at the measured sections. The asymmetries were up to 3% within the runner and 7% at the runner outlet.
[DOI: 10.1115/1.4031609]

Keywords: water turbine, flow in rotating components, LDA, rotating vortex rope

Introduction

The flow condition in the cascade of axial turbomachines is rather complicated from fluid dynamics point of view, as mentioned by Bradshaw [1], who stated that "Of all the fluid-dynamic devices invented by the human race, axial-flow turbomachines are probably the most complicated." Formation of different vortices and secondary flows in axial turbines is an important issue affecting turbines performance [2]. Secondary flows formed close to tip clearances can affect the flow condition within the cascade and the turbine efficiency. Lifting surfaces with free tips, as is the case in turbomachines, are in general susceptible to over-the-tip flow from the pressure surface to the suction surface. The associated losses in a turbine stage with a realistic clearance of 1% of the blade span accounts for 20–40% of the overall losses within the cascade [3]. Sjolander and Amrud [4] examined the structure of the tip leakage flow and its effects on the blade loading in a large-scale planar cascade of turbine blades at different tip clearances. The tip leakage was shown to be normal to the camber line from the runner blade pressure side to the suction side. At large tip clearances, the leakage flow rolled up and formed a tip vortex, and a separation point formed on the casing wall. Dreyer et al. [5] investigated the effect of tip clearance size on tip leakage vortex structures and occurrence of cavitation. The results showed that the vortex trajectory and intensity are affected by the wall proximity. The smaller the clearance, the more the vortex is pulled away from the hydrofoil. Moreover, at each hydrofoil incidence angle there is a specific tip clearance at which the vortex intensity is maximum. Since operating points with maximum vortex intensity

are the most prone to generating cavitation, the authors suggested to avoid the critical tip clearance gap in hydraulic axial turbines.

Although studies on stationary cascades provide valuable information about the physics of the secondary flows, the actual flow condition in the axial turbines can be affected by the centripetal and Coriolis forces as well as the relative motion of the casing, see Refs. [6–10]. McCarter et al. [11] investigated flow conditions at the tip clearance of an axial flow turbine using a rotating five-hole probe and LDA system. The measurement results showed that the tip leakage flow from the pressure surface of the runner blade clings the suction surface until mid-chord, then a tip vortex forms at the final 20% of the blade chord in the studied test case. The highest turbulence intensity was measured at the center of the tip vortex. The tip clearance can be more critical in pumps and compressors compared to turbines due to the negative pressure gradients. The particle image velocimetry (PIV) measurements performed close to the tip clearance area of a pump turbine showed similar flow features compared to those in turbines [12]. One of the main differences between the two cases is the vortex bursting phenomenon in pumps caused by the adverse pressure gradient.

The efficiency of hydraulic turbines under off-design conditions may also drastically decrease due to a significant increase in the hydraulic losses. Moreover, the off-design operation of the turbine can increase the pressure fluctuations in the turbine conduit and increase the noise and mechanical vibration, which affect the turbine's lifetime [13]. The off-design operation of hydraulic turbines is becoming more frequent with the introduction of renewable energy resources to the electricity market because turbines are generally not designed to operate under the corresponding conditions [14]. Part load (PL) operation of single regulated water turbines (Francis and propeller) decreases the flow rate and increases the swirl exiting the runner. The strong swirl exiting the runner at partial load may induce a vortex breakdown in the draft
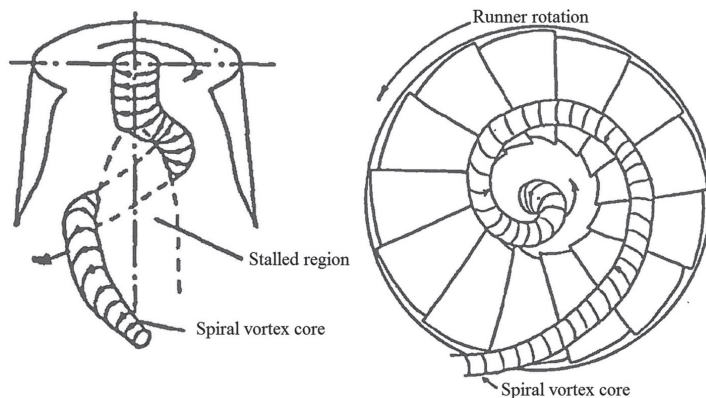
Fig. 1 Sketch of the RVR inside the draft of a Francis turbine [15]

tube cone; a recirculation bubble at the central part forms with an RVR swinging around the recirculating region [15]. A sketch of an RVR is presented in Fig. 1. The recirculation region decreases the effective area of the draft tube and produces flow acceleration between the draft tube cone and the recirculation bubble area. This results in a poor performance of the draft tube, an essential element especially in low-head machines [14]. The RVR induces large pressure pulsations with the revolving frequency of the RVR, which has been shown to be a harmful phenomenon that affects the turbine's performance and lifetime. The initial results concerning this phenomenon were reported by Rheingans [16]; generator resonance was observed due to the formation of RVR at PL operating points. The RVR remains a subject of research due to the associated flow complexity. Iliescu et al. [17] investigated meridional velocity distributions inside the draft tube cone of a Francis turbine while a cavitating vortex rope was formed inside the draft tube using PIV measurements. Jonsson et al. [14] performed pressure and LDA measurements inside the draft tube cone of a Kaplan turbine and showed that the RVR swings around a dead zone of water located at the center of the draft tube cone and that there is an upstream flow at the center of the RVR filament. More recently, the pressure measurements performed on the blades of a Kaplan turbine showed that the RVR induces pressure pulsations on the runner with two modes: rotating and plunging with two different frequencies due to the rotating frame of reference [18]. Various methods have been proposed to mitigate the RVR: air injection [19,20], the use of a tangential water jet at the discharge cone wall [21], fins mounted on the draft tube cone [22], extending cones attached to the runner hub [23], using J-grooves [24], and injecting water jets from the runner hub [25]. However, no method is universally used to address the problem due to the specific limitations associated with each method. Regardless, air injection is the most commonly used method. For more information about the RVR, refer to the review paper by Nishi and Liu [26].

RVR formation in the draft tubes of Kaplan turbines is not a typical phenomenon because such turbines are doubly regulated, i.e., both guide vanes and the runner blade angles are adjustable. However, certain power suppliers have investigated regulating power at a constant blade angle to decrease wear despite a decrease in efficiency. Furthermore, the power required to adjust the runner blades is also significant and decreases the machine's overall efficiency for temporary off-design operations [18]. Moreover, the results of Kaplan turbine investigations under off-cam operation can be applicable to propeller turbines due to the geometrical similarities between Kaplan and propeller turbines (Table 1).

The flow condition inside the conduit of water turbines and the effect of the RVR formation are mainly studied in the stationary parts of water turbines, and limited numbers of measurements are performed within the runner. Pressure measurements on the runner of Francis and pump turbines were performed with special focus on the rotor–stator interaction during steady-state [27–29] and transient operating conditions [30]. Pressure measurements on the runner of a propeller turbine have also been performed under steady-state [31], runaway and speed-no-load [32] conditions. Amiri [33] investigated the pressure pulsations exerted on the runner blades of a Kaplan turbine runner at steady-state operating points, load acceptance and load rejection, with a main focus on RVR formation/mitigation effects. The blade pressure measurements only provided information about periodic forces exerted on the runner and may not be appropriate for detailed investigations of flow condition within the rotating parts.

Optical-based velocity measurement techniques have mainly been employed to investigate flow conditions in draft tubes. LDA measurements have been performed to investigate the flow conditions in the draft tube of Francis [34–36], propeller [37–39], and Kaplan turbines [14,40–42]. PIV has also been mainly employed to explore the flow conditions in the draft tube of hydraulic turbines [17,35,43]. Aeschlimann et al. [44] used stereoscopic PIV to measure the velocity distribution inside the runner blade channels of a propeller turbine under different operating conditions ranging from PL to high load (HL). The main velocity field and secondary flows inside the runner were investigated by acquiring three velocity components. The formation of horseshoe vortices and their propagation within the runner blade channels at PL operating points were observed during the measurements. An important limitation regarding the investigation, as mentioned by the authors, was the restricted measurement area resulting from the selected method of study. The curved shape of the runner blade channel and restrictions on the optical access limited the interrogation window size in the azimuthal direction. The measurements were performed at different radial locations, ranging from 0.62 to 0.77 of the runner radius, covering the middle part of the runner blades in the spanwise direction. Hence, probable secondary flows formed near the hub, and the region near the tip could not be captured. Lemay et al. [45] integrated endoscopic cameras to a stereoscopic PIV system to perform velocity measurements in the interblade channels of a bulb turbine covering 62% of the rotor interblade flow. The PIV measurements were compared with LDA measurements to assess the intrusiveness of the endoscopes. Although inserting the endoscopes to the flow induced a shift in global model performance, the flow was not altered inside the measurement section. The
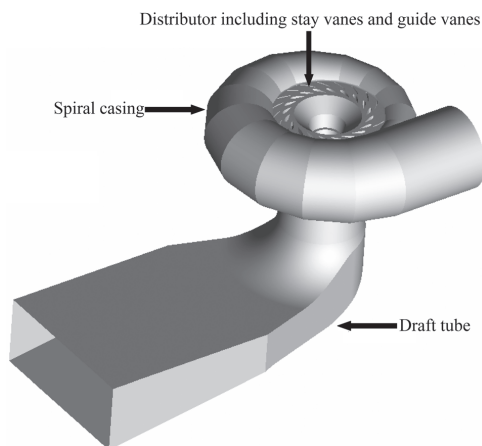
Fig. 2 Sketch of the model illustrating the spiral casing, distributor, and draft tube

guide vane wakes and the runner blade leading edge vortex at PL were captured by the PIV system.

The current study includes an experimental investigation of a Kaplan turbine model known as Porjus U9. The study presents the results of the LDA measurements performed at the runner outlet section and within the runner blade channels. The main goal of this study is to investigate the flow features and the effect of the operating conditions on the velocity fields at the measurement sections. Secondary flows at the measurement sections due to the hub and tip clearances are presented and discussed using phase-averaged contour plots. The effects of manufacturing imprecision on flow asymmetries are also presented.

Experimental Apparatus and Procedures

The Porjus U9 Model. A 1:3.1-scaled model of the Porjus U9 Kaplan turbine was employed for the study. The model geometry illustrating the spiral casing, distributor and draft tube is presented in Fig. 2. The corresponding prototype has an operational head of 55 m for a maximum power of 10 MW at a discharge of 20 m³/s. The water supply system consists of a spiral casing with 20 guide vanes and 18 stay vanes. The runner diameter is 1.55 m and is composed of six blades. An elbow draft tube is installed downstream of the runner for pressure recovery.

The corresponding model was investigated with an operational net head of $H = 7.5$ m under all operating conditions. The runner's rotational speed was set to $N = 696.3$ rpm to assure kinematic similarity between the model and the corresponding prototype. The model was investigated at six operating points located on two propeller curves of $\beta_b = 0.8$ and 4 deg. The model was tested at the flow rates corresponding to the BEPs of each propeller curve. Velocity measurements were also performed at two operating points on each propeller curve with higher and lower flow rates than that of the corresponding BEP. The operating characteristics of each operating point are shown in Table 1. A larger blade angle produces a larger runner blade opening and a higher flow rate for the same guide vane angle. Modification of the runner blade installation angle changes the hub and tip clearances shown in Figs. 3(a)–3(e). The variations in the tip and hub clearances with changing runner blades angle are presented in Table 2. Figure 3(f), extracted from the numerical simulations of Mulu et al. [46], shows a schematic of the hub and tip vortices formed in the clearances.

The investigation was performed at the Vattenfall Research and Development model test facility in Älvkarleby, Sweden. The closed-loop test rig is designed for testing bulb, Kaplan and Francis turbines, and attains accuracies of ±0.13% for the flow rate, ±0.1% for the head, and ±0.016% for the turbine's rotational speed [47]. The test bench parameters are set to a given flow condition, and the resulting efficiency is measured. The hydraulic
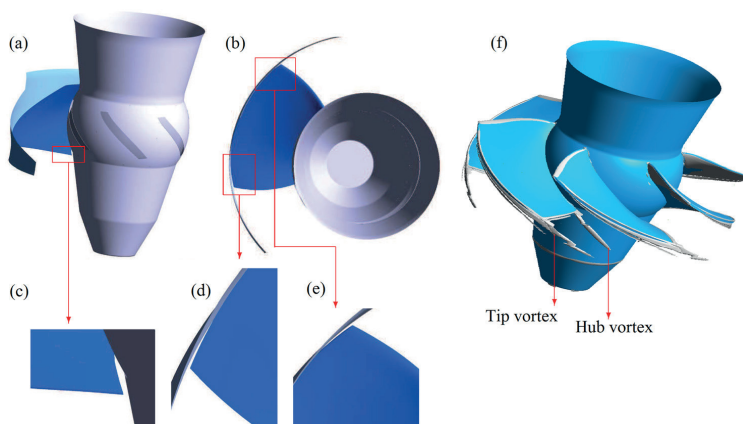
Fig. 3 Schematic of the hub and tip clearances: (a) side view of the runner, (b) bottom view of the runner, (c) hub clearance at the trailing edge, (d) tip clearance at the leading edge, (e) tip clearance at the trailing edge, and (f) vortices formed at the runner blade's hub and tip

Table 2 Hub and tip clearance variations at the two blade angles; dimensions in mm

	Tip-LE	Tip-Mid	Tip-TE	Hub-LE	Hub-Mid	Hub-TE
$\beta_b = 0.8\,\text{deg}$	2.25	0.3	1.25	0.25	0	4.8
$\beta_b = 4\,\text{deg}$	2.5	0.3	2.5	0.15	0	3

LE: leading edge, Mid: middle, and TE: trailing edge.

efficiency is estimated with an uncertainty of less than ±0.18%. The model is installed between an upstream high-pressure tank and a downstream low-pressure tank. The pressure difference between the two tanks can be adjusted to establish the desired head for the test case. The absolute pressure of the two tanks can be adjusted to either trigger or prevent cavitation. The current measurements were performed under cavitation-free conditions.

Experimental Procedure. The LDA measurement sections are shown with the horizontal lines named "RB" and "RC" in Fig. 4(a). Windows with a diameter of 50 mm and a thickness of 12.7 mm composed of high-quality glass were installed on the runner chamber to provide the required optical accesses for the LDA measurements, as presented in Fig. 4(b). Measurements within the blade channels were performed along RB, located 8 mm below the runner hub center. The measurements at the runner outlet were performed along RC, located 137 mm below the runner hub center. The optical access windows contained parallel faces to prevent optical aberrations. Installation of the window at RC, where the wall exhibits a conical shape, resulted in deformation of the hydraulic surface of the draft tube cone and produced a discontinuity between the cone and the window. The glass was flush with the draft tube wall on its bottom, which resulted in a step of approximately 3 mm (1.2% of the measurement section radius) on top of the window; see Fig. 4(b). This affects the measurements in the region adjacent to the draft tube wall. The discontinuity at the RB was approximately 1 mm (0.4% of the measurement section radius) on the left and right sides of the window, whereas it was mounted flush with the bottom and top due to the cylindrical shape of the chamber at this location.

A two-component LDA system with an 85 mm optical fiber probe from Dantec was used to measure the velocity distribution in the blade channels and at the runner outlet. A probe with a backscattering configuration was used to enable velocity measurements inside the blade channels because the turbine hub blocks the light beam in the forward direction. A front lens with a 600 mm focal length was employed. The measuring volume size

based on the e^{-2} Gaussian intensity cutoff point was estimated to be $2.229 \times 0.140\,\text{mm}$ and $2.426 \times 0.147\,\text{mm}$ for the axial and tangential components, respectively. The velocity measurements were performed in burst and coincidence mode; one velocity was recorded in the axial and tangential directions for each passing particle. The sampling time at each measurement point was set to 600 s. This sampling time corresponded to a range of 130,000–500,000 velocities recorded at each measurement point at the runner outlet depending on the radial coordinate. More than 250,000 velocities were recorded at each measurement point at the runner outlet section, with the exception of the measurement points adjacent to the runner hub and shroud. The number of recorded velocities decreased to approximately 130,000 at these two points. The number of recorded velocities inside the blade channels ranged from 30,000 to 300,000 at each point; the number was greater than 100,000 at all measurement points, with the exception of the measurement locations closest to the runner hub, which was approximately 30,000. The measurement results at the locations with low sampling rates are not presented in this paper because the accumulated mean values did not converge. The seeding particles used in this investigation consisted of Expancel 461 WU 20 with an average diameter of $6\,\mu m$.

The signal from a magnetic encoder, which was installed on the main shaft of the turbine, was used to determine the runner's angular position at each instant. The encoder signal consists of one step per revolution. The azimuthal position of the magnetic instrument installed on the main shaft of the turbine for producing the stepwise signal was constant during all the measurements performed after the runner and within the blade channels. The accuracy of the sensor was 0.5 deg, as reported by the manufacturer.

The shaft torque signal was simultaneously recorded using hydrostatic bearing systems with an accuracy of 0.08%. The signal was recorded with a sampling rate of 8 Hz. For more details about the data acquisition system, refer to Amiri [33].

All of the runner blades were scanned using a three-dimensional optical scanning apparatus (ATOS III system from GOM) with an accuracy of ±0.03 mm. The results revealed various geometrical differences between the blades. The differences among the blade geometries were found to increase close to the tip and trailing edges. The variations close to the trailing edge of the runner blades at $r^* = 0.91$ are presented in Fig. 5 as an example. The figure shows the blade scanning results when they are not installed on the runner hub. The differences in the blade surface shape and angle can be clearly observed. Another difference can be observed in the trailing edge shapes: some are blunt and others are round. The accuracy of the stagger angle of the runner blades was estimated to be approximately 0.01 deg; this is considered to
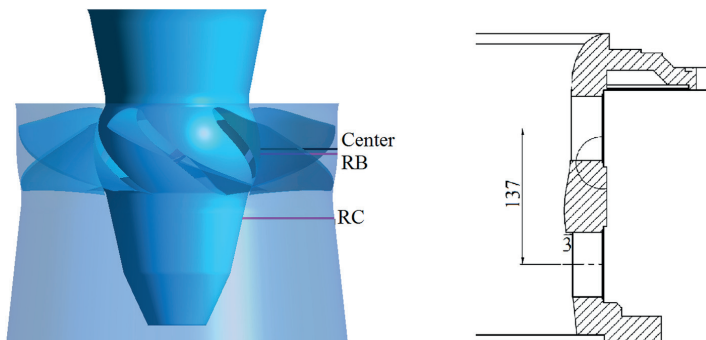
Fig. 4 (a) LDA measurement locations; Center: radius along the runner hub center; RB: measurement section between the runner blades; RC: measurement section below the runner blades. (b) Sketch of the optical access windows; the dashed lines in (b) represent the window's centerline. The top glass center is aligned with the runner hub center.
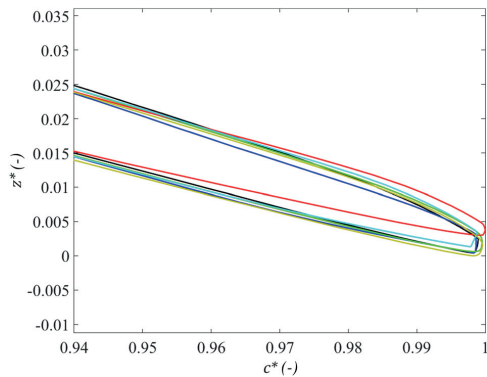
Fig. 5   Differences between the blade geometries close to the trailing edge at $r^* = 0.91$

Fig. 6   Amplitude spectra of dynamic pressure obtained from tangential velocity components within the runner at $BEP_{0.8}$

be sufficiently accurate to not contribute to flow deviations from one channel to another. Variations in the accuracy of the installation of the chamber around the runner produce variations in the tip clearance gap. The tip clearance in the middle of the runner blade chord was measured to be 0.3 ± 0.15 mm at different blades when standing still.

Data Processing and Phase Averaging

Time-weighted average velocities based on the residence time of the bursts were used to calculate the mean and Reynolds stress components of the velocities measured with the LDA system, which reduces the bias [48]. Thus, each acquired signal $\phi(x,t)$ was decomposed into three components, the time-averaged $\bar{\phi}(x)$, periodic oscillations $\tilde{\phi}(x,t)$, and random fluctuations $\phi'(x,t)$, according to the Reynolds triple decomposition as follows:

$$\phi(x,t) = \langle \phi(x,t) \rangle + \phi'(x,t) = \bar{\phi}(x) + \tilde{\phi}(x,t) + \phi'(x,t) \quad (1)$$

where $\langle \phi(x,t) \rangle$ is the phase-averaged signal over the defined period.

Spectral analysis of the LDA signals was conducted in the same manner as that proposed by Mulu et al. [41]. The randomly distributed velocity measurement results in the time domain were resampled through a linear interpolation. Welch's method with a Hanning window was then applied to the resampled data for the spectral analysis. The dominant frequency and harmonics calculated by this method are expected to be similar to those identified by the Lomb-normalized periodogram method, where evenness of the acquired data is not mandatory [41]. The amplitude spectra acquired from the tangential velocity component within the runner at $BEP_{0.8}$ is presented in Fig. 6 as an example. The spectra are presented in dynamic pressure form $((1/2)\rho u^2)$ as presented by Mulu et al. [41]. The results revealed that the runner's rotational frequency and its harmonics are the only distinct peaks in the amplitude spectrum of the velocities at the BEPs and HLs. Similar results were presented by Mulu et al. [41] for the LDA measurements performed after the runner. Hence, the frequency of the periodic oscillations in Eq. (1) is considered to be the runner frequency, and the results are phase resolved according to the runner's rotational frequency. The LDA measurement results at a point downstream of the runner, phase resolved according to the runner's rotational frequency, are presented in Fig. 7. The black dots represent the phase-resolved velocity during the measurements. The measurement results at each point are a function of the runner's angular position, which is determined by the magnetic encoder. One period, a rotation of the runner in this case, was divided into phase intervals of size $\Delta\theta$ to calculate the phase-
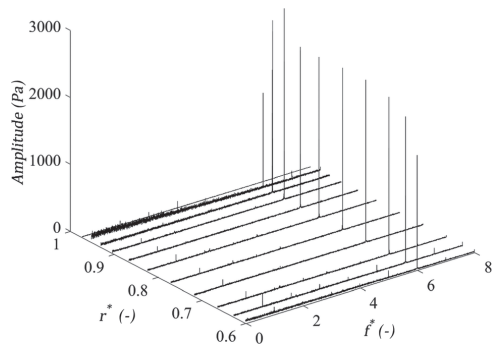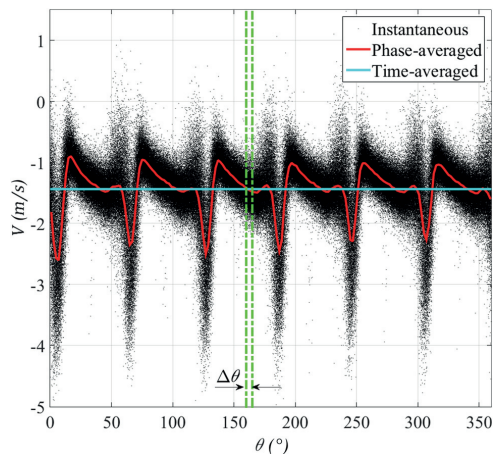
Fig. 7   Illustration of the phase-averaged velocity over one runner revolution; the initial signal contains 358 ks, and the bin size used for the phase averaging is $\Delta\theta = 1$ deg

averaged curve (the red curve) in Fig. 7. The phase intervals are referred to as bins in the remainder of the paper. The phase-resolved data within each bin centered at θ_0, i.e., $[\theta_0 - \Delta\theta/2, \theta_0 + \Delta\theta/2]$, are averaged to extract the phase-averaged velocities and root-mean-square (RMS) values. The bin size should be selected to accurately estimate the phase-averaged results. Because a distinct criterion for this parameter is not available, a tradeoff between phase resolution and statistics is required. The number of samples contained in each interval and the bin size affect the phase-averaged plot and the RMS values that are calculated for each bin. Small bins should be used to capture the systematic fluctuations in the phase-averaged curve, especially when the data exhibit strong local gradients [49]. However, a sufficient amount of data in each interval is required to minimize the effect of the random fluctuations on the periodic fluctuations. The influence of the phase-averaging window size was investigated at a number of runner rotational positions and measurement volume locations. Various window sizes, ranging from 0.5 to 3 deg with a 0.5 deg increment, were selected to assess the window size's influence on the measured velocity and on the RMS. The calculations for a window size of $\theta < 1$ deg were not reliable due to the limited amount of data in each interval and due to the resolution of the

magnetic encoder, which was 0.5 deg. Thus, a bin size of 1 deg, which was an appropriate compromise between statistical uncertainty and phase resolution, was employed for the computation of the phase-resolved velocity data. The same bin size was used to analyze the results obtained within the runner. The gradient compensation method (parabolic regression) presented by Glas et al. [50] was used for the phase averaging.

Intermittent passage of the runner blades prevented the formation of the control volume for the LDA measurements within the runner. The bin centers within the runner are presented in Fig. 8, which displays the top view of the runner cross section at the measurement section within the runner. The velocities could be measured adjacent to the pressure side of the runner blades. However, the maximum distance between the blade suction surface and the first azimuthal LDA position is 9.5 mm due to the blade shape and the angle between the laser beams, which was approximately 5.2 deg in water.

The acquired results at BEPs and HLs were phase resolved with respect to the runner rotational frequency using the encoder signal recorded simultaneous with the LDA measurements. However, at PLs, no signal is recorded to capture the RVR rotational frequency. The method developed by Jonsson et al. [14] was used to phase resolve the data with respect to the RVR frequency ($f^* = 0.171$). In this method, the LDA signal from the tangential component is used to phase resolve both velocity components with respect to the RVR frequency. The corkscrew-type RVR revolving after the runner around the draft tube centerline results in an increased tangential velocity between the RVR and the draft tube cone as it passes through the measurements location. Hence, the tangential velocity signals acquired at each radius were filtered with a band pass filter with a width of 0.1 Hz around the RVR frequency. The resulting signal was used to phase resolve the original signals. The bin size used in the phase resolving procedure was 1 deg; equal to the phase resolving with respect to the runner frequency. Hence, the number of the data points per bin was similar to that when resolving the results with respect to the runner frequency. The uncertainties in the velocity and RMS values are presented in Table 3.

The total uncertainty in a measurement can be found by combining the random and systematic errors. LDA measurements exhibit multiple types of error sources; a detailed description of these error sources can be found in Mulu [40]. The precision error
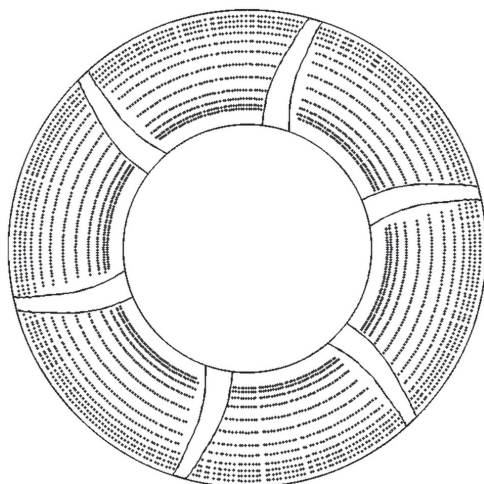
Table 3 Uncertainty analysis of the LDA measurements

	Within blade channels (%)	At the runner outlet (%)
U	±0.71	±0.65
u	±1.10	±0.96
V	±0.88	±0.75
v	±1.22	±1.12

of the LDA measurements was estimated by a repeatability test with a 95% confidence level. A weighting method was used to correct the velocity bias. Although the weighting method, which is based on the residence time, was applied to correct the velocity bias, uncertainty still remained and was estimated from the weighted mean and instantaneous velocity. The system noise, which was caused by the vibration of the test rig, was estimated using a velocity measurement on the surfaces of the test section. The magnitude of the system noise was insignificant; however, the measured noise contribution to the velocities was deducted from the velocity data. Table 3 presents the maximum total uncertainty in the measurements for most of the measurement locations with different operational points. However, close to the hub and tip, the total measurement uncertainty at a 95% confidence interval is within 2.1% at different operating points. In addition, due to the RVR at the PL operation, the uncertainty is higher compared to the BEP, i.e., the accuracy at BEP is smaller than that reported in Table 3. The accuracy of the traverse used for the measurement was 0.01 mm. The normality of the LDA probe to the window was measured using optical methods and exhibited an accuracy of 0.02 deg, which correspond to an accuracy of 0. 03%.
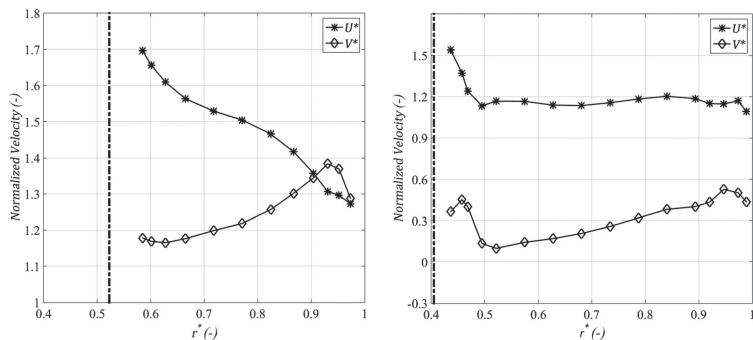
Results and Discussion

The time- and phase-averaged velocities and turbulent quantities are presented in this section. The velocities are normalized using the reference velocity obtained from the flow rate through the turbine and the draft tube inlet area, which was 0.196 m². The positive directions for the velocities are defined as downward for the axial component and clockwise from the top view for the tangential component, which is in the direction of the runner's rotation.

Measurement results obtained at the investigated BEPs and HLs showed similar flow features within and after the runner blades. Hence, the results at $BEP_{0.8}$ are presented and discussed as representative of the operating points. The results acquired at $PL_{0.8}$ are also presented as demonstrating a case where the RVR forms in the draft tube.

BEP Conditions. Figure 9 shows the time-averaged velocity profiles measured within the runner and at the runner outlet at $BEP_{0.8}$. U^* and V^* are the normalized axial and tangential velocity components, respectively. The tangential velocity within the blade channels, as shown in Fig. 9(a), increases with the radius in the inner part of the blade due to the combined effect of the twisted blades, the solid body rotation of the runner and the upstream condition. An inflection in the velocity profile exists near the runner tip. The axial velocity decreases with increasing radius along the measurement section as a result of the blade twist and converging flow passage channel near the hub compared to the tip, which is due to the spherical runner hub and higher blade thickness near the hub which accelerate the flow close the this region.

As shown in Fig. 9(b), the axial velocity at the runner outlet is almost constant at all radii, with the exception of the blade endings. The axial velocity increases near the hub. The phase-averaged results show that this is attributed to the hub clearance. The axial velocity profile is in agreement with the measurement results performed inside the draft tube downstream of the runner hub presented by Mulu et al. [41]. The results showed that the axial velocity is nearly constant in the outer part of the draft tube. The axial velocity at their measurement location (∼190 mm

Fig. 8 Phase-averaging bin center positions in the runner blade passage relative to the runner blades, top view

Fig. 9 Time-averaged velocity profiles within the runner and at the runner outlet: (*a*) axial and tangential velocity profiles at section RB. (*b*) Axial and tangential velocity profiles at the runner outlet: BEP$_{0.8}$. The bold lines at approximately *r** = 0.4 and *r** = 0.5 represent the runner hub.

downstream compared with the current measurement section) is approximately 30% lower compared with the current measurement results due to the decelerating effect of the draft tube. The tangential component also increases close to the hub. The phase-averaged results indicate that this increase is due to the combined effect of the rotating hub and the hub vortices generated within the hub clearance gap of the runner blades. The tangential velocity linearly increases with the radius in the mid-part of the blades and resembles a solid body rotation; similar to the tangential velocity at the outer part of the draft tube in the results presented by Mulu et al. [41]. The higher swirl near the tip results in a centrifugal force, which helps to prevent separation on the conical draft tube wall. This effect is present downstream in the cone, as presented by Mulu et al. [41]. Both velocity components decrease in the vicinity of the draft tube wall (*r** > 0.97) due to the boundary layer developing along the draft tube wall. The fact that the optical access window is not completely flush with the draft tube wall at this location (see Fig. 4(*b*)) may result in the formation of a cavity in the vicinity of the optical access window. This can disturb the flow measurements close to the wall and result in an overestimation of the boundary layer thickness at this location.

Figure 10 shows the Reynolds stresses within the runner and at the runner outlet. The phase-averaged component of the signals, $\langle \phi(x,t) \rangle$ in Eq. (1), was subtracted from the original component to calculate the random velocity fluctuations. The random fluctuations were used to calculate the Reynolds stresses. The largest stresses inside the blade channels, as shown in Fig. 10(*a*), appear

near the tip due to the large velocity gradients and tip leakage in this section, as presented in the phase-averaged results. Near the hub, the stresses decrease with increasing radius due to the shear created by the rotation of the runner hub. Figure 10(*a*) illustrates that the stresses in the axial and tangential directions are equivalent.

The Reynolds stresses at the runner outlet, shown in Fig. 10(*b*), are nearly constant far from the runner hub and tip. The normal stresses are equal, and the shear stress is approximately zero, which can be an indication of isotropic turbulence in this region. The radial velocity component should also be measured to determine if the flow is effectively isotropic. The radial component of the turbulence intensity can be higher than the other components due to centrifugal and Coriolis forces [11]. The stresses increase near the shroud (*r** > 0.9) due to the effects of the runner tip clearance and the wall. The results presented by Mulu et al. [41] show that this region will expand in the draft tube cone and almost completely dissipate at the end of the cone. A sharp increase in the normal stresses is detected near the hub due to the effects of the hub clearance leakage and rotating hub.

The contour plots of the phase-averaged velocities within the blade channels are shown in Fig. 11. The figure shows the top view of the contour plots in the measurement section, whereas the runner rotates in the clockwise direction. The axial velocity contour exhibits a lower axial velocity close to the pressure side of the blade compared to the suction side. The axial velocity increases in the azimuthal direction in each blade channel from
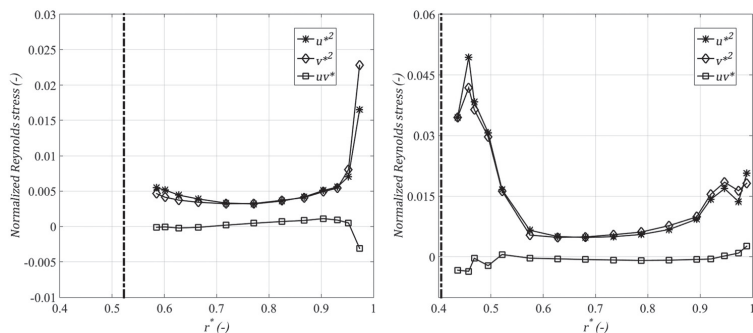
Fig. 10 Reynolds stresses *u**^{2}, *v**^{2}, and *uv**: (*a*) within the blade channels, and (*b*) at the runner outlet at the BEP$_{0.8}$. The bold lines at approximately *r** = 0.4 and *r** = 0.5 represent the runner hub.
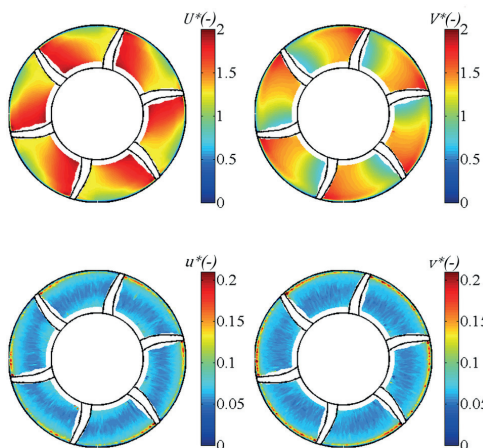
Fig. 11 Normalized phase-averaged velocities with the corresponding RMS values at section RB: BEP$_{0.8}$

the pressure side of one blade to the suction side of the adjacent blade where water exits the runner.

The tangential velocity in Fig. 11 decreases from the blade pressure side to the suction side in each blade channel. The phase-averaged RMS contour plots of the axial and tangential velocities presented in Fig. 11 do not indicate any specific variation in the azimuthal direction except close to the tip region. The RMS values increase close to the tip region and are higher near the suction side compared to the pressure side of the blades. The flow close to the runner tip is affected by the flow passing through the tip clearances. The increased RMS values close to the blade's suction side compared to the pressure side is due to the flow leakage from the tip clearance upstream of the measurement section. The results are in agreement with those presented by Wu et al. [12], who showed that the turbulent kinetic energy increases close to the suction side of the blade at the tip clearance area. Although the results demonstrated the presence of tip leakage from the pressure side to the suction side at this location, no tip vortex was observed. This is in agreement with the results of McCarter et al. [11], whereby the tip vortex started to form on the last 20% of the chord.

Figure 12 shows the deviation of the axial and tangential velocity fields within the six blade channels from the averaged axial and tangential velocity fields in these channels. The resulting contours indicate the velocity differences in different blade-to-blade channels. The contours are extracted from the LDA measurement results obtained along the radial direction at one azimuthal location. Thus, they represent the velocity variations induced by the geometrical differences between the runner channels on the velocity field. The circumferential variations associated with the
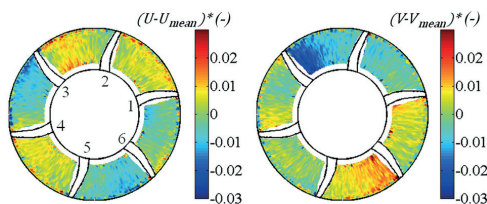
stationary components (e.g., spiral casing, guide vanes, and draft tube bend) are not included. Figure 12 reveals a maximum deviation of approximately 3% of the bulk velocity in both cases, which contributes to an asymmetrical force on the runner. The variations in the velocities between blade channels are attributed to the previously discussed differences in the blade manufacturing process and to the turbine assembly process. The effect of the blade surface angle resulting from the precision of the manufacturing process is visible in certain regions in the vicinity of some runner blade surfaces, in which the variations in the axial and tangential velocity components are reversed with respect to each other. For instance, the axial velocity increases in the vicinity of the suction side of blade 3, whereas the tangential velocity decreases in this region. The greatest variations in the velocities are located close to blades 3 and 6.

The phase-averaged velocities at the runner outlet are shown in Fig. 13. The results show that the passing of the blade trailing edge causes a momentum loss in the axial velocity due to the wake at the blade trailing edge. At the same location in the tangential velocity contour, the velocity increases in the wake region. Six high-axial-velocity regions are located near the runner hub. These regions correspond to the vortices formed in the hub clearances. Each high-axial-velocity spot is coupled with a low-axial-velocity region demonstrating the formation of vortices at the hub clearances; the region is marked with "hub vortex" in Fig. 13. The results show that the hub leakage flow rolls up and forms a vortex in this region. The numerical study performed by Mulu et al. [46] showed that the presence of the vortices around the runner cone is beneficial for controlling boundary layer separation on the runner hub. This is one of the differences between the flow conditions after the runner of a Kaplan turbine and propeller turbines where no hub clearance is present. Although the centrifugal force associated with the swirl exiting the runner is necessary to prevent separation on the draft tube cone, it contributes to separation on the runner hub. The high-velocity flow from the hub clearance is attached to the rotating hub due to the Coanda effect. The high velocity decreases the pressure in the central part of the draft tube, resulting in streamlines bending toward the middle part of the draft tube, thereby compensating for the centrifugal force on the flow. The phase-averaged contour plots presented by Mulu et al. [41] show that the high-velocity regions are attached to the runner hub.

There are six high-axial-velocity spots close to the shroud coupled with low-axial-velocity in their vicinity. The region is
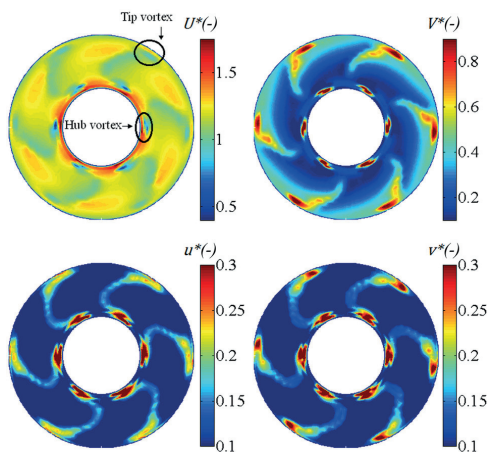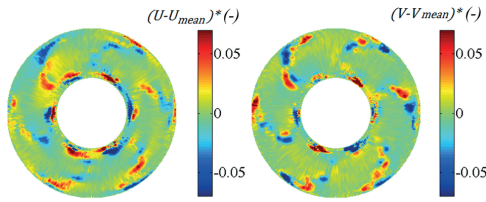

Fig. 12 Deviation of the axial and tangential velocity contours in different blade channels from the mean contour: BEP$_{0.8}$

Fig. 13 Normalized phase-averaged velocities at the runner outlet: BEP$_{0.8}$

Fig. 14 Phase-averaged deviation of the axial and tangential velocity contours in different blade channels from the mean contour at the runner outlet: $BEP_{0.8}$

marked in the axial velocity contour. The high-velocity spots are caused by the tip vortices formed in the tip clearance region. The tangential velocity increases in the hub and tip vortices regions.

The corresponding RMS values of the axial and tangential velocity components in Fig. 13 show that the velocity fluctuations at the blade channel outlets are minimized and homogeneous for both components. The increased RMS values in the blade wakes indicate the higher turbulence in these regions. The maximum RMS values in both directions occurred near the hub, where the rotating hub and hub clearance effects create a high level of turbulence. The spots with a high RMS near the tip in the tangential RMS contour are related to the presence of the tip vortices formed in the tip clearances, which is in agreement with Ref. [12].

A procedure similar to the one used for Fig. 12 was applied to the velocity contours acquired at the runner outlet to investigate the effect of the runner asymmetry on the flow entering the conical draft tube. The corresponding results are presented in Fig. 14. The results show that both velocity components deviate substantially from the mean contours in the wakes of the blade trailing edges. Because the blade geometry has a significant effect on the wake, the effect on the wake-free region, which is far from the blades, should be smaller than the effect on the wake. As seen in the axial velocity contour plot, the deviations in the wakes associated with blades 3 and 6 are higher than those of the other blades. The flow within the runner is observed to have the maximum deviation close to these blades as well; see Fig. 12. This finding demonstrates the importance of the geometrical similarity between the blades to the flow symmetry at the runner outlet. The effect of the geometrical variation in the blades on the performance of a propeller turbine was numerically investigated by Nicolle et al. [51] and Vu et al. [52]. The numerical simulations indicated that the geometrical differences among blades may create inaccurate power output, misplaced efficiency peak or unexpected behavior of the draft tube. Nicolle et al. [51] demonstrated that even with similar tip clearance gaps, a variation in efficiency

of approximately 1.2% and a variation in the output power of approximately 8% were observed at the turbine's nominal flow rate when the scanning results of different blades of the runner were employed for the simulations.

PL Operating Conditions. The time-averaged velocity profiles at $PL_{0.8}$ within and beyond the runner are presented in Fig. 15. A comparison of the velocity profiles within the runner at $PL_{0.8}$ to the ones at $BEP_{0.8}$ indicates that the axial velocity profile remains nearly unchanged. However, the average tangential velocity is approximately $0.7V^*$ higher at this location due to a greater swirl created by the smaller guide vane angle. The tangential velocity profile within the runner is also distorted at this operating point. The tangential velocity within the runner at $BEP_{0.8}$ decreases, whereas it increases approaching the runner hub at $PL_{0.8}$. This may be due to the change in the flow conditions at the runner inlet or due to the recirculation bubble (also referred to as a stalled region or dead zone) that is formed downstream in the middle part of the draft tube cone at this operating point, see Fig. 1. The flow passage blockage caused by the recirculation bubble that forms downstream may result in the deformation of the streamlines and increasing tangential velocity profile within the runner close to the hub.

Both velocity profiles at the runner outlet are distorted at $PL_{0.8}$ compared to $BEP_{0.8}$. The tangential velocity at the runner outlet is larger than that in the previous case due to the larger swirl generated by the guide vanes at this operating point. The linear increase in the tangential velocity profile in the middle part of the blade, as shown in the $BEP_{0.8}$, is not present at $PL_{0.8}$, which results in even higher tangential velocities near the hub. The results presented by Jonsson et al. [14] showed a similar velocity distribution inside the draft tube at this operating point, i.e., constant tangential velocity. There is a decrease in the axial velocity profile at $0.5 < r^* < 0.6$. The decreased axial velocity and increased tangential velocity in this region can also be attributed to the blockage effect of the recirculation bubble that formed downstream of the measurement section.

The phase-averaged velocity contours with respect to the runner frequency at the runner outlet at $PL_{0.8}$ are shown in Fig. 16. The main flow features in the middle and outer parts of the passage are similar to those at $BEP_{0.8}$, as presented in Fig. 13, with the exception that both dimensionless velocities are larger at $PL_{0.8}$. However, the flow in the region near the hub is distorted. The decrease in the axial velocity and increase in the tangential velocity close to the hub (indicated with a black circle) compared with the results at the BEP can be attributed to the presence of the RVR and recirculation bubble in the middle region of the draft tube that deforms the streamlines upstream. The results presented by Jonsson et al. [14] showed that the RVR center is located at
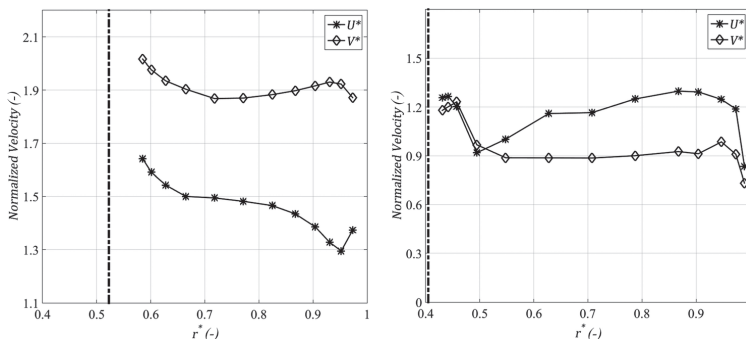
Fig. 15 Time-averaged velocity profiles at $PL_{0.8}$ (a) within the runner and (b) at the runner outlet
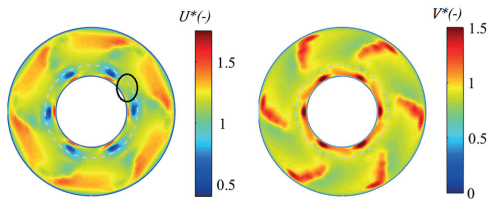
Fig. 16 Normalized phase-averaged velocities with respect to the runner frequency at the runner outlet: PL$_{0.8}$. The dashed gray circle shows the RVR center at the trailing edge of the runner hub.

Fig. 18 Normalized phase-averaged axial and tangential velocities with respect to the RVR frequency at the runner outlet: PL$_{0.8}$

Fig. 19 Normalized phase-averaged contours of the oscillating axial and tangential velocities with respect to the RVR frequency within the runner: PL$_{0.8}$

$r* \sim 0.55$, slightly after the runner hub. The location is indicated by a gray dashed circle in Fig. 16. The figure shows that both axial and tangential components are distorted in the region where the RVR is located downstream; $r* < 0.55$. The recirculation bubble region may block the flow downstream of the measurement section and deform the streamlines, thereby resulting in lower axial and higher tangential velocities.

Figure 17 presents the amplitude of the dynamic pressure obtained from axial and tangential velocity components at the RVR frequency ($f^* = 0.171$). Amplitude of the tangential component is higher than the axial component both within and after the runner. The results are in agreement with the pressure measurements performed on the runner blades and at the draft tube inlet where rotating mode of the RVR was shown to dominate the plunging mode [18,33]. The amplitude of the tangential component at RC decreases with radius because the distance from the RVR increases in radial direction.

The phase-averaged velocity contours at PL$_{0.8}$ with respect to the RVR frequency at the runner outlet are presented in Fig. 18. The variations with the azimuthal position in the color maps represent the temporal evolution of the velocity fields over one period of the RVR rotation because the LDA measurements are performed along one radial direction. The figures show the asymmetric axial and tangential velocity distributions induced by the RVR upstream. The axial velocity at each radius varies by approximately 7–10% in the azimuthal direction. The maximum variation of the tangential component is in the order of 20% of the reference velocity. The flow asymmetry results in an asymmetric force
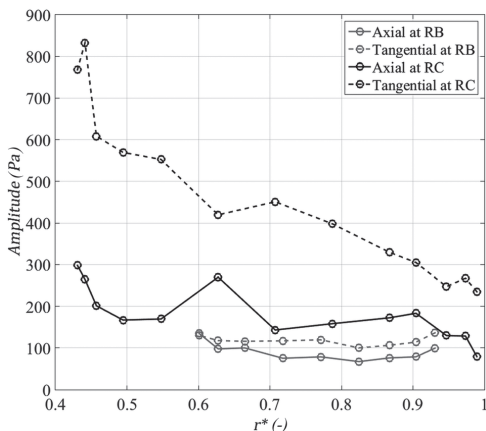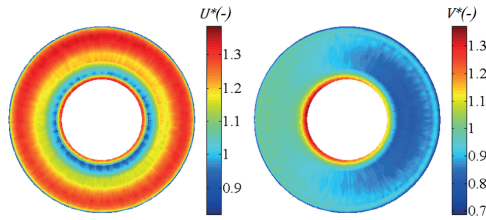
exerted on the runner. Moreover, because the asymmetric flow rotates with the RVR frequency, which is different from the runner frequency, periodic forces are exerted on the runner blades. The results are in agreement with the pressure measurement results performed on the runner blades of the same turbine model [18]. The results showed pressure oscillations exerted on the runner induced by the RVR.

Although the frequency analysis demonstrated the existence of the RVR frequency in the axial and tangential velocity signals acquired within the runner, the azimuthal variation in the velocities was much smaller than the radial variation of the velocities in this section. Hence, the asymmetry due to the RVR could not be easily visualized when presenting the normalized phase-averaged velocities. At this section, the time-averaged velocities at each radius were subtracted from the signal, and then, the phase-averaging process was applied to the resulting signals. This method does not affect the variation in the velocity in the azimuthal direction at each radius when removing the radial variation in the signals. The results are presented in Fig. 19. The blank areas resulting from the runner blade passage present in Fig. 11 are not observed in this figure because all phenomena occurring with frequencies other than those corresponding to the harmonics of the RVR frequency are filtered out by the phase averaging process. The figure shows the flow asymmetry within the runner blade channels induced by the RVR formed downstream of the draft tube. This results in an asymmetry in the blade loads on two sides of the runner. Moreover, this asymmetry induces a periodic fluctuation on the runner and its blades because the RVR rotates with a frequency that is different from the runner frequency. The presence of the asymmetry is in agreement with the pressure measurement results performed on the runner [18]. However, the power spectrum of the torque signal did not show any specific fluctuations with the RVR frequency. This demonstrates that the fluctuations were damped by the runner and the turbine's bearings.

Fig. 17 Amplitude of the dynamic pressure obtained from axial and tangential velocity measurement results at the RVR frequency

Conclusion

The velocity fields within the interblade region and at the outlet of a Kaplan runner model were investigated at the BEPs of two

propeller curves. Two operating points on each of the propeller curves, with higher and lower flow rates than those of the corresponding BEP, were also investigated during off-cam operation of the turbine. Time- and phase-averaged velocity profiles were presented for both measurement sections.

The results demonstrated that the main flow features inside and after the runner are similar when the turbine operates at the BEPs and HLs. The time-averaged results showed that the clearance leakages were the main sources of velocity fluctuations producing higher Reynolds stresses near the hub and tip. The tip leakage from the region between the runner blade leading edge and the middle of the blade induced large fluctuations in the velocities close to the tip region. The fluctuations were larger close to the blade suction side. No sign of a tip vortex was found in the measurement results acquired within the blade channels. The phase-averaged velocity contours showed that manufacturing tolerances resulted in various deviations in the flow behavior in different blade channels and at the runner outlet. The hub and tip vortices formed in the blade clearances were captured by the LDV measurements at the runner outlet.

PL operation of the turbine resulted in the formation of a recirculation bubble and RVR in the draft tube. The results demonstrated that the revolution of the RVR in the draft tube caused an asymmetric flow distribution at the runner outlet and within the blade channels located upstream of the RVR. This produces an imbalanced force on the runner and pulsating forces on the runner blades.

Acknowledgment

Nomenclature

c = hydrofoil chord (m)
D = turbine diameter (m)
f = frequency (Hz)
H = turbine head (m)
N = turbine rotational speed (rpm)
n_{11} = turbine reduced speed (rpm/$\sqrt{\text{m}}$)
Q = turbine flow rate (m^3/s)
Q_{11} = turbine reduced flow rate ($\sqrt{\text{m}}$/s)
r = radius (m)
u = fluctuating part of axial velocity (m/s)
U = axial velocity (m/s)
v = fluctuating part of tangential velocity (m/s)
V = tangential velocity (m/s)
z = vertical position (m)
α_{gv} = guide vane angle (deg)
β_b = runner blade installation angle (deg)
η = turbine efficiency (%)
θ = angular position (deg)
ρ = density (kg/m^3)
ϕ = arbitrary parameter

Subscripts, Superscripts, and Operators

mean = average of velocity contours captured within six runner blade channels
$'$ = random fluctuation of the signal
$\tilde{}$ = periodic oscillation of the signal
$-$ = time-averaged
$*$ = normalized parameter; velocities, lengths, and frequencies are made dimensionless using reference

velocity, runner diameter, and runner frequency, respectively.
$<>$ = phase-averaged signal
0.8 = parameter presented at runner blade angle of 0.8 deg
4 = parameter presented at runner blade angle of 4 deg

References

[1] Bradshaw, P., 1996, "Turbulence Modeling With Application to Turbomachinery," Prog. Aerosp. Sci., **32**(6), pp. 575–624.
[2] Langston, L. S., 2001, "Secondary Flows in Axial Turbines: A Review," Ann. N. Y. Acad. Sci., **934**(1), pp. 11–26.
[3] Pitdiwala, U. J., Patel, H. C., and Parmar, P. K., 2014, "A Review on Tip Clearance Flow and Secondary Flow Losses in Linear Turbine Cascade," J. Mech. Civil Eng., **11**(3), pp. 33–37.
[4] Sjolander, S. A., and Amrud, K. K., 1987, "Effects of Tip Clearance on Blade Loading in a Planar Cascade of Turbine Blades," ASME J. Turbomach., **109**(2), pp. 237–244.
[5] Dreyer, M., Decaix, J., Münch-Alligné, C., and Farhat, M., 2014, "Mind the Gap: A New Insight Into the Tip Leakage Vortex Using Stereo-PIV," Exp. Fluids, **55**(1849), pp. 1–13.
[6] Yaras, M. I., and Sjolander, S. A., 1992, "Effects of Simulated Rotation on Tip Leakage in a Planar Cascade of Turbine Blades—Part I: Tip Gap Flow," ASME J. Turbomach., **114**(3), pp. 652–659.
[7] Yaras, M. I., and Sjolander, S. A., 1992, "Effects of Simulated Rotation on Tip Leakage in a Planar Cascade of Turbine Blades: Part II—Downstream Flow Field and Blade Loading," ASME J. Turbomach., **114**(3), pp. 660–667.
[8] Graham, J. A. H., 1986, "Investigation of a Tip Clearance Cascade in a Water Analogy Rig," ASME J. Eng. Gas Turbines Power, **108**(1), pp. 38–46.
[9] Yamamoto, A., Tominaga, J., Matsuunuma, T., and Outa, E., 1994, "Detailed Measurements of Three-Dimensional Flows and Losses Inside an Axial Flow Turbine Rotor," ASME Paper No. 94-GT-348.
[10] Yamamoto, A., Matsuunuma, T., and Outa, E., 1994, "Unsteady Endwall/Tip-Clearance Flows and Losses Due to Turbine Rotor–Stator Interaction," ASME Paper No. 94-GT-461.
[11] McCarter, A. A., Xiao, X., and Lakshminarayana, B., 2001, "Tip Clearance Effects in a Turbine Rotor. Part II: Velocity Field and Flow Physics," ASME J. Turbomach., **123**(2), pp. 305–313.
[12] Wu, H., Miorini, R. L., and Katz, J., 2011, "Measurements of the Tip Leakage Vortex Structures and Turbulence in the Meridional Plane of an Axial Water-Jet Pump," Exp. Fluids, **50**(4), pp. 989–1003.
[13] Nishi, M., Matsunaga, S., Okamoto, M., Uno, M., and Nishitani, K., 1988, "Measurements of Three-Dimensional Periodic Flow in a Conical Draft Tube at Surging Condition," Flows in Non-Rotating Turbomachinery Components, FED, **69**, pp. 81–88.
[14] Jonsson, P. P., Mulu, B. G., and Cervantes, M. J., 2012, "Experimental Investigation of a Kaplan Draft Tube—Part II: Off-Design Conditions," Appl. Energy, **94**, pp. 71–83.
[15] Nishi, M., Matsunaga, S., Kubota, S., and Senoo, Y., 1982, "Flow Regimes in an Elbow-Type Draft Tube," 11th IAHR Symposium, Amsterdam, The Netherlands, Paper No. 38, pp. 1–13.
[16] Rheingans, W. J., 1940, "Power Swings in Hydroelectric Power Plants," Trans. ASME, **62**(3), pp. 171–184.
[17] Iliescu, M. S., Ciocan, G. D., and Avellan, F., 2008, "Analysis of the Cavitating Draft Tube Vortex in a Francis Turbine Using Particle Image Velocimetry Measurements in Two-Phase Flow," ASME J. Fluids Eng., **130**(2), p. 021105.
[18] Amiri, K., Cervantes, M. J., and Mulu, B., "Experimental Investigation of the Hydraulic Loads on a Kaplan Turbine Runner Model and Corresponding Prototype," J. Hydraul. Res. (published online).
[19] Papillon, B., Sabourin, M., Couston, M., and Deschenes, C., 2002, "Methods for Air Admission in Hydro Turbines," 21st IAHR Symposium on Hydraulic Machinery and Systems, Lausanne, Switzerland, pp. 1–6.
[20] Thicke, R. H., 1981, "Practical Solutions for Draft Tube Instability," Int. Water Power Dam Constr., **33**(2), pp. 31–37.
[21] Kjeldsen, M., Olsen, K., Nielsen, T., and Dahlhaug, O., 2006, "Water Injection for the Mitigation of Draft Tube Pressure Pulsations," IAHR International Meeting of the Workgroup on Cavitation and Dynamic Problems in Hydraulic Machinery and Systems, Barcelona, Spain, pp. 1–11.
[22] Miyagawa, K., Sano, T., Kunimatsu, N., Aki, T., and Nishi, M., 2006, "Flow Instability With Auxiliary Parts in High Head Pump—Turbines," 23rd IAHR Symposium on Hydraulic Machinery and Systems, Yokohama, Japan, Paper No. F307.
[23] Vekve, T., 2004, "An Experimental Investigation of Draft Tube Flow," Ph.D. thesis, Norwegian University of Science and Technology, Trondheim, Norway.
[24] Kurokawa, J., Kajigaya, A., Matusi, J., and Imamura, H., 2000, "Suppression of Swirl in a Conical Diffuser by Use of J-Groove," 20th IAHR Symposium on Hydraulic Machinery and Systems, Charlotte, NC, Paper No. DY-01, pp. 1–10.
[25] Bosioc, A. L., Susan-Resiga, R., Muntean, S., and Tanasa, C., 2012, "Unsteady Pressure Analysis of a Swirling Flow With Vortex Rope and Axial Water Injection in a Discharge Cone," ASME J. Fluids Eng., **134**(8), p. 081104.
[26] Nishi, M., and Liu, S., 2013, "An Outlook on the Draft-Tube-Surge Study," Int. J. Fluid Mach. Syst., **6**(1), pp. 33–48.
[27] Farhat, M., Avellan, F., and Seidel, U., 2002, "Pressure Fluctuation Measurements in Hydro Turbine Models," 9th International Symposium on Transport Phenomena and Dynamics of Rotating Machinery, Honolulu, HI, pp. 1–6.

---

[2]www.svc.nu

[28] Kobro, E., 2010, "Measurement of Pressure Pulsation in Francis Turbines," Ph.D. thesis, Norwegian University of Science and Technology, Trondheim, Norway.

[29] Trivedi, C., Cervantes, M. J., Gandhi, B. K., and Dahlhaug, O. G., 2013, "Experimental and Numerical Studies for a High Head Francis Turbine at several Operating Points," ASME J. Fluids Eng., 135(11), p. 111102.

[30] Trivedi, C., Cervantes, M. J., Gandhi, B. K., and Dahlhaug, O. G., 2014, "Experimental Investigations of Transient Pressure Variations in a High Head Model Francis Turbine During Start-Up and Shutdown," J. Hydrodyn., 26(2), pp. 277–290.

[31] Houde, S., Fraser, R., Ciocan, G., and Deschênes, C., 2012, "Part 1—Experimental Study of the Pressure Fluctuations on Propeller Turbine Runner Blades During Steady-State Operation," 26th IAHR Symposium on Hydraulic Machinery and Systems, Beijing, Paper No. 022004.

[32] Houde, S., Fraser, R., Ciocan, G., and Deschênes, C., 2012, "Experimental Study of the Pressure Fluctuations on Propeller Turbine Runner Blades: Part 2, Transient Conditions," Earth Environ. Sci., 15, p. 062061.

[33] Amiri, K., 2014, "An Experimental Investigation of Flow in a Kaplan Runner: Steady-State and Transient," Licentiate thesis, Luleå University of Technology, Luleå, Sweden.

[34] Ciocan, G. D., Avellan, F., and Kueny, J. L., 2000, "Optical Measurement Techniques for Experimental Analysis of Hydraulic Turbines Rotor–Stator Interaction," ASME Paper No. FEDSM2000-11056.

[35] Iliescu, M. S., Ciocan, G. D., and Avellan, F., 2002, "3D PIV and LDV Measurements at the Outlet of a Francis Turbine Draft Tube," ASME Paper No. FEDSM2002-31332.

[36] Susan-Resiga, R., Ciocan, G. D., Anton, L., and Avellan, F., 2006, "Analysis of the Swirling Flow Downstream a Francis Turbine Runner," ASME J. Fluids Eng., 128(1), pp. 177–189.

[37] Gagnon, J. M., Deschenes, C., Ciocan, G. D., and Iliescu, M., 2008, "Numerical Simulation and Experimental Investigation of the Flow in an Axial Turbine," 24th IAHR Symposium on Hydraulic Machinery and Systems, Foz Do Iguassu, Brazil, Paper No. IAHR 096.

[38] Gagnon, J. M., Aeschlimann, V., Houde, S., Flemming, F., Coulson, S., and Deschenes, C., 2012, "Experimental Investigation of Draft Tube Inlet Velocity Field of a Propeller Turbine," ASME J. Fluids Eng., 134(10), p. 101102.

[39] Gouin, P., Deschenes, C., Iliescu, M., and Ciocan, G. D., 2009, "Experimental Investigation of Draft Tube Flow of an Axial Turbine by Laser Doppler Velocimetry," 3rd IAHR International Meeting of the Workgroup on Cavitation and Dynamic Problems in Hydraulic Machinery and Systems, Brno, Czech Republic, pp. 87–97.

[40] Mulu, B., 2012, "An Experimental and Numerical Investigation of a Kaplan Turbine Model," Ph.D. thesis, Luleå University of Technology, Luleå, Sweden.

[41] Mulu, B. G., Jonsson, P. P., and Cervantes, M. J., 2012, "Experimental Investigation of a Kaplan Draft Tube—Part I: Best Efficiency Point," Appl. Energy, 93, pp. 695–706.

[42] Jonsson, P., 2011, "Flow and Pressure Measurements in Low-Head Hydraulic Turbines," Ph.D. thesis, Luleå University of Technology, Luleå, Sweden.

[43] Müller, A., Bullani, A., Dreyer, M., Roth, S., Favrel, A., Landry, C., and Avellan, F., 2012, "Interaction of a Pulsating Vortex Rope With the Local Velocity Field in a Francis Turbine Draft Tube," 26th IAHR Symposium on Hydraulic Machinery and Systems, Beijing, Paper No. 032040.

[44] Aeschlimann, V., Beaulieu, S., Houde, S., Ciocan, G., and Deschênes, C., 2013, "Inter-Blade Flow Analysis of a Propeller Turbine Runner Using Stereoscopic PIV," Eur. J. Mech. B, 42, pp. 121–128.

[45] Lemay, S., Aeschlimann, V., Fraser, R., Fraser, R., Ciocan, G. D., and Deschênes, C., 2015, "Velocity Field Investigation Inside a Bulb Turbine Runner Using Endoscopic PIV Measurements," Exp. Fluids, 56(6), p. 120.

[46] Mulu, B. G., Cervantes, M. J., Devals, C., Vu, T. C., and Guibault, F., "Simulation-Based Investigation of Unsteady Flow in Near-Hub Region of a Kaplan Turbine With Experimental Comparison," Eng. Appl. Comput. Fluid Mech., 9(1), pp. 139–156.

[47] Marcinkiewicz, J., and Svensson, L., 1994, "Modification of the Spiral Casing Geometry in the Neighbourhood of the Guide Vanes and Its Influence on the Efficiency of a Kaplan Turbine," XVII Symposium on Hydraulic Machinery and Cavitation, Beijing, pp. 429–434.

[48] George, W. K., 1975, "Limitations to Measuring Accuracy Inherent in the Laser Doppler Signal," Proceedings of the LDA-Symposium, Denmark, Copenhagen, pp. 20–63.

[49] Zhang, Z., Eisele, K., and Hirt, K., 1997, "The Influence of Phase-Averaging Window Size on Determination of Turbulence Quantities in Unsteady Turbulent Flows," Exp. Fluids, 22(3), pp. 265–267.

[50] Glas, W., Forstner, M., Kuhn, K., and Jaberg, H., 2000, "Smoothing and Statistical Evaluation of Laser Doppler Velocimetry Data of Turbulent Flows in Rotating and Reciprocating Machinery," Exp. Fluids, 29(5), pp. 411–417.

[51] Nicolle, J., Labbe, P., Gauthier, M., and Lussier, M., 2010, "Impact of Blade Geometry Differences for the CFD Performance Analysis of Existing Turbines," IOP Conference Series: Earth and Environmental Science, Timisoara, Romania, Paper No. 012028.

[52] Vu, T. C., Koller, M., Gauthier, M., and Deschenes, C., 2010, "Flow Simulation and Efficiency Hill Chart Prediction for a Propeller Turbine," IOP Conference Series: Earth and Environmental Science, Timisoara, Romania, Paper No. 012040.

Paper C

Experimental Study on Flow Asymmetry after the Draft Tube Bend of a Kaplan Turbine

Reprinted with permission

EXPERIMENTAL STUDY ON FLOW ASYMMETRY
AFTER THE DRAFT TUBE BEND OF
A KAPLAN TURBINE

**Kaveh Amiri[1,*], Berhanu Mulu[2], Mehrdad Raisee[3] and
Michel J. Cervantes[1,4]**

[1]Department of Engineering Science and Mathematics
Luleå University of Technology
Luleå, Sweden
e-mail: kaveh.amiri@ltu.se

[2]Vattenfall AB
Älvkarleby, Sweden

[3]School of Mechanical Engineering
College of Engineering
University of Tehran
P.O. Box: 11155-4563
Tehran, Iran

[4]Department of Energy and Process Engineering
Water Power Laboratory
Norwegian University of Science and Technology
Trondheim, Norway

*Corresponding author

Communicated by Shahrdad G. Sajjadi

Abstract

Flow condition in a Kaplan turbine draft tube is investigated using laser Doppler anemometry (LDA) and particle image velocimetry (PIV). The investigated draft tube is composed of a cone followed by an elbow and a straight diffuser. The three velocity components were measured after the elbow at two different locations across the straight diffuser to quantify the flow asymmetry as well as the secondary flows formed in this region. The velocity profiles at the draft tube inlet are measured using a 2D LDA system allowing estimation of the draft tube inlet swirl. The results are presented at three operating points of the turbine. The flow condition after the draft tube bend was shown to be highly dependent on the vortex structures within the straight draft tube; namely Dean vortices and the swirl leaving the runner. At operating points with high flow rates and low swirl, Dean vortices dominate the upstream swirl; a symmetric but inhomogeneous flow resembling flow after a pipe bend forms within the straight diffuser. At part load operating points with high swirl and low flow rate, the flow after the bend is dominated by the upstream swirl resulting in asymmetric flow after the draft tube bend. The flow asymmetry is shown to be a 2nd order function of the swirl-to-Dean ratio.

Notation

The following symbols are used in this paper:

A Area

D Runner diameter of turbine model

D_b Pipe diameter

De Dean number

f^* Dimensionless frequency with respect to runner rotational frequency

g Gravitational acceleration

H Head during model test

n Runner rotational speed

n_{ED}	Turbine reduced speed
P_m	Output power
Q	Model flow rate
Q_{ED}	Turbine reduced flow rate
r	Radius
R_c	Bend radius
R_t	Tip radius
R_h	Hub radius
Re	Turbine Reynolds number
Sw	Swirl number
U	Axial velocity inside draft tube
u	rms of axial velocity
U_a	Axial velocity at the runner outlet
U_θ	Tangential velocity at the runner outlet
V	Lateral velocity inside draft tube
v	rms of lateral velocity
W	Vertical velocity inside draft tube
X	Axial direction inside draft tube
Y	Lateral direction inside draft tube
Z	Vertical direction inside draft tube
α_{GV}	Guide vane angle
η	Turbine efficiency
μ	Dynamic viscosity
ν	Kinematic viscosity
ρ	Fluid density

Superscripts

  *   Made dimensionless using reference velocity, runner diameter
             or runner frequency in case of velocity, dimension or
             frequency, respectively.

1. Introduction

Draft tube is an important part of reaction turbines. From fluid dynamics perspective, draft tube is a diffuser converting the kinetic energy of the flow leaving the runner to pressure and increases the effective head of the turbine. It is usually composed of a conical diffuser, an elbow and a straight diffuser, see Figure 1. Most of the pressure recovery, up to 70%, occurs in the conical diffuser of hydraulic turbines, also named draft tube cone. The elbow has usually a converging cross section to avoid separation on its inner section due to the centrifugal forces induced to the flow by the elbow curvature. A straight diffuser follows the elbow ejecting the flow to the tailrace water.

In low head reaction turbines, i.e., propeller and Kaplan, the turbine efficiency is significantly affected by the performance of the draft tube because the kinetic energy leaving the runner is a substantial part of the available head [17]. At the same time, numerical and experimental investigation of the flow inside the draft tubes is a challenge for researchers due to the flow complexity. Adverse pressure gradient, highly unsteady large scale vortices, turbulence, separation, pulsating and swirling flow can be mentioned as some of the main challenges. Moreover, the runner hub in the middle of the draft tube inlet as a rotating bluff body affects the flow condition inside the draft tube. The large dimensions of prototypes are another challenge for performing accurate measurements and numerical simulations. Thus, studying the scaled model of the turbines is a common tool to investigate reaction turbines.
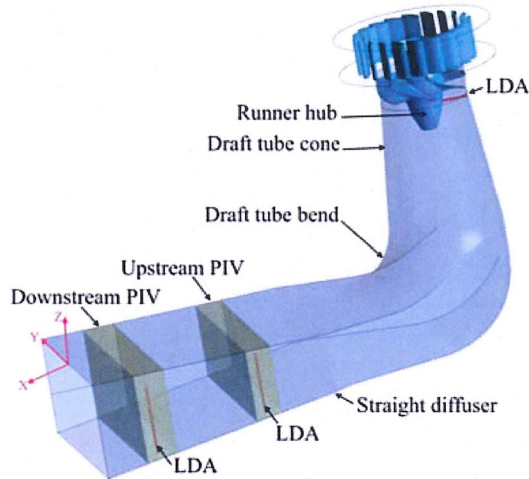
Figure 1. Schematic of the draft tube with the measurement sections (the green areas show the PIV measurement sections and the red lines show the LDA measurement sections.

Different measurement techniques have been used to analyse the flow inside the draft tube of turbine models. Draft tube wall pressure measurements may be referred as the oldest method used for draft tube flow investigation. The pressure recovery and pulsations of turbine models at different operating conditions are the main issues addressed in such studies [10, 13, 17-20]. Special attentions have also been dedicated to the draft tube surge phenomenon and the formation of the rotating vortex rope (RVR) [2, 3]. Optical based velocity measurement techniques, LDA and PIV, have also been used to investigate flow condition within the draft tube of reaction turbines. However, PIV technique has widely been used to investigate flow condition inside the draft tube cone where most of the pressure recovery occurs [7, 10, 12, 15]. LDV measurements have also been performed at the inlet of the draft tubes. Gagnon et al. [6] performed LDV measurements at the entrance of the draft tube cone to study the velocity fluctuations at the runner outlet of a propeller turbine. Flow development along the draft tube cone of a Kaplan turbine was investigated at on-design and off-design operating points [1, 13, 4].

Despite of the numerous studies on flow investigation within the draft tube of reaction turbines, flow condition after the elbow has rarely been

investigated. Gubin et al. [9] investigated flow asymmetry at the outlet of the draft tube of a Kaplan turbine at different operating points and with different geometries of the draft tube. The results showed that the asymmetry in the axial velocity is a function of the swirl entering the draft tube. The results indicated that in case of a positive swirl (co-rotating with the runner), most of the turbine discharge enters the left side of the straight diffuser in their test case. A larger portion of the discharge enters the right side of the draft tube when a negative swirl is imposed to the flow at the draft tube entrance. The greater the swirl at the draft tube entrance was, the greater the discharge non-uniformity was over the cross section of the draft tube outlet. An extensive work was performed by Arpe and Avellan [5] to characterize the pressure fields on the pierced draft tube walls of a Francis turbine model. The results showed the presence of asymmetric flow after the draft tube bend; the flow rate passing through the left part of the draft tube can be larger or smaller than the other half depending on the turbine operating condition. 3D-PIV and LDA measurements at the outlet of the draft tube confirmed the flow asymmetry at the draft tube outlet and the presence of secondary flows at this measurement section [11]. Such non-uniform flow distribution increases the turbine losses and decreases the turbine efficiency.

Although the flow asymmetry within straight draft tubes is reported in different studies, the physical mechanism behind this phenomenon is not understood yet. Despite the fact that the complex geometry of water turbine draft tubes contributes in the flow condition within the draft tube by inducing adverse pressure gradient, changing the cross section shape of the draft tube streamwise, etc., the flow condition after a 90° pipe bend can be used as a guideline to interpret the physical phenomenon. Such flows are studied more in detail due to their applications in human respiratory and blood systems as well as industrial systems like nuclear power plants. Kalpakli and Örlü [14] performed stereoscopic PIV after a 90° pipe bend and investigated the effect of swirl intensity of a rigid body swirl at the pipe inlet on the flow condition after the bend. The results showed that increasing the swirl number unsettles the symmetry of the Dean vortices after the bend. Moreover, asymmetric axial velocity forms at this location resulting in higher flow rate through

the half part of the bend where the dominating Dean vortex is formed. The dominating vortex moves towards the dominated one, pushes it to the side wall and finally removes it from the flow while the swirl number increases.

The current study presents the results of 2D PIV and LDA measurements performed inside the draft tube of a Kaplan turbine, allowing the determination of the 3 velocity components. The three velocity components were obtained at 2 different locations across the straight diffuser; downstream of the draft tube bend and a section close to the draft tube outlet shown in Figure 1. Axial and tangential velocity components were measured at the runner outlet of the investigated turbine using 2D LDA system; the measurement section is shown in Figure 1. Three operating points were selected to investigate the effects of the turbine operating condition on the draft tube performance. The results shed light on the physical phenomena resulting in asymmetric flow after the draft tube bend of reaction turbines captured in the previous studies and the most important parameters affecting the flow asymmetry.

2. Experimental Setup

2.1. Model specification and operating conditions

Velocity measurements were performed in the draft tube of a 1:3.1 scaled model of a Kaplan turbine called *Porjus U9*. The model runner diameter is $D = 0.5m$ and its hub to tip ratio is 0.52. The operational net head during all measurements was $H = 7.5m$. The penstock, having a 90° elbow to mimic the prototype flow condition, supplies water to the spiral casing with a distributor consisting of 20 guide vanes and 18 stay vanes. The flow rate through the turbine can be controlled by changing the guide vanes angle while the turbine operates in off-cam mode, i.e., the runner blades angle is constant. Another effect of changing the guide vanes angle while turbine operates at off-cam is variation in the flow swirl at the draft tube entrance. The runner is composed of 6 blades and an elbow type draft tube is installed after the runner. The runner rotational speed during the measurements was independent of the turbine operating condition and equal to $N = 696.3rpm$.

The model was investigated at the best efficiency point (BEP) of the turbine as well as at two operating points with higher and lower flow rates than the one at the BEP, namely high load (HL) and part load (PL), respectively. The operating parameters at each operating point are shown in Table 1. The presented parameters in the table are defined as:

$$\eta_{ED} = \frac{nD}{\sqrt{gH}}, \tag{1}$$

$$Q_{ED} = \frac{Q}{D^2\sqrt{gH}}, \tag{2}$$

$$Re = \frac{QD}{\vartheta A}, \tag{3}$$

$$\eta = \frac{P_m}{\rho gHQ}, \tag{4}$$

where η_{ED} is turbine's reduced speed, Q_{ED} is reduced flow rate, Re is the turbine's Reynolds number based on the turbine's flow rate and the draft tube inlet area, and η is the turbine efficiency. All the other variables are defined at the end of the paper. n is turbine rotational frequency, D is runner diameter, g is the gravitational acceleration, H is the turbine head, Q is the flow rate through the turbine, ϑ is the kinematic viscosity, A is the area, P_m is the turbine mechanical power and ρ is the fluid density.

Dean number is used to characterize flows in curved pipes:

$$De = \frac{\rho QD_b}{A\mu}\sqrt{\frac{D_b}{2R_c}}, \tag{5}$$

where μ is the dynamic viscosity, D_b is the pipe diameter and R_c is the bend radius. The Dean number is the product of the Reynolds number and curvature ratio, i.e., the ratio of the product of the inertia and centrifugal forces to the viscous forces. Since secondary flow after a bend is induced by centrifugal forces and their interaction primarily with viscous forces, the Dean number is a measure of the magnitude of the secondary flow [21]. In

the current case study, the flow passage area through the bend changes from a circular section at the bend entrance to a rectangular cross section at its outlet. Since the centers of curvature of the inner and outer walls of the bend do not coincide, the above definition for the Dean number is not applicable in the current case. The presented numbers in Table 1 are based on the average of the hydraulic diameter at the bend inlet and outlet and the average of the curvature radii of the inner and outer walls of the bend.

Table 1. Operating condition parameters

Operating point		Part load	BEP	High load
Guide vane angle	α_{GV} (deg)	20	26.5	32
Volume flow rate	Q (m^{3}s^{-1})	0.62	0.71	0.76
Reduced flow rate	Q_{ED} (-)	0.281	0.322	0.345
Reduced speed	n_{ED} (-)	0.676	0.676	0.676
Reynolds number	Re (-)	1.56×10^6	1.8×10^6	1.93×10^6
Relative efficiency to BEP	$\eta - \eta_{BEP}$ (%)	−5.6	0.0	−1.6
Dean number	De (-)	7.92×10^5	9.07×10^5	9.71×10^5

2.2. Test rig

The model measurements were performed in Vattenfall R&D model test facility at Älvkarleby, Sweden. The test rig is a closed loop system designed for testing of Kaplan, bulb and Francis turbines. Figure 2 shows the sketch of the test rig while Porjus U9 model is installed between the upstream and downstream pressure tanks. The uncertainties in the flow rate and hydraulic efficiency measurements are ±0.132% and ±0.19%, respectively. The head of the turbine model is set by adjusting the pumps rotational speed, the pressure in the upstream high pressure tank and downstream low pressure tank. The possibility to independently adjust the pressure in the upstream and downstream tanks makes it possible to perform the measurements either with or without cavitation. The current measurements were performed under cavitation free condition.
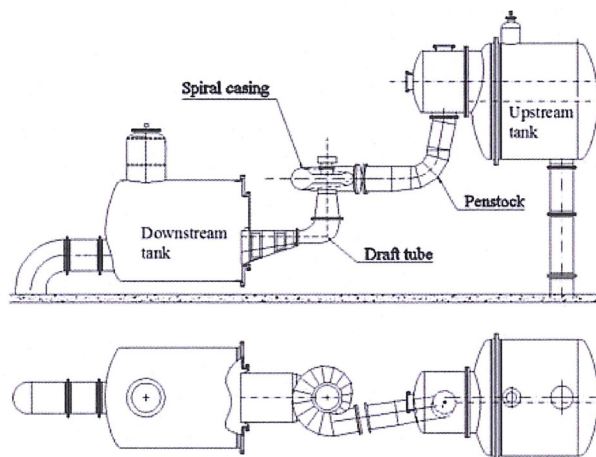
Figure 2. Side and top view of the test rig with installed Porjus U9 model.

2.3. Instruments and measurement techniques

PIV measurements were performed after the bend of the draft tube as well as at a section close to the draft tube outlet. The measurement sections are shown with green areas in Figure 1. The PIV measurements at each section were performed on a net formed by three horizontal planes and five vertical planes covering an area of 1270mm × 375mm (lateral and vertical directions) in the upstream window and 1270mm × 485mm in the downstream window. Each horizontal measurement plane was divided into eleven sub-windows measuring the axial and lateral velocities. Each vertical measurement plane was also divided into three sub-windows measuring the axial and vertical velocities. This results in 96 PIV measurements at each operating point. The measurement results are stitched together to visualize velocity distribution within the draft tube.

PIV system from Dantec was used during the measurements. Two Nd:YAG 400mJ/pulse lasers were used to generate pulsed light sheets with thickness of ~3mm. The pulse duration was 4ns. The illuminated area was visualized by a CCD FlowSense EO 4M camera with resolution of 2048 × 2048 pixels. The time between the paired images was set to 200-300μs as function of the investigated operating point and the

measurement location. The seeding particles consisted of Expancel 461 WU 20 powder with an average diameter of 6μm. One thousand pairs of images were recorded with a sampling rate of 10Hz at each measurement. The spatial resolution of the velocity measurements is approximately $2\text{mm} \times 2\text{mm}$.

A two-component LDA system with an 85mm optical fiber probe from Dantec was used to measure the velocity distribution along two vertical lines in the middle of the PIV measurement sections. The measurement sections are located in the middle of the windows and 136mm inside the draft tube presented with red lines in Figure 1. A front lens with 310mm focal length was employed during the measurements. Triangular laser beam configuration was used to allow measurements close to the draft tube wall. The measuring volume size based on the e^{-2} Gaussian intensity cut-off point was estimated to be $0.85 \times 0.097\text{mm}$ and $0.91 \times 0.1\text{mm}$ for the axial and vertical components, respectively. The velocity measurements were performed in burst and coincidence mode; one velocity pair was recorded for each passing particle through the control volume. The sampling time at each measurement point was set to 300s. This sampling time corresponded to a range of 50,000-210,000 velocities recorded at each measurement point. Similar seeding particles as the one used for the PIV measurements were used for the LDA measurements.

The LDA system was also used to measure axial and tangential velocities at the runner outlet along the radius marked with RC in Figure 3. RC is located 137mm below the runner hub center. A window with a diameter of 50mm and a thickness of 12.7mm composed of high-quality glass was installed on the draft tube cone wall to provide the required optical accesses for the LDA measurements. The sampling time at each measurement point was set to 600s. This sampling time corresponded to a range of 130,000-500,000 velocities recorded at each measurement point at the runner outlet depending on the radial coordinate. The higher sampling time is required to resolve the measurements angularly, i.e., resolve the blades wakes. Such

resolution is not necessary in the straight diffuser as the blade wakes have diffused.
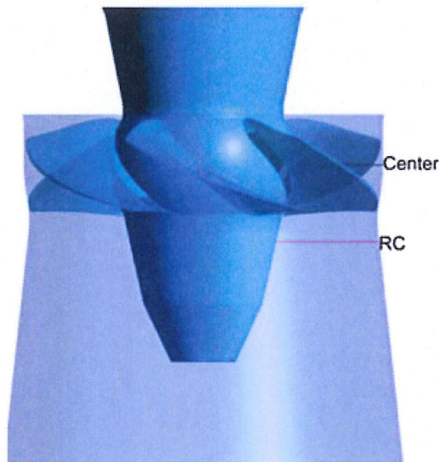
Figure 3. LDA measurement location at the runner outlet.

3. Data Analysis

The commercial PIV software, dynamics studio from Dantec dynamics, was used for image processing and PIV data analysis. Adaptive correlation scheme with two refinement steps and 50% overlap between the adjacent windows was applied on the acquired data after performing calibration. Although the draft tube optical accesses were composed of flat glasses with parallel surfaces, 2D calibration target was used for calibration to compensate the perspective effects on the acquired images. Each PIV measurement section was divided into 48 measurement windows composed of 33 horizontal windows and 15 vertical ones as discussed in Subsection 2.3. All the results from the measurement windows were stitched together to present the flow condition inside the draft tube. Each presented velocity contour plot consists of the results of 96 PIV measurements stitched together.

Time-weighted average velocities based on the residence time of the bursts were used to calculate the mean velocities measured with the LDA system, which reduces the bias [8]. Spectral analysis of the LDA signals was conducted as proposed by Mulu et al. [17]. The randomly distributed velocity

measurement results in the time domain were resampled through a linear interpolation. Welch's method with a Hanning window was then applied to the resampled data for the spectral analysis. The dominant frequency and harmonics calculated by this method are expected to be similar to those identified by the Lomb-normalized periodogram method, where evenness of the acquired data is not mandatory [17].

4. Uncertainty Analysis

The total uncertainty in a measurement can be found by combining the random and systematic errors. LDA measurements exhibit multiple types of error sources; a detailed description of these error sources can be found in Mulu [16]. Among many sources leading to bias in LDA measurements, velocity fluctuations have been concerned to play a primary role [22]. It arises from the mechanism that the high velocity particles will be more frequently sampled than the low velocity ones. Weighting method based on the particles residence time was used to correct the velocity bias. The velocity bias associated with other sources of bias like fringe distortion and special velocity gradient effects is considered to be negligible during this measurement due to the high accuracy in adjusting the normality of the laser beams to the optical access windows and low velocity gradients within the measurement section. The normality of the LDA probe to the window was measured using optical methods and exhibited an accuracy of $0.02°$, which correspond to an accuracy of 0.03%.

The precision (random) error of the LDA measurements was estimated by a repeatability test at randomly selected positions with a 95% confidence level. The maximum total uncertainty in the measurements performed at the runner outlet for most of the measurement locations with different operational points was less than 0.71% for the axial velocity and 0.88% for the tangential velocity component. However, close to the hub and tip, the total measurement uncertainty at a 95% confidence interval was within 2.1% at different operating points. The maximum uncertainties were found to be at PL operating point. The accuracy of the traverse used for the LDA measurements was 0.01mm. The maximum uncertainties estimated for the

axial and lateral velocity components measured after the draft tube bend were 0.3% and 0.6%, respectively. The LDA measurement after the draft tube bend was performed to check the validity of the PIV measurements.

The PIV measurement uncertainties with 95% confidence level were estimated by performing repeatability tests at some sections while turbine was operating at the PL. This operating point showed to have maximum uncertainties. The uncertainties associated with the axial, lateral and vertical velocities were found to be less than 0.05, 0.01 and 0.005m/s, respectively. These correspond to 4.5%, 15% and 7% uncertainties in the axial, lateral and vertical velocities, respectively. The high percentage of the uncertainties in the lateral and vertical velocities is related to the low velocity magnitudes in these directions. The accumulated mean values for each measurement were checked to assure statistical convergence of the acquired data recorded by PIV and LDA systems.

5. Results and Discussion

This section presents the velocity measurement results acquired at the three measurement sections for each operating point; LDA measurements at the runner outlet and the measurements within the straight diffuser. The velocities are made dimensionless with respect to the reference velocity calculated from the volume flow rate at the corresponding operating point and the runner diameter. All the geometrical dimensions are made dimensionless with respect to the runner diameter. The dimensionless parameters are marked with superscript (*) in the following sections.

5.1. High load

Figure 4 shows the time-averaged velocity profiles measured at the runner outlet at HL. U_a^* and U_θ^* are the normalized axial and tangential velocity components, respectively. The axial velocity at the runner outlet is almost constant at all radii except close to the blade endings. The axial velocity increases near the hub due to the hub clearance effects. The axial velocity profile is in agreement with the measurement results performed

inside the draft tube downstream of the runner hub presented by Mulu et al. [17]. The results showed that the axial velocity is nearly constant in the outer part of the draft tube. The axial velocity at their measurement location (~190mm downstream compared with the current measurement section) is approximately 30% lower compared with the current measurement results due to the decelerating effect of the draft tube cone. The tangential velocity linearly increases with the radius in the mid-part of the blades and resembles a solid body rotation; similar to the tangential velocity at the outer part of the draft tube in the results presented by Mulu et al. [17]. Detailed discussion about the secondary flows formed at the runner outlet is presented by Amiri [1], Mulu et al. [17], Jonsson et al. [13] and Amiri et al. [4].

The LDA measurement results at the runner outlet are used to calculate the swirl number at the runner outlet, i.e., the beginning of the draft tube cone. It should be noted that the swirl within the draft tube cone is slightly different from the one calculated from the current LDA measurements because of the presence of the runner hub at the measurement location. The rotating hub induces some positive swirl to the flow within the draft tube, however, since the runner rotational speed is constant in all investigated points, it can be assumed that the effect of the rotating hub on the swirl number is closely similar in all cases. The swirl number is defined as:

$$Sw = \frac{\int_{R_h}^{R_t} U_a U_\theta r^2 dr}{(R_t - R_h) \int_{R_h}^{R_t} U_a^2 r dr},$$

(6)

where Sw is the swirl number at the measurement section, U_a and U_θ are the axial and tangential velocity components, respectively, r is the radius at the measurement location and R_h and R_t are the runner hub and runner tip radii, respectively. The calculated swirl number at the measurement location was around 0.092. This operating point has the minimum swirl at the draft tube inlet between all the three investigated operating points.
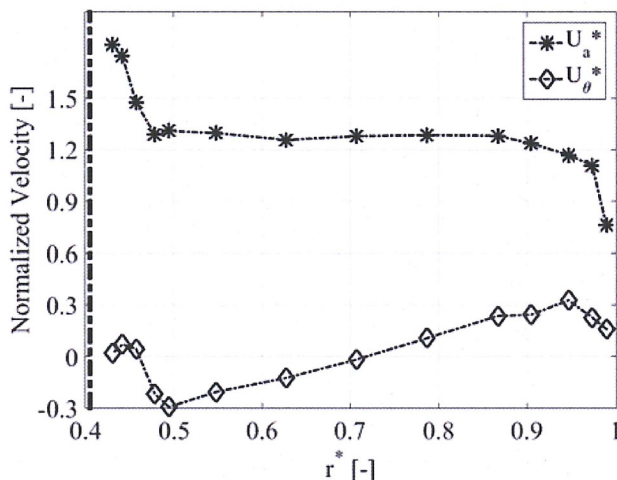
Figure 4. Axial and tangential velocity profiles at the runner outlet at HL. The vertical dashed line close to $r^* = 0.4$ shows runner hub position.

Figure 5 presents the dimensionless axial (U^*) and vertical (W^*) velocity components acquired by the LDA and PIV systems along the LDA measurement line in the downstream window shown in Figure 1. The error bars associated with the LDA measurement results represent one standard deviation of the acquired data around the mean velocity value during one set of measurement and they do not represent the measurements uncertainty. Around 68% of the acquired data are expected to lie within the error bars band due to the normal distribution of the acquired data. Comparing the PIV and LDA measurement results shows that the maximum relative error in the axial velocity measurements acquired by the two systems is 15%. The uncertainties associated with setting the test rig parameters, adjusting the probe in the measurement locations and the uncertainties in the measurement systems contribute in the deviation. However, the PIV results are in good agreement with the LDA data, showing that the PIV results are representative of the flow condition inside the draft tube. The LDA data is not captured all along the bottom to the top of the draft tube due to the restriction on the length of the LDA traverse system.
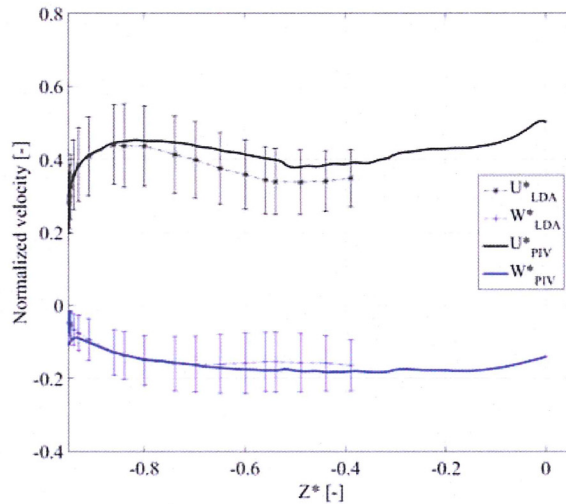
Figure 5. Normalized axial and vertical velocities acquired by PIV and LDA in the downstream window at HL.

Figure 6 presents the axial velocity contour within the draft tube at the HL operating point. This operating point has the minimum swirl $(Sw = 0.092)$ and maximum flow rate $(Q = 0.76 \text{m}^3/\text{s})$ between the investigated operating points. Illustrated in the figure, the regions with higher axial velocities, in the upstream window, are located close to the draft tube walls and the low axial velocity region is located close to the center of the straight diffuser and inner part of the bend. This resembles the flow condition after a bend in a swirl-free pipe flow where two counter-rotating vortices of similar strength, called *Dean vortices*, form after the bend. The elbow curvature induces a centrifugal force on the flowing fluid, pushing the high velocity fluid towards the pipe outer walls [14]. Dean vortices formed after a bend in a circular pipe from a non-swirling flow at the entrance of the bend are symmetrical with the same vortex strength. This results in symmetrical velocity fields in the axial, lateral and vertical directions after the bend. Figures 7(a) and 7(b) present the lateral and vertical flow velocities inside the draft tube, respectively. The black arrows in the figures present the flow direction at each measurement plane. Figure 7(c) shows the sketch of the large vortices deduced from the arrows shown in Figures 7(a) and 7(b). The results show the existence of Dean-like vortices formed after the draft tube bend. However, flow

asymmetry is present after the bend for all velocity components indicating that the Dean vortices are perturbed. Figures 7(a) and 7(c) show that the right vortex is stronger than the left one and pushes it back towards the left wall. The zero lateral velocity point, expected to be at $Y^* = 0$ under no swirl at the draft tube entrance, is shifted to $Y^* = 0.28$ in the upstream window. Moreover, unequal amount of the flow passes through the right and left half of the draft tube; 52% through the right half (looking at the flow from the draft tube outlet). The existence of such an asymmetry has previously been reported in other types of turbines, see [9, 11].
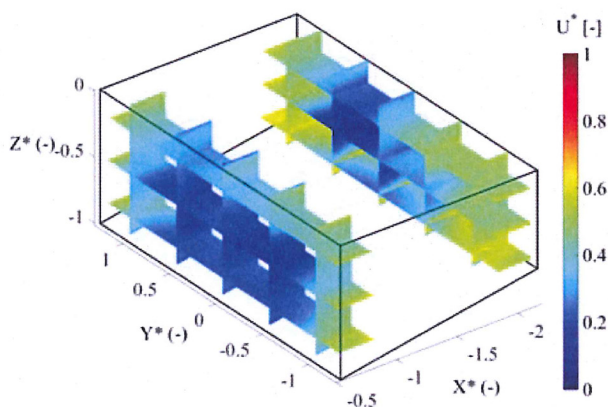
Figure 6. Axial velocity contours within the straight diffuser at HL.

The mechanism behind the formation of such vortical flow structure may be explained by analyzing the flow condition downstream a $90°$ bend pipe of circular and constant cross section. The effect of superimposed swirl on the flow in a $90°$ bend pipe was investigated by Kalpakli and Örlü [14]. Their stereoscopic PIV measurement results showed that under swirl-free condition, Dean vortices with equal strength form symmetrically after the bend and the axial velocity increases close to the outer wall. Both the axial velocity distribution and the vortices were shown to be symmetrical after the bend. When swirl was induced to the flow upstream of the bend, the symmetry of the Dean vortices was broken and the axial velocity distribution started to become asymmetrical. They showed that when a small swirl $(Sw = 0.1)$ was induced to the flow entering the bend, the swirl strength was superimposed to each of the Dean vortices. Hence, the strength of the Dean

vortex co-rotating with the upstream swirl was increased and the other one was decreased. The co-rotating vortex dominated the counter-rotating one and pushed it to the side wall. Under this condition, the high axial velocity region was still located close to the pipe walls. However, the flow passing through the half pipe cross section where the dominating vortex existed was higher.
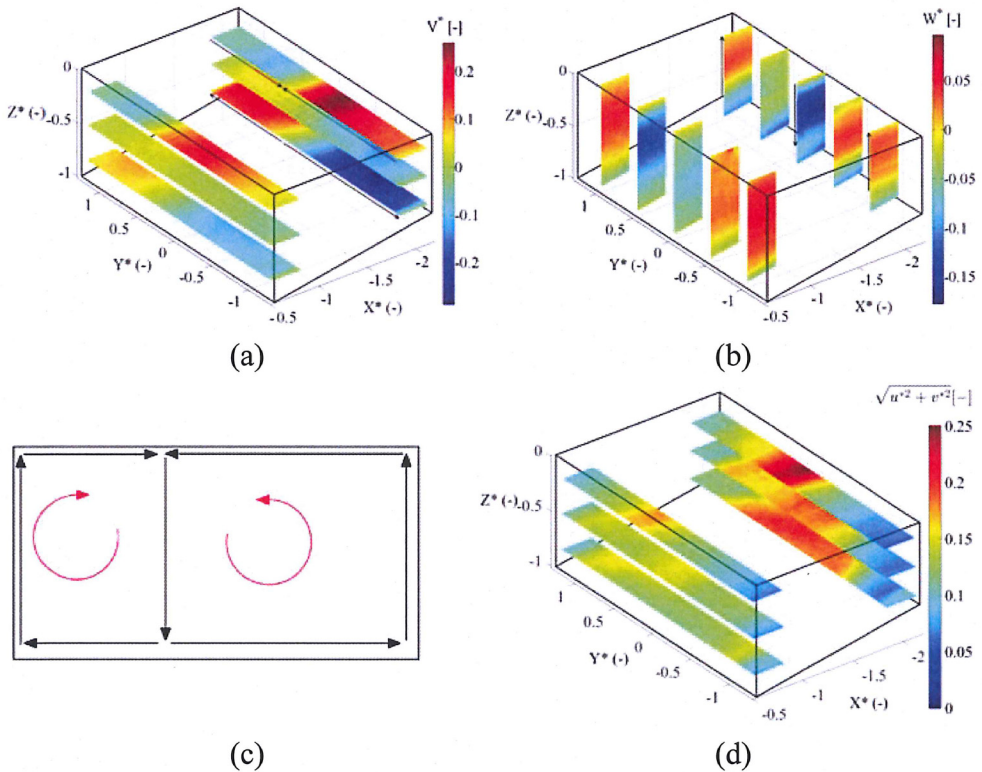
Figure 7. Velocity contours within the straight diffuser at HL: (a) lateral velocity; (b) vertical velocity; (c) schematic of the vortices formed after the draft tube bend; (d) normal Reynolds stress.

The velocity distribution after the draft tube bend at HL is qualitatively similar to the simplified case where a weak swirl ($Sw = 0.1$) is imposed to the flow at the entrance of a bend. The imposed swirl strengthens the right vortex which co-rotates with the upstream swirl and decreases the left vortex strength. The high axial velocity regions are located close to the outer walls of the draft tube straight diffuser. The portion of the flow rate passing

through the right half of the draft tube is slightly higher than the one passing through the left half.

Figure 7(d) presents the contour of the resultant normal stress in *X-Y* plane at the PIV measurement sections. The maximum Reynolds stress is captured in the upper part of the upstream PIV measurement window at $Y^* = 0.28$, i.e., where right and left Dean vortices meet each other resulting in maximum turbulence energy production. The increase in the Reynolds stress magnitude is because of the mixing effect of the Dean vortices where they meet each other. The Reynolds stress decreases in the streamwise direction. However, still the maximum value is captured where the Dean vortices meet each other.

5.2. Best efficiency point

Figure 8 shows the axial and tangential velocity profiles at the runner outlet while the turbine operates at the BEP. The main features of the velocity profiles are similar to the ones at HL operating point presented in Figure 4. The only difference is the tangential velocity magnitude which is higher at the BEP compared to the one at the HL. This results in increasing the swirl number at this operating point to 0.381.
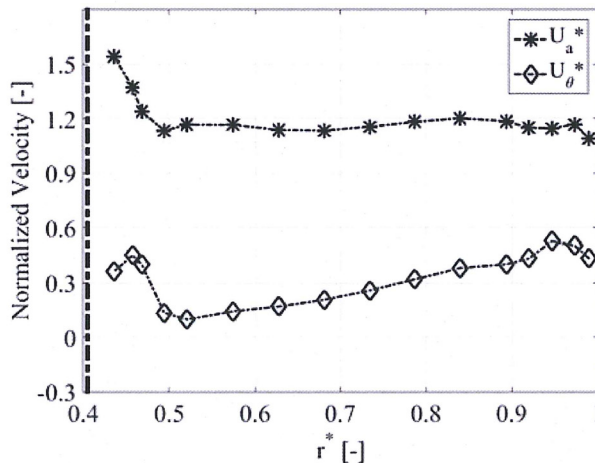
Figure 8. Axial and tangential velocity profiles at the runner outlet at the BEP. The vertical dashed line close to $r^* = 0.4$ shows the runner hub position.

Velocity distribution after the draft tube bend is also investigated at the BEP presented in Table 1. At the BEP, the flow rate entering the draft tube is lower compared with the one at the HL and Dean vortices with lower strength are expected to form after the bend. Moreover, swirl at the draft tube inlet is increased at this point compared with the one at the HL. Hence, flow condition after the draft tube bend is expected to be more affected by the upstream swirl at this operating point compared to the HL.

Figure 9 shows the contour of the axial velocity inside the straight diffuser at the BEP. Changing the turbine operating point from the HL to the BEP increased the flow asymmetry after the draft tube bend; 56% of the flow rate passes through the right half of the draft tube.
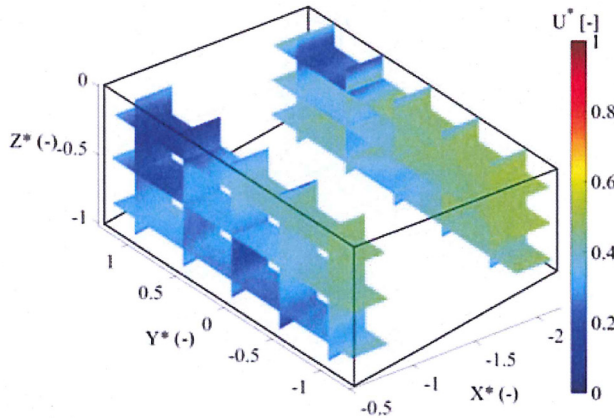
Figure 9. Axial velocity contours within the straight diffuser at the BEP.

Figures 10(a) and 10(b) present the contours of the lateral and vertical velocities within the straight diffuser, respectively. Schematic of large scale vortices after the draft tube bend, deduced from the lateral and vertical velocity contours is presented in Figure 10(c). The Dean vortices still exist after the draft tube bend. However, the larger swirl magnitude at the draft tube inlet increased the strength of the right vortex co-rotating with the upstream swirl and decreased the strength of the other vortex counter-rotating with the upstream swirl. The dominant vortex pushes the other one further to the left side of the draft tube. The zero lateral velocity line is shifted to $Y^* = 0.75$ in the upstream window. Qualitatively similar results

are reported in the simplified case of a bend pipe by Kalpakli and Örlü [14] when the swirl strength increases from 0.1 to 0.3. Their results showed that the co-rotating Dean vortex becomes stronger as the upstream swirl increases and the strength of its counter-part decreases. The stronger vortex dominates the other and pushes it further towards the pipe wall. The majority of the flow passes through the half of the pipe where the stronger swirl exists.

The maximum Reynolds stresses at both measurements section are located at the Dean vortices interface similar to the previous case, see Figure 10(d). This location is on the top left part of the draft tube.

(a)   (b)

(c)   (d)
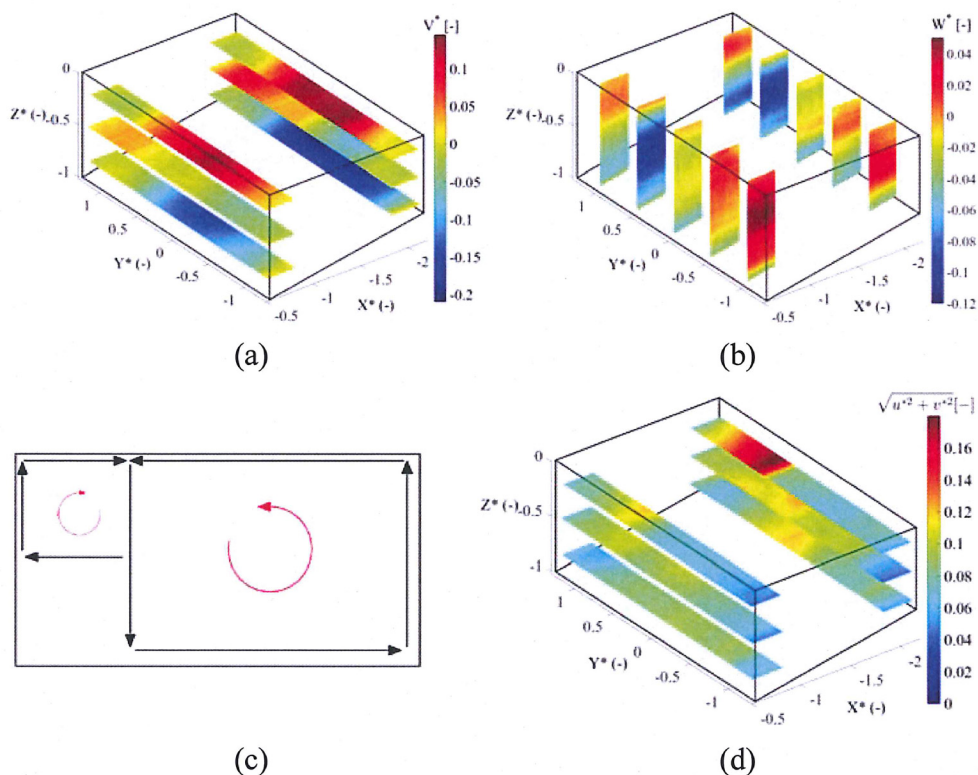
Figure 10. Velocity distribution within the straight diffuser at the BEP: (a) lateral velocity; (b) vertical velocity; (c) schematic of the vortices formed after the draft tube bend; (d) normal Reynolds stress.

5.3. Part load

The PIV measurement results performed at the PL operating point are presented in this section. Flow rate through the turbine at this operating point

is decreased by 13% compared with the BEP which results in decreasing Dean number, see Table 1.

The time-averaged velocity profiles at PL at the runner outlet are presented in Figure 11. A comparison of the velocity profiles after the runner at PL with the ones at the BEP indicates that the axial velocity profile remains nearly unchanged. However, the average tangential velocity is approximately $0.7V^*$ higher at this operating point due to the smaller guide vane angle creating a stronger swirl before the runner. The tangential velocity profile within the runner is also distorted at this operating point [4]. The velocity profile shows constant tangential velocity along the radius at this operating point compared with the two other operating points where the tangential velocity resembled nearly rigid body rotation. The consequence of the smaller guide vane angle is a larger swirl number at the runner outlet; $Sw = 1.044$ compared with 0.092 and 0.3981 at the HL and BEP, respectively.
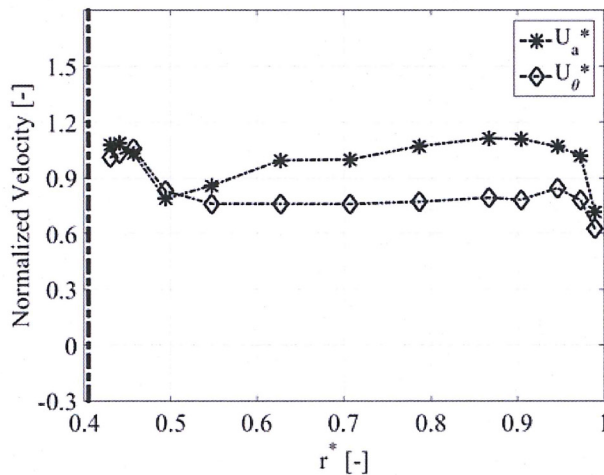
Figure 11. Axial and tangential velocity profiles at the runner outlet at PL. The vertical dashed line close to $r^* = 0.4$ shows the runner hub position.

Figure 12 shows the axial velocity contour plot within the straight diffuser. The flow asymmetry after the draft tube bend and at the draft tube outlet is larger than the one for the other operating points; 80% of the flow

now passes through the right half of the draft tube. The axial velocity in the region near the draft tube centerline is close to zero indicating the formation of a dead zone region affecting the pressure recovery of the draft tube. The flow tends to go toward the right wall of the draft tube in the streamwise direction. Nearly 40% of the flow passes through about 15% of the right part in the upstream measurement section while this ratio increases to 53% in the downstream section. This results in a more inhomogeneous flow distribution at the draft tube outlet. The existence of some regions with high local velocities leads to a poor performance of the draft tube and decreased the overall efficiency of the turbine as presented in Table 1.
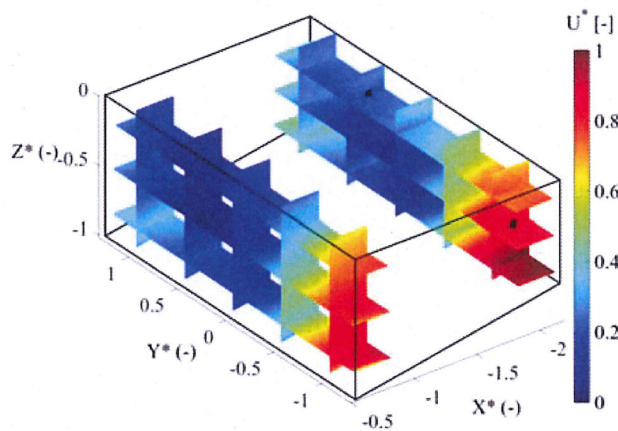
Figure 12. Axial velocity contours within the straight diffuser at the PL. The two black marks in upstream window show the locations where the frequency analysis results are presented.

Figure 13 shows the lateral and vertical velocity contours together with the sketch of the large vortices formed after the draft tube bend. Similar to the previous cases, two counter-rotating vortices are formed after the draft tube bend. Although the vortices resemble the Dean vortices after a bend, their rotational direction is opposite to the Dean vortices, i.e., the right vortex rotates in the clockwise direction and the left one rotates counter-clockwise.

The effect of the swirl on the flow after a $90°$ bend investigated by Kalpakli and Örlü [14] showed that increasing the swirl results in formation of a swirl dominated flow after the bend. The Dean vortex counter-rotating

with the upstream swirl completely disappears and the velocity field after the bend resembles a swirling flow rotating in the same direction as the upstream swirl with the vortex core being geometrically off-axis. The dominating vortex moves towards the pipe centerline with increasing the swirl number and even passes through this line at high swirl numbers. High axial velocity region forms in the other side of the pipe. The counter-rotating Dean vortex will be disappeared when the upstream swirl number reaches to 0.85.

The PIV measurement results acquired after the draft tube bend are qualitatively in agreement with the measurement results of Kalpakli and Örlü [14] with some differences related to the geometrical differences between the two cases. As discussed in Subsection 5.2, increasing the swirl at the draft tube inlet by moving from HL to the BEP resulted in the formation of a weakened clockwise vortex in the left part of the draft tube. The counter-clockwise vortex formed in the right part of the draft tube dominated the weak vortex and started to extend to the left part of the draft tube. By moving to the PL, the clockwise rotating vortex is dominated by the counter-clockwise one and disappeared. The strong vortex moves further to the left compared to the BEP and settles in the left half of the draft tube which is similar to the flow condition after a pipe bend at high swirl numbers, see Kalpakli and Örlü [14]. The counter-clockwise rotating flow hits the upper wall of the draft tube at $Y^* = 0.09$ and a secondary vortex, rotating clockwise forms on the right half of the draft tube due to the rectangular cross section of the draft tube.

Figure 13(d) presents the Reynolds stresses within the draft tube. Despite the other investigated operating points, the maximum Reynolds stress in this case is located where the bulk velocity passes through the draft tube which is located close to the bottom right part of the draft tube. This is because of the velocity fluctuations associated with the RVR formed within the draft tube cone at this operating point. The RVR induces velocity fluctuations with the frequency of $0.17 f^*$ within the draft tube as discussed in the following paragraphs. The high velocity gradient at this location contributes in increasing the Reynolds stress.

(a)

(b)

(c)

(d)
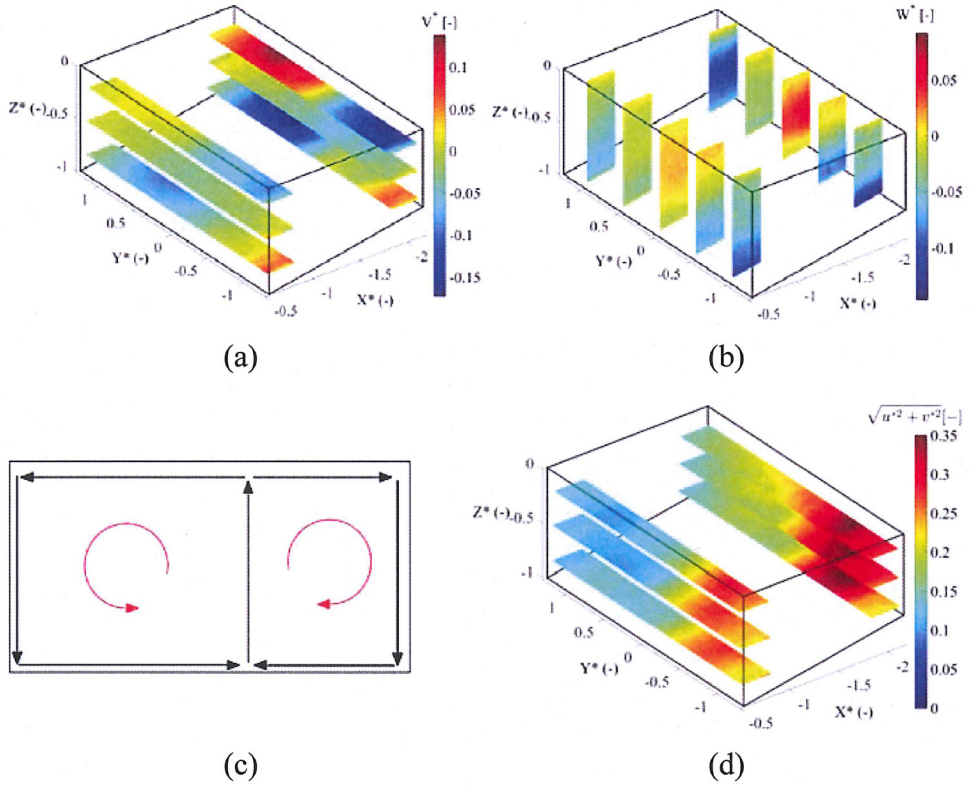
Figure 13. Velocity distribution within the draft tube at PL: (a) lateral velocity; (b) vertical velocity; (c) schematic of the vortices formed after the draft tube bend; (d) normal Reynolds stress.

Figure 14 presents the amplitude spectrum of the axial and lateral velocities at two points located after the draft tube bend, i.e., at $(2, -1, -0.4)$ and $(2, 0.5, -0.15)$ marked with black marks in Figure 12. The results at $(2, -1, -0.4)$ where the high axial velocity region exists showed that a peak at $f^* = 0.17$ dominates the spectrum in both velocity components. This frequency is related to the RVR formed inside the draft tube cone of the turbine at the part load operating point. Jonsson et al. [13] showed that vortex breakdown happens inside the draft tube cone at the PL and as a result a RVR forms. The RVR revolves with a frequency $f^* = 0.17$ around the draft tube cone centerline. Frequency analysis of the axial and lateral velocity components in the low axial velocity region showed that the flow oscillations

do not exist in such regions. For instance, the amplitude spectrums of the velocity components at (2, 0.5, –0.15) are shown in Figure 14. Hence, special attention should be paid to the regions with high flow rate during the structural design of draft tube to suppress crack propagation due to the RVR fluctuations which may happen in machines operated for long periods at PL.
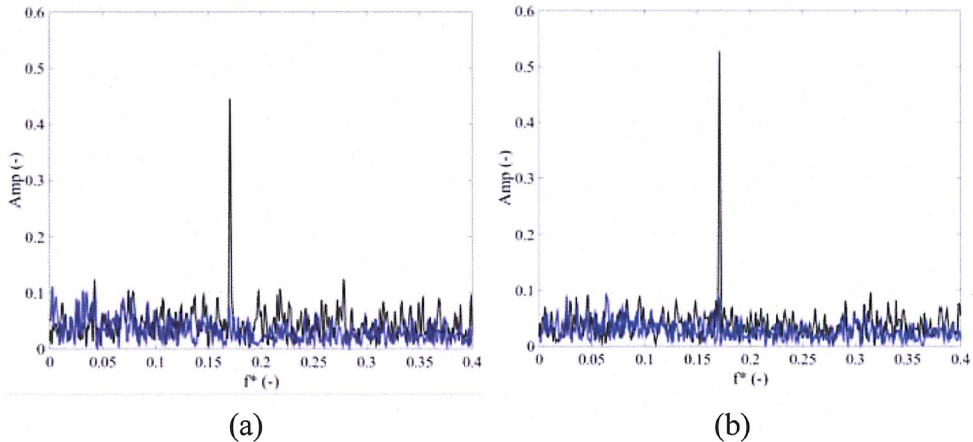
(a) (b)

Figure 14. Amplitude spectrum of the velocities within the draft tube at PL: (a) axial velocity; (b) lateral velocity. Black: at (2, –1, –0.4); Blue: at (2, 0.5, –0.15).

In summary, flow investigation at the three operating points of the turbine showed that the flow condition after the draft tube bend can be characterized by the secondary flows. The main vortices formed at this location which dominates the flow condition are the result of a combination of the Dean vortices and the swirl leaving the runner. The relative intensity of the above mentioned swirling flows can be used to determine the flow condition and specifically flow asymmetries after the elbow. The Dean number is a dimensionless parameter which is representative of the intensity of the Dean vortices. The swirl intensity at the runner outlet can be quantified by the swirl number. Figure 15(a) presents the flow rate ratio passing through the right half of the draft tube as a function of swirl-to-Dean ratio. It is assumed that the flow after the bend is completely symmetric in case of no swirl at the draft tube inlet. The results show that the flow asymmetry can be estimated as a 2nd order polynomial of the swirl-to-Dean ratio. However, the

2nd order curve shows some discrepancy with the measurement results at low swirl numbers. This is due to the fact that the swirl entering the draft tube is higher than the measured values after the runner because of the induced swirl to the flow by the rotating hub of the runner.

Jonsson et al. [13] measured swirl number inside the draft tube outlet of the model beneath the runner hub. Figure 15(b) shows the flow asymmetry within the draft tube as a function of swirl-to-Dean ratio using results of Jonsson et al. [13]. The measurement data shows really good agreement between the measurement results and the 2nd order polynomial fitted to the results when the runner hub effect on the swirl is considered. The swirl numbers measured in the middle of the draft tube cone and at its end showed the same results. In all cases, the flow asymmetry is a 2nd order function of the swirl-to-Dean ratio and the fitted curve meets the y-axis at 50%.

(a)   (b)
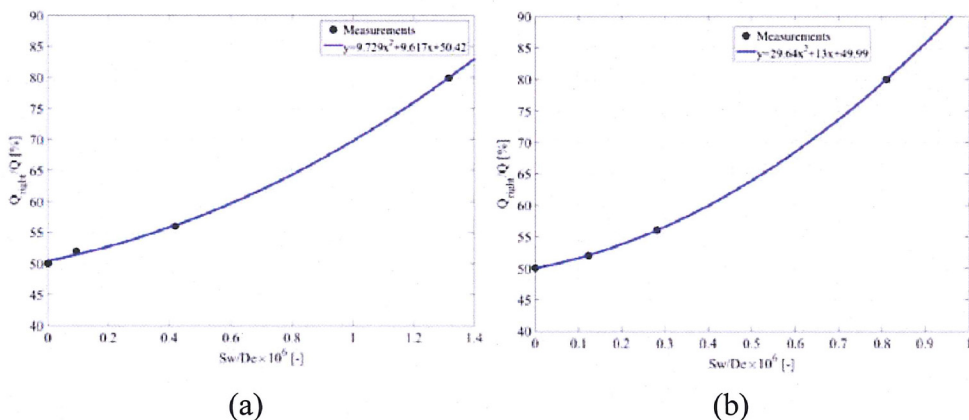
Figure 15. Flow asymmetry within the draft tube as a function of the swirl-to-Dean ratio: (a) based on the swirl after the runner blades; (b) based on the swirl after the runner hub.

Figure 16 illustrates the variation of the flow asymmetry with changing the guide vane angle while the turbine is operating under off-cam condition. It shows that the flow asymmetry is highly dependent on the guide vane angle. However, the investigated operating points are so limited to even be able to derive any general relationship between the flow asymmetry and the guide vane angle for the investigated test case.
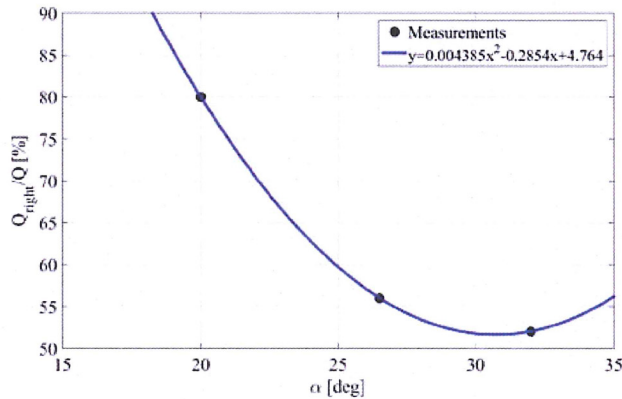
Figure 16. Flow asymmetry within the draft tube as a function of the guide vane angle.

6. Conclusion

Flow condition after the draft tube bend of a Kaplan turbine model has been investigated at different operating conditions. The effect of the turbine operating condition on draft tube performance and velocity distribution in the draft tube has been examined by performing PIV and LDA measurements within the diffuser and LDA measurements at the draft tube inlet.

The velocity distributions within the diffuser were shown to be affected by the large scale flow structures after the bend, i.e., the Dean vortices and the swirl at the draft tube inlet. The draft tube performance and the flow condition after the draft tube bend are affected by the turbine's operating point since the latter is directly related to the swirl at the runner outlet. The flow after the draft tube bend was dominated by the Dean vortices toward the lowest swirl intensity at the draft tube inlet, i.e., at the high load operating point. The two closely symmetric counter-rotating vortices after the bend induced centrifugal force to the flow. Hence, closely axisymmetric (but inhomogeneous) velocity distribution with higher axial velocity regions near the draft tube walls formed in the straight diffuser. Increasing the swirl at the draft tube inlet resulted in formation of a swirl dominated flow after the bend. The strength of the Dean vortex co-rotating with the main swirl increases when the swirl increases and diminished the other. This results in

more asymmetry in the flow after the bend. At the part load operating point, where the swirl intensity was higher than the other operating points, the Dean vortex counter-rotating with the main swirl completely disappeared and was replaced by the co-rotating vortex. The results showed that the major part of the flow passes through 20% of the draft tube cross section area and the draft tube performance is strongly affected. The flow asymmetry was shown to be a 2nd order function of the swirl-to-Dean number ratio. Velocity fluctuations associated with the RVR were captured in the right part of the draft tube where the dominating Dean vortex forms after the draft tube bend and highest portion of the flow passes through at PL. Special attention should be paid to this region during structural design of draft tubes. The other half of the draft tube is mainly filled with still water and no velocity fluctuation related to the RVR was captured at this area during PL operation of the turbine.

Acknowledgement

References

[1]   K. Amiri, An experimental investigation of flow in a Kaplan runner: steady-state and transient, Licentiate Thesis, Luleå University of Technology, 2014.

[2]   K. Amiri, M. J. Cervantes and B. Mulu, experimental investigation of the hydraulic loads on a Kaplan turbine runner model and corresponding prototype, J. Hydraulic Research 53(4) (2015), 452-465.

[3]   K. Amiri, M. J. Cervantes and B. G. Mulu, Unsteady pressure measurements on the runner of a Kaplan turbine during load acceptance and load rejection, J. Hydraulic Research, Published online: 26 Nov. 2015. DOI: 10.1080/00221686.2015.1110626.

[4]   K. Amiri, B. G. Mulu and M. J. Cervantes, Experimental investigation of the inter-blade flow in a Kaplan runner at several operating points using LDA, J. Fluids Engineer. 138 (2016), 1-12.

[5]   J. Arpe and F. Avellan, Pressure wall measurements in the whole draft tube: steady and unsteady analysis, Proceedings of the 21st IAHR Symposium on Hydraulic Machinery and Systems, Lausanne, Switzerland, 2002.

[6]   J. Gagnon, V. Aeschlimann and S. Houde, Experimental investigation of draft tube inlet velocity field of a propeller turbine, J. Fluids Engineer. 134(10) (2012), 1-12.

[7]   J. M. Gagnon, C. Deschenes and G. D. Ciocan, Numerical simulation and experimental investigation of the flow in an axial turbine, 24th IAHR Symposium on Hydraulic Machinery and Systems, Foz do Iguaçu, Brazil, 2008, Paper No.: IAHR 096.

[8]   W. K. George, Limitations to measuring accuracy inherent in the laser Doppler signal, Proceedings of the LDA-Symposium, Denmark, Copenhagen, 1975, pp. 20-63.

[9]   M. F. Gubin, V. V. Volshanik and V. V. Kazennov, Investigation of curved draft tubes with long exit cones, Gidrotekhnicheskoe Stroitel'stvo 10 (1974), 32-36.

[10] S. Houde, M. S. Iliescu and R. Fraser, Experimental and numerical analysis of the cavitating part load vortex dynamics of low-head hydraulic turbines, Proceedings of ASME-JSME-KSME Joint Fluids Engineering Conference 2011, Hamamatsu, Japan, 2011.

[11] M. S. Iliescu, G. D. Ciocan and F. Avellan, 3D PIV and LDV measurements at the outlet of a Francis turbine draft tube, Proceedings of FEDSM'02: The 2002 Joint US ASME-European Fluids Engineering Summer Conference, Montreal, Quebec, Canada, Paper No.: FEDSM2002-31332, 2002.

[12] M. S. Iliescu, G. D. Ciocan, and F. Avellan, Analysis of the cavitating draft tube vortex in a Francis turbine using particle image velocimetry measurements in two-phase flow, J. Fluids Engineer. 130 (2008), 1-10.

[13] P. P. Jonsson, B. G. Mulu and M. J. Cervantes, Experimental investigation of a Kaplan draft tube - part II: off-design conditions, Applied Energy 94 (2012), 71-83.

[14] A. Kalpakli and R. Örlü, Turbulent pipe flow downstream a 90° pipe bend with and without superimposed swirl, International Journal of Heat and Fluid Flow 41 (2013), 103-111.

[15] A. Müller, A. Bullani and M. Dreyer, Interaction of a pulsating vortex rope with the local velocity field in a Francis turbine draft tube, 26th IAHR symposium on Hydraulic Machinery and Systems, Beijing, China, 2012, Paper No.: 032040.

[16]   B. Mulu, An experimental and numerical investigation of a Kaplan turbine model, Ph.D. Thesis, Luleå University of Technology, 2012.

[17]   B. G. Mulu, P. P. Jonsson and M. J. Cervantes, Experimental investigation of a Kaplan draft tube - part I: best efficiency point, Applied Energy 93 (2012), 695-706.

[18]   C. Nicolet, A. Zobeiri and P. Maruzewski, Experimental investigations on upper part load vortex rope pressure fluctuations in Francis turbine draft tube, Int. J. Fluid Machinery Systems 4(1) (2011), 179-190.

[19]   T. Vekve, H. Brekke and P. E. Skåre, Analyzing techniques for dynamic pressure data applied on Francis turbines, 10th International Meeting of the Work Group on the Behaviour of Hydraulic Machinery Under Steady Oscillatory Conditions, Trondheim, Norway, 2001.

[20]   T. Vekve and P. E. Skåre, Velocity- and pressure measurements in the draft tube on a model Francis pump turbine, Proceeding of XXIst Symposium on Hydraulic Machinery and Systems, Lausanne, Switzerland, 2002.

[21]   L. Wang, D. Gao and Y. Zhang, Numerical simulation of turbulent flow of hydraulic oil through 90° circular-sectional bend, Chinese J. Mech. Engineer. 25(5) (2012), 905-910.

[22]   Z. Zhang, LDA Application Methods: Laser Doppler Anemometry for Fluid Dynamics, Springer, Berlin, 2010.

Paper D

Unsteady Pressure Measurements on the Runner of a Kaplan Turbine during Load Acceptance and Load Rejection

Research paper

Unsteady pressure measurements on the runner of a Kaplan turbine during load acceptance and load rejection

KAVEH AMIRI (IAHR Member), PhD student, *Department of Engineering Science and Mathematics, Luleå University of Technology, Luleå, Sweden*
Email: *Kaveh.amiri@ltu.se (author for correspondence)*

BERHANU MULU, Senior Researcher, *Vattenfall Research and Development, Älvkarleby, Sweden*
Email: *berhanu.mulu@vattenfall.com*

MEHRDAD RAISEE, Professor, *Mechanical Engineering Department, University of Tehran, Tehran, Iran*
Email: *mraisee@ut.ac.ir*

MICHEL J. CERVANTES, Professor, *Department of Engineering Science and Mathematics, Luleå University of Technology, Luleå, Sweden; Department of Energy and Process Engineering, Water Power Laboratory, Norwegian University of Science and Technology, Trondheim, Norway*
Email: *Michel.Cervantes@ltu.se*

ABSTRACT
The paper addresses unsteady pressure measurements on the blades and stationary parts of a Kaplan turbine model (Porjus U9) during load variation. The turbine was studied in various load acceptance and load rejection scenarios in off-cam mode to investigate the effect of the transients on the turbine performance. The formation and mitigation processes for the rotating vortex ropes and their effects on the forces exerted on the runner were also investigated. The results show a smooth transition during load variations between high load and the best efficiency point, at which no rotating vortex ropes form in the draft tube. However, load variation to part load resulted in a draft tube surge and the formation of a rotating vortex rope with two fluctuating components: rotating and plunging. The rotating vortex ropes began to form at the end of the draft tube cone during the closure of the guide vanes and travelled upstream with further guide vane closure. The plunging mode induced flow oscillation throughout the entire turbine conduit, whereas the rotating mode resulted in local pressure fluctuations. The rotating vortex ropes induced wide-band pressure fluctuations on the suction side of the runner close to the hub section. The formation of the rotating vortex ropes near the runner resulted in a sudden change in the pressure exerted on the suction side of the blades, whereas the rotating vortex rope mitigation process proceeded in a smooth manner.

Keywords: Kaplan turbine; load acceptance; load rejection; load variation; rotating vortex rope formation; rotating vortex rope mitigation; runner pressure measurements

1 Introduction

On-demand electricity production is achieved through a combination of intermittent and continual production systems. The relatively new trend of encouraging the use of renewable energy sources for electricity production, driven by both environmental issues and the financial benefits of such energy sources, has increased the proportion of solar- and wind-based energy production in recent years. A study performed by Liébard, Nahon, and Auzet (2012) showed that solar and wind power underwent the highest annual growth in electricity production in the period of 2001 to 2011, with averages of 45.8% and 28.3% per year, respectively. Flexible electricity production systems such as hydraulic turbines are required to maintain the grid parameters within a specific range. Consequently, this rapid growth of intermittent power generation methods combined

with the deregulation of electricity markets has caused an increase in the number of emergency shut-downs, starts/stops and load variations in hydropower plants, as reported by Trivedi (2013). A recent review of transient phenomena in Francis turbines by Trivedi, Gandhi, and Cervantes (2013) reported that Francis turbines experience cyclic stresses, asymmetric forces on the runner, and wear and tear during load variations, all of which reduce the operating lifetimes of the components. Axial turbines, i.e. Kaplan, bulb and propeller turbines, experience similar conditions under load variations. At the same time, the reduced sustainability of turbine bearings with a design based on the concept of water-lubricated power plants has resulted in increased concerns about the loads on rotating parts (Golchin, 2013).

From a control perspective, these transients are also a challenge. A hydro turbine is a nonlinear and non-stationary multi-variable system and its characteristics vary significantly under unpredictable loads, presenting difficulties in the design of an efficient and reliable controller. One of the main problems is the regulation of turbines with large load variations in a power system. This problem has not been adequately solved and continues to pose challenges to the control community (Kishor, Saini, & Singh, 2007). When modelling Kaplan turbines, the fact that the regulation of the turbine is performed by both the positions of the guide vanes and the angles of the runner blades significantly complicates the formulation of a model suitable for analysis of large disturbances. Turbine characteristics are obtained from prototypes operating at different steady-state operating points. However, it has been shown that during a dynamic perturbation in the system, the turbine behaviour departs from the values defined during steady-state operation (Arnautovic & Milijanovic, 1985).

Francis turbines have rarely been the subject of transient investigations. An overview of the effects of transients on water turbines was provided by Trivedi et al. (2013). This review shows that there have been a limited number of experimental investigations of water turbines under load-varying conditions. In most cases, global parameters such as the guide vane angle, head, flow rate and runner rotational speed have been investigated in various transient scenarios. The results of pressure measurements in the vaneless space of a bulb turbine during total shut-down were presented by Kolsek, Duhovnik, and Bergant (2006) and compared with numerical simulations. Liu, Zhou, Liu, Wu, and Nishi (2010) investigated the flow in a Kaplan turbine model under runaway conditions using numerical simulations.

Several researchers have recently initiated experimental investigations of the effect of transients on the rotating parts of hydro turbines, i.e. runner blades and turbine bearings, because of the high level of vulnerability of these parts to transient operations. An analysis performed by Gagnon, Tahan, Bocher, and Thibault (2010) demonstrated the effect of start-stop schemes on crack propagation in a Francis turbine runner blade and the need for further investigations to efficiently optimize start-stop

schemes for hydropower plants. The pressure fluctuations on the blades of a propeller turbine under runaway and speed-no-load conditions were investigated by Houde, Fraser, Ciocan, and Deschênes (2012). The frequency spectrum of the results indicated that in both cases, the pressure fluctuations with the highest amplitudes occur during transient time intervals. Pressure measurements on a Francis turbine runner blade during load acceptance/rejection using various schemes were performed by Trivedi (2013). During the guide vane movement interval, it was observed from the measurements that the amplitude of the fluctuations was increased at the rotor-stator interaction frequency. The unsteady pressure field that forms during load variation may result in an unbalanced pressure distribution on the runner.

The present work addresses unsteady pressure measurements on the blades of Porjus U9 model, a Kaplan turbine, under various load variation schemes. This model has previously been investigated during steady-state operations. The flow conditions in the draft tube of the model at the best efficiency point (BEP) and during off-design operation of the turbine have been investigated using a laser Doppler anemometry (LDA) system (Jonsson, Mulu, & Cervantes, 2012; Mulu, Jonsson, & Cervantes, 2012). The off-design results showed that the flow features at high load (HL) are qualitatively similar to those at the BEP; however, at part load (PL), the rotating vortex rope (RVR) that develops in the draft tube results in an abrupt decrease in turbine efficiency. The pressures exerted on the runner blades of the model together with the forces exerted on the main shaft and bearing pads of the corresponding prototype, investigated by Amiri, Cervantes, and Mulu (2015), revealed the existence of asymmetry at the spiral casing distributor, resulting in deformation of the runner blades and wobbling of the shaft. This investigation also proved the existence of the RVR at PL in two modes: plunging and rotating.

The objective of the current study was to investigate the effect of load variation on the pressure distributions and loads exerted on the blades and other rotating parts of the turbine. Hence, pressure measurements were performed on the runner blades and stationary parts of the turbine during six possible types of load variation among three operating points, namely, PL, BEP and HL, located along a propeller curve. Variations in the operating parameters of the turbine and pressure variations on the runner blades and stationary parts of the turbine are presented. Another focus of the paper is on the transient process of the formation and mitigation of the RVR inside the draft tube cone as a harmful phenomenon affecting the turbine's lifetime.

2   Experimental set-up

2.1   *Model specifications and operating conditions*

Pressure measurements on the stationary parts and runner blades of a Kaplan turbine model were performed during various load variation processes. The runner diameter of the investigated model is $D = 0.5\,\text{m}$, and its hub-to-tip ratio is 0.52.

(a)

Flow from high-pressure tank
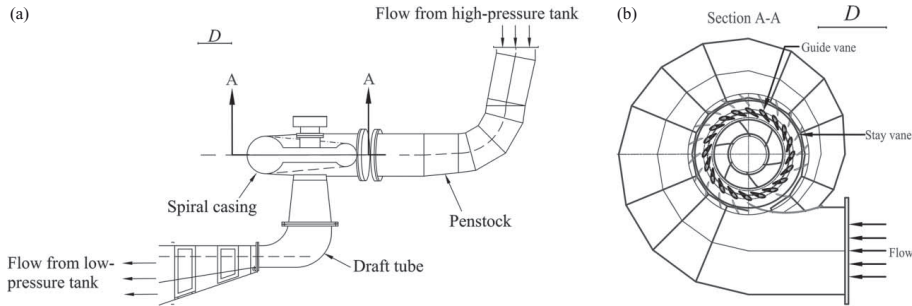
(b)   Section A-A   *D*

Figure 1   Sketch of the entire turbine (a) and water supply system, including the spiral casing, stay vanes and guide vanes (b)

Table 1   Operating condition parameters

Operating point		PL	BEP	HL
Guide vane angle	α_{GV} (deg)	16	26.5	37.5
Volume flow rate	Q_m (m^3 s^{-1})	0.51	0.71	0.77
Reduced flow rate	Q_{ED} (−)	0.238	0.322	0.359
Reduced speed	n_{ED} (−)	0.676	0.676	0.676
Reynolds number	R (−)	9.11×10^6	9.11×10^6	9.11×10^6
Efficiency relative to the BEP	$\eta - \eta_{BEP}$ (%)	− 15.2	0.0	− 3.7
Output power	$(P_{out} - P_{out,BEP})/P_{out,BEP}$ (%)	− 26	0	12

The operational net head in all investigated conditions was $H = 7.5$ m. The penstock, which has an elbow to mimic the prototype experimental conditions, supplies water to the spiral casing, as shown in Fig. 1. Twenty equally spaced guide vanes and 18 stay vanes form the distributor. The stay vanes are unevenly distributed in the spiral casing, as illustrated in Fig. 1b. The runner is composed of six blades, and an elbow-type draft tube is installed after the runner for pressure recovery.

The rotational speed of the runner during the measurements was $N = 696.3$ rpm. This rotational speed was selected to ensure similar n_{ED} values in the model and the prototype to ensure their kinematic similarity. The BEP along the propeller curve was determined by analysing the model performance at different guide vane angles while holding the runner blade angle constant. During the load variations, the runner blade angle was held constant and the load variations were applied along the propeller curve, i.e. the turbine was run in off-cam mode. The turbine was investigated under load variations among the three operating points presented in Table 1. The reduced parameters are defined as follows:

$$n_{ED} = \frac{nD}{\sqrt{gH}} \tag{1}$$

$$Q_{ED} = \frac{Q}{D^2\sqrt{gH}} \tag{2}$$

$$R = \frac{\pi ND^2}{60\nu} \tag{3}$$

$$\eta = \frac{P_{out}}{\rho gHQ} \tag{4}$$

where n is the rotational frequency of the turbine, n_{ED} is the reduced speed of the turbine, Q is the flow rate through the turbine, Q_{ED} is the reduced flow rate through the turbine, R is the Reynolds number, η is the turbine efficiency, P_{out} is the output power of the turbine, and ρ is the fluid density. The measurements were performed for all possible load variations among the operating points presented in Table 1, i.e. six cases. The operating parameters before and after stabilization of the operating conditions are presented in Table 2.

2.2   Test rig

The model measurements were performed in the Vattenfall R&D model test facility in Älvkarleby, Sweden. The test rig is a closed-loop system designed for testing of Kaplan, bulb and Francis turbines. The uncertainties in the flow rate and hydraulic efficiency measurements are ±0.13% and ±0.18%, respectively. The head of the turbine model is set by adjusting the rotational speed of the pumps and the pressures in the upstream high-pressure tank and the downstream low-pressure tank. The ability to independently adjust the pressure in the upstream and downstream tanks makes it possible to perform measurements either with or without cavitation. The current measurements were performed under cavitation-free conditions to isolate the effects of changing operating conditions and load variations.

2.3   Instruments and measurement techniques

Twelve piezoresistive pressure sensors manufactured by Kulite (Leonia, NJ, USA) (LL-080 series) were flush mounted on the suction and pressure sides of two adjacent blades, six on each.

Table 2   Variations in parameters during load variations. Subscripts 0 and 1 indicate the conditions before the onset of load variation and after test stabilization, respectively. t_{gen} represents the load variation time, and ω_{GV} represents the average angular velocity of the guide vanes during load variation

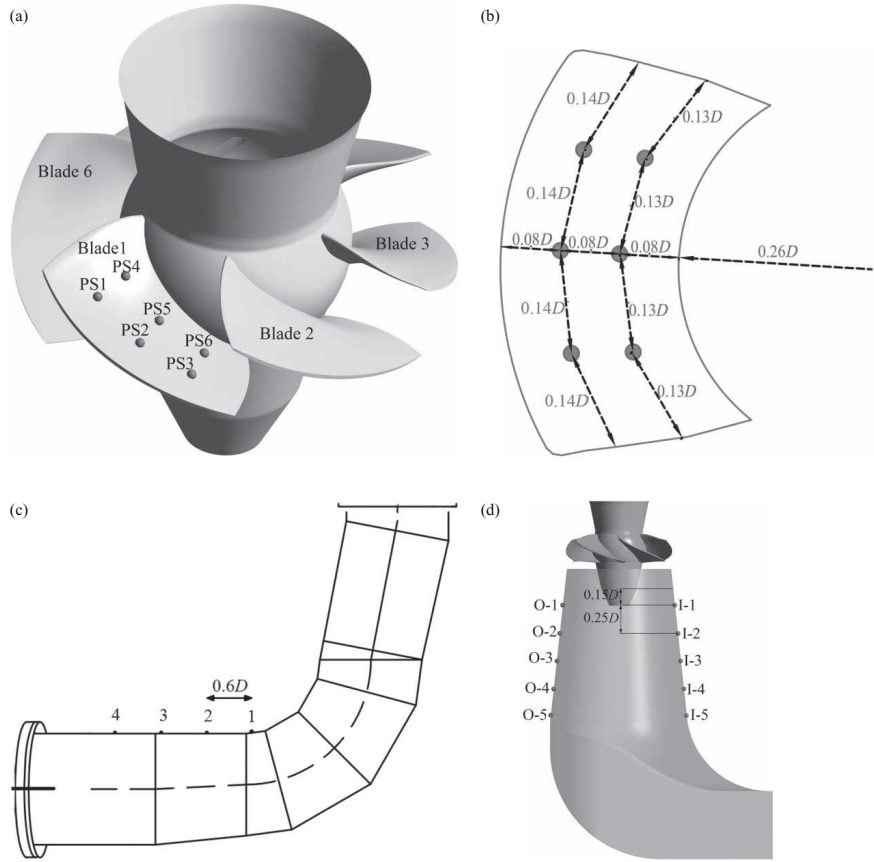|	α_{GV0} (deg)	α_{GV1} (deg)	Q_0 (m^3 s^{-1})	Q_1 (m^3 s^{-1})	H_{m0} (m)	H_{m1} (m)	t_{gen} (s)	ω_{GV} (deg s^{-1})
Load acceptance								
Case 1	26.7	37.5	0.71	0.77	7.5	7.5	12.92	0.836
Case 2	16.2	26.7	0.71	0.51	7.6	7.6	13.44	0.781
Case 3	16	37.5	0.51	0.77	7.6	7.5	26.98	0.797
Load rejection								
Case 4	37.5	26.6	0.77	0.71	7.5	7.5	16.55	0.659
Case 5	26.5	16	0.71	0.51	7.6	7.5	12.2	0.859
Case 6	37.6	16	0.77	0.51	7.5	7.6	24.79	0.871

Figure 2   Schematic diagrams of the locations of the pressure sensors: (a) the sensors (circles) on the pressure surface of the blade (note that the suction-side pressure sensors are mounted on Blade 2 and are not visible in the figure); (b) the top view of Blade 1; (c) the penstock elbow; (d) the draft tube cone with the locations of the pressure sensors

The sensors were placed on the blades such that the pressure distributions on the surfaces of blades forming a blade-to-blade channel could be measured. The sensors were located at the vertices of a net formed by imaginary circles passing through 1/3 and 2/3 of the blade span and 1/4, 1/2 and 3/4 of the blade chord lines; see Fig. 2a and b. In the figure, PS indicates the pressure side of a blade and SS indicates the suction side. The numbering begins with the sensor located nearest to the leading

edge and tip and proceeds to the one at the trailing edge hub. The transducer wires were run through grooves on the blade surfaces to the hollow shaft, where they were connected to a transmitter. These grooves were filled with a resin to preserve the hydraulic shape of the blades.

Calibration was performed by placing the blades in a specially designed nitrogen-tight pressure tank together with radio transmitters. The Plexiglass cap of the calibration tank permitted the radio transmission of the data from inside the tank. In this set-up, it was not necessary for the transducer wires to be run out of the pressurized tank, thereby avoiding any leakage around the wires and decreasing the calibration uncertainty. The pressure could be set with an accuracy of 3 Pa in this set-up. A DPI 610 pressure sensor calibrator from Druck (now GE Sensing, Leicester, UK) was used to determine the reference pressure for calibration. The maximum calibration uncertainty for all sensors was lower than 50 Pa.

Two identical telemetry systems (SRI-500e) from Summation Research, Inc. (Melbourne, FL, USA) were used during the calibration process and the measurements, one for each blade. Each system could accommodate up to eight sensors. The analogue signal received by the receiver was fed directly to a data acquisition (DAQ) system.

Three differential pressure sensors from Honeywell (FDW series) were used to measure the pressure differences between point 1 and the other three pressure taps on the penstock indicated in Fig. 2c. Tap 1 was located immediately after the bend in the penstock, and the others were located at a distance of 0.6D from each other. Ten pressure sensors from Druck (PDCR810) were also flush mounted on the draft tube cone, with five taps equally spaced in the vertical direction along both the inner and outer radii of the draft tube bend, as presented in Fig. 2d.

The DAQ system was a PXI chassis with four Ni-4472 DAQ cards. The resolution of these cards is 24 bits, and each card can accommodate up to eight channels and has a built-in anti-aliasing filter. The results were recorded during the measurements at a sampling frequency of 4 kHz for approximately 330 s beginning a few seconds prior to the load variation process.

The head, flow rate and guide vane angle were also recorded simultaneously with the pressure sensors on the same DAQ system. The main shaft torque was also recorded simultaneously, for power calculations, but using another DAQ system. This signal was recorded at a sampling rate of 8 Hz. The torque was measured using hydrostatic bearing systems to enable a frictionless torque measurement. The static head was measured as the difference in static pressure between the intake and the draft tube outlet of the turbine model, in accordance with IEC (1999). The discharge was measured using two Krone electromagnetic flow meters mounted in series. The uncertainties in the torque, head and flow rate measurements were 0.082%, 0.102% and 0.132%, respectively. The signals acquired by the two DAQ systems were synchronized before data analysis using the guide vane angle signals recorded by both DAQ systems.

3　Data analysis

The main analysis tools used to investigate flow features were developed in MATLAB. Spectral analysis of the steady-state results was performed using the standard fast Fourier transform method (FFT) because the signals were uniformly sampled. FFT with Welch's method and a Hanning window was applied to the fluctuating component of the pressure results, $\hat{P}_i(t)$:

$$\hat{P}_i(t) = P_i(t) - \bar{P}_i \qquad (5)$$

where $P_i(t)$ is the pressure measured on sensor i and $\bar{P}_i$ is the time-averaged value of the pressure on that sensor. This method was used to obtain better approximations of the amplitudes in the spectral analysis results (Vekve, 2004). The original set of the data recorded in steady cases had a length of approximately 250 s and a sampling frequency of 4 kHz. The data were divided into six subsamples with 50% overlap for the spectral analysis. The maximum non-aliased frequency in the results was 2 kHz, with a frequency resolution of 0.004 Hz.

The analysis of the data acquired during the load variation processes began with the smoothing of the calibrated signals. A MATLAB smoothing function with a Savitzky-Golay filter was applied to determine the time-averaged values using a moving average filter. Subtraction of the smoothed signal from the original signal yielded the fluctuating component of the signal. Examples of such figures are presented in Fig. 4 for the pressure variations on the suction and pressure sides of the runner during the load variation from HL to the BEP. Afterwards, the fluctuating signal components were used for further frequency analyses. Smoothing with polynomials of different orders and frame sizes was applied on the fluctuating signals to ensure that none of the investigated frequencies, i.e. frequencies in the range from the RVR frequency to the passing frequency of the guide vanes, were filtered out of the signal during the first step of smoothing. The results showed that when a polynomial of order 2 and a frame size of 5 s were used, all frequencies equal to or higher than the RVR frequency that were captured in the original data were still present in the fluctuating component of the signal.

The fluctuating signals were used for unsteady spectral analysis of the pressure on the blades to decrease the effect of the mean pressure variation on the spectrogram calculation. The Goertzel algorithm was used in the data analysis. A window size of 2.05 s with a 96% overlap was selected following a sensitivity analysis. An example of the spectrograms recorded during the load variation from the BEP to HL is presented in Fig. 5. The colour bars show the power spectral density (*PSD*) determined from the frequency analysis on a logarithmic scale:

$$PSD_{\log} = 10 \, \log(10 \, PSD) \qquad (6)$$

The formation of an RVR in the draft tube cone of a water turbine may result in pressure oscillations in both rotating and plunging modes. The pressure signals recorded at the draft tube

cone were used to decompose the plunging and rotating modes of the RVR in the draft tube. Because the sensors were located on the stationary frame, both the plunging and rotating modes contributed to the pressure oscillations at $f_{RVR,st}$. The plunging mode resulted in a synchronous oscillation in the pressure signals of the two sensors located at the same height on the inner and outer parts of the draft tube cone at $f_{RVR,st}$. The rotating mode also resulted in pressure oscillations at $f_{RVR,st}$ but with a phase difference equal to the difference in the angular position of the sensors, namely, 180° in the present case. The pressure signals recorded at the draft tube cone were filtered using a narrow band-pass filter centred at $f_{RVR,st}$ to isolate the effect of the RVR and were then subtracted from the average signals. The resulting signals could be written as a superposition of the plunging and rotating modes:

$$\tilde{P}_I(t) = A\sin(2\pi f_{RVR,st}t + \varphi_{st}) + B\sin(2\pi f_{RVR,st}t + \varphi_{rot})$$

$$\tilde{P}_O(t) = A\sin(2\pi f_{RVR,st}t + \varphi_{st}) + B\sin(2\pi f_{RVR,st}t + \varphi_{rot} + \pi)$$

$$(7)$$

where $\tilde{P}_I(t)$ and $\tilde{P}_O(t)$ are the oscillating components of the pressure signals from sensors located on the inner and outer parts, respectively, of the draft tube cone. A and B are the amplitudes of the plunging and rotating modes, respectively. φ_{st} and φ_{rot} are the phases of the plunging and rotating modes, respectively, of the filtered signals at the inner part of the draft tube. The amplitudes of the rotating and plunging modes can be calculated as follows:

$$A = \mathrm{amp}\left(\frac{\tilde{P}_I(t) + \tilde{P}_O(t)}{2}\right), \quad B = \mathrm{amp}\left(\frac{\tilde{P}_I(t) - \tilde{P}_O(t)}{2}\right) \quad (8)$$

where amp(x) is the amplitude of the oscillation of x. The method was applied to both the steady-state and load-variation results to decompose the two modes of the RVR.

4   Results and discussion

Experimental measurements were performed considering the various load acceptance and load rejection cases presented in Table 1. The results showed that the main features of the flow during load acceptance from the BEP to HL are similar to those in the case of load rejection from HL to the BEP, i.e. where no RVR forms in the turbine draft tube. Thus, the results for the load rejection from HL to the BEP are presented as representative of both cases. The load acceptance from PL to HL includes all the features of the load acceptance from PL to the BEP; hence, the former is presented and discussed in detail. The results of load rejection from HL to PL are also presented as representative of both cases 5 and 6 for the same reason.
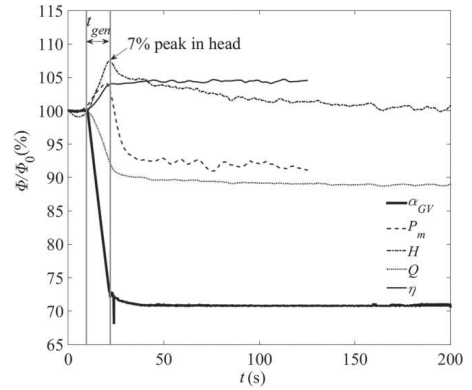

Figure 3   Variations in the fundamental parameters of the turbine during load rejection from HL to the BEP; Φ and Φ_0 refer to each parameter presented in the plot and its initial value, respectively

4.1   *Load rejection from high load to the best efficiency point*

Figure 3 shows the variations in the fundamental parameters, including the guide vane angle, power, head and flow rate, during load rejection from HL to the BEP. All parameters represented in the plot are normalized with respect to their initial values, which may be found in Table 2. The turbine efficiency and output power were recorded for 120 s during the load variations. The results show that the variations in all parameters begin simultaneously with the onset of movement of the guide vanes. Closing the guide vanes from 37° to 26.5° results in a smooth decrease in the flow rate by approximately 12%. Following the start of the closure of the guide vanes, there is a temporary increase in the pressure in the upstream high-pressure tank and a 7% increase in head, as shown in Fig. 3. This is due to the flow deceleration in the turbine penstock. The results presented by Trivedi (2013) show that the deceleration of fluid in the penstock can result in an increase of up to 7% in head in a Francis turbine model tested in an open-loop test rig. The control of the test rig pumps may result in a certain delay in head adjustment, as well. As a result, the head increases during the closure of the guide vanes and reaches a maximum almost at the same time as completion of the movement of the guide vanes. The head stabilizes after approximately 120 s. The mechanical output power, $P_{out} = \eta\rho gHQ$, is decreased at the end of the load rejection process compared with its initial value. However, at the beginning of the load variation, there is an increase in the output power. During the closure of the guide vanes, the flow rate is continuously decreasing; however, the head and the turbine efficiency are simultaneously increasing. Hence, the effect of this increase in the efficiency and head is larger than that of the decrease in the flow rate, which results in an increase in mechanical power during guide vane closure. After completion of the guide vane movement, because of the simultaneous decrease in the head and flow rate and the nearly constant efficiency, the power begins to decrease and then stabilizes. All parameters
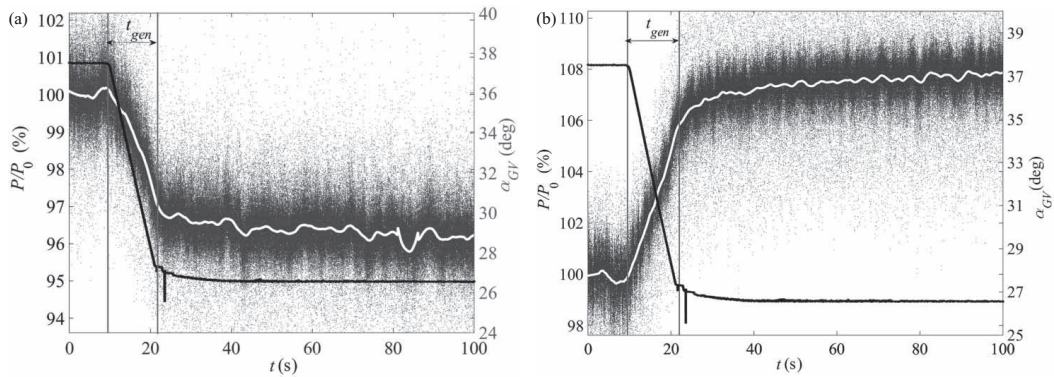
Figure 4　Pressure variations on the runner blade surfaces during load rejection from HL to the BEP. Dots: instantaneous pressures; white line: smoothed pressure; black line: guide vane angle. (a) Pressure-side sensor (PS6); (b) suction-side sensor (SS6)

shown in the figure stabilize approximately 30 s after the end of the guide vane movement, with the exception of the head, which stabilizes after approximately 120 s. The results show that the smooth variation in the head does not affect the spectrograms of the pressure signals.

The pressure variations recorded by the sensors located close to the trailing edge and hub of each runner blade (PS6 and SS6) are presented in Fig. 4. The pressure signals were made dimensionless by normalizing them with respect to their initial values. The results show that load rejection results in a smooth decrease in pressure on the pressure surfaces of the runner blades and a smooth pressure increase on the suction side, resulting in a lower pressure difference on the blades, a lower torque and a lower output power. The standard deviation of the fluctuating component of the signal acquired at PS6 decreases from 0.99% of the turbine head to 0.86% during load rejection, and that at SS6 similarly decreases from 1.18% to 1.05%. This finding is attributed to the higher kinetic energy of the flow and the consequently higher turbulence level at HL compared with that at the BEP. The kinetic energy of the flow per unit mass at the entrance of the spiral casing decreases from 3.05 to 2.59 $m^2 \, s^{-2}$, and the Reynolds number based on the entrance diameter of the spiral casing decreases from 1.56×10^6 to 1.44×10^6, resulting in a lower level of turbulence.

The spectrograms of the four pressure sensors during the transition from HL to the BEP are presented in Fig. 5, with an emphasis on the low-frequency region of $(0–4)f^*$. The presented sensors are distributed over the surfaces of the blades, i.e. close to the hub and shroud of the blades on both the suction and pressure surfaces. The spectrograms indicate that for all sensors, the runner frequency and its harmonics are present in the pressure signals. The same results were reported by Amiri et al. (2015) for the steady-state operation of the turbine. As illustrated in the figure, the amplitude of the runner frequency decreases smoothly during the load variation. This is because of the higher flow rate and the higher momentum of the flow at HL compared with those at the BEP, as discussed before. It should

be noted that the colour bar presents the *PSD* on a logarithmic scale to ensure the visibility of the level of the fluctuations during transients, as discussed in the data analysis section. The results show that the transition proceeds in a smooth manner and that no specific frequency appears in the spectrogram during the transition. Identical results were observed for load acceptance from the BEP to the HL operating point.

4.2　Load rejection from high load to part load

The investigation of the load variation process from HL to PL began with steady-state operation of the turbine at HL. As presented in Table 2, the turbine guide vane angle was initially set to 37.5°. Then, the guide vanes were continuously closed from their initial position to 16°. In this scenario, as illustrated in Fig. 6, the flow rate begins to decrease simultaneously with the onset of guide vane movement, similar to the case of the load variation from the HL operating point to the BEP. The same process as in that previous case occurs for the head of the turbine. Closing the guide vanes by nearly 21° results in a peak in the turbine head. The head reaches a maximum of approximately 20% of its initial value, as indicated by an arrow, and then decreases. The variation in mechanical power is a function of the turbine efficiency, the head and the flow rate. The head and efficiency increase at the beginning of the load variation process, whereas the flow rate decreases, resulting in an increase in power at the beginning of the process. Further closure of the guide vanes results in the formation of an RVR in the draft tube cone and, consequently, a decrease in the efficiency of the turbine. At this point, the effect of the decrease in the flow rate and efficiency is larger than that of the increasing head, and the power begins to decrease. As seen by comparing Fig. 6 with Fig. 3, the efficiency is monotonically increasing during the load variation from HL to the BEP; hence, the peak in the output power curve occurs at the same time as the peak in the head, both of which are also simultaneous with the end of the guide vane closure in Fig. 3. However, in the load variation from HL
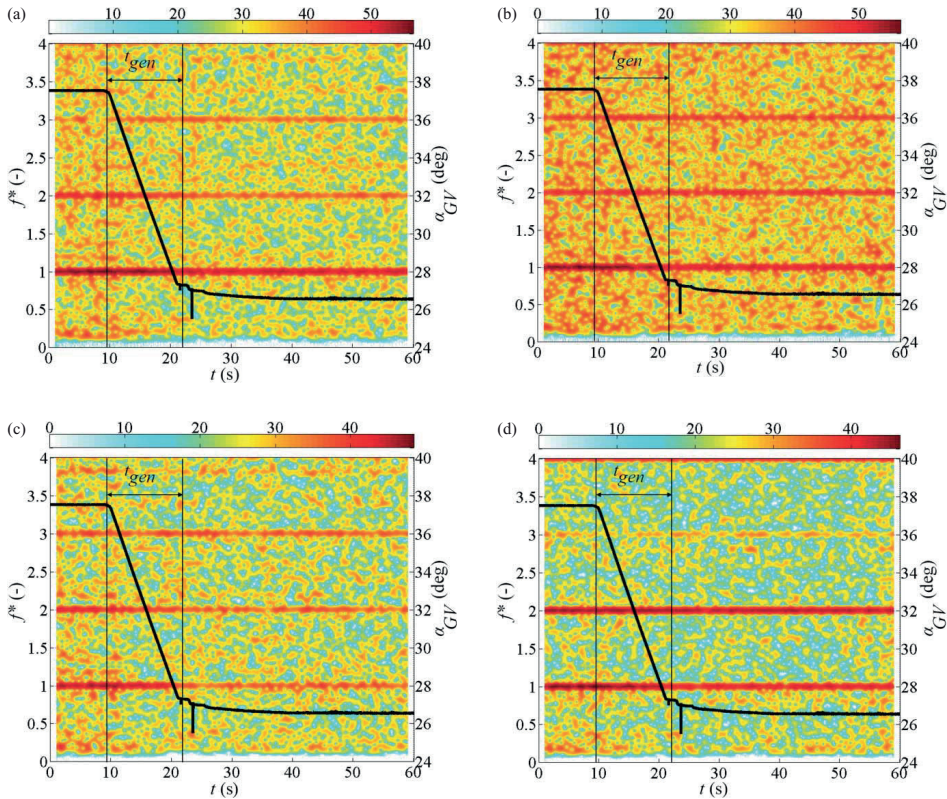
Figure 5   Spectrograms of the pressure sensor data acquired during load rejection from HL to the BEP. The black curve represents the variation in the guide vane angle. The scale of the pressure amplitude is logarithmic and differs slightly from one figure to another. (a) Suction-side hub sensor (SS4); (b) suction-side tip sensor (SS1); (c) pressure-side hub sensor (PS6); (d) pressure-side tip sensor (PS2)

to PL presented in Fig. 6, the peak in the output power does not occur at the same time as the peak in the head. The output power increases by approximately 5% at the beginning of the load variation process (as indicated by an arrow in the graph), and then, the effect of the decrease in efficiency and flow rate dominates over the effect of the head increase, and the output power consequently decreases. The percentage decrease in the output power is larger than that in the flow rate during the load variation. This is attributed to the 11.5% lower efficiency of the turbine at PL compared with that at HL. All parameters shown in the figure stabilize approximately 20 s after the completion of the guide vane movement, with the exception of the head, which stabilizes after approximately 120 s.

The pressure signals recorded at different rotating and stationary locations on the turbine indicate that all signals fluctuate with the revolution frequency of the RVR, i.e. $0.2f^*$, under PL operation. The amplitudes of the pressure signals at different locations at $0.2f^*$ are presented in Fig. 7. This figure shows that the RVR induces flow oscillations throughout the entire turbine conduit. The amplitudes of the oscillations at the sensors located on the penstock were found to be relatively high (higher than
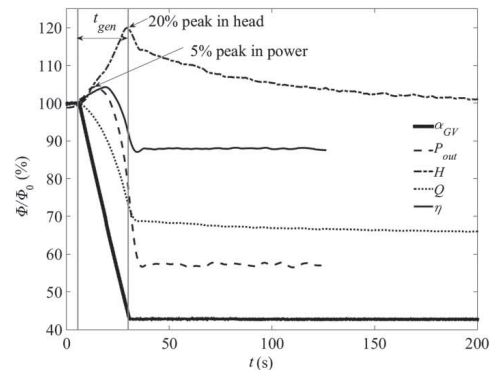

Figure 6   Variations in the fundamental parameters of the turbine during load rejection from HL to PL; Φ and Φ_0 refer to each parameter presented in the plot and its initial value, respectively

those at the runner and with the same order as those on the draft tube cone). This may be attributable to the difference in the type of pressure signals acquired. Differential pressure measurements
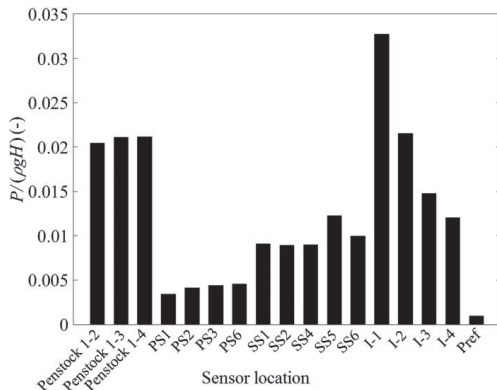
Figure 7　RVR amplitudes at various locations in the test rig under PL operation. "Pref" is located at the draft tube outlet
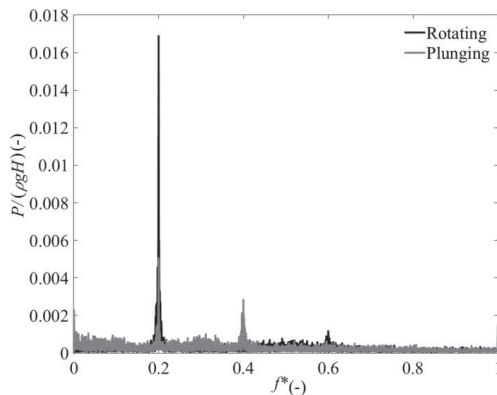

Figure 8　Spectra of the rotating and plunging modes of the RVR at the draft tube cone inlet (calculated from the I-1 and O-1 signals)

were performed on the penstock, whereas the other signals were absolute pressures. The method presented in the data analysis section was used to decompose the plunging and rotating modes of the RVR at the draft tube cone inlet with the turbine operating at PL. The results obtained from the pressure sensors at I-1 and O-1 are presented in Fig. 8. The results show that the rotating mode amplitude dominates over the plunging mode amplitude at the draft tube entrance.

Figure 9 illustrates the variations in pressure on the pressure and suction sides of the runner blades together with the variations in the standard deviation of the results. The smooth decrease in the pressure following the completion of the guide vane movement in both plots is due to the change in the turbine head before the stabilization of the test rig. With the onset of the load rejection process, the pressure on the pressure side of the blades decreases, whereas it increases on the suction side, resulting in a lower pressure difference on the blades and a lower output power. Further closing of the guide vanes results in eventual RVR formation. In the following paragraphs, it

is demonstrated that the plunging and rotating components of the RVR do not appear/subside simultaneously in the signals acquired on the runner blades during the load variations. The onset times of the formation of the plunging and rotating components are indicated in the figures by dashed and dash-dotted vertical lines, respectively. As seen in the figure, during the evolution of the rotating component of the RVR, the pressure on the suction side tends to decrease momentarily. This phenomenon was captured only on the sensors located close to the hub of the runner blade, where the RVR is close to the sensors; it was not captured on the sensors close to the tip.

Figure 9c illustrates the variations in the pressure difference between the two pressure sensors located on the pressure and suction sides of the runner blades close to the hub and trailing edge, namely PS6 and SS6. The plot shows the momentary change in the pressure difference on the two sides of the blades due to RVR formation. Theoretically, this phenomenon should result in an instantaneous change in the torque on the main shaft and the force on the turbine thrust bearings. However, no such effect can be observed in the power output presented in Fig. 6. This may be related to the fact that the phenomenon occurs only in the inner part of the runner at low radius and the effect can be damped out by the high inertia of the rotating parts and the damping effect of the bearings.

At PL, the turbine efficiency is significantly affected; a 15.2% decrease in turbine efficiency compared with the BEP is observed, as presented in Table 1. This finding may be attributed to the flow in the runner and draft tube cone. First, the pressure on the pressure side of the runner blade is lower than that on the suction side close to the hub region at this operating point; see Fig. 9c, which shows the pressure coefficient calculated based on the pressure difference between PS6 and SS6 normalized with respect to the turbine head. Hence, the inner section of the runner produces a negative torque, resulting in a lower output power compared with that at the BEP; see Table 1. Second, the stagnant region formed in the middle of the draft tube during PL operation decreases the effective area of the draft tube and thus results in lower pressure recovery (Mulu, 2012).

Figure 9d shows the variation in the standard deviation of the pressure signals during the load rejection process. With the onset of the load rejection process from HL, the standard deviations of the pressure signals on both sides of the blades slightly decrease until the guide vane angle reaches approximately 24°. This is caused by the higher flow energy and turbulence at HL compared with those at this guide vane angle, which is close to the BEP case. Afterwards, the standard deviations drastically increase on both sides of the runner after RVR formation. The effect is higher on the suction side because of the formation of the RVR in the immediate vicinity of the suction side of the blade.

The spectrograms of the pressure sensors located on the pressure and suction sides of the blades are presented in Fig. 10. Similar to the previous case, the runner frequency and its harmonics are present in the plots. Unlike the previous case, two
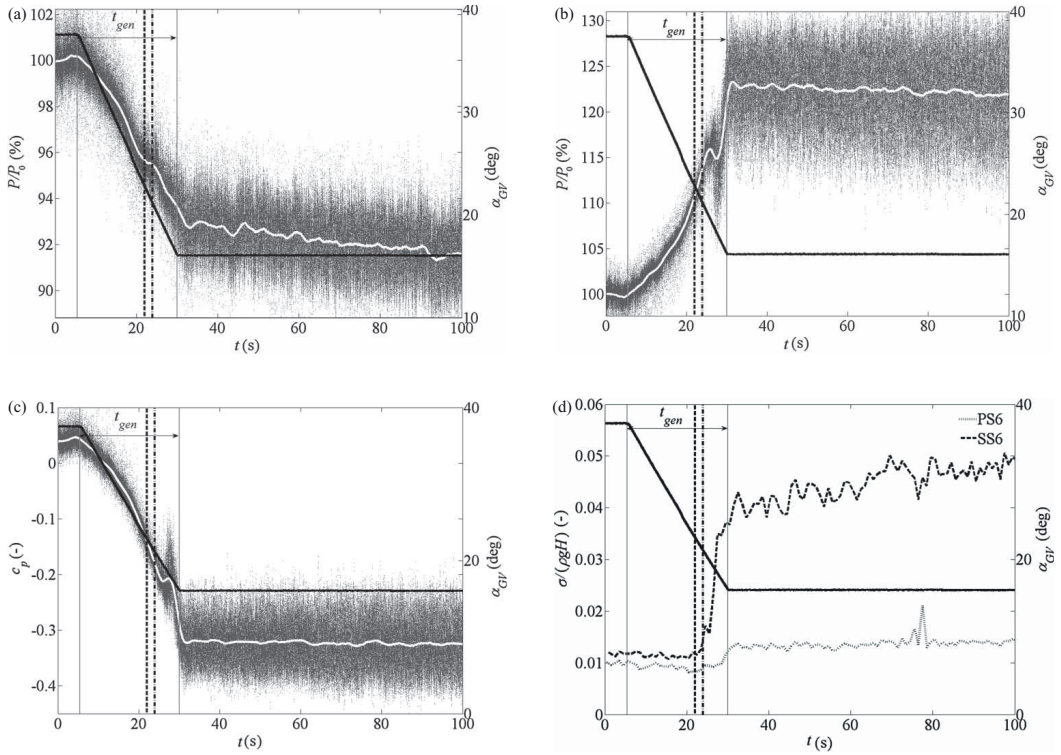
Figure 9   Pressure development on the runner blade surfaces during load rejection from HL to PL. Dots: instantaneous pressures; white line: smoothed pressure; black line: guide vane angle; dashed vertical line: onset of the formation of the RVR plunging mode; dash-dotted vertical line: onset of the formation of the RVR rotating mode. (a) Pressure-side sensor (PS6); (b) suction-side sensor (SS6); (c) c_p; (d) standard deviation

sub-asynchronous frequencies appear in the plots during load rejection and dominate the spectrogram. The frequencies are close to $0.2f^*$ and $0.8f^*$. The pressure measurements recorded simultaneously at the draft tube cone together with the flow visualization indicate the existence of an RVR in the draft tube cone at PL. The frequency spectrum of the pressure sensors on the stationary parts of the turbine shows that the RVR revolves with a frequency of $f^*_{RVR,st} = 0.2f^*$ at this operating point. Because the RVR revolves with a frequency that differs from the rotational speed of the runner, the effect of the RVR should also be observed in the rotating domain. Based on the co-rotation of the RVR with the runner, a frequency of $f^*_{RVR,rot} = f^* - f^*_{RVR,st} = 0.8f^*$ is expected in the rotating domain. The peak at $0.2f^*$ is related to the axial oscillations of the flow throughout the entire turbine conduit after the formation of the RVR in the draft tube cone, as discussed before, i.e. the plunging mode of the RVR.

Another phenomenon observed in the spectrograms is the emergence of the RVR. As illustrated in Fig. 10, an amplitude at $f_{RVR,st}$ appears at approximately 21.5 s. The rotating mode amplitude begins to appear in the spectrum with a delay of

approximately 2 s, followed by a rapid growth in its intensity. The method for decomposing the rotating and plunging modes of the RVR in the stationary frame was applied to the transient measurement results. The data were divided into bins of 0.5 s intervals, and the method was applied to the data in each bin. The results are presented in Fig. 11. There were several discrepancies in the estimations of the amplitudes between the steady-state results and those calculated during the load variation because of the limited number of samples in each bin. Hence, the calculated amplitudes were made dimensionless by normalizing them with respect to the sum of the maximum plunging and rotating amplitudes. As illustrated in Fig. 11a, the plunging mode begins to emerge at approximately 21.5 s. This mode appears simultaneously along the draft tube cone; this behaviour is compatible with the definition of the plunging mode as a synchronous phenomenon. The rotating mode emerges at the bottom of the draft tube cone (Cone4) almost simultaneously with the formation of the plunging mode. Then, the rotating mode emerges sequentially from Cone3 to Cone1. These observations are consistent with the RVR formation process proposed by Dörfler, Sick, and Couto (2013). These authors
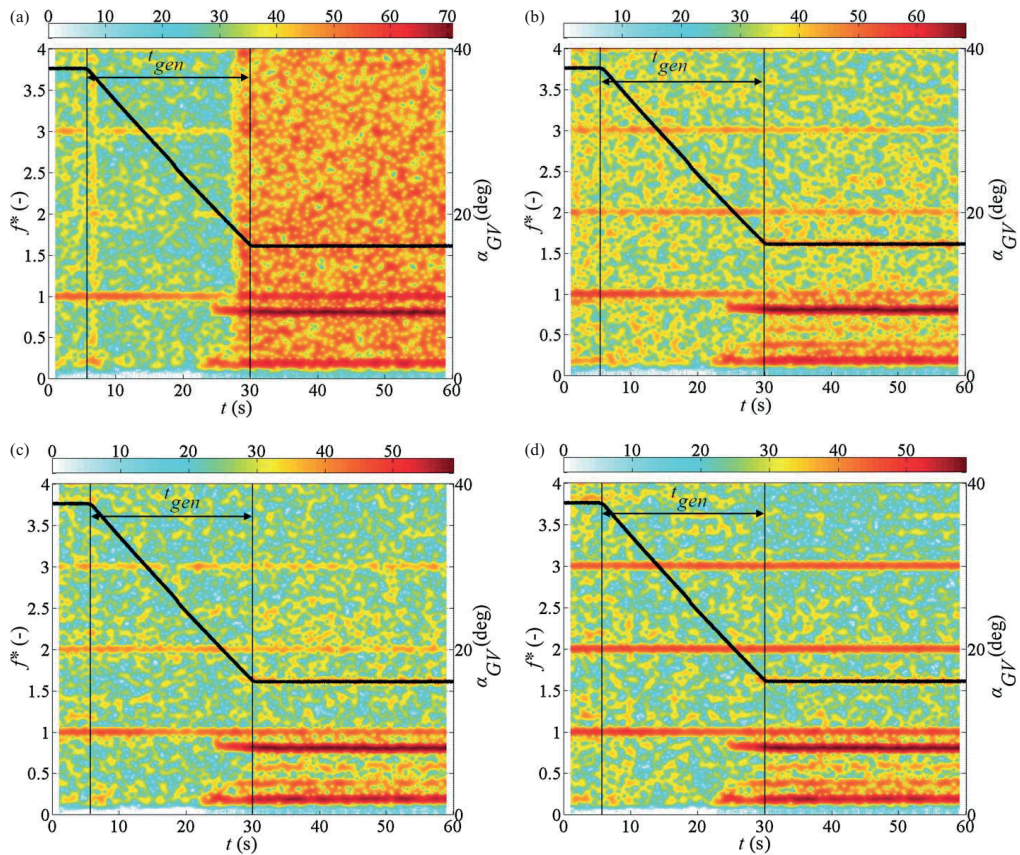
Figure 10   Spectrograms of the pressure sensor data acquired during load rejection from HL to PL. The black curve represents the variation in the guide vane angle. The scale of the pressure amplitude is logarithmic and differs slightly from one figure to another. (a) Suction-side hub sensor (SS5); (b) suction-side tip sensor (SS1); (c) pressure-side hub sensor (PS6); (d) pressure-side tip sensor (PS3)

stated that RVR formation begins with the formation of a stagnation point at the draft tube exit, with a separated flow at its downstream when the swirl of the flow entering draft tube exceeds a certain threshold value. This stagnation point moves upstream as the swirl ratio increases. In the current study, closing the guide vanes was found to trigger RVR formation at the end of the draft tube cone at approximately 21.5 s, and simultaneously, the plunging mode was captured by all sensors along the draft tube cone and on the runner. This shows that the RVR plunging mode results in flow oscillation upstream and downstream. The results of Amiri et al. (2015) indicate that the plunging mode in the studied model is a global phenomenon resulting in flow oscillation throughout the entire turbine conduit when the turbine is operating under PL operating conditions. With a smaller angle of the guide vanes, the RVR moves upstream and the rotating mode can be sensed by the draft tube sensors. This shows that rotating mode pulsations cannot propagate far upstream in the flow.

After the formation of the RVR in the draft tube, wide-band noise manifests in the signals recorded by the sensors located on the suction side of the runner blade and close to the hub; see Fig. 10a. This wide-band noise spans a frequency range from nearly zero up to approximately 500 Hz. This noise is not present in the signals acquired by the other sensors, neither on the suction side close to the tip nor on the pressure side. This finding is attributed to the shape of the RVR. The typical shape of an RVR is presented in Fig. 12. The sensors placed on the suction side close to the hub are located in the immediate vicinity of the RVR core. The observed wide-band noise proves the existence of a high level of fluctuations close to the RVR region. The non-existence of this wide-band noise in the spectrogram near the beginning of RVR formation does not mean that the wide-band noise does not exist on the runner. This is because of the change in the RVR radius that occurs as the guide vane angle varies. Decreasing the guide vane angle, and consequently the flow rate, results in a growth in the dead
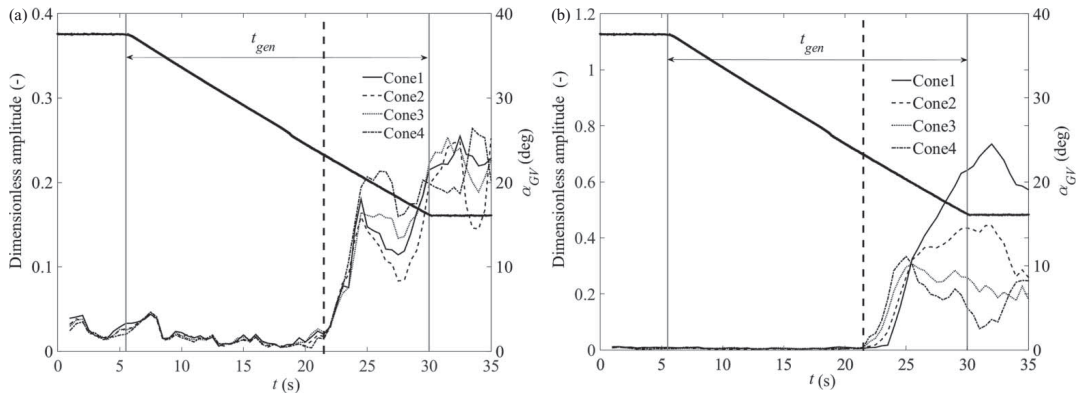
Figure 11   Decomposition of the RVR on the conical draft tube during load variation from HL to PL: (a) plunging mode; (b) rotating mode. The dashed line indicates the formation time of the plunging mode

zone region downstream of the runner blades and an increase in the diameter of the RVR orbit. As the guide vane angle reaches approximately 19°, the RVR reaches the sensors located close to the hub, resulting in the manifestation of the wide-band noise in the signal. A further decrease in the guide vane angle causes the RVR to reach the sensors located close to the hub section of the runner, and the wide-band noise then appears in the signals recorded by these sensors. It can be concluded that the RVR frequency may not be the only source of the problems encountered by turbines operating at PL; they may also be related to the noise in a wide band of frequencies exerted on the turbine runner. These wide-band pressure pulsations exert fluctuations with a high level of energy on the turbine's rotating parts, which can result in resonance in certain parts of the turbine if the natural frequency of the components lies in the relevant frequency band. Such wide-band noise has also been observed during the start-up process of the prototype corresponding to the model investigated here; see Jansson (2013).

The variations in the *PSD* and frequency of the RVR in the plunging and rotating modes during the load variation from HL to PL are presented in Fig. 13. A comparison of parts (a) and (b) of the figure reveals that the amplitude of the rotating mode is higher than that of the plunging mode in all sensors, a finding that is compatible with the results recorded at the draft tube inlet presented in Fig. 8. It is also observed that in all cases, the *PSD* on the suction side is higher than that on the pressure side, indicating that the disturbance propagates from the draft tube, upstream to the runner. Meanwhile, the runner blades attenuate the wave propagation. After passing through the runner, the decrease in the *PSD* of the $f_{RVR,rot}$ is higher than that at $f_{RVR,st}$. This is because of the large mass of water contained in the entire test rig, which oscillates at $f_{RVR,st}$ in the axial direction. In this situation, the runner blades cannot have such a large damping effect on the oscillation of this large mass of water oscillating in the axial direction. The variations in the plunging and rotating frequencies are presented in parts (c) and (d) of the
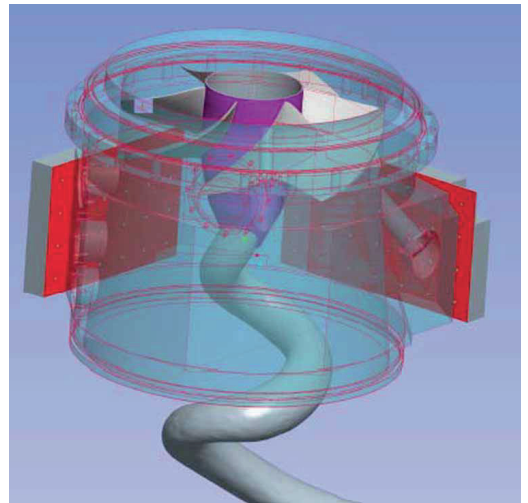

Figure 12   Simulation of the RVR in a draft tube (Houde et al., 2011)

figure. The horizontal axis in each plot begins at the onset of the formation of the RVR in the corresponding mode. The formation of the RVR starts with a relatively high level of fluctuations in the frequency of the plunging mode. After approximately 5 s, the frequency stabilizes at approximately $0.17f^*$. The frequency then increases with the closure of the guide vanes and stabilizes at a frequency of approximately $0.2f^*$. The higher level of fluctuations in the frequency of the RVR captured by the sensor located on the suction side of the blade close to the hub is due to the wide-band noise induced in the inner region of the suction side of the blade after RVR formation, as discussed before. Compared with the plunging mode, there is no strong oscillation in the frequency of the rotating mode of the RVR. The frequency of the rotating mode decreases with the closure of the guide vanes in such a way that the sum of the RVR frequencies in the
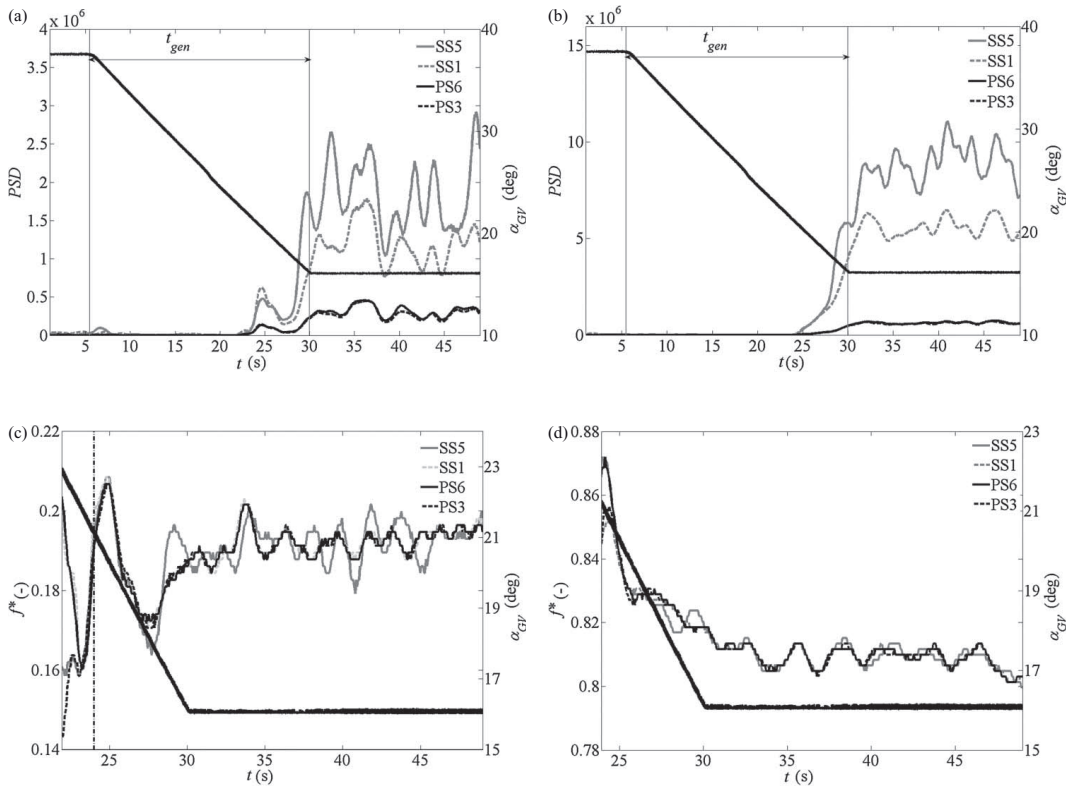
Figure 13   Power spectral densities and frequencies of the plunging and rotating modes of the RVR during load variation from HL to PL: (a) RVR plunging mode amplitude; (b) RVR rotating mode amplitude; (c) RVR plunging mode frequency; (d) RVR rotating mode frequency. The dash-dotted vertical line in subfigure (c) indicates the time of the emergence of the rotating mode. The locations of points SS1, SS5, PS3, and PS6 are shown in Fig. 2
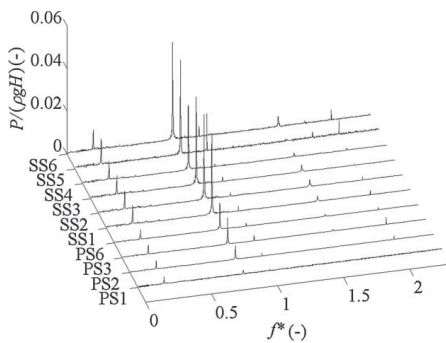

Figure 14   Amplitude spectra of the sensors located on the blades at PL, with $\alpha_{GV} = 16°$. The Y axis represents the positions of the sensors on the blade surfaces, as presented in Fig. 2

Figure 15   Variations in the fundamental parameters of the turbine during load rejection from PL to HL; Φ and Φ_0 refer to each parameter presented in the plot and its initial value, respectively

plunging and rotating modes after RVR stabilization is equal to the runner frequency.

Figure 14 shows the amplitude spectra of the pressure sensors located on the pressure and suction sides of the runner
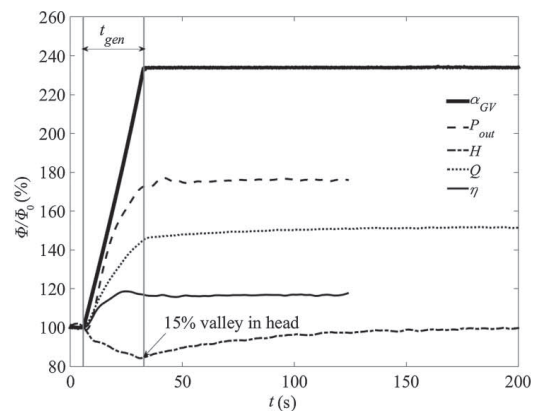
blades when the turbine is operating in a steady state at the PL operating point. A comparison between this figure and the results of PL measurements at a guide vane angle of 20° reported

by Amiri (2014) reveals that the RVR frequency increases by approximately 17% (from 0.17*f** to 0.2*f**) upon a change in the guide vane angle from 20° to 16°. The amplitude of the RVR frequency in the current PL case is also nearly three times larger than the amplitude at a guide vane angle of 20°. The results of this comparison between the steady-state operating characteristics of the turbine at two different guide vane angles are compatible with those of the transient investigations, i.e. closing the guide vanes results in a higher amplitude and revolution frequency of the RVR in both cases.

4.3 *Load acceptance from part load to high load*

The load acceptance investigation began with steady-state operation of the turbine at PL. Then, the guide vane opening process was initiated at a constant rate; see Fig. 15. All parameters were made dimensionless by normalizing them with respect to their initial values, which may be found in Table 2. In this scenario, the changes in the other parameters begin simultaneously with the guide vane movement. Opening the guide vanes from 16° to 37° results in a smooth increase in the flow rate by approximately 50%. This increase in the guide vane angle results in a

temporary decrease in the turbine head by approximately 15%, as indicated by an arrow in Fig. 15. This change in the head is a combined effect of the flow acceleration in the turbine conduit and the pressure drop in the upstream pressure tank due to the control of the test rig pumps, as discussed with regard to the previously considered cases. The head recovers afterwards with an increase in the rotation speed of the test rig pumps. Unlike the load rejection cases, the power curve follows the head curve for a comparably short interval. The minimum value in this case is lower than the peak observed in the case of load rejection from HL to PL, namely 1.2% (barely visible in the graph) in the load acceptance case compared with approximately 5% in the load rejection case. The difference is that at the beginning of the load rejection process, the flow rate decreases while the head and the turbine efficiency simultaneously increase. Hence, the efficiency and head contribute to an increase in the maximum power value. By contrast, in the load acceptance case, although the head decreases with the opening of the guide vanes, the flow rate and efficiency simultaneously increase. The outcome is that the effect of the decrease in the head contributes to decreasing the output power, whereas the other two parameters contribute to an increase in the power, and the variation in the head cannot
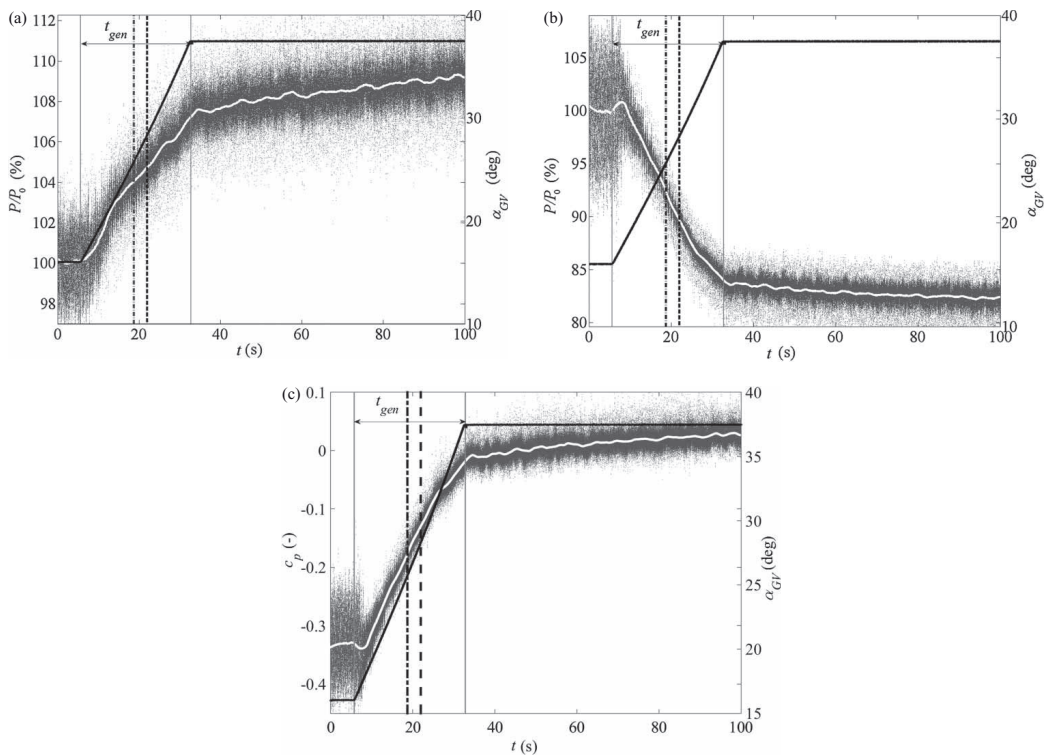

Figure 16 Pressure development on the runner blade surfaces during load acceptance from PL to HL. Dots: instantaneous pressures; white line: smoothed pressure; black line; guide vane angle; dash-dotted line: disappearance of the RVR rotating mode; dashed line: disappearance of the RVR plunging mode. (a) Pressure-side sensor (PS6); (b) suction-side sensor (SS6); (c) c_p
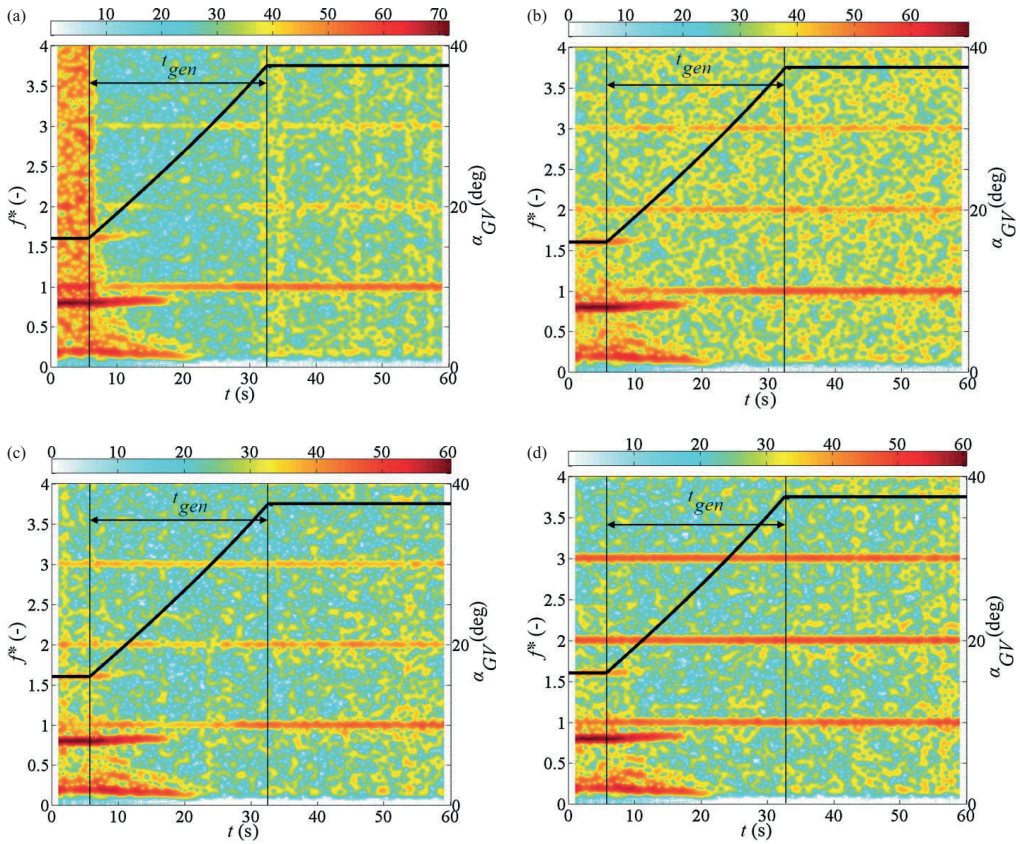
Figure 17   Spectrograms of the pressure sensor data acquired during load acceptance from PL to HL. (a) Suction-side hub sensor (SS5); (b) suction-side tip sensor (SS1); (c) pressure-side hub sensor (PS6); (d) pressure-side tip sensor (PS3)

dominate over the effect of the other parameters for a long time. All parameters shown in the figure stabilize after approximately 15 s following the completion of the guide vane movement, with the exception of the head, which stabilizes at approximately 150 s.

Figure 16 illustrates the pressure variations in the sensors located on the pressure and suction sides of the runner blades during the load variation from PL to HL. As seen in the figure, the pressure signals still have not stabilized after 100 s because head stabilization does not occur until 150 s, as presented in Fig. 15. The results show that after stabilization, the pressure at PS6 is increased by approximately 10%, and that at SS6 is decreased by approximately 18%, resulting in a higher pressure difference on the blades and thus a higher output power. By comparing the results for load rejection (case 6, presented in section 4.2) with the current results for load acceptance, a difference between the formation and disappearance of the RVR in the draft tube of the turbine can be observed. As shown in Fig. 9c, the formation of the RVR in the draft tube coincides with

a temporary increase in the pressure difference on the runner blades. However, there is no such effect on the runner during RVR mitigation, as presented in Fig. 16c. The pressure signals on both the pressure and suction sides of the runner blades vary smoothly from PL to the RVR-free condition, as shown in Fig. 16.

The spectrograms of the signals of several pressure sensors distributed over the pressure and suction sides of the runner blades are presented in Fig. 17. The main features of the plots are similar to those recorded in the case of load rejection from HL to PL, as presented in section 4.2, but in the reverse order. The runner frequency and its harmonics are present in all spectrograms. During PL operation, the existence of the RVR in the draft tube is captured by all sensors distributed on both sides of the blades. The amplitude of the RVR is higher on the suction side than on the pressure side, as expected. A wide-band noise with a clear edge, as captured in the case of load rejection from HL to PL, is again present in the signals recorded by the sensors located on the suction side and close to the hub. As the guide
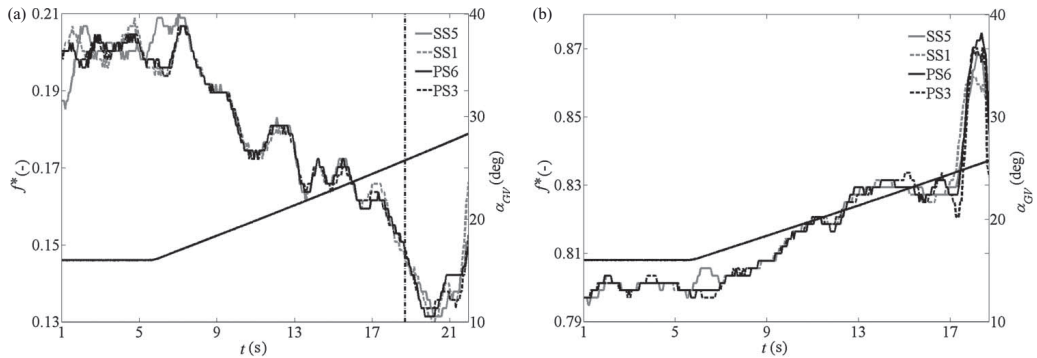
Figure 18   Frequencies of the plunging and rotating modes of the RVR during load variation from PL to HL. (a) RVR plunging mode frequency; (b) RVR rotating mode frequency. The dash-dotted vertical line indicates the time of the disappearance of the rotating mode

vane angle increases, the wide-band noise suddenly disappears. This disappearance is attributed to the reduction in the RVR radius. $f_{RVR,st}$ decreases as the load increases during the load variation process, and consequently, $f_{RVR,rot}$ increases. The mitigation of the rotating and plunging modes of the RVR does not occur simultaneously during load acceptance. Indeed, these modes also do not begin to form at the same time during load rejection, as described in section 4.2. In this case, the axial component of the RVR lasts approximately 3–4 s longer than the rotating component. Decomposition of the plunging and rotating modes of the RVR during load acceptance (not presented) shows that the RVR mitigation process is similar to that of RVR formation but in the reverse order. With the opening of the guide vanes, the rotating mode at Cone1 begins to subside and then sequentially disappears from the signals of the sensors from the top of the draft tube cone to the bottom. The rotating mode disappears at Cone4 with a delay of approximately 2.5 s compared with Cone1. The plunging mode has disappeared at all positions on the draft tube cone after the elimination of the rotating mode at Cone4.

Figure 18 illustrates the variations of the RVR frequency in the plunging and rotating modes during the load acceptance process. The variations in the amplitudes are similar to those in the load rejection case but in the reverse order. Hence, the amplitude results are not presented here. The end point of the horizontal axis corresponds to the time of the disappearance of the RVR in the corresponding mode. The main features of the plots are similar to those observed for the load rejection case in Fig. 13. The main difference in the plunging mode is associated with the oscillation in the plunging frequency during RVR formation, which is not captured during RVR mitigation. In this case, RVR mitigation proceeds smoothly, and there is no rapid variation in the RVR frequency. Another difference is that the range of the frequency variation in this case is higher than that in the load rejection case. During RVR mitigation, the plunging mode frequency decreases to $0.13f^*$, compared

with the minimum frequency of $0.17f^*$ observed during RVR formation. This may be attributed to the resistance of the fluid to the formation of the RVR during load rejection or the more rapid guide vane movement during load rejection compared with the load acceptance case, as presented in Table 2.

5   Conclusions

Unsteady pressure measurements on the runner blades and stationary parts of a Kaplan turbine model were performed during load variations among three operating points: PL, the BEP and HL. The study was performed to investigate the effects of these transitions on the loads exerted on the runner and on the RVR formation/mitigation processes. The results showed that the load variation between HL and the BEP proceeds smoothly, i.e. with a smooth increase in the pressure on the suction side of the runner and a smooth pressure decrease on the pressure side during the load rejection. When the guide vane angle reaches a sufficiently low threshold during the load rejection from HL to PL, an RVR forms at the end of the draft tube cone. The RVR then moves from the end of the draft tube cone towards the draft tube inlet upon further closure of the guide vanes. The results show that the RVR has two modes: plunging and rotating. The plunging mode results in global flow oscillation, whereas the rotating mode results in local oscillations of the flow. The formation of an RVR at the draft tube inlet results in the induction of fluctuations at two frequencies on the runner. The amplitude of the rotating mode is larger than that of the plunging mode both on the runner and at the entrance to the draft tube cone. The formation of the RVR also results in the induction of noise on the runner in a wide band of frequencies ranging from 0 to 500 Hz. Decreasing the load increases the RVR frequency, amplitude and radius, resulting in larger fluctuations in the wideband noise on the runner. The onset of the RVR close to the runner blades results in a momentary decrease in the pressure

on the suction side of the blades, resulting in a sudden pressure change on the runner blades and most likely fluctuations in the torque and the lift on the blades. Similar phenomena were observed during the load acceptance from PL to HL but without any sudden changes in the blade pressure during the mitigation of the RVR.

Funding

Notation

$c_p = \Delta P/(\rho g H)$	=	pressure coefficient (−)
D	=	runner diameter of the turbine model (m)
f	=	rotational frequency of the runner (Hz)
$f_{RVR,st}$	=	frequency of the rotating vortex rope in the stationary frame (plunging mode) (Hz)
$f_{RVR,rot}$	=	frequency of the rotating vortex rope in the rotating frame (Hz)
f_s	=	sampling frequency (Hz)
g	=	gravitational acceleration (m s^{-2})
H	=	head during the model test (m)
N	=	rotational speed of the runner in the model (rpm)
n	=	rotational frequency of the runner in the model (Hz)
n_{ED}	=	reduced speed of the turbine (−)
P	=	static pressure (Pa)
$\hat{P}$	=	fluctuating component of pressure (Pa)
$\tilde{P}$	=	oscillating component of pressure (Pa)
$\bar{P}$	=	time-averaged pressure (Pa)
P_{out}	=	output power (kW)
Q	=	model flow rate (m^3 s^{-1})
Q_{ED}	=	reduced flow rate of the turbine (−)
R	=	Reynolds number of the turbine (−)
t	=	time (s)
t_{gen}	=	transition time (s)
α_{GV}	=	guide vane angle (deg)
η	=	turbine efficiency (−)
ν	=	kinematic viscosity (m^2 s^{-1})
ρ	=	fluid density (kg m^{-3})
$\sigma = \sqrt{\frac{\sum_{i=1}^{N}(P_i - \bar{P})^2}{N}}$	=	standard deviation
φ_{rot}	=	phase of the pressure fluctuations due to the rotating mode of the RVR (rad)
φ_{st}	=	phase of the pressure fluctuations due to the plunging mode of the RVR (rad)
ω_{GV}	=	guide vane angular velocity (deg s^{-1})
*	=	frequency is made dimensionless with respect to the rotational frequency of the runner
I	=	sensors is located on the inner part of draft tube
O	=	sensors is located on the outer part of draft tube

References

Amiri, K. (2014). *An experimental investigation of flow in a Kaplan runner: Steady-state and transient* (Licentiate thesis). Luleå University of Technology, Luleå, Sweden. doi:978-91-7439-849-6

Amiri, K., Cervantes, M. J., & Mulu, B. (2015). Experimental investigation of the hydraulic loads on a Kaplan turbine runner model and corresponding prototype. *Journal of Hydraulic Research*, *53*(4), 452–465. doi:10.1080/00221686.2015.1040085

Arnautovic, D., & Milijanovic, R. (1985). An approach to the analysis of large perturbations in hydro-electric plants with Kaplan turbines. *Electric Power Systems Research*, *9*, 115–121.

Dörfler, P., Sick, M., & Couto, A. (2013). *Flow-induced pulsation and vibration in hydroelectric machinery*. London: Springer.

Gagnon, M., Tahan, S. A., Bocher, P., & Thibault, D. (2010). Impact of startup scheme on Francis runner life expectancy. *Earth and Environmental Science*, *12*. doi:10.1088/1755-1315/12/1/012107.

Golchin, A. (2013). *Tribological behaviour of polymers in lubricated contacts* (Licentiate thesis). Luleå University of Technology, Luleå, Sweden.

Houde, S., Fraser, R., Ciocan, G., & Deschênes, C. (2012). Experimental study of the pressure fluctuations on propeller turbine runner blades: Part 2, transient conditions. *Earth and Environmental Science*, *15*, 062061.

Houde, S., Iliescu, M. S., Fraser, R., Lemay, S., Ciocan, G. D., & Deschenes, C. (2011). Experimental and numerical analysis of the cavitating part load vortex dynamics of low-head hydraulic turbines. *Proceedings of ASME-JSME-KSME Joint Fluids Engineering Conference 2011*, Hamamatsu, Japan.

IEC. (1999). *International standard IEC 60193: second edition 1999–11: Hydraulic turbines, storage pumps and pump-turbines − model acceptance tests*. Geneva: International Electrotechnical Commission. Retrieved from http://www.normservis.cz/download/view/iec/info_iec60193%7Bed2.0%7Den_d.pdf.

Jansson, I. (2013). *Vibrant bodies of swirling flow: On the limits of mechanical power transformation* (PhD thesis). Luleå University of Technology, Luleå, Sweden.

Jonsson, P. P., Mulu, B. G., & Cervantes, M. J. (2012). Experimental investigation of a Kaplan draft tube – part II: Off-design conditions. *Applied Energy*, *94*, 71–83.

Kishor, N., Saini, R. P., & Singh, S. P. (2007). A review on hydropower plant models and control. *Renewable and Sustainable Energy Reviews*, *11*(5), 776–796.

Kolsek, T., Duhovnik, J., & Bergant, A. (2006). Simulation of unsteady flow and runner rotation during shut-down of an axial water turbine. *Journal of Hydraulic Research*, *44*(1), 129–137.

Liébard, A., Nahon, C., & Auzet, M. (2012). *Worldwide electricity production from renewable energy sources* (annual report). Observ'ER. Retrieved from http://www.energies-renouvelables.org/observ-er/html/inventaire/Eng/preface.asp.

Liu, S., Zhou, D., Liu, D., Wu, Y., & Nishi, M. (2010). Runaway transient simulation of a model Kaplan turbine. *Earth and Environmental Science*, *12*. doi:10.1088/1755-1315/12/1/012073.

Mulu, B. (2012). *An experimental and numerical investigation of a Kaplan turbine model* (PhD thesis). Luleå University of Technology, Luleå, Sweden.

Mulu, B. G., Jonsson, P. P., & Cervantes, M. J. (2012). Experimental investigation of a Kaplan draft tube – part I: Best efficiency point. *Applied Energy*, *93*, 695–706.

Trivedi, C. (2013). *Transients in high head Francis turbines* (Licentiate thesis). Luleå University of Technology, Luleå, Sweden.

Trivedi, C., Gandhi, B. K., & Cervantes, M. J. (2013). Effect of transients on Francis turbine runner life: A review. *Journal of Hydraulic Research*, *51*(2), 121–132.

Vekve, T. (2004). *An experimental investigation of draft tube flow* (PhD Thesis). NTNU, Trondheim, Norway.

Paper E

Effects of Load Variation on a Kaplan Turbine Runner

Reprinted with permission

Original Paper

Effects of load variation on a Kaplan turbine runner

K. Amiri[1], B. Mulu[2], M.J. Cervantes[1, 3], M. Raisee[4]

[1]Department of Engineering Science and Mathematics, Division of Fluid and Experimental Mechanics,
Luleå University of Technology, Luleå, 971 87, Sweden, kaveh.amiri@ltu.se, michel.cervantes@ltu.se
[2]Vattenfall Research and Development, Älvkarleby, 814 70, Sweden, berhanu.mulu@vattenfall.com
[3]Department of Energy and Process Engineering, Water Power Laboratory, Norwegian University of Science
and Technology, Trondheim, 7491, Norway
[4]Mechanical Engineering Department, University of Tehran, 14155-6448, Tehran, Iran, mraisee@ut.ac.ir

Abstract

Introduction of intermittent electricity production systems like wind and solar power to electricity market together with the deregulation of electricity markets resulted in numerous start/stops, load variations and off-design operation of water turbines. Hydraulic turbines suffer from the varying loads exerted on their stationary and rotating parts during load variations since they are not designed for such operating conditions. Investigations on part load operation of single regulated turbines, i.e., Francis and propeller, proved the formation of a rotating vortex rope (RVR) in the draft tube. The RVR induces pressure pulsations in the axial and rotating directions called plunging and rotating modes, respectively. This results in oscillating forces with two different frequencies on the runner blades, bearings and other rotating parts of the turbine. This study investigates the effect of transient operations on the pressure fluctuations exerted on the runner and mechanism of the RVR formation/mitigation. Draft tube and runner blades of the Porjus U9 model, a Kaplan turbine, were equipped with pressure sensors for this purpose. The model was run in off-cam mode during different load variations. The results showed that the transients between the best efficiency point and the high load occurs in a smooth way. However, during transitions to the part load a RVR forms in the draft tube which induces high level of fluctuations with two frequencies on the runner; plunging and rotating mode. Formation of the RVR during the load rejections coincides with sudden pressure change on the runner while its mitigation occurs in a smooth way.

Keywords: Kaplan turbine, Runner pressure measurement, Load variations, Rotating vortex rope formation, Rotating vortex rope mitigation.

1. Introduction

Transient events are known as harmful conditions for hydraulic turbines in the literature. They may lead to high pressure fluctuations on different parts of the turbine, including the rotating parts. Such fluctuations affect the turbine lifetime [1]. Hence, transient events often account for most of the damages sustained by hydroelectric turbines during their operation [2]. They affect the turbine lifetime both by accelerating crack propagation on the runner blades [3] and damaging the bearings. The exerted unsteady fluctuations during the transients are a challenge for the turbine designers and power plant owners because they are difficult to predict during the design stage. Hydraulic turbines are subject to cyclic stresses, asymmetric forces on the runner, wear and tear during transient operations; each of them may affect the components lifetime [4]. From a controlling point of view, the turbines behavior varies significantly with unpredictable loads, mainly because of the turbines complexity as non-linear and non-stationary multivariable systems. Consequently, the transient operation of the turbines poses challenges to the control community and the existing problems has not been completely solved yet [5]. At the same time, intermittent power generation has increased the average number of transient events that a power plant may experience during its lifetime period [6].

Most of the studies are focused on the steady state operation of the turbines and more studies on transient operation of the turbines are required as presented in the review paper prepared by Trivedi et al., [4]. Gagnon and Leonard [2] investigated runner blades deformation of two hydropower plants during load rejection. The study showed that in both cases the fatigue damage increases during load variation. Gagnon et al. [3] showed that the damage to a Francis runner during start-up event is significantly dependent on the start-up scheme. Houde et al., [1] directly measured the pressure fluctuations exerted on the runner blades of a propeller turbine during runaway and speed-no-load conditions. The results showed that in both cases the highest amplitudes

appeared in the signals during the transient events. The dominant frequencies were found to be in the sub-synchronous range, showing that the source of the fluctuations is associated with draft tube instabilities. Trivedi et al. investigated the effect of load variation [6] and also start-up and shutdown sequences [7] on the pressure fluctuations exerted on the runner of a high head Francis turbine with the main focus on the rotor-stator interaction. The first paper results showed that the torque starts to oscillate with the start of the guide vane movement. An unsteady vortical flow also developed in the vaneless space during load variations resulting in large pressure difference between the guide vanes. Runner blades experience pressure fluctuations at their leading edge as well. The second paper showed that the pressure fluctuations on the runner were higher during shut-down process compared to start-up. The fluctuations in the vaneless space were also higher during shut-down. Simmons et al., [8] and Simmons [9] investigated the effect of start-up on the loads exerted on the bearings of a Kaplan turbine prototype. The results showed that the exerted loads on the journal bearings of the turbine during start-up are higher compared with the load during steady state operation of the turbine. Jansson [10] used the same turbine to investigate the effect of start-up on the stresses exerted on the rotating parts of the turbine. The results showed the presence of a wide band frequency in the torque and axial strain of the turbine main shaft during start-up process. The abovementioned studies mostly focus either on the high frequency phenomena happening during load variations such as rotor stator interaction or general effects of load variations on turbines life time. Focusing on low frequencies during load variation processes is valuable for understanding physics of sub-synchronous phenomena in hydraulic turbines such as RVR formation process and its effects on turbine performance.

The hydraulic turbine investigated for the study is a 1:3.1 scaled model of the prototype investigated during start-up by Simmons et al, [8], Simmons [9] and Jansson [10]. The model has been the case study for different experimental and numerical studies during on-design and off-design operating conditions [11-14]. This paper deals with the effects of load acceptance and load rejection on the pressure variations on the runner blades of the above mentioned turbine. Different load variation schemes were investigated to estimate the exerted pressures on the runner and find the most critical load variations for the turbine. The turbine was investigated in off-cam mode to trigger the RVR formation which its formation and mitigation are investigated.

2. Experiments and experimental setup

2.1. Model specification and operating conditions

The model used during this study is a 1:3.1 geometrically similar scaled model of a Kaplan turbine, named Porjus U9, which is located in northern Sweden. The turbine consists of a penstock, spiral casing, distributor, runner and an elbow type draft tube. The runner has 6 blades and the spiral casing's distributor consists of 20 guide vanes and 18 stay vanes. The model was investigated under a head of 7.5 m and at a rotational speed of 696.3 rpm. The guide vanes angle corresponding to the best efficiency point of the investigated propeller curve was found to be 26.5°. Operating points with guide vanes angles of 16° and 37.5° were selected as part load and high load for this study, respectively. The turbine operating parameters at these three operating points are presented in Table 1. The turbine was investigated during load variations between the three operating points. Similar operating conditions were selected by Amiri et al. [15] to investigate transitions from one operating point to the other, but with different load variation scenarios.

Measurements were performed at Vattenfall Research and Development, Sweden. More information about the test rig can be found in [11].

Table 1 Operating condition parameters (PL: part load; BEP: best efficiency point; HL: high load)

Operating point		PL	BEP	HL
Guide vane angle	α_{GV} [deg]	16	26.5	37.5
Volume flow rate	Q_m [m³/s]	0.51	0.71	0.77
Reduced flow rate	$Q_{ED} = \frac{Q}{D^2\sqrt{gH}}$ [-]	0.238	0.322	0.359
Reduced speed	$n_{ED} = \frac{nD}{\sqrt{gH}}$ [-]	0.676	0.676	0.676
Turbine Reynolds number	$Re = \frac{\pi ND^2}{60\nu}$ [-]	9.11×10^6	9.11×10^6	9.11×10^6
Relative efficiency to BEP	$\eta - \eta_{BEP}$ [%]	-15.2	0.0	-3.7
Output power	$(P_{out} - P_{out,BEP})/P_{out,BEP}$ [%]	-26	0	12

2.2. Instruments and measurement techniques

Twelve pieso-resistive pressure sensors manufactured by Kulite (LL-080) were installed on the pressure and suction sides of two adjacent runner blades to measure the pressure distribution in a blade channel; six on each. The sensors were installed at the vertices of a net formed by the imaginary circles of 1/3 and 2/3 of the blade span and 1/4, 1/2 and 3/4 of the blade chord; see Fig. 1. Calibration was performed in a specially manufactured tank [14]. The maximum uncertainty for all the sensors calibrations was less than 50 Pa. The data acquisition is described in [14]. Five membrane-type pressure transducers from Druck (PDCR810) separated by 127.5 mm were installed along the inner part of the draft tube cone and five others were installed along the outer part

(see Fig. 1b). The maximum uncertainty in the calibration of the cone pressure sensors was less than 100 Pa.

The signals from all the runner pressure sensors, a magnetic encoder and 10 pressure sensors installed on the inner and outer part of the draft tube cone were recorded with a sampling frequency of 4 kHz. The encoder signal was used for phase resolving the measurement results and runner angular velocity calculation. Its accuracy was 0.03°. The data were recorded 330 s in each case, starting a couple of seconds before the start of the load variation process.
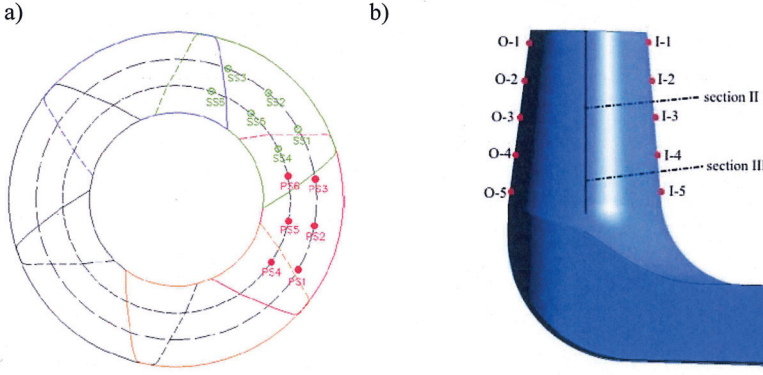

Fig. 1 Pressure and LDA measurements locations. a: on the runner; b: in the draft tube cone

Laser Doppler anemometry (LDA) measurements were performed close to the middle and at the end of the draft tube cone. These locations are shown and denominated as "section II" and "section III" in Fig. 1b. The measurement locations are 493 and 691 mm downstream the runner hub center, respectively. More details about the measurements, LDA system and data acquisition can be found in [13].

3. Data Analysis

The main data analysis tools were developed in MATLAB. Analysis of the load variation data started with smoothing the acquired signals of the pressure sensors installed on the stationary and the rotating parts of the turbine. Each signal can be decomposed to a mean and fluctuating part:

$$P(t) = \bar{P}(t) + \hat{P}(t) \tag{1}$$

where $P(t)$ is the acquired pressure signal, $\bar{P}(t)$ is the mean part and $\hat{P}(t)$ is the fluctuating part of the signal. A Matlab smooth function using the Savitsky-Golay filter was applied on the measured signals. A smooth function with a polynomial order of 8 and a frame size of 2 s were used to keep the frequencies ranging from the RVR frequency to the guide vanes passing frequency for further analysis. Then the mean signal was subtracted from the original one to get the fluctuating part of each signal. Short Time Fourier Transform (STFT) was applied on the fluctuating part of the signals to get the spectrograms. Goertzel algorithm was used for the data analysis. Window size of 2.05 s with a 96% overlap was selected after sensitivity analysis. For detailed data analysis procedure refer to [14,15].

Experimental investigation of the model performed by Amiri et al. [13] showed that RVR formation in the draft tube cone of the water turbine results in pressure oscillations with rotating and plunging modes. The pressure signals acquired at the draft tube cone were used to decompose the plunging and rotating modes of the RVR in the draft tube. Since the sensors are located on the stationary frame, both plunging and rotating modes contribute in pressure oscillations at $f_{RVR,st}$. The plunging mode results in a synchronous oscillation in the pressure signals of the two sensors located at the same height on the inner and outer part of the draft tube cone at $f_{RVR,st}$. Whereas, the rotating mode results in oscillation of the pressures with $f_{RVR,st}$ but with 180° phase difference. The pressure signals acquired at the draft tube cone were filtered with a narrow band pass filter around $f_{RVR,st}$ to isolate the effect of the RVR and then subtracted from the average of the signals as proposed by Amiri et al. [15]. The resulting signals can be written as the superposition of the plunging and rotating modes:

$$\widetilde{P}_I(t) = A\sin(2\pi f_{RVR,st}t + \varphi_{st}) + B\sin(2\pi f_{RVR,st}t + \varphi_{rot}) \tag{2}$$

$$\widetilde{P}_O(t) = A\sin(2\pi f_{RVR,st}t + \varphi_{st}) + B\sin(2\pi f_{RVR,st}t + \varphi_{rot} + \pi) $$

where $\widetilde{P}_I(t)$ and $\widetilde{P}_O(t)$ are the oscillating parts of the pressure signal from a sensors located on the inner and outer part of draft tube cone, respectively. A and B are the plunging and rotating mode amplitudes, respectively. φ_{st} and φ_{rot} are the phase of the plunging and rotating modes of the filtered signals at the inner part of the draft tube, respectively. The amplitude of the rotating and plunging modes can be calculated as:

$$A = amp\left(\frac{\bar{P}_I(t) + \bar{P}_O(t)}{2}\right), B = amp\left(\frac{\bar{P}_I(t) - \bar{P}_O(t)}{2}\right) \tag{3}$$

where amp (x) is the amplitude of the oscillating part of signal x. The method is applied both on the steady state and the load

variation results to decompose the two modes of the RVR.

The LDA measurement results were used to find the location of the RVR center. For that reason, the velocity measurement results have been phase resolved with respect to the RVR frequency. Since no reference pressure measurements was recorded simultaneous to the LDA measurements, the results were phase averaged using the tangential velocity component. Similar procedure to the one used by Amiri et al. [16] and Jonsson et al. [12] was employed for phase resolving purpose.

4. Results and Discussion

The model was investigated during transitions between the three different operating points presented in Table 1. It was run during off-cam mode to investigate the formation and mitigation process of the RVR. The results showed that the main features of the flow is similar in each of the following pairs of load variations; high load to BEP and BEP to high load, high load to part load and BEP to part load, part load to BEP and part load to high load. In the following sections, the acquired results from one of each pairs are presented and discussed.
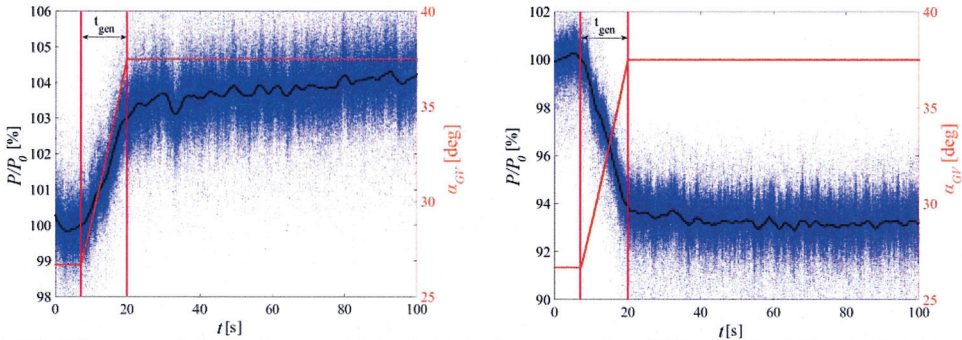
4.1. Load acceptance from BEP to high load

The load acceptance from the BEP to the high load starts with steady state operation of the turbine while the guide vanes angle is set to 26.5°. After system stabilization, the guide vanes angle starts to increase linearly to 37.5°. The load variation process takes about 13 s as presented in Fig. 2. The pressure signals are normalized with respect to their initial values, P_0, in the figure. Since the test rig is a closed loop one, there is a delay in the test rig head adjustments due to the head control system. Opening of the guide vanes in this case results in a sudden decrease of the turbine head in the beginning of the guide vanes movement. This is due to the fluid acceleration in the test rig circuit and pressure drop in the upper pressure tank. It takes around 130 s after the start of the load variation process before the turbine head is completely recovered.

Figure 2 illustrates the pressure variation on two pressure sensors located at the runner blades suction side and pressure side, close to the blade hub and trailing edge. The results show that during the load acceptance process, the pressure on the pressure side increases whereas it decreases on the suction side. This results in higher pressure difference on the blade, higher torque and higher output power. The results show that the variation happens in a smooth way and no specific phenomenon was captured during the transition. Similar results were obtained by the other blade pressure sensors as well as the sensors installed on the draft tube cone. The standard deviation of the signals increased on both blade sides during the guide vanes opening process due to the higher flow rate, higher Reynolds number of the flow and thus increased turbulence in high load compared to the BEP.

a) pressure side sensor, PS6   b) suction side sensor, SS6

Fig. 2 Pressure variation on the runner blades during load acceptance from BEP to high load. Blue dot: instantaneous pressure, black line: smoothed pressure, green line: guide vanes angle.

As discussed in the data analysis section, the fluctuating part of the signals are used to obtain the spectrograms. The spectrograms of four different sensors located on the pressure and suction sides of the runner blades close to the hub and tip are presented in Fig. 3. For all cases, the runner frequency has the largest amplitude before the start of the load variation process. The other distinct frequencies in the spectrograms are the harmonics of the runner frequency. The amplitude of the runner frequency increases with the guide vanes opening because of the higher energy level at the high load compared to the energy content at the BEP. The noise in the signal increases because of the increased turbulence level as mentioned before. The transition between the two operating points happens without occurrence of any special phenomenon; i.e., there is not any frequency appearing or mitigating during the load variation. The acquired results during the load variation from the high load to the BEP were similar; see Amiri et al, [15].
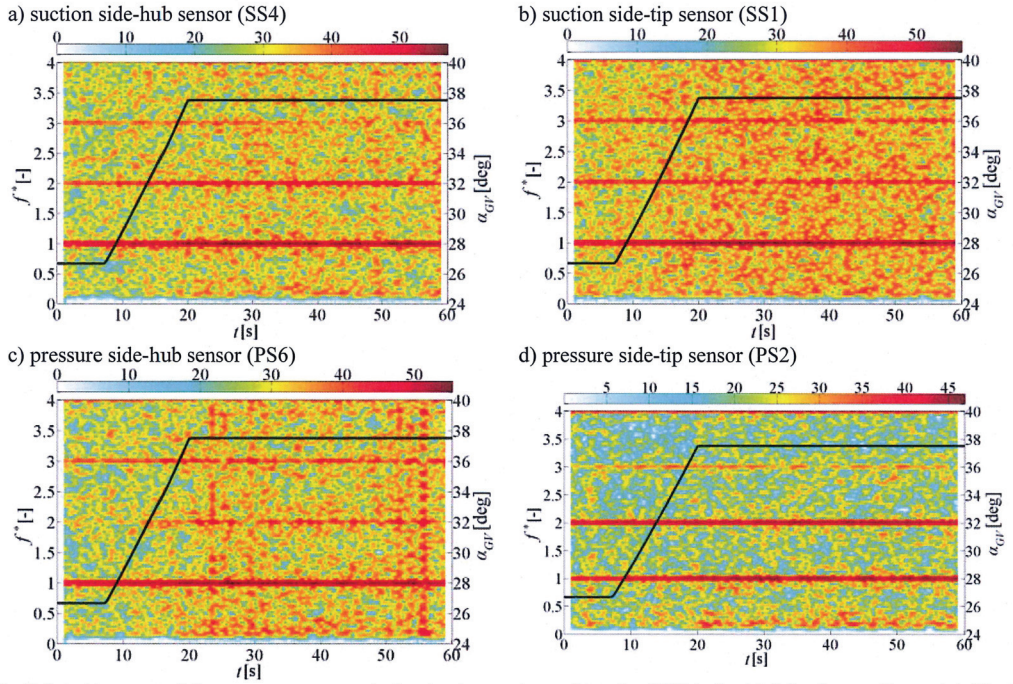
Fig. 3 Spectrograms of the pressure sensors during load acceptance from the BEP to the high load operating point. The black curve represents the variation of the guide vanes angle. The scale of the power spectral density is logarithmic and slightly different for the figures.

4.2. Load rejection from BEP to part load

Investigation of the load rejection process from the BEP to the part load starts with steady state operation of the turbine at the BEP followed by a linear guide vanes angle change from 26.5° to 16°. Pressure signals from the sensors located on the blades suction and pressure sides close to the blade hub and the trailing edge are presented in Fig. 4. Figure 4a and 4b present the raw and smoothed signals from the two sensors. The dashed red and green lines indicate the time of appearance of the RVR plunging and rotating modes, respectively. The two modes and their appearance in the signals will be discussed in the following paragraphs. In the beginning of the load rejection process, the pressure on the pressure side starts to decrease whereas it increases on the suction side. The swirl at the runner inlet increases with the guide vanes closure; however, the runner blades are unable to extract all the energy from the flow. The combination of the increased swirl and decreased flow rate results in the formation of a RVR in the draft tube during the load variation [12]. At the same time as the RVR rotating component forms, the pressure on the sensors close to the hub and trailing edge drops suddenly and then increases again. This phenomenon is marked with a red circle in Fig. 4b. This variation was just found on the suction side for the sensors close to the hub. This results in a sudden pressure difference between the two sides of the runner blade as presented in Fig. 4c. This may result in a sudden change in the turbine's torque and an axial lift affecting the forces on the thrust bearing. Following the RVR formation, the pressure signals standard deviation increases suddenly, especially on the suction side sensors which are located in the vicinity of the RVR; see Fig. 4d. This is because of the pressure fluctuations with respect to the RVR frequency. Formation of RVR within the draft tube induces fluctuation with respect to the RVR frequency to the runner which is the main source of increased pressure fluctuations.

Spectrograms of the signals from different pressure sensors during the load variation process are presented in Fig. 5. Before the start of the guide vanes movement, the only significant frequencies in the spectrograms are the runner frequency and its harmonics. Decreasing the guide vanes angle results in a vortex breakdown in the draft tube with the formation of a RVR. The RVR induces pressure fluctuations in the circumferential and axial directions; referred as rotating and plunging mode, respectively [13]. The plunging mode induces pressure fluctuations with dimensionless frequency of $0.2f^*$ and the rotating mode induces pressure fluctuations with dimensionless frequency of $0.8f^*$ on the runner. Figure 5 shows that the plunging mode appears in the signal 1.3 seconds before the rotating mode appearance in the signal independent of the sensors location (this may not be clearly seen in Fig. 5 due to the small time difference). After the RVR formation, frequency of the plunging mode increases with the guide vanes closure; see Amiri et al, [15]. The RVR amplitude in both the rotating and plunging modes increases as well. The rotating mode of the RVR is the dominant frequency after the load variation process. Further closure of the guide vanes induces a wide band noise ranging from zero to around 500 Hz on the sensors located on the blades suction side close to the hub. This is explained by the increase in the dead zone diameter below the runner with the guide vanes closure. At a guide vane angle, the RVR radius is equal to the sensors located close to the hub and the RVR covers the sensors in this location. The wide band noise indicates a high level of fluctuations exerted to the runner by the RVR. The fluctuations may result in the resonance and eventual failure of some components if their natural frequencies lie within the frequency band.
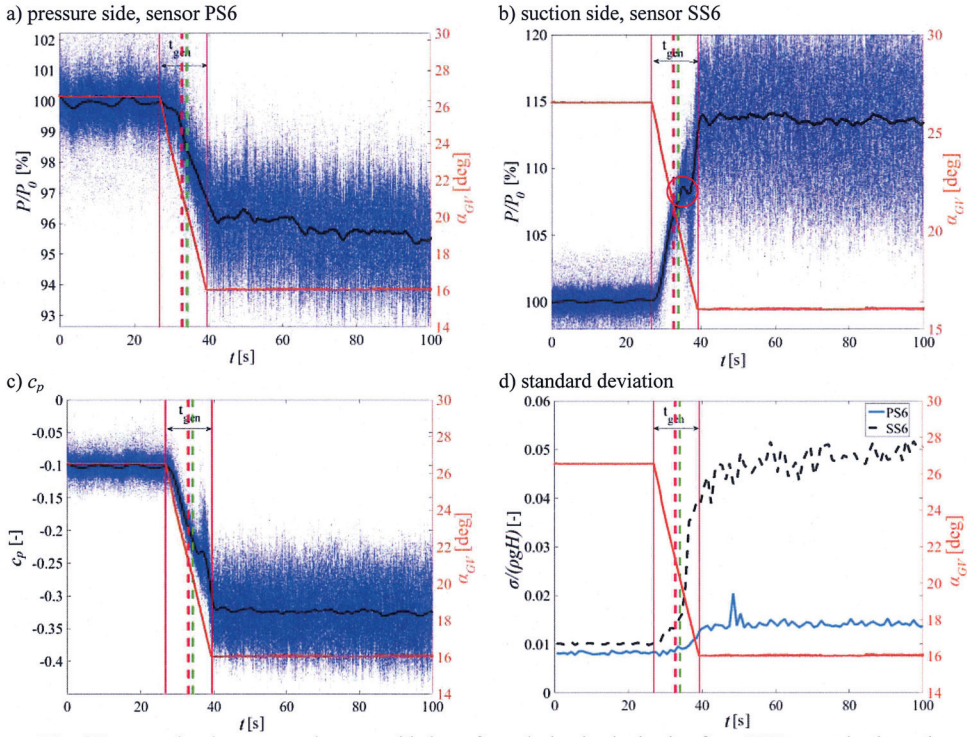
Fig. 4 Pressure development on the runner blade surfaces during load rejection from BEP to part load together with the variation in the standard deviation of the results. Blue dot: instantaneous pressure, black line: smoothed pressure and red line: guide vanes angle; dashed red: start of the formation of the RVR plunging mode; dashed green: start of the formation of the RVR rotating mode

The method explained in the data analysis section was used to decompose the plunging and rotating modes of the RVR from the pressure signals captured by the pressure sensors installed on the draft tube cone. Figure 6 shows the amplitude growth of the plunging and rotating modes of the RVR within the cone during load rejection from the BEP to part load. Shown in Fig. 6a, the plunging mode starts to appear simultaneously in all pressure signals captured on the draft tube cone at around 29 s. This is compatible with the definition of the plunging mode which results in pressure fluctuations in axial direction. The phase of the plunging mode oscillation along the draft tube cone has also been checked. FFT has been applied on the average of the pressure signals at each DT location (Cone1 to Cone4) after test rig stabilization; i.e. starting from 75 s. Phase of plunging mode at each location was found using the FFT results at the RVR frequency. Presented in Fig. 7, the phase is nearly 12.5° at locations Cone2 to Cone4 which is in agreement with the definition of plunging mode. The 7° deviation of the phase at Cone1 compared with the other locations, can be attributed to the high level of disturbances and fluctuations induced to the flow by the runner resulting in some inaccuracy in FFT results. Comparing Fig. 6a and b, amplitude of the rotating mode close to draft tube cone inlet dominates the amplitude of the plunging mode which is in agreement with the results of the runner where the rotating mode has a larger amplitude. Illustrated in Fig. 6b, the appearance of the rotating mode starts from the end of the draft tube cone and then appears sequentially from downstream to upstream (location Cone 4 to location Cone 1). This shows that the RVR starts to form at the end of the draft tube and moves upstream with the guide vane closure. There is a delay of about 1.22 s in the appearance of the rotating mode in location Cone 1 compared with location Cone 4 which can be translated to a RVR travelling velocity of 0.31 m/s in upstream-wise direction. The results also show that the amplitude of the plunging mode is almost equal all along the draft tube cone, whereas, the rotating mode has higher amplitude at the cone entrance compared with its amplitude at the cone outlet. This can be either related to the shorter distance between the RVR and the draft tube wall at the cone inlet compared to the one at the cone outlet or stronger vortex induced to the flow by the RVR at the cone inlet compared to the cone outlet. Location of the RVR center within the draft tube should be found accurately in order to find the distance between the RVR and the draft tube wall and find the main source of higher amplitude at the cone entrance compared to the one at the outlet. The RVR radius at each location can be found using the LDA measurement results performed in the draft tube cone. The RVR does not induce any tangential velocity to the water at its center. Hence, after phase resolving the tangential velocity with respect to the RVR frequency, the RVR center can be considered as the point where the tangential velocity fulfills the condition of $V=2\pi r \times f_{RVR,st}$.
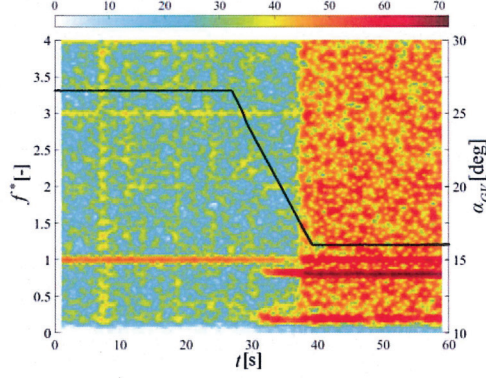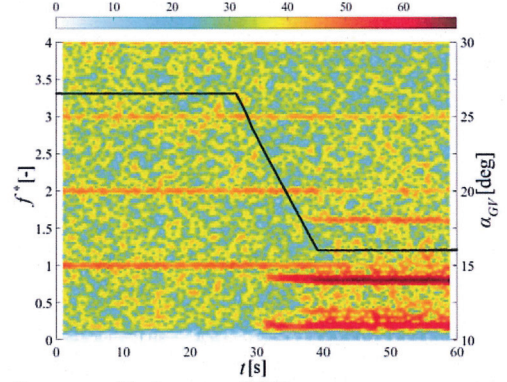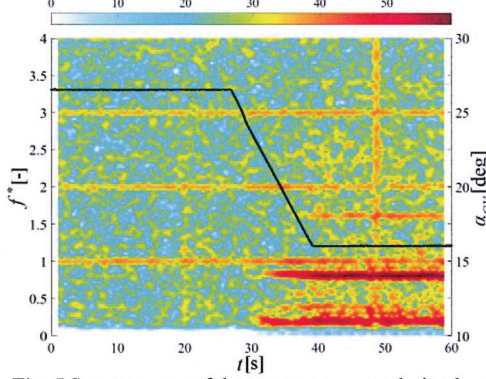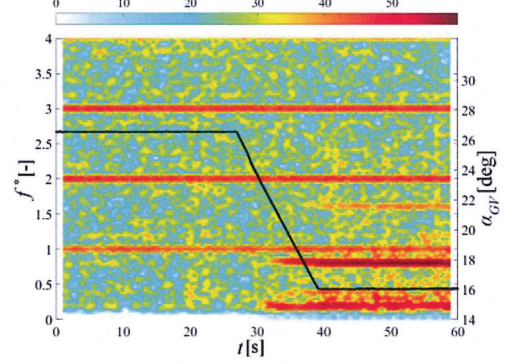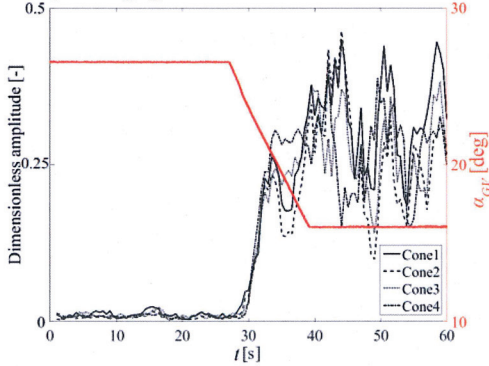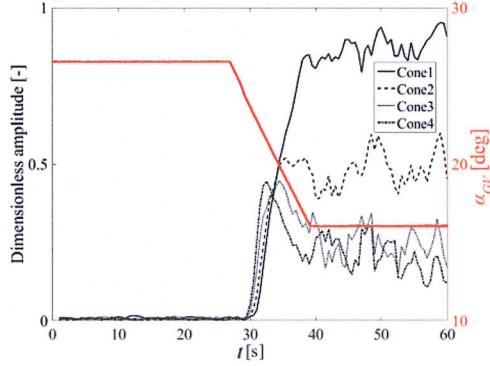
Fig. 5 Spectrograms of the pressure sensors during load rejection from BEP to part load. The black curve represents the variation of the guide vanes angle. The scale of the pressure amplitude is logarithmic and slightly different for the figures

Fig. 6 RVR amplitude growth during load variation from BEP to part load. a) Plunging mode, b) rotating mode.
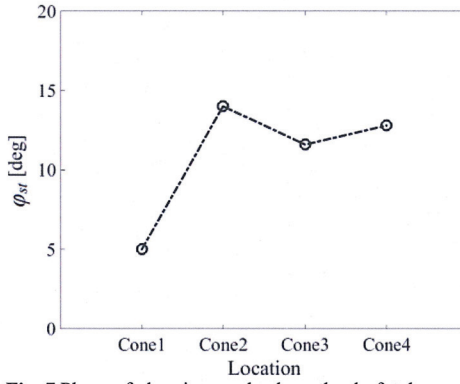
Fig. 7 Phase of plunging mode along the draft tube cone.

Figure 8a and b show contours of tangential velocities acquired by the LDA system at sections II and III shown in Fig. 1b and phase resolved with respect to the RVR frequency, respectively. The black circles at each sub-figure show the center of the RVR at the measurement locations. The radius of the RVR precession at section II is close to $0.6r*$ and its distance from the draft tube cone is approximately $0.5r*$. At section III, the RVR precession radius is close to $0.7r*$ and the distance from the RVR to the draft tube cone is equal to the one at section II; i.e. $0.5r*$. Since the distance from the RVR to the draft tube cone is equal at these two sections, it can be concluded that the RVR strength decreases in the draft tube cone in stream-wise direction.
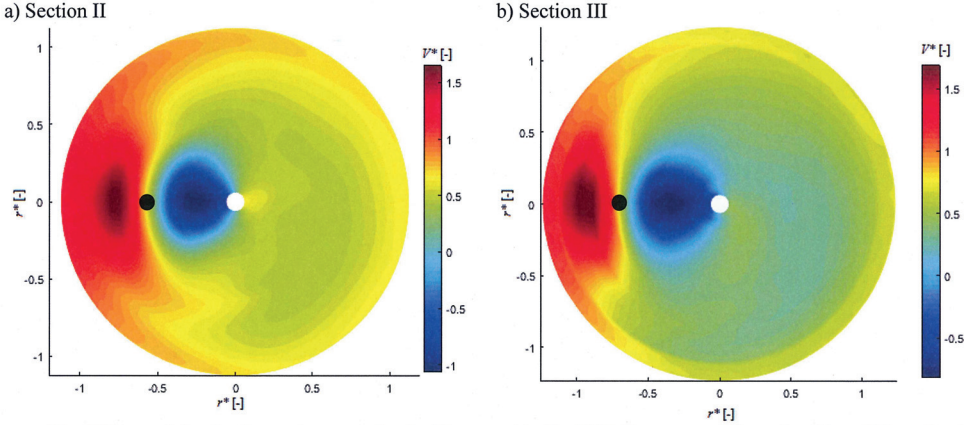
a) Section II   b) Section III

Fig. 8 Tangential velocity contours resolved with respect to the RVR frequency at a) section II, and b) section III. The black circles show the RVR center at each of the two positions.

4.3. Load acceptance from part load to the BEP

The mitigation process of the RVR was investigated during load acceptance from the part load operating point to the BEP. The signals of the sensors located close to the hub and trailing edge of the blades are presented in Fig. 9. The results show that the pressure on the pressure side increases whereas it decreases on the suction side during the load acceptance process. The larger pressure difference between the pressure and suction side results in a higher torque and thus a higher output power at the BEP compared to the part load operating point. The standard deviation of the pressure fluctuations decreased during the load acceptance process because of the RVR mitigation. The dashed green and red lines in Fig. 9 represent the mitigation time of the rotating and plunging mode of the RVR, respectively. As shown in the figure, the RVR mitigates at a guide vane angle of approximately 26° while this angle correspond to the BEP of the turbine. It shows that the transition process cannot be considered as a quasi-steady phenomenon. The RVR mitigation happens in a smooth way and the sudden change in the pressure of the sensors located on the suction side and close to the hub cannot be seen as during RVR formation. This is in agreement with the results captured by Amiri et al. [16].

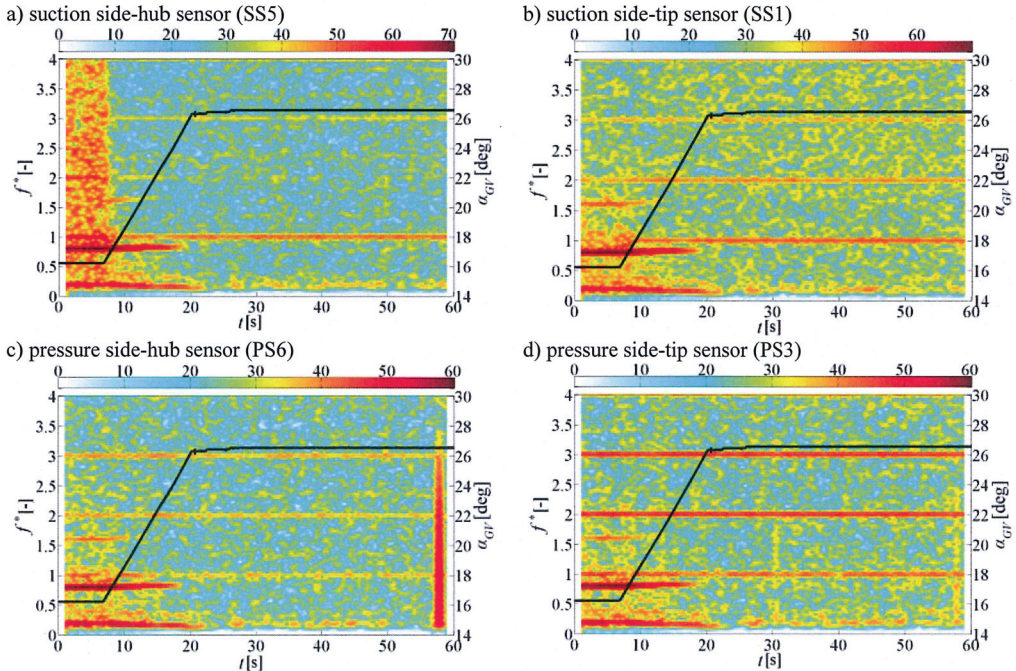a) Pressure side, sensor PS6   b) Suction side, sensor SS6
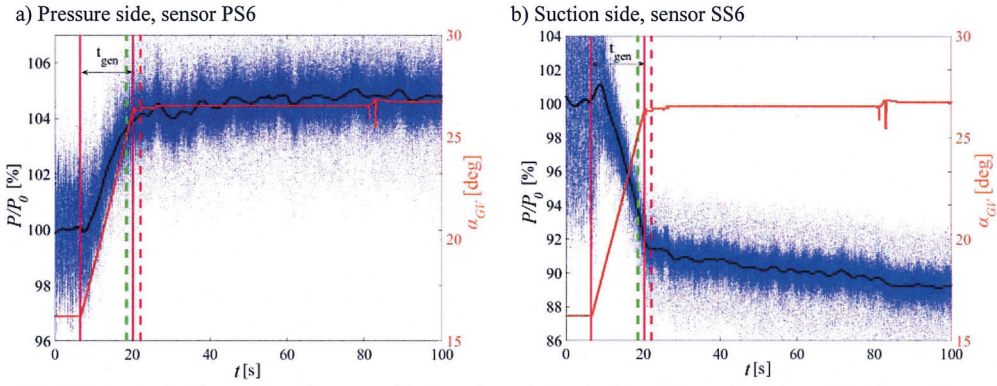
Fig. 9 Pressure development on the runner blade surfaces during load acceptance from the part load operating point to the BEP. Blue dot: instantaneous pressure, black line: smoothed pressure, red line: guide vane angle, dashed green line: rotating mode mitigation time, dashed red line: plunging mode mitigation time

The spectrograms of the fluctuating part of the pressure signals are presented in Fig. 10. The spectrograms are similar to the previous case, but in a reverse order. The runner frequency and its harmonics are present in the spectrograms during the steady state operation of the turbine at the part load operating point. However, the rotating and plunging frequencies of the RVR dominate the spectrogram. A wide band noise is present in the signals of the sensors located on the suction side and close to the hub. The RVR radius decreases with the guide vanes opening and the wide band noise disappears. The RVR frequency of the plunging mode decreases, while it increases for the rotating mode with the guide vane opening; see Amiri [14]. Both RVR related amplitudes decrease during the load acceptance process as well. The plunging mode of the RVR is more persistent than the rotating mode like in the previous case. The plunging mode mitigates around 3 s after the rotating mode disappearance.

Variation in the plunging and rotating modes of the RVR extracted from the pressure signals of the draft tube cone sensors during the load acceptance process is presented in Fig. 11. Opening the guide vanes is followed by a decrease in the amplitude of both plunging and rotating modes of the RVR. This starts with mitigation of the rotating mode at the draft tube cone entrance, i.e. location Cone1. This is followed by a sequential mitigation of the rotating mode from the cone entrance to its outlet. The rotating mode of the RVR disappears from the signals of the sensors at location Cone4 at around 23 s and simultaneously, the plunging mode disappears in all the signals. There is a delay of about 1.87 s in the disappearance of the rotating mode in Cone4 compared with Cone1 which can be translated to a RVR travelling velocity of 0.2 m/s in downstream-wise direction.

a) suction side-hub sensor (SS5)   b) suction side-tip sensor (SS1)

c) pressure side-hub sensor (PS6)   d) pressure side-tip sensor (PS3)

Fig. 10 Spectrograms of the pressure sensors during load acceptance from part load to the BEP.
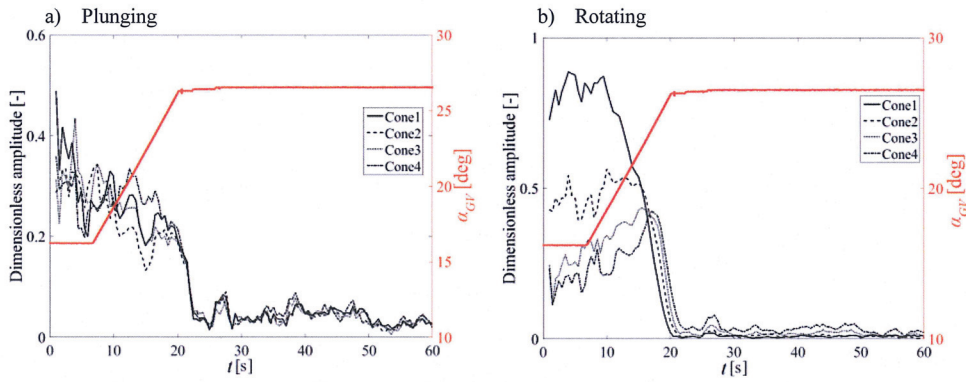
Fig. 11 Variation of the RVR amplitude during load acceptance from the part load operating point to the BEP.

Figure 12 shows the RVR travelling velocity along the draft tube cone during the load variations. The x-axis shows the absolute value of the guide vane movement velocity. The results show that the RVR travelling velocity increases with increasing the guide vane angular velocity in both cases of RVR formation and mitigation. Although, there is not any overlap between the angular velocity of the guide vanes in two cases of RVR formation and mitigation, 50% higher velocity during RVR formation can be an indication of higher RVR travelling velocity during RVR formation in comparison with RVR mitigation case.
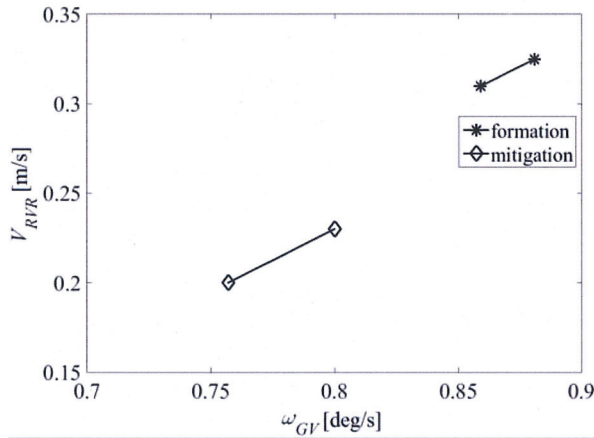
Fig. 12 RVR travelling velocity vs. guide vane angular velocity.

5. Conclusion

The effect of the load variations on the pressure fluctuations exerted on the rotating parts and the draft tube of a Kaplan turbine model was investigated. Different load acceptance and load rejections were investigated while the turbine operated under off-cam mode. The results showed that the transitions between the high load operating point and the BEP occur in a smooth manner. The distinctive phenomenon happening during a load rejection to the part load operating point was the RVR formation in the draft tube. The RVR formation starts with a sudden change in the pressure on the suction side of the blade, which can result in a sudden change of the thrust bearings load and output torque. The standard deviation of the pressure signals increases suddenly after the RVR formation. The RVR results in induction of two dominant frequencies on the runner; the rotating and plunging mode frequencies. The rotating component showed to be the dominant frequency during the part load operation. The plunging mode frequency appeared on the signals a couple of seconds ahead of the rotating mode. This is explained by the formation of the RVR at the end of the draft tube cone where the swirl number is higher. The RVR travels upstream with the guide vanes closure. The amplitude of the RVR in the plunging and rotating mode increases with the guide vane closure. The RVR mitigation process is showed to be similar but in a reverse order. The only difference was in the smooth disappearance of the RVR during the load acceptance compared to the RVR formation. Generally, the load rejection to the part load was the the most harmful load variation process for the turbine runner blades between the investigated load variations while the load variation in a RVR-free region was comparably safe.

Nomenclature

$c_p = \Delta P/(\rho g H)$	Pressure coefficient [-]	r	Radius [m]
f	Rotational frequency of the runner [Hz]	Re	Reynolds number of the turbine [-]
$f_{RVR,st}$	Frequency of the rotating vortex rope in the stationary frame (plunging mode) [Hz]	t	Time [s]
g	Gravitational acceleration [m/s^2]	t_{gen}	Transition time [s]
H	Head during the model test [m]	U	Axial velocity [m/s]
n_{ED}	Reduced speed of the turbine [-]	V	Tangential velocity [m/s]
P	Static pressure [Pa]	α_{GV}	Gguide vane angle [deg]
$\hat{P}$	Fluctuating component of pressure [Pa]	η	Turbine efficiency [-]
$\widetilde{P}$	Oscillating component of pressure [Pa]	ρ	Fluid density [kg/m^3]
$\overline{P}$	Time-averaged pressure [Pa]	$\sigma = \sqrt{\dfrac{\sum_{i=1}^{N}\left(P_i - \overline{P}\right)^2}{N}}$	Standard deviation
P_{out}	Output power [kW]	φ_{rot}	Phase of the pressure fluctuations due to the rotating mode of the RVR [rad]
Q_m	Model flow rate [m^3/s]	φ_{st}	Phase of the pressure fluctuations due to the plunging mode of the RVR [rad]
Q_{ED}	Reduced flow rate of the turbine [-]	ω_{GV}	Guide vane angular velocity [deg/s]

Super- and sub-scripts

*	Frequency is made dimensionless with respect to the rotational frequency of the runner, dimensions with respect to the runner diameter and velocities with respect to the reference velocity	O	Sensors is located on the outer part of draft tube
I	Sensors is located on the inner part of draft tube	BEP	best efficiency point

References

[1] Houde, S., Fraser, R., Ciocan, G., Deschênes, C., 2012, "Experimental study of the pressure fluctuations on propeller turbine runner blades: part 2, transient conditions," Earth and Environmental Science, Vol. 15, 062061.

[2] Gagnon, M., Leonard, F., 2013, "Transient response and life assessment: Case studies on the load rejection of two hydroelectric turbines," Proceedings of the International Conference Surveillance, Chartres, France, pp. 1-11.

[3] Gagnon, M., Tahan, S. A., Bocher, P., Thibault, D., 2010, "Impact of startup scheme on Francis runner life expectancy," Earth and Environmental Science, Vol. 12, 012107.

[4] Trivedi, C., Gandi, B. K., Cervantes, M. J., 2012, "Effect of transients on Francis turbine runner life: a review," Journal of Hydraulic Research, Vol. 51, No. 2, pp. 121-132.

[5] Kishor, N., Saini, R. P., Singh, S. P., 2007, "A review on hydropower plant models and control," Renewable and Sustainable Energy Reviews, Vol. 11, No. 5, pp. 776-796.

[6] Chirag, T., Cervantes, M. J., Bhupendrakumar, G., Dahlhaug, O. G., 2014, "Pressure measurements on a high-head Francis turbine during load acceptance and rejection," Journal of Hydraulic Research, Vol. 52, No.2, pp. 283-279

[7] Trivedi, C., Cervantes, M. J., Gandhi, B. K., Dahlhaug, O. G., 2014, "Experimental investigations of transient pressure variations in a high head model Francis turbine during start-up and shutdown," Journal of Hydrodynamics, Vol. 26, No., 2, pp. 277-290.

[8] Simmons, G. F., Aidanpää, J., Cervantes, M. J., Glavatskih, S., 2013, "Operational transients in the guide bearings of a 10 MW Kaplan turbine," International journal on hydropower and dams, Vol. 20, No.5, pp. 94-100.

[9] Simmons, G. F., 2013, "Journal Bearing Design, Lubrication and Operation for Enhanced Performance," Ph. D. Thesis, Luleå Univ. of Tech., Luleå, Sweden.

[10] Jansson, I., 2013, "Vibrant bodies of swirling flow: On the limits of mechanical power transformation," Ph. D. Thesis, Luleå Univ. of Tech., Luleå, Sweden.

[11] Mulu, B. G., Jonsson, P. P., Cervantes, M. J., "2012 Experimental investigation of a Kaplan draft tube – Part I: Best efficiency point," Applied Energy, Vol. 93, pp. 695-706.

[12] Jonsson, P. P., Mulu, B. G., Cervantes, M. J., 2012, "Experimental investigation of a Kaplan draft tube – Part II: Off-design conditions," Applied Energy, Vol. 94, pp. 71-83.

[13] Amiri, K., Cervantes, M. J., Mulu, B. G., 2015, "Experimental investigation of the hydraulic loads on the runner of a Kaplan turbine model and the corresponding prototype," Journal of Hydraulic Research, Vol. 53, No.4, pp. 452-465.

[14] Amiri, K., 2014, "An Experimental Investigation of flow in a Kaplan runner: steady-state and transient," Licentiate Thesis, Luleå Univ. of Tech, Luleå, Sweden.

[15] Amiri, K., Mulu, B. G., Raisee, M., Cervantes, M. J., 2015, "Unsteady pressure measurements on the runner of a Kaplan turbine during load acceptance and load rejection," Journal of Hydraulic Research, DOI:10.1080/00221686.2015.1110626.
[16] Amiri, K., Mulu, B. G., Cervantes, M. J., 2015, "Experimental Investigation of the Interblade Flow in a Kaplan Runner at Several Operating Points Using Laser Doppler Anemometry," Journal of Fluids Engineering, Vol. 138, 021106-2.

Paper F

Effects of Upstream Flow Conditions on Runner Pressure Fluctuations

Effects of upstream flow conditions on runner pressure fluctuations

K. Amiri[1], B. Mulu[2], M.J. Cervantes[1, 3], M. Raisee[4]

[1]Department of Engineering Science and Mathematics, Division of Fluid and Experimental Mechanics, Luleå University of Technology, Luleå, 971 87, Sweden, kaveh.amiri@ltu.se, michel.cervantes@ltu.se
[2]Vattenfall Research and Development, Älvkarleby, 814 70, Sweden, berhanu.mulu@vattenfall.com
[3]Department of Energy and Process Engineering, Water Power Laboratory, Norwegian University of Science and Technology, Trondheim, 7491, Norway
[4]Mechanical Engineering Department, University of Tehran, 14155-6448, Tehran, Iran, mraisee@ut.ac.ir

manuscript

Abstracts
The rotor-stator interaction and the corresponding pressure fluctuations represent one of the sources of pressure and load fluctuations on the rotating parts of rotating machineries. The high-Reynolds flow is subject to rotation in the comparably large vaneless space of axial turbines, causing wake interaction and wake dissipation in this region. This increases the level of flow complexity in this region. This study examined the effect of the flow condition entering the spiral casing on the flow condition within the distributor and the runner and the physical source of pressure fluctuations exerted on the runner of a Kaplan turbine model. Simulations were performed within the water supply system, including the upstream tank, penstock, and the volute, to determine the flow condition entering the spiral casing; the results were compared with laser Doppler anemometry (LDA) results. The results were considered as the inlet boundary condition for simulation of the turbine model from the spiral inlet to the draft tube outlet to investigate the flow condition within the distributor and the runner.

Introduction
The constant increase in demand for electricity has encouraged hydropower production companies to manufacture hydraulic turbines with higher output power and higher efficiency. In this context, manufacturing turbines with a wider operating range is desirable due to the fast growth rate of intermittent electricity generation systems and the use of hydraulic turbines in grid regulation. The responsibility of grid regulation increases transient and off-design operations in hydraulic turbines. This responsibility, together with the demand for manufacturing turbines with higher output power, contributes to increasing the level of fluctuations exerted on the rotating parts of turbines, i.e., the runner, runner bearings and bearings of the runner blades of Kaplan turbines. Among all fluctuation sources, the rotor-stator interaction is of particular importance because it always induces pressure fluctuations in the runner during both the steady-state and transient operation of turbines.

The rotor-stator interaction in Francis turbines has been subject of various experimental investigations. Farhat et al. [1] performed pressure measurements on the blades of a pump turbine model to measure pressure fluctuations exerted on the rotating parts of the turbine. The pressure fluctuations exerted on the runner blades of a Francis model and its corresponding prototype were investigated by Kobro [2]. Trivedi et al. used the same model as Kobro for pressure measurements on the runner blades during steady-state operation [3] and load variations [4-6]. In these studies, frequency analysis was performed on the acquired data to clarify the dominant frequencies exerted on different parts of the blades. The results indicated the presence of fluctuating forces at the runner frequency that could be due to the likely introduction of structural asymmetry in the manufacturing process, induction of flow asymmetries by the draft tube bend located downstream or an asymmetry in the flow entering the runner provided by the water supply system. However, the source of the disturbances was not clarified.

Although there is a close rotor-stator interaction in Francis turbines, the degree of interaction is lower in the case of axial turbines because of the comparably large vaneless space. The flow in this region is subject to rotation and wake dissipation, which make the flow condition more complicated compared to that in Francis turbines. Pressure measurements on the runner of a Kaplan model, known as Porjus U9, showed clear flow asymmetries at the distributor outlet [7]. Such asymmetry caused pressure fluctuations on the runner with respect to the runner frequency and guide vanes (GVs) passing frequency. However, the main source of pressure fluctuations cannot be determined by pressure measurements due to the limited information provided by such point measurements.

Numerical simulations can be used as a complementary tool for investigating flow conditions within a turbine conduit. They provide detailed information about the velocity and pressure fields over the computational domain and are proven to be capable of predicting different flow phenomena in axial hydraulic turbines. Petit et al. [8] simulated stationary parts of a Kaplan turbine model using steady-state incompressible RANS models. The simulation domain consisted of stationary parts located upstream of the runner, including the penstock, spiral casing, and the distributor. Simulations have also been performed to study the flow condition inside the draft tube separately. The results were validated using LDA measurements performed at the spiral inlet, within the spiral, and within the draft tube. Javadi and Nilsson [9] simulated the GVs, runner and draft tube of the turbine model using RANS equations with the RNG k-ε turbulence model to perform more detailed investigations of the flow condition within the runner and the draft tube. Liu et al. [10] performed an unsteady numerical simulation of a Kaplan turbine model to investigate pressure fluctuations in the distributor and the draft tube of the model. Liu et al. [11] simulated both the model of the Kaplan turbine used in the previous study and the corresponding prototype. They also studied the effect of the fluid-solid coupling during the numerical simulations on the pressure fluctuations of the prototype Kaplan turbine. Wu et al. [12] extended the previous studies by performing numerical simulations during on-cam and off-cam operations of the Kaplan turbine model and its prototype to perform a similarity study between the two cases. Vu et al. [13] and Nicolle et al. [14] investigated the effect of non-homologous blade geometries on the overall performance and flow condition within a propeller turbine model (named AxialT) and a Francis turbine. A numerical simulation of the flow in the complete model of the AxialT turbine was performed to investigate circumferential non-uniformities in the distributor and at the stay vanes inlet of an axial turbine by Gagnon et al. [15]. The results showed that flow non-uniformities are initiated at the admission duct. The simulation results were validated against LDA and PIV measurements to investigate the performance of the numerical models. Mulu et al. [16] performed

transient flow simulations on a Kaplan turbine model while operating at the best efficiency point (BEP), investigating 3D flows formed near the hub region and propagating downstream. Liu et al. [17] solved the equation of rotational motion of a runner, the continuity equation and unsteady RANS equations with the RNG k −ε turbulence model to simulate the runaway transient operation of a Kaplan turbine model. Fortin et al. [18] analyzed the AxialT turbine during runaway, with a special focus on the effect of the runaway on the pressure pulsations exerted on the runner. Compressible and incompressible simulations were performed to assess the impact of the weakly compressibility of water on the dynamic behavior of the flow. During the simulation, the variations in the head and the rotational speed acquired during the measurements were considered as input to the CFD solver to eliminate the associated potential source of error that can have a dramatic effect on the flow simulations. Kolsek et al. [19] proposed a novel tool for performing mesh generation that changes over time to take into account significant geometrical changes in the computational domain. The proposed method involves a moving computational mesh, which is a practically valuable method for simulating transient operating conditions in turbines involving GVs and/or runner blade movements. The method was implemented to simulate the shut-down of a bulb turbine as a complex case incorporating movements of both GVs and runner blades. Nennemann and Vu [20] simulated the GVs and runner of a Kaplan turbine prototype to predict the effects of cavitation on the runner and discharge ring in the case study. More recently, Kumar and Bhingole [21] implemented CFD methods to analyze the combined effect of cavitation and slit erosion on a Kaplan turbine.

The foregoing review of previous studies demonstrates the applicability of unsteady RANS methods in predicting different phenomena occurring within the conduit of axial turbines, such as separation, wake propagation, transient operations, and cavitation. However, the performance of numerical simulations in studying such flows is still under investigation. The fact that most numerical simulations investigating the flow condition inside hydraulic turbines are accompanied by experimental results for validation indicates that more investigations on the numerical simulation of hydraulic turbines are required to increase the reliability of the technique. More specifically, unlike in the case of Francis turbines, the interaction between the rotor and stator has not been deeply investigated in the case of Kaplan turbines. Although there is a close rotor-stator interaction in Francis turbines, the level of interaction is lower in the case of axial turbines because of the comparably large vaneless space. The flow in this region is subject to rotation and wake dissipation, which makes the numerical simulations more challenging compared with those of Francis turbines. The mesh quality, mesh element size, numerical dissipation and the effect of the mandatory use of general grid interface (GGI) between the stages should be controlled, and their effect on simulation of rotor-stator interaction should be considered.

The main purpose of the current study was to conduct a numerical investigation of the pressure fluctuations exerted on the runner of the Porjus U9 Kaplan model due to the interaction between the runner and the spiral casing/distributor of the model. Experimental investigations of the pressure fluctuations exerted on the runner of the Kaplan model showed clear flow asymmetries delivered to the runner of the model [7]. The source and location of the asymmetry were not identified by the measurements. The source of the asymmetry could be the flow condition at the spiral inlet, the geometry of the spiral casing or the distributor. The whole turbine model, starting from the upper tank of the test rig to the draft tube outlet, was simulated using the SAS-SST turbulence model. The model was divided into two sub-domains, and flow was simulated within each domain. The first domain included the inlet of the upstream tank to the outlet of the spiral casing, and the second included the inlet of the spiral casing to the draft tube

outlet. The results of the first simulation were used as the inlet boundary condition for simulating the second domain to investigate the effect of the flow condition at the inlet of the spiral casing on the fluid structure interaction. The results of the second domain clarified the source and the location of the asymmetries at the distributor outlet. The results were compared with LDA measurement results at the entrance of the spiral casing and pressure measurements performed on the runner blades.

Test case

A 1:3.1-scale model of a Kaplan turbine known as Porjus U9 was selected as the test case for numerical simulations and experimental investigations. The turbine is composed of a penstock to mimic the flow condition at the power plant, a spiral casing, a distributor consisting of 18 stay vanes and 20 GVs, a Kaplan runner with 6 blades, and an elbow-type draft tube following the runner. The model has a runner diameter of 0.5 m. It was tested at the head and rotational speed of 7.5 m and 696.3 rpm, respectively, to ensure kinematic similarity between the model and the prototype during the measurements. The BEP of the turbine was selected for this study. The corresponding GV angle for this operating point is 26.5º, resulting in a flow rate of 0.7 m^3/s through the model.

The model measurements were performed at the Vattenfall R&D model test facility in Älvkarleby, Sweden. The test rig is a closed-loop system designed for testing Kaplan, bulb and Francis turbines. Figure 1 shows the test rig with the Porjus U9 model installed between the upstream high-pressure tank and the downstream low-pressure one. The turbine head can be controlled by setting the power of the test rig pumps and independent adjustment of the pressure inside the upstream and downstream tanks. The ability to adjust the pressure inside each tank independently allows for adjustments of the turbine head as well as the absolute pressure within the draft tube to either trigger or prevent cavitation. Measurements were performed under cavitation-free conditions. The uncertainty in the flow rate and that in the hydraulic efficiency measurements were ±0.13% and ±0.18%, respectively; see Mulu et al. [22] for additional information about the test rig.
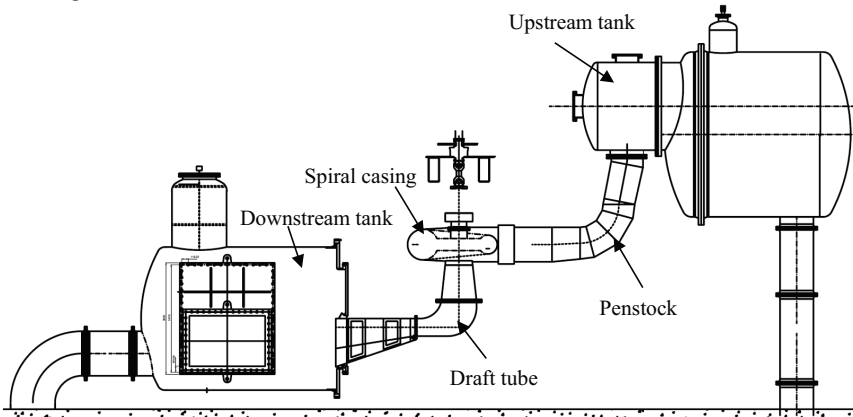

Figure 1   Schematic of the U9 model installed on the test rig.

Experimental measurements

Preliminary velocity measurements at the inlet of the spiral casing showed a complex flow condition at the measurement section, which may affect its performance [23]. In

4

this study, velocity measurements were performed at the inlet of the spiral casing to obtain the inlet boundary condition for the numerical simulation of the turbine. The goal of the simulations was to investigate the effect of the flow condition at the inlet of the spiral casing on the performance of the spiral casing in providing symmetrical flow to the runner.

The spiral casing was made of a stainless steel pipe with an inner radius of 316 mm at its inlet. A 290 mm long Plexiglas pipe was installed between the penstock and the spiral casing to provide the required optical access for LDA measurements; see Figure 2. The local index-matching box shown in Figure 2 was used to improve the measurement quality. A specific index-matching box consisting of a Plexiglas pipe with an axis normal to the axis of the penstock and high-quality glass with a diameter of 100 mm was manufactured to measure axial and tangential velocities along arbitrary radii. One end of the Plexiglas pipe was shaped to match the penstock pipe to prevent water leakage. The glass was mounted on the other side of the Plexiglas pipe. The space inside the index-matching box was filled with water as the index-matching liquid.
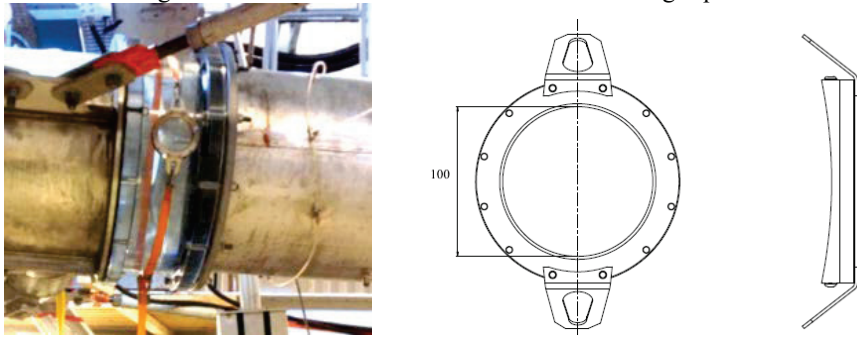

Figure 2   Inlet section of the spiral casing together with a sketch of the index-matching box.

The measurements at the inlet of the spiral casing were performed along five different radii separated by 45º. The measurement locations are presented in Figure 3. The limited power of the lasers restricted the possible measurement depth in water to approximately 430 mm. Hence, measurements along C-G were performed from both sides of the pipe to obtain the full velocity profile along the diameter. However, measurements from the top half of the pipe were not possible because of practical limitations.
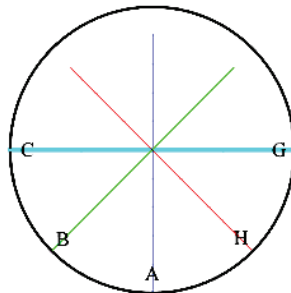

Figure 3   Location of the velocity measurements at the inlet of the spiral casing.

A two-component LDA system with an 85 mm optical fiber probe from Dantec was used to measure the velocity distribution at different locations of the turbine. A front lens with a 600 mm focal length was used for the measurements. The measuring

5

volume sizes based on the e^{-2} Gaussian intensity cut-off point were estimated to be 2.229 × 0.140 mm^2 and 2.426 × 0.147 mm^2 for the axial and tangential components, respectively. The measurements were performed in burst and coincidence mode, recording one pair of velocities (axial and tangential) for each passing particle during the measurements. The total sampling time was set to 240 s for each measurement point, which showed a good statistical convergence of the acquired signals. This sampling time corresponded to 100,000-200,000 bursts at each measurement location function of the position.

Pressure measurements were performed on the runner blades of the model while the turbine was operating at the BEP. Six piezo-resistive miniature pressure sensors manufactured by Kulite (LL-80 series) were flush mounted on the pressure side of one runner blade. The sensors were located on the vertices of a net formed by the imaginary circles passing through 1/3 and 2/3 of the blade span and 1/4, 1/2 and 3/4 of the blade chord lines. Six pressure sensors were also installed on the suction side of the adjacent blade to investigate the flow condition in one runner passage. Figure 4 shows the position of the sensors on the pressure side of Blade 1 and suction side of Blade 2. The signals from all the sensors were simultaneously recorded at a constant sampling frequency of 4 kHz. For more information about the measurements and the data acquisition system, see Amiri et al. [7].
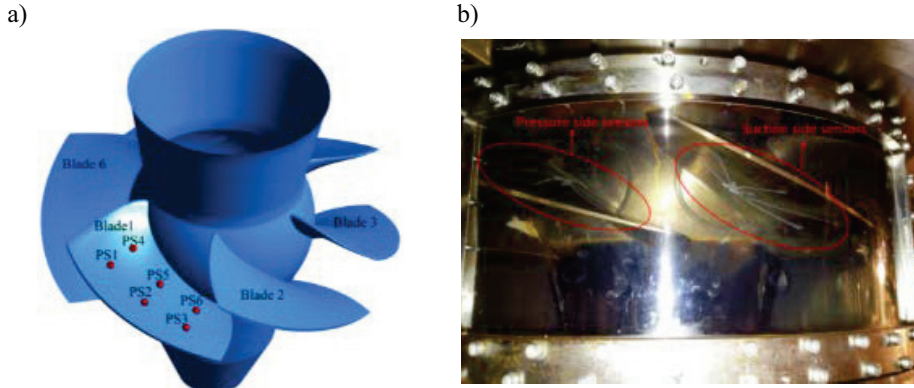
a)

b)

Figure 4   The position of the pressure sensors on the suction and pressure sides of the runner blades.

Numerical method

The main purpose of the numerical simulations was to determine the source of the pressure pulsations exerted on the runner while the turbine was operated at steady state. The source of the pulsations was assumed to be related to the inappropriate design of the spiral casing resulting in an asymmetric delivery of water to the runner or due to the flow condition at the spiral inlet. The flow condition in the whole turbine conduit was simulated through two separate domains to analyze the effects of each parameter on pressure pulsations exerted on the runner.

Computational domains and meshes

Flow was simulated within two computational domains to clarify the source of the pressure pulsations exerted on the runner presented by Amiri et al. [7]. The first domain comprised the parts located upstream of the distributor of the model: the complete upstream tank of the test rig incorporated with the penstock and the volute of the model

6

(water supply system domain). The second domain included different parts of the turbine from the inlet of the spiral casing to the draft tube outlet (turbine domain).

Water supply system domain

Initial investigations by Mulu and Cervantes [23] showed that the flow condition at the inlet of the spiral casing of Porjus U9 model is far from the ideal case of a fully developed pipe flow. Their measurements showed the presence of Dean-like vortices at the measurement location due to the upstream bend in the penstock, resulting in an inhomogeneous axial flow and vortical flow structures at the inlet of the spiral casing.

Refined LDA measurements were performed to investigate the flow condition at the inlet of the spiral casing to use the results as the inlet boundary condition for the "Turbine domain". However, the 2D LDA measurements do not provide any information about the radial component, making it impossible to predict the structure of the secondary flows at the measurement section. Such structures may disturb the flow condition within the spiral casing and affecting its performance. Hence, the flow was simulated within the penstock to capture the secondary flow structures and the radial velocity. The LDA results were used to validate the numerical simulations.

The numerical simulations of the penstock showed that the flow condition at the inlet of the spiral casing is influenced by the interaction between the penstock, upstream tank, and the spiral casing. Hence, these parts were included in the simulation. Figure 5 shows different parts incorporated to form the water supply system domain: the upstream tank in orange, the penstock in blue and the spiral casing in green.
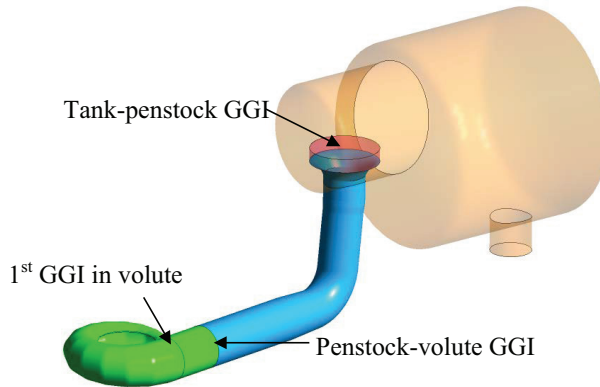

Figure 5   Different parts of the water supply sytem domain. Orange: upstream tank, blue: penstock, green: spiral casing, red: GGI between the upstream tank and the penstock.

The domain was composed of four mesh regions generated separately using ICEM CFD 16.0. A comparably course tetra mesh comprising ~147,000 nodes and ~822,000 elements with higher densities close to the funnel of the penstock was used to simulate the flow within the tank. The main interest in simulating the flow inside the tank was to approximate the flow condition at the inlet of the penstock instead of considering the mass flow rate as the inlet boundary condition of the penstock.

A high-quality hexahedral mesh with 1.9 million nodes was generated inside the penstock. The y^+ parameter was kept near unity to resolve the boundary layer. The minimum angle achieved in the mesh was 28.3º, which is higher than the recommended value of 20º for CFD simulations using ANSYS CFX software. The penstock mesh was interfaced with the tank mesh through a GGI. The GGI was cylindrical and located on top of the funnel at the penstock entrance instead of a simple circular one to increase the mesh quality close to the interface area. The geometric angle approached zero at the

funnel entrance, decreasing the mesh minimum angle to the geometrical value when using a circular interface at this location.

The spiral casing mesh was divided into three hexahedral mesh regions connected to each other through planar GGIs. The mesh was composed of approximately 2.1 million nodes. A few elements had an orthogonal angle less than 20º, with a minimum angle of 18.6º. The maximum y^+ was 40. The spiral casing was connected to the penstock through a planar GGI as well.

Turbine domain

The "turbine domain" incorporated all parts of the turbine model, including the volute; the distributor, which features 18 stay vanes and 20 GVs; the six-bladed Kaplan runner; and the elbow-type draft tube. This study focused on the interaction between the distributor and the runner.

The mesh generated for the volute to simulate the flow within the "water supply system domain" was used for this simulation as well. The distributor consisted of three types of water passages: two passages with only one GV (type one), seventeen passages incorporating a GV and a stay vane (type 2), and one passage with a GV and an extended stay vane operating as the tongue of the volute entrance (type 3); see Figure 6a. Each passage featured a separate mesh, and the meshes were connected to each other through GGIs at their interfaces, forming the whole distributor. The mesh quality was improved by using this method from a minimum mesh angle perspective. The minimum angle achieved in the distributor mesh was 20º. All specific features of the geometry in the distributor, including the overhang region, were considered during meshing. The distributor was connected to the volute through a GGI. The distributor mesh was composed of 4.3 million nodes. The maximum y^+ in the distributor was 80.

The runner blades were scanned using a 3D optical scanning apparatus (ATOS III system from GOM) with an accuracy of ±0.03 mm. A procedure similar to that used for meshing the distributor passages was considered for meshing the runner blade passages. The runner was composed of six identical runner blades. One passage was meshed using hexahedral elements, and the mesh was transformed and copied to form the whole runner. The minimum angle achieved was 16.8º. The mesh included all features of the geometry, including hub and tip clearances; see Mulu et al. [16]. A GGI was used at the interface between each two adjacent mesh regions. The runner mesh was composed of 2.7 million nodes, and y^+ was kept below 200 in the runner mesh region. A sketch of the runner is presented in Figure 6b. The runner is shown in gray, whereas the runner interfaces with the distributor and the draft tube are indicated by the blue and orange surfaces, respectively.

The runner was followed by the elbow-type draft tube shown in red in Figure 6c. The draft tube exit was extended by a 2 m long straight duct, and the outlet boundary condition was applied at the end of the duct. This is a standard procedure implemented in the simulation of draft tubes for the sake of convergence of the numerical simulations. The value of y^+ was kept close to unity in the draft tube mesh. The number of nodes in the draft tube mesh was 3.7 million. A GGI was used as an interface between the rotating runner mesh and the draft tube mesh.
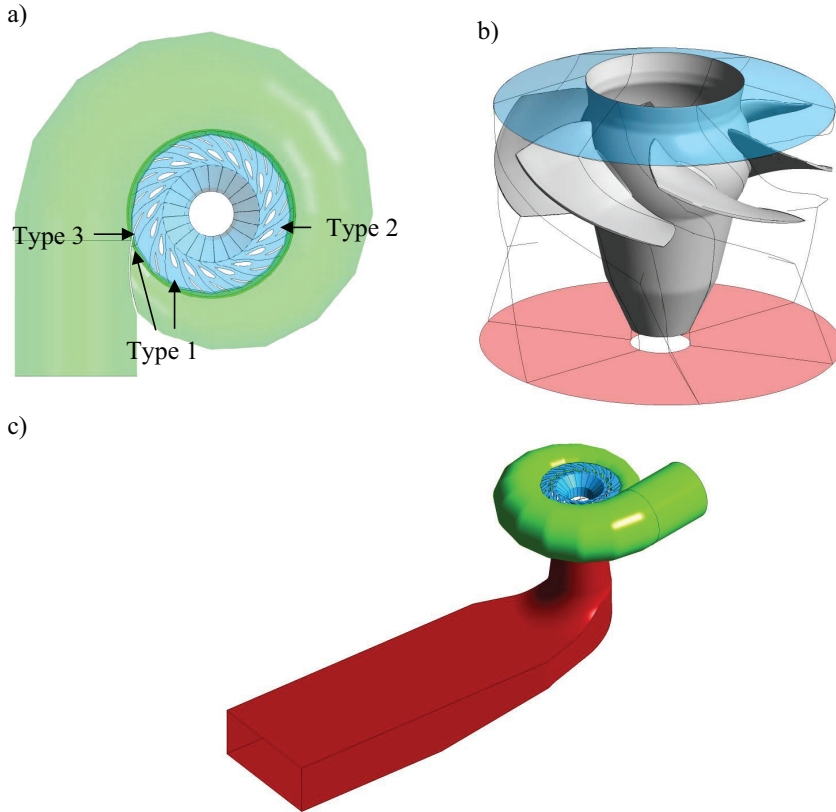
Figure 6   Sketch of different parts of the turbine domain: a) volute and the distributor, b) runner, and c) the whole domain.

Simulations

The commercial software ANSYS-CFX-16.0 was used in this study. The governing equations were the continuity and momentum equations for incompressible flows. The simulation methods and parameters considered in simulating the water supply system domain and the turbine domain are presented in the following sections.

Water supply system domain

Unsteady Reynolds-averaged Navier-Stokes equations (URANS) were solved considering incompressible flow. Flow within the penstock of the case study may undergo unsteadiness and flow separation due to the penstock bend, followed by a slightly diverging section. The Scale-Adaptive Simulation based on Shear Stress Transport (SAS-SST) model was used for turbulence modeling for the sake of closure of the equations. The SAS method is an improved URANS formulation, with the ability to adapt the length scale to resolve turbulent structures, resulting in LES-like behavior in unsteady regions of the flow field. The model provides standard RANS capabilities in stable flow regions. The SST model accounts for the transport of the turbulent shear stress and yields highly accurate predictions of the onset and the amount of flow separation under adverse pressure gradients.

The mass flow rate measured during the experimental investigation of the test case was considered as the inlet boundary condition to the inlet pipe of the upstream tank: $Q=0.7$ m^3/s. A medium turbulence intensity of 5% was considered for the flow

entering the tank. It is expected that this parameter does not affect the flow condition within the penstock due to the presence of the upstream tank. Flow at the outlet of the volute showed complex features comprising reverse flows. Hence, an "opening" boundary with 5% turbulence intensity was considered at the outlet of the volute, allowing for reverse flow to the domain. A relative pressure of zero Pascal was applied at this section. All the walls were considered to be smooth with a no-slip condition. An automatic near-wall function was employed for the treatment of the boundary layer. This feature automatically switches from wall functions to a low-Re near-wall formulation as the mesh is refined. Thus, flow is resolved in the near-wall region of the penstock, which is the main focus for this simulation.

"High resolution" was chosen for both the advection scheme and turbulence modeling in the solver. This scheme employs a blend factor that varies throughout the domain between second- and first-order accuracy based on the local solution field to avoid non-physical oscillations. The implicit time stepping of the second-order backward Euler method was implemented for the transient scheme, which is the recommended scheme for transient simulations in CFX.

The simulation started with a steady-state simulation of the domain using the SST turbulence model. The steady-state simulation result was considered as the initial guess to initiate the unsteady SAS-SST simulations. The transient simulation was run for 30 s with a time step of 0.01 s. The results were averaged over the last 10 s of the simulation when the flow was supposed to be developed inside the domain to present the average flow condition.

Turbine domain

The SAS-SST model was used to simulate the turbine model with advection, transient, and turbulence modeling schemes similar to those used for simulation of the water supply system domain. Two types of inlet boundary conditions were used at the inlet of the spiral casing: a mass flow rate of 0.7 m^3/s and the result of the numerical simulations from the water supply system domain at the inlet of the spiral casing. Using these conditions allowed for the investigation of the effect of the penstock geometry on the flow condition within the turbine and, more specifically, the interaction between the distributor and the runner.

The simulations began with a steady-state simulation of the turbine considering a frozen rotor at the interface between the runner domain and stationary domains located up- and downstream. The SST turbulence model was employed for the steady-state simulation. The result of the frozen rotor simulation was considered as the initial guess of the transient simulation, which employed a transient rotor-stator simulation at the interfaces between the runner and the stationary domains. The time step during the simulation was 0.239 ms, corresponding to approximately 1º of runner rotation. The simulation was run for approximately 2.7 s, corresponding to approximately 30 runner revolutions.

Results and discussions

Water supply system results

Flow within the water supply system of the turbine model was simulated to find the appropriate boundary condition that should be implemented at the inlet of the spiral casing for the numerical simulation of the turbine. Investigations of the flow condition within the penstock began with a simulation of the penstock together with the straight section of the volute, i.e., inlet of the spiral casing to the location of the "1st GGI in volute" shown in Figure 5. Three different meshes with 1.9, 3 and 7.5 million nodes in

10

the penstock were used for mesh sensitivity analysis using the SST model. The results of the streamwise velocity along Line A are presented in Figure 7. The figure also shows the streamwise velocity distribution after a pipe bend implementing PIV measurements [24] and LES simulations [25] of the case for comparison. The numbers in the legend of the figure represent the mesh size used for this study and the Reynolds number used during measurements and LES simulations. Two conclusions can be drawn from the results. First, the simulation results are independent of the mesh size when a mesh containing more than 1.9 million is used for the simulation. Second, the numerical simulation results are qualitatively similar to the PIV measurements of Kalpakli and Örlü [24] and the LES simulations of Röhrig et al. [25]. The quantitative differences can be explained by the difference in Reynolds numbers, and the difference in geometries and measurement locations between the current one and the ones presented in the references. However, the LDA results do not follow the variations in the current numerical simulations or those presented in the references. This finding suggests that the flow within the penstock is different from Dean-vortex-dominated flow after a pipe bend. Hence, it was concluded that the disturbances from either downstream or upstream components distort the flow within the penstock. The stationary components located after the penstock, i.e., the volute and distributor, were added to the domain; however, this placement did not affect the results at the LDA measurement section. Including the upper tank in the computational domain drastically affected the flow condition within the penstock.
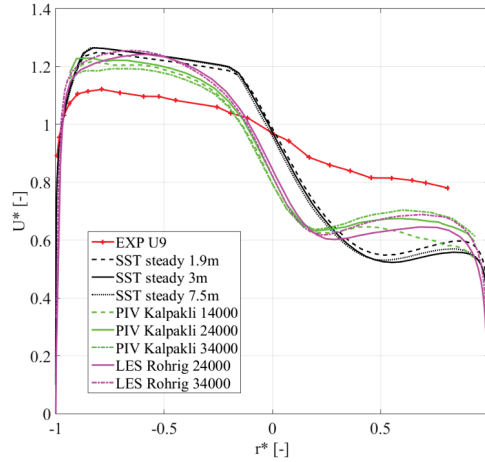

Figure 7   Numerical and experimental results at the inlet of spiral casing together with the results of Kalpakli and Örlü [24] and Röhrig et al. [25].

Figure 8 compares the streamwise velocity components obtained from CFD simulations with those acquired by LDA measurements. Adding the upper tank solved the problem associated with the high gradient of the streamwise velocity close to the pipe center. One of the main differences between the CFD and experimental results is the annular distribution of the streamwise velocity captured by the CFD simulations in sections Line A, Line B and Line H, which cannot be observed in the experimental data. In other words, the CFD results showed an increase in streamwise velocity close to the penstock walls, whereas the experimental results showed a decrease close to $r^*=1$ at sections Line A and Line B and close to $r^*=-1$ at Line H. Because the main phenomena resulting in such an annular flow distribution are the centrifugal forces exerted on the flow by vortices inside the flow, it can be concluded that the numerical simulations overestimated the strength of the vortices at this section. This overestimation may have

11

been due to either the performance of the turbulence model used for the simulations or the simulation of flow inside the upstream tank. As previously mentioned, a course tetra mesh was used to simulate the flow inside the tank, which may have affected the flow condition at the inlet of the penstock. Further investigation of these parameters is required to enhance the quality of the results. However, the results can still be used to study the effect of the flow condition entering the spiral casing on the flow condition within the volute and the distributor for the sake of sensitivity analysis.
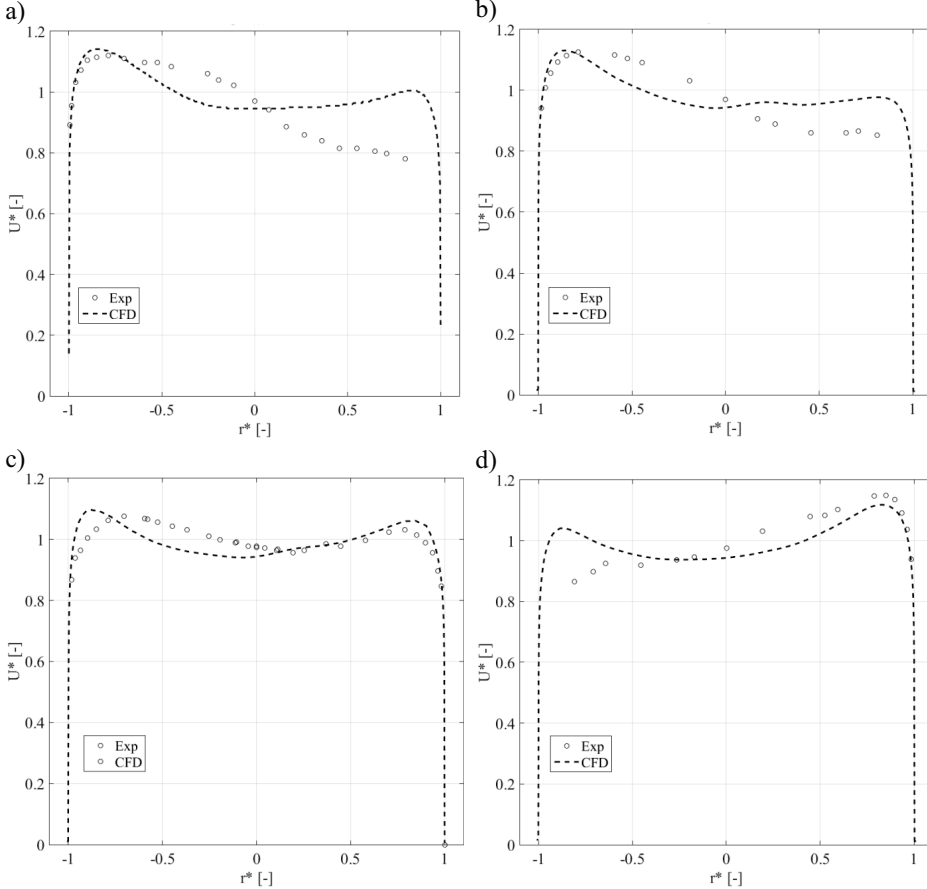

Figure 8   Streamwise velocities from experiments and CFD simulations: a) Line A, b) Line B, c) Line C-G, and d) Line H.

The contour of the streamwise velocity together with the corresponding in-plane vector map in the LDA measurement section is presented in Figure 9. The main flow features are qualitatively similar to those after a pipe bend: two counter-rotating vortices identical to Dean vortices after a pipe bend are clearly visible at this location, and flow is pushed towards the penstock walls. However, certain differences exist between the two cases. The symmetry of the Dean vortices is distorted at this location, and the axis connecting the centers of the vortices, indicated by a red line in Figure 9, is not horizontal. The asymmetry between the right and left halves of the penstock can also be observed in the contour of the axial velocity. The fact that the asymmetry was introduced into the penstock after considering the upstream tank in the computational domain confirms that the asymmetry was caused by the non-homogeneous flow fed to

the penstock by the upstream tank. Figure 10 shows a top view of the location where the penstock was connected to the tank through a bell-mouth. The contour and the vector map show the contour of the streamwise velocity and the corresponding in-plane vector map at the inlet of the penstock. It is worth noting that the axis of the tank was rotated by approximately 8.2° with respect to the axis of the penstock.
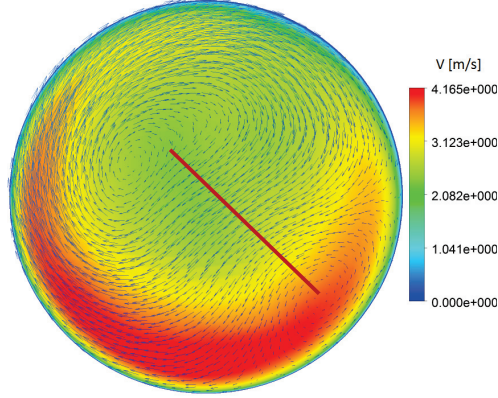

Figure 9   Contour of the streamwise velocity together with the corresponding in-plane vector map at the inlet of spiral casing. The red line connects the centers of the vortices.
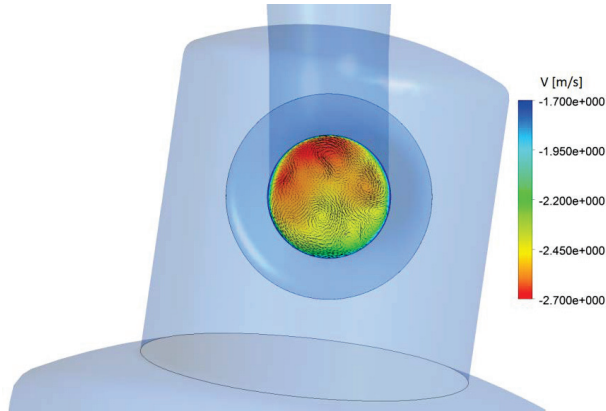

Figure 10   The contour of the streamwise velocity together with the corresponding in-plane vector map at the inlet of the penstock.

Turbine model

Two different velocity profiles were applied to the inlet of the spiral casing: plug flow and the results from the simulation of the water supply system domain. Figure 11 illustrates contours of velocity at the mid-section of the GVs together with the vector maps in two GV channels: one with flow separation and one without separation. The flow conditions within the distributor were similar when plug flow or the CFD result obtained from the water supply system simulation was used as the inlet boundary condition. In both cases, flow separation was captured on stay vanes 2 to 7. This is in agreement with the pressure fluctuations captured on the blades of the runner reported by Amiri et al. [7], where the results showed significant pressure fluctuations with respect to the GV/SV passing frequency on the runner for about 100° rotation of the runner.
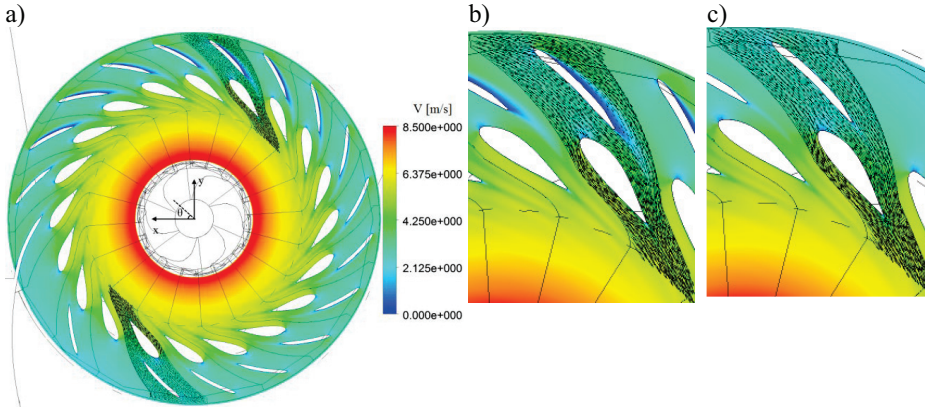
Figure 11   a) Velocity contours at the mid-volute section while plug flow is considered as inlet boundary condition to the spiral casing; b) flow conditions around GV number 6 (with separation) and c) flow conditions around GV number 16 (without separation).

Figure 12 presents the velocities and flow angle profiles upstream of the stay vanes and at the mid-height section of the distributor. The velocity components are presented in the cylindrical coordinate system where the axial component is aligned with the turbine axis; U_θ, U_r, and U_{ax} represent the circumferential, radial and axial velocities, respectively. The horizontal axis shows the circumferential position, θ, which is shown in Figure 11a. The flow angle is defined as the angle between the circumferential velocity and the velocity vector. The lip-entrance junction of the volute is represented by a sudden change in the profiles in each figure at approximately $\theta=340°$. As shown in the figure, changing the inlet boundary condition does not have any distinctive effect on either the flow angle or the radial and circumferential velocitiy components. However, the axial velocity profiles are different between these cases. The axial velocity is nearly zero in the case in which a straight plug flow is used as the inlet boundary condition, whereas it is almost negative along the entire circumference of the volute in the case in which the CFD simulation results are used as the inlet boundary condition. This finding demonstrates that the swirling flow structure implemented as the inlet boundary condition (see Figure 9) influences the flow in the whole circumstance of the volute. However, the flow condition downstream of this location, i.e. within the distributor shown in Figure 11, shows that the axial component of the velocity at the distributor inlet does not affect the flow condition within the distributor.

Figure 12d shows variations in the flow angle in the circumference of the volute. The two vertical green lines indicate the circumferential interval where the flow separates on the SVs. The lower flow angle at this location compared with the angles at the other circumferential locations causes a high angle of attack on the stay vanes, and ultimately, the flow is separated on the suction side of the stay vanes located close to this circumferential position. Optimizing the volute to prevent such flow asymmetry at the inlet of the distributor can always be considered as an option to improve flow symmetry delivered to the distributor and decrease flow losses associated with flow separation. However, because the flow is separated on the stay vanes by changing the angle of attack by only ~3° (see Figure 12d), another alternative can be replacing the current stay vanes with more hydraulically shaped ones using hydrofoils with a higher thickness-to-chord ratio. This option is more feasible for already manufactured turbines because it does not require design optimization of the spiral casing or modifying water supply systems that typically are not refurbished in power plants.
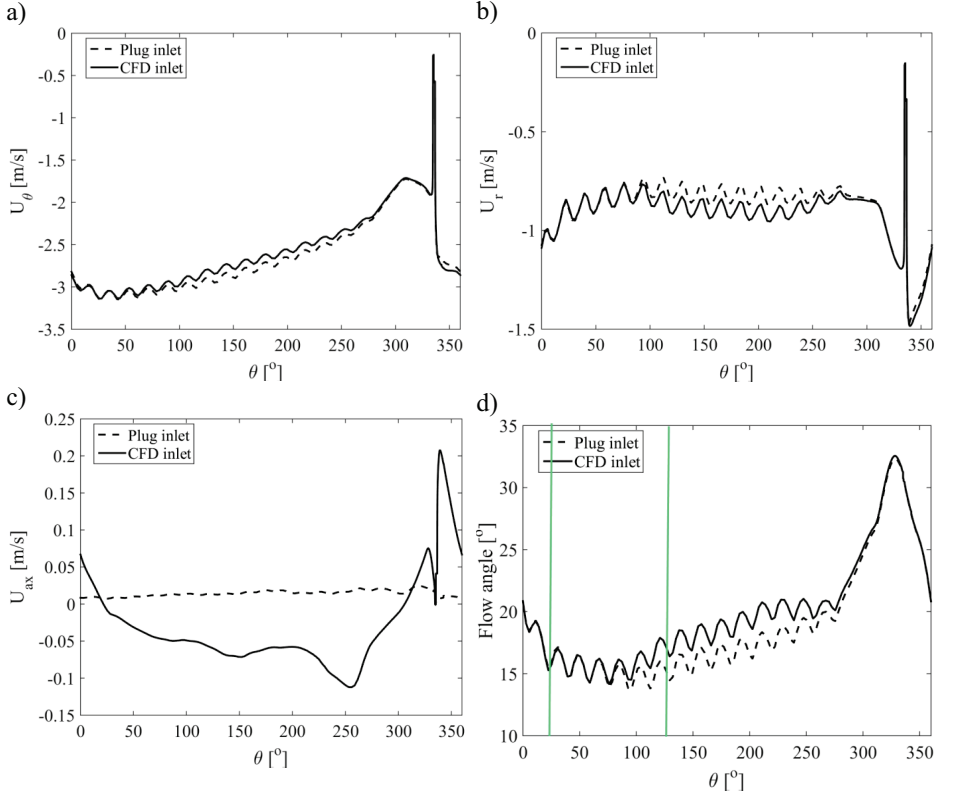
Figure 12   Velocity profiles and flow angle at the inlet of the distributor.

The velocity profiles together with the flow angle profile at the inlet of the runner are presented in Figure 13. As shown in the figures, the inlet boundary condition does not have any distinct effect on the magnitude of the velocity or flow angle fluctuations at the inlet of the runner.

Figure 14 presents amplitude spectra of the pressure signals from the sensors located on the suction and pressure sides of the runner blades, whereas the two different inlet boundary conditions are used for the simulations. The figure presents the results obtained from sensors located close to the shroud of the runner near the leading and trailing edges of the blades, PS1, PS3, SS1 and SS3 shown in Figure 4. In both simulations, the distinct frequencies in the spectra were the runner frequency and its harmonics. Similar results were obtained at the other sensors located on the runner blades. The results show that changing the velocity distribution at the inlet of the spiral casing due to the simulation of water supply system does not have any noticeable effect on the pressure fluctuations exerted on the runner. The results demonstrate that the dominant frequency is the runner frequency attributed to the variable flow angle and velocity magnitude at the inlet of the runner because of different signature for each guide vane wake.
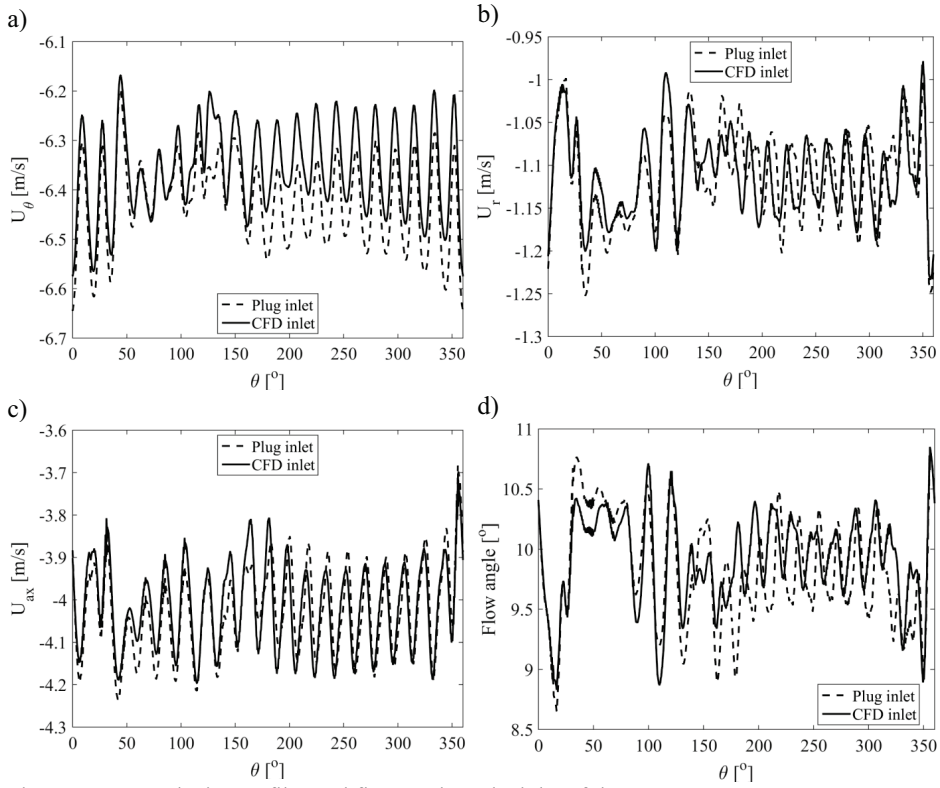
a)

b)

c)

d)

Figure 13   Velocity profiles and flow angle at the inlet of the runner.

Waterfall plots of the pressure signals obtained from all the pressure sensors on the runner blades from the numerical simulations as well as experimental investigations of Amiri et al. [7] are presented in Figure 15. The results presented in Figure 15a are the ones that were acquired from the numerical simulations using the CFD results at the inlet of the spiral casing. The results show that the frequencies are estimated accurately in the numerical simulations; however, the corresponding amplitudes are not. The amplitudes estimated by the numerical simulations are approximately one-third of the amplitudes determined experimentally. This discrepancy can be related to either the early dissipation of the wakes traveling downstream from the distributor due to the turbulence modeling and numerical dissipation or to the mesh density, which may not be appropriate in the distributor or the runner regions.
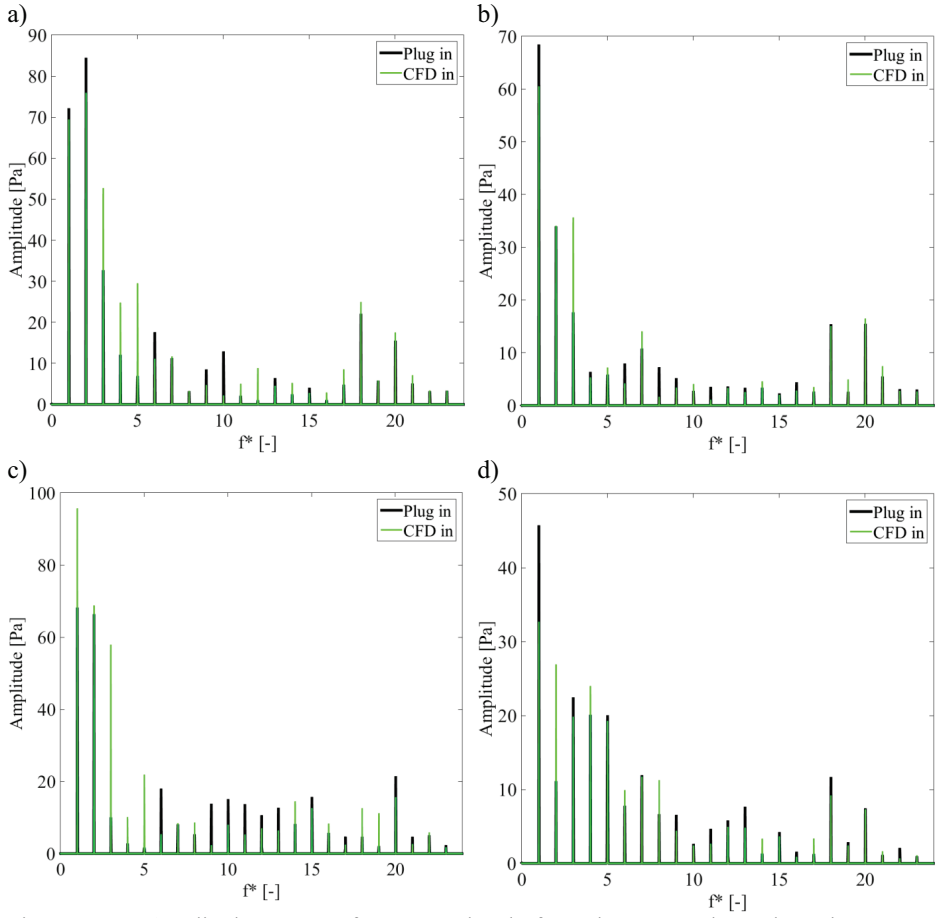
16

Figure 14   Amplitude spectra of pressure signals from the sensors located on the runner blades: a) PS1, b) PS3, c) SS1, and d) SS3.
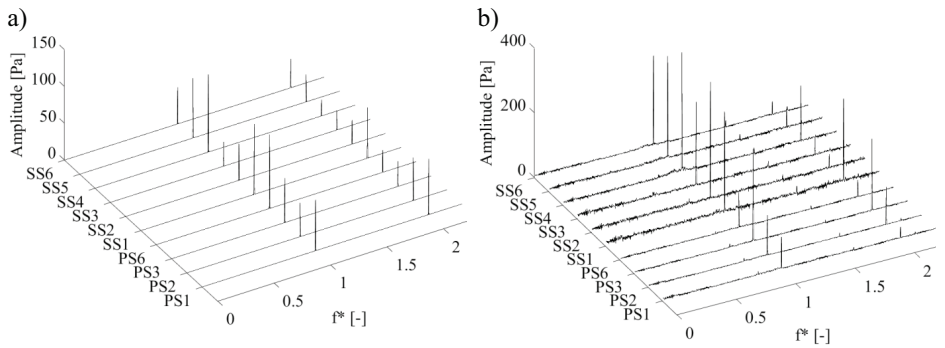

Figure 15   Waterfall plots of pressure sensors located on the runner: a) CFD simulations and b) experimental results from Amiri et al. [7]. The scales of the vertical axes are different in the two waterfalls.

Conclusions

Numerical simulations were performed to investigate the flow condition within the water supply system of the Porjus U9 model as well as within the turbine, and the results were validated against LDA and pressure measurement results. CFD simulations of the water supply system, including the upstream tank, the penstock, and the volute, showed that inhomogeneous flow with swirling structures was fed to the inlet of the spiral casing, in agreement with the LDA measurements performed at this location. Investigations demonstrated that the asymmetric flow fed by the upstream tank to the penstock affected the flow condition within the penstock and that at the inlet of the spiral casing. Hence, the inclusion of the upstream tank was essential for the flow simulation.

Two inlet boundary conditions were implemented at the inlet of the spiral casing for flow simulation within the model to investigate flow sensitivity within the turbine and pressure fluctuations in particular on the runner blades to the inlet boundary condition. The results showed that the inlet boundary condition does not have any distinctive effect on the flow condition within the volute and the distributor. In both cases, flow was separated on the suction side of stay vanes 2 to 7. The dominant frequencies were estimated accurately based on the amplitude spectra of the pressure fluctuations exerted on the runner blades. However, the corresponding amplitudes were underestimated by a factor of approximately 3. The preliminary results showed that numerical simulations are capable of predicting the effect of flow asymmetry at the distributor outlet of the model on pressure fluctuations exerted on the runner blades. However, further investigations are required to study the effect of the mesh quality and the modeling techniques on the results.

References

[1] Farhat, M., Avellan, F., and Seidel, U., 2002, "Pressure fluctuation measurements in hydro turbine models," 9th International Symposium on Transport Phenomena and Dynamics of Rotating Machinery, Honolulu, Hawaii, USA.

[2] Kobro, E., 2010, "Measurement of Pressure Pulsation in Francis Turbines," PhD thesis, Norwegian University of Science and Technology (NTNU).

[3] Trivedi, C., Cervantes, M. J., Gandhi, B. K., 2013, "Experimental and Numerical Studies for a High Head Francis Turbine at several Operating Points," Journal of Fluids Engineering, 135(11), pp. 1-17.

[4] Trivedi, C., Cervantes, M. J., Dahlhaug, O. G., 2015, "Experimental Investigation of a High Head Francis Turbine during Spin-no-Load Operation," Journal of Fluids Engineering, 137(6), pp. 1-10.

[5] Trivedi, C., Gandhi, B. K., Cervantes, M. J., 2015, "Experimental Investigations of a Model Francis Turbine during Shutdown at Synchronous Speed," Renewable Energy, 83, pp. 828-836.

[6] Trivedi, C., Cervantes, M. J., and Gandhi, B. K., 2016, "Investigation of a High Head Francis Turbine at Runaway Operating Conditions," Energies, 9(3) , pp. 1-22.

[7] Amiri, K., Cervantes, M. J., and Mulu, B., 2015, "Experimental Investigation of the Hydraulic Loads on a Kaplan Turbine Runner Model and Corresponding Prototype," J. of Hydraulic Research, 53(4), pp. 452-465.

[8] Petit, O., Mulu, B. G., Nillson, O., 2010, "Comparison of numerical and experimental results of the flow in the U9 Kaplan turbine model," 25th IAHR Symposium on Hydraulic Machinery and Systems, Timisoara, Romania.

[9] Javadi, A., and Nilsson, H., 2014, "Unsteady numerical simulation of the flow in the U9 Kaplan turbine model," 27th IAHR Symposium on Hydraulic Machinery and Systems, Montreal, Canada.

[10] Liu, S., Li, S., and Wu, Y., 2009, "Pressure Fluctuation Prediction of a Model Kaplan Turbine by Unsteady Turbulent Flow Simulation," Journal of Fluids Engineering, 131, pp. 1-9.

[11] Liu, S., Jie, S., Wu, S., 2008, "Numerical Simulation of Pressure Fluctuation in Kaplan Turbine," Sience in China Series E: Technological Sciences, 51(8), pp. 1137-1148.

[12] Wu, Y., Liu, S., Dou, H., 2012, "Numerical Prediction and Similarity Study of Pressure Fluctuation in a Prototype Kaplan Turbine and the Model Turbine," Computers & Fluids, 56, pp. 128-142.

[13] Vu, T. C., Koller, M., Gauthier, M., 2010, "Flow simulation and efficiency hill chart prediction for a Propeller turbine," IOP Conf. Series: Earth and Environmental Science, Timisoara, Romania.

[14] Nicolle, J., Labbe, P., Gauthier, M., 2010, "Impact of blade geometry differences for the CFD performance analysis of existing turbines," IOP Conf. Series: Earth and Environmental Science, Timisoara, Romania.

[15] Gagnon, J. M., Deschenes, C., Ciocan, G. D., 2008, "Numerical simulation and experimental investigation of the flow in an axial turbine," 24th IAHR Symposium on Hydraulic Machinery and Systems, Foz Do Iguassu, Brazil.

[16] Mulu, B. G., Cervantes, M. J., Devals, C., 2015, "Simulation-Based Investigation of Unsteady Flow in Near-Hub Region of a Kaplan Turbine with Experimental Comparison," Engineering Application of Computational Fluid Mechanics, 9(1), pp. 139-156.

[17] Liu, S., Zhou, D., Liu, D., 2010, "Runaway Transient Simulation of a Model Kaplan Turbine," Earth and Environmental Science, 12, 012073.

[18] Fortin, M., Houde, S., and Deschênes, C., 2014, "Validation of simulation strategies for the flow in a model propeller turbine during a runaway event," 27th IAHR Symposium on Hydraulic Machinery and Systems, Montreal, Canada.

[19] Kolsek, T., Duhovnik, J., and Bergant, A., 2006, "Simulation of Unsteady Flow and Runner Rotation during Shut-Down of an Axial Water Turbine," Journal of Hydraulic Research, 44(1), pp. 129-137.

[20] Nennemann, B., and Vu, T. C., 2007, "Kaplan turbine blade and discharge ring cavitation prediction using unsteady cfd," 2nd IAHR International Meeting of the Workgroup on Cavitation and Dynamic Problems in Hydraulic Machinery and Systems, Timisoara, Romania.

[21] Kumar, D., and Bhingole, P. P., 2015, "CFD Based Analysis of Combined Effect of Cavitation and Silt Erosion on Kaplan Turbine," Materials Today: Proceedings, 2, pp. 2314-2322.

[22] Mulu, B., 2012, "An Experimental and Numerical Investigation of a Kaplan Turbine Model," PhD thesis, Luleå University of Technology.

[23] Mulu, B., and Cervantes, M., 2010, "LDA Measurements in a Kaplan Spiral Casing Model," 13th Symposium on Transport Phenomena and Dynamics of Rotating Machinery, Honolulu, Hawaii, USA.

[24] Kalpakli, A., and Örlü, R., 2013, "Turbulent Pipe Flow Downstream a 90° Pipe Bend with and without Superimposed Swirl," International Journal of Heat and Fluid Flow, 41, pp. 103-111.

[25] Röhrig, R., Jakirlić, S., and Tropea, C., 2015, "Comparative Computational Study of Turbulent Flow in a 90° Pipe Elbow," International Journal of Heat and Fluid Flow, 55, pp. 120-131.